

Development of a magnetoresistive biosensor for the detection of biomolecules

PhD thesis in physics
by **Jörg Schotter**
born July 19th, 1975
in Friedrichshafen, Germany

University of Bielefeld
Department of Physics
Nano Device Group

October 28th, 2004

Declaration

I wrote this thesis by myself and used none but the indicated resources.

Bielefeld, October 28th, 2004

(Jörg Schotter)

Reviewers:

Dr. Hubert Brückl
Prof. Dr. Dario Anselmetti

Date of submission: October 28th, 2004

Motivation

This thesis is about a new detection method for molecular recognition reactions based on magnetic markers and magnetoresistive sensors. The markers are specifically attached to the target molecules, and their magnetic stray field is picked up by embedded magnetoresistive sensors as a change of electrical resistance. Compared to the established fluorescent detection method, magnetic biosensors have a number of advantages, including low molecular detection limits, flexibility and the direct availability of an electronic signal suitable for further automated analysis. This makes magnetic biosensors a promising choice for the detection units of future widespread and easy to use lab-on-a-chip systems or biochips.

Magnetic biosensors were made possible by the fast development of devices based on physical effects that relate an electrical resistance to external magnetic fields, namely the giant magnetoresistance (GMR) and the tunneling magnetoresistance (TMR). Due to their direct electronic translation and their small and scalable size which is also compatible with standard CMOS (Complementary Metal-Oxide Semiconductor) processing, magnetoresistive devices experienced a great boost within the last decade.

The GMR effect is based on spin-dependent scattering of the conduction carriers at ferromagnetic layers separated by non-magnetic metallic spacer layers. Depending on the interlayer thickness, the magnetization directions of the ferromagnetic layers spontaneously align antiparallel or parallel to each other, which is due to the so-called interlayer exchange coupling. It is based on the oscillating RKKY ([Ref. 1](#); [Ref. 2](#); [Ref. 3](#)) interaction between magnetic impurities in a non-magnetic base metal mediated by spin-polarized conduction electrons, and was first observed in the case of ferromagnetic thin films by Grünberg in 1986 ([Ref. 4](#)). At about the same time, it was discovered that the electrical resistance of such a sandwich system depends on the relative orientation of the magnetization directions of adjacent ferromagnetic layers, which can be forced from the initial antiparallel configuration into a parallel state by applying an external magnetic field ([Ref. 5](#)). Due to the large magnitude of the observed change of resistance compared to the usual anisotropic magnetoresistance (AMR), this effect was named giant magnetoresistance.

Another type of magnetoresistance was already observed in 1975 ([Ref. 6](#)), which is based on spin dependent tunneling of electrons from one ferromagnetic layer to another through a thin insulating barrier. Due to experimental challenges, it was not until 1995 that good quality magnetic tunnel junctions with large magnetoresistance ratios at room temperature could be fabricated ([Ref. 7](#)). The effect is called tunneling magnetoresistance (TMR). Other than in GMR systems, there is no interlayer exchange coupling through the barrier. Therefore, in TMR sensor applications the magnetization direction of one of the two ferromagnetic electrodes is generally pinned in a fixed direction, while the other one can rotate freely and follows an applied external magnetic field.

Initially, GMR based sensors were introduced as an improvement to already existing magnetic applications. For example, they replaced the previously employed AMR read heads in hard drives, initially launched by IBM in 1997 ([Ref. 8](#)). However, due to their excellent sensitivity to even small magnetic fields, GMR based field sensors now are also employed in other areas like rotary sensors in automotive applications ([Ref. 9](#)), current monitors ([Ref. 10](#)) or displacement sensors ([Ref. 11](#)).

While GMR devices experienced great success as direct magnetic field sensors, TMR systems will find their applications more in the field of computer memory or programmable logic. Other than GMR sensors, TMR devices include a thin insulating

barrier through which the electrons have to tunnel, which ensures a measurable electrical resistance even for very small sensor areas. Thus, by tailoring their characteristics to incorporate two separate resistance states at zero external magnetic field, integrated small-scale TMR sensor elements are a promising choice for nonvolatile memory arrays with storage densities comparable to today's DRAM (Dynamic Random Access Memory) technology. A great number of research teams both at universities and industrial companies are working towards this so-called MRAM (Magnetic Random Access Memory) chip, and the first commercial 4 Mbit demonstrator was presented by Motorola in October 2003 (Ref. 12).

Another promising application of TMR devices is the market of programmable logic. Other than conventional gates, logic devices composed of magnetoresistive elements can be switched to any functionality by adjusting the magnetization configuration of individual elements with the help of local magnetic fields induced by current pulses (Ref. 13). For example, Richter demonstrated a two input spin-logic gate consisting of four individual TMR elements that can be programmed on-chip to form a logic NOR or NAND function (Ref. 14). Such a concept enables a universal processor which can be reprogrammed to an optimized architecture for each specific task by suitable software, thus further decreasing computation times.

A rather recent idea is to combine magnetic markers and magnetoresistive detectors into a magnetic biochip. The pioneering work in the field of magnetoresistive biosensors was carried out by scientists at the Naval Research Laboratory (NRL), who developed the first prototype magnetoresistive biosensor called BARC (Bead Array Counter; Ref. 15; Ref. 16). It consists of patches of single GMR-type stripe sensors, each of which is capable of detecting a single magnetic microsphere. By now, a number of research groups are actively pursuing magnetoresistive biosensors, and the respective literature is summarized in chapter 1.3.

This thesis is focusing on large area magnetoresistive biosensors. The guideline for the design of the sensor elements is the size of a single probe DNA spot, which is typically from 70-150 μm in diameter for standard microarray spotters. Other than carried out by the NRL group, the distribution of magnetic markers within a single probe DNA spot is not resolved, but the average signal of each spot is measured. Therefore, the sensor elements are designed large enough to cover the entire area of a single probe DNA spot. Sensors based both on GMR and TMR are presented in chapter 1 and 1, and different methods of detecting magnetic markers with magnetoresistive sensors are demonstrated. The basic structure of currently available magnetic markers and their required properties are reviewed in chapter 1. Finally, a comparative DNA hybridization experiment between a magnetoresistive biosensor on GMR basis and standard fluorescent detection is presented in chapter 1.

Publications

J. Schotter, P.B. Kamp, A. Becker, A. Pühler, G. Reiss, H. Brückl, 2004. Comparison of a prototype magnetoresistive biosensor to standard fluorescent DNA detection. *Biosensors & Bioelectronics*, 19, 1149-1156

M. Brzeska, M. Panhorst, P.B. Kamp, J. Schotter, G. Reiss, A. Pühler, A. Becker, H. Brückl, 2004. Detection and Manipulation of Biomolecules by Magnetic Carriers. *Journal of Biotechnology*, 112, 25-33

W. Schepper, J. Schotter, H. Brückl, G. Reiss, 2004. Analysing a magnetic molecule detection system - computer simulation. *Journal of Biotechnology*, 112, 35-46

H. Brückl, M. Brzeska, D. Brinkmann, J. Schotter, G. Reiss, W. Schepper, P.B. Kamp, A. Becker, 2004. Magnetoresistive Logic and Biochip. *Journal of Magnetism and Magnetic Materials* (in print)

W. Schepper, J. Schotter, H. Brückl, G. Reiss, 2004. Single molecule detection with magnetic beads. *Journal of Magnetism and Magnetic Materials* (in print)

M. Brzeska, M. Justus, J. Schotter, G. Reiss, H. Brückl, 2004. Development of magnetoresistive sensors for the detection of single molecules by magnetic markers. *Molecular Physics Reports*, 39, 32

H. Brückl, J. Schotter, 2003. Magnetoresistiver Nachweis von Biomolekülen. *Technisches Messen*, 70, 577-581

H. Brückl, A. Thomas, J. Schotter, J. Bornemeier, G. Reiss, 2003. New Developments with Magnetic Tunnel Junctions. *Advances in Solid State Physics* 43, Springer Verlag Berlin, 397-411

H. Brückl, J. Schotter, 2003. Magnetoresistiver Nachweis von Biomolekülen. 6. Dresdner Sensorsymposium – Sensoren für zukünftige Hochtechnologien und Neuentwicklungen für die Verfahrenstechnik, Band 20, 83-88 (ISBN 3-935712-92-8)

J. Schotter, P. B. Kamp, A. Becker, A. Pühler, D. Brinkmann, W. Schepper, H. Brückl, and G. Reiss, 2002. A Biochip Based on Magnetoresistive Sensors. *IEEE Transactions on Magnetics*, 38, 3365-3367, 2002

Conferences

Talk at the “NATO Workshop Nanoscale Devices and Applications”, Kishinev, Moldawia, September 18th-22nd, 2004

Poster at the “1. BMBF Symposium Nanobiotechnologie“, Hannover, October 7th-9th, 2003

Talk at the “International Symposium on Bioconjugated Nanoparticles in Molecular Diagnostics and Therapy“, Jena, May 22nd-24th, 2003

Talk at the “Frühjahrstagung des Arbeitskreises Festkörperphysik der Deutschen Physikalischen Gesellschaft“, Dresden, March 24th-28th, 2003

Poster at the “293th Wilhelm und Else Heraeus Seminar Nanobionics II – from Molecules to Applications“, Marburg, September 22nd-26th, 2002

Talk at the “IEEE International Magnetics Conference“, Amsterdam, April 28th – Mai 2nd, 2002

Poster at the “Frühjahrstagung des Arbeitskreises Festkörperphysik der Deutschen Physikalischen Gesellschaft“, Hamburg, March 26th-30th, 2001

Table of contents

1. INTRODUCTION	1
1.1. Biochips: idea and applications	1
1.2. Classification of biosensor types	4
1.2.1. Detection methods employing markers	4
1.2.1.1. Fluorescent detection.....	4
1.2.1.2. Nanoparticle based detection.....	9
1.2.1.3. Electrochemical detection	10
1.2.1.4. Radioactive detection.....	12
1.2.2. Marker-free detection methods	13
1.2.2.1. Mass sensitive detection	13
1.2.2.2. Charge sensitive detection.....	14
1.2.2.3. Refractive index sensitive detection	15
1.2.2.4. Electrochemical oxidation of guanine bases	17
1.3. Magnetic biosensors	17
1.4. Summery	20
2. PREPARATION AND ANALYTICAL TOOLS	22
2.1. Film deposition	22
2.2. Vacuum furnace	23
2.3. Lithography	23
2.3.1. Resists and processing chemicals	23
2.3.2. Electron-beam lithography	23
2.3.3. Optical lithography	23
2.4. Etching	24
2.5. Energy dispersive X-ray sensor (EDX)	24
2.6. Film thickness measurement system	24
2.7. Atomic force microscope (AFM)	24
2.8. Magneto-transport measurements	25
2.9. Alternating gradient magnetometer (AGM)	27
3. MAGNETIC MARKERS	28
3.1. Basic requirements for magnetic markers in biosensors	28
3.2. Structure and common applications of magnetic microspheres	28
3.2.1. Principles of magnetic microsphere detection	29
3.2.2. Choosing microspheres as magnetic markers	32
3.2.2.1. Molecular recognition to biotin-labeled test DNA	33
3.2.2.2. Magnetic properties	35
3.2.2.3. Conclusions	38
3.3. Outlook: ferromagnetic nanoparticles as magnetic markers	38
4. THE SURFACE OF THE MAGNETIC BIOSENSOR	41
4.1. Passivation of the sensor	41
4.2. Probe-DNA immobilization	44
5. GMR-TYPE MAGNETIC BIOSENSOR	47
5.1. GMR theory	47
5.1.1. Interlayer exchange coupling	47
5.1.1.1. Introduction	47
5.1.1.2. Quantum well model	48

5.1.1.3. Phenomenological model.....	53
5.1.2. Giant Magnetoresistance	54
5.2. Sensor layout and characteristics.....	57
5.3. OOMMF model.....	61
5.4. Detection of magnetic markers.....	65
5.4.1. Reference signal	65
5.4.2. Response to magnetic markers.....	69
5.4.3. Dependence of the sensor signal on the marker coverage	77
5.5. Conclusions	81
6. TMR-TYPE MAGNETIC BIOSENSOR.....	82
6.1. TMR theory	82
6.1.1. Introduction	82
6.1.2. Tunneling through a barrier	84
6.1.3. Tunneling magnetoresistance	86
6.1.4. Exchange bias.....	88
6.1.5. Orange peel coupling	90
6.2. Sensor layout	91
6.3. Sensor characteristics	95
6.4. OOMMF model.....	99
6.5. Detection of magnetic markers.....	101
6.5.1. Perpendicular field method.....	101
6.5.2. Observation of the full free layer hysteresis curve.....	107
6.6. Conclusions	111
7. COMPARISON OF GMR- AND TMR-TYPE MAGNETIC BIOSENSORS	112
8. DNA-DETECTION AND COMPARISON TO FLUORESCENT METHOD	115
8.1. Outline of the experiment.....	115
8.2. Comparison of the signals	116
9. SUMMERY AND OUTLOOK	122
BIBLIOGRAPHY	124
ACKNOWLEDGEMENTS	138

1. Introduction

1.1. Biochips: idea and applications

Selective and quantitative detection of all kinds of biomolecules plays an important role in the biosciences, in clinical diagnostics and medical research, and also in environmental pollution control. So far, it is standard procedure to collect the samples on site and send them to specialized laboratories for analysis, which is pretty cost intensive and time consuming, since the required instrumentation is quite large and expensive and also calls for qualified personnel to carry out and judge the outcome of the multiple steps involved in the analysis. From an originally unprocessed specimen, for example a blood sample, these steps typically include separation and amplification as well as chemical modification and detection of the molecules in question.

Recently, the idea of integrating all these common laboratory tasks into a single easy-to-use portable device has received growing attention both by researchers and biotechnology companies (Ref. 17; Ref. 18; Ref. 19). The proposed lab-on-a-chip systems would effectively simplify many standard tasks in the areas of medical treatment or biochemical research, and could even open up completely new applications. For example, self-supporting body implants that constantly check the blood picture of patients carrying a great risk of lethal diseases are thinkable. Other possible applications include air or soil analyzers in possibly hazardous surroundings, or anywhere else where an immediate on-site test result is of importance. In fact, lab-on-a-chip systems are believed to possess a similar potential now as microelectronics did in the 1980s (Ref. 20), and the combination of these two fields will certainly lead to radically new technologies and devices with great impact on modern society.

In the past few years, there has been tremendous progress in the field of microfluidics. For example, Thorsen (Ref. 21) reported on large-scale integration using a fluidic multiplexor analogous to electronic integrated circuits, which enables individual addressing of one thousand independent compartments by only 22 outside control lines. Additional work on microfluidic DNA amplification (Ref. 22), microfabricated reaction and separation systems (Ref. 20) or entire lab-on-chip systems (Ref. 23) suggests that the preparation of biological samples for molecular detection in an integrated microfluidic device is evolving and will be commercially available within the next few years.

Concerning the molecular detection units of future lab-on-a-chip devices, different techniques are currently employed or actively researched. They are summarized in chapter 1.2. All of them rely on the principle of detection by hybridization, which allows a highly parallel analysis of many different biomolecules, each of them within a separate specifically functionalized sensor area. This method makes use of the lock and key principle common to most biomolecules. For example, antibodies bind specifically to certain antigens, and DNA always appears in two complementary strands. Therefore, by functionalizing specific small areas of a detector with a common sequence of single stranded DNA (so-called probe DNA), this area becomes sensitive to complementary DNA sequences in its vicinity (so-called analyte or target DNA). This principle is employed in DNA microarrays (also called DNA assays or DNA chips), where each micron-sized DNA spot consists of a specific sequence that probes the presence of complementary DNA strands in the sample solution. A DNA chip can consist of thousands of these spots, and they are typically produced by microarray spotters that put small drops (0.1–1 nl) of probe DNA onto a

sensor surface. Following the spotting procedure, the probe DNA strands are covalently coupled to the sensor surface in a so-called immobilization step. To analyze the composition of DNA sequences of a given sample, the solution is spread across the entire sensor surface, and matching probe and analyte strands hybridize to each other. Since the sequence and position of every probe DNA spot is known, the composition of the sample is mapped if the amount of hybridized analyte DNA is detected for each spot. The detection of the hybridization can be either direct or indirect. In the latter case, markers (e.g. fluorescent, radioactive or magnetic) are specifically bound to the hybridized analyte DNA only. This can be achieved by modifying the analyte DNA before hybridization with the probe. A common method is to attach functional molecular groups (positioned either at the 5' or 3' end of the sequence or internally; e.g. biotin) that bind specifically to the surface of the markers (e.g. streptavidin).

Most widely accepted is an indirect detection method with fluorescent dyes of different color, i.e. rhodamine (red) and fluorescein (green). In the future, the dyes will probably be more and more replaced by functionalized fluorescent semiconductor nanocrystals (e.g. CdSe or ZnS, [Ref. 24](#)), but the principle remains the same. The markers are stimulated by laser or ultraviolet light, and the fluorescent signal intensity is measured from each DNA spot with a suitable scanner. The color and intensity give information about the relative abundance of the corresponding analyte DNA sequence in the sample solution.

A typical task for DNA microarrays is the expression analysis of cells, which is about resolving the type and abundance of mRNA (messenger RNA) within a specific cell. Since the activity of proteins is directly connected to their corresponding mRNA abundance, information about the state of the cell can be derived, which is important for example to analyze the effect of viruses or active medicine ingredients. Normally, the cell of interest is compared to an untreated reference cell, so that the expression profile has to be taken from two samples. [Figure 1](#) displays the different steps involved in a comparative cellular expression analysis of HeLa cells (human epithelial or skin cells, [Ref. 25](#)). One group consists of non-infected reference cells, while the other is infected by HSV-1 viruses (Herpes simplex viruses type 1). The mRNA of each group of cells is isolated and transcribed into dye-labeled cDNA (complementary DNA), whereby red labels are used for the infected cells and green labels for the non-infected cells. Now, both cDNA samples are put together and hybridized to a previously produced DNA microarray, on which every probe DNA spot consists of sequences characteristic to one specific protein. After hybridization, the fluorescent signals of each probe DNA spot are taken by a laser scanner. Due to the different labeling, red spots indicate proteins mainly produced by the infected cells, whereas green spots reveal a decreased activity of the respective proteins in the infected cells compared to the non-infected cells. If both groups of cells produce about the same amount of a specific protein, the corresponding probe DNA spot appears yellow (equivalent mixture of red and green). Therefore, the complete impact of HSV-1 viruses on HeLa cells is studied in just one highly parallel experiment. Before the introduction of DNA microarrays, it was only possible to analyze one protein at a time, which greatly limited the throughput of genetic research and clinical diagnostics. By now, DNA microarrays are available from a large number of vendors, both prefabricated for specific common tasks and custom made. The most important companies include Agilent ([Ref. 26](#)), Affymetrix ([Ref. 27](#)) and Nanogen ([Ref. 28](#)).

Chapter 1: Introduction

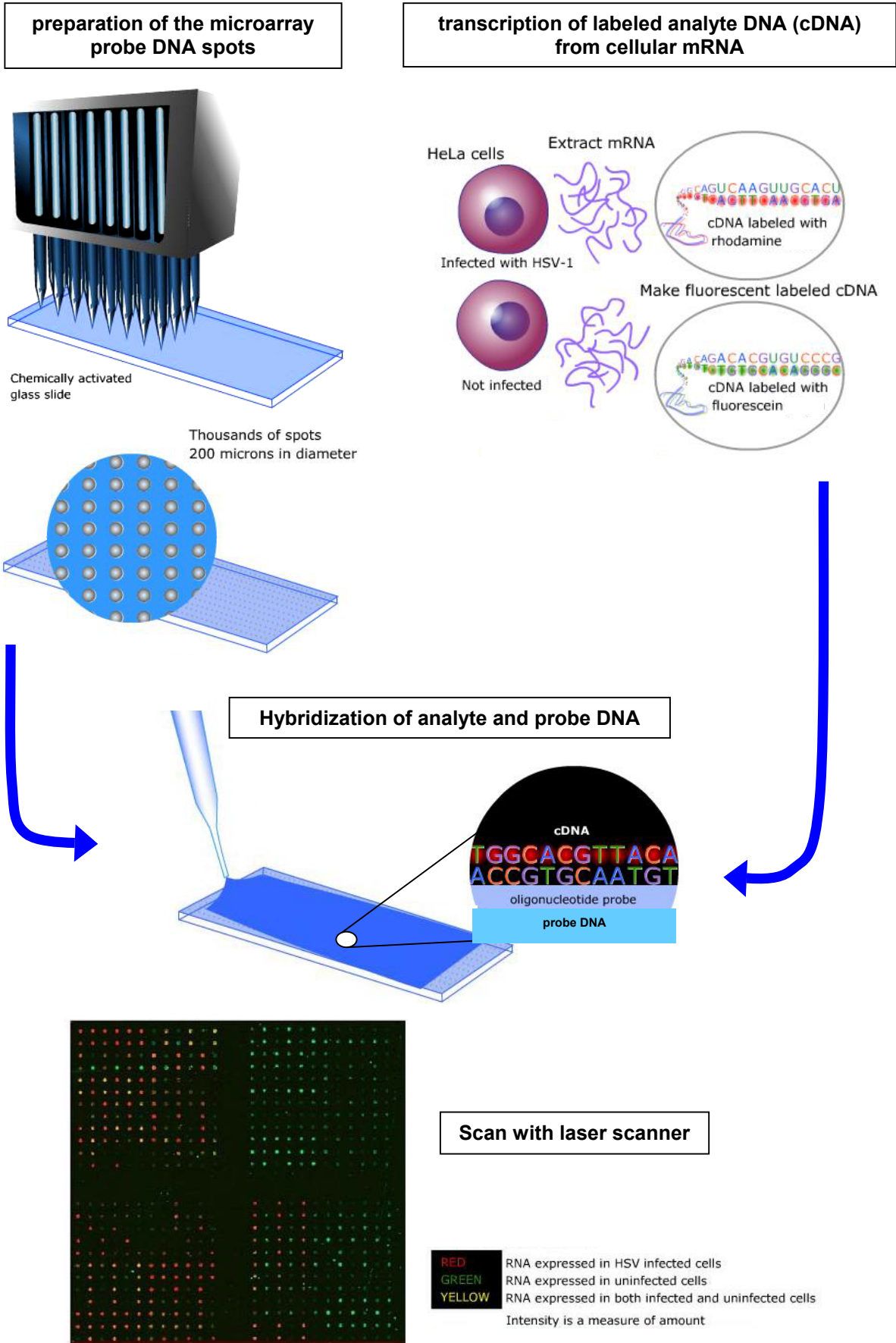


Figure 1: Gene expression analysis of non-infected and HSV-1 infected HeLa cells (taken from Ref. 25)

1.2. Classification of biosensor types

While the principle of sequence analysis by hybridization is common to all detection methods currently under consideration, there is a wide range of possibilities about how to identify the abundance of hybridized molecular pairs within a specific probe DNA spot. They can be classified into two major categories: the ones which add additional markers and the ones that try to detect the hybridization events directly. The former method has the advantage of large signals and low noise levels since the markers generally possess properties that can easily be distinguished from the other materials involved in the hybridization procedure (e.g. they emit light, transfer charge in an electrochemical redox process, or, as investigated within this thesis, produce a magnetic stray field). However, the use of markers requires an additional molecular recognition step, and because these are always dynamic equilibrium process between binding and unbinding events, they can never reach 100 % efficiency. Thus, there is always a percentage of hybridized pairs which do not contribute to the signal because no markers are bound to them.

From this point of view, a direct detection of hybridized molecular pairs would be advantageous, but sensing these events is rather challenging because there is no inherent difference in the kind of signal between single strands and hybridized pairs. Possible measurands are the mass or the charge of the molecules, but these signals only change incrementally when small amounts of analyte DNA are added to an already existing large number of probe DNA strands. Furthermore, other ingredients of the surrounding solution like trapped ions can falsify the outcome of the measurements, so that great care has to be taken in interpreting the results.

In the following subchapters, different current approaches for direct and indirect hybridization detection are presented.

1.2.1. Detection methods employing markers

In order to maintain the specificity of sequence recognition by hybridization, the markers must be coupled to the hybridized analyte DNA alone. Depending on the type of application, the analyte DNA is either transcribed from the original sample (e.g. RNA strands) or taken directly. In the former case, it is possible to directly incorporate labels into the transcribed DNA strands, but only if the marker molecules are small enough and can be coupled covalently to the nucleotides. A more general approach uses linkers like amino groups or biotin which offer specific binding sites to the markers. These capture molecules can both be attached to nucleotides for transcription processes or linked to complete analyte DNA strands, thus making this method very versatile. A comparison of different labeling methods for fluorescent tags can be found in [Ref. 29](#).

1.2.1.1. Fluorescent detection

In this type of detection method, the probe DNA is normally spotted onto silanized glass slides. Following immobilization and analyte hybridization, the fluorescent markers are excited either by a monochromatic (e.g. laser or LED) or a white light source (e.g. tungsten lamp or xenon arc lamp), and their emission is picked up by a suitable detector (e.g. a CCD camera). For microarrays, either the excitation or the detection has to be local in order to obtain separate data from the various probe DNA spots. The latter can be achieved by fluorescence microscopy, but the most common configuration relies on local excitation by scanning lasers with a typical spatial

resolution of a few microns, and photomultiplier tubes for signal detection. These so-called DNA microarray scanners are commercially available from a number of vendors, including for example Agilent (Ref. 26), Affymetrix (Ref. 27) or Nanogen (Ref. 28).

With respect to labeling, the first applicable organic dyes were fluorescein and rhodamine. Their emission maxima lie in the red and green, respectively. Though widely used, they have some serious disadvantages like rapid bleaching and a strong dependence of their emission spectra on the pH of the surrounding solution. Thus, great effort has been put into developing fluorescent dyes with improved characteristics, and by now, high quality labels can be obtained from a number of different sources. The most prominent include Alexa Fluor™ synthetic fluorochromes from Molecular Probes (Ref. 30) and CyDye™ fluorescent dyes from Amersham Biosciences (Ref. 31). The latter are cyanine dyes which consist of two aromatic units that are connected via a polyalkene bridge of varying carbon number that mainly governs the characteristic absorption and emission spectrum (see Figure 2 a). Most widely employed are dyes with 3 and 5 carbon atoms in the polyalkene bridge (denoted as Cy3 and Cy5), which emit light in the green and red spectral range, respectively (see Figure 2 b). Compared to traditional markers, these cyanine dyes show an enhanced water solubility, photostability, and higher quantum yields. They are also more stable and less sensitive to pH than their traditional counterparts. Additionally, the excitation wavelengths of the Cy series synthetic dyes are tuned specifically for use with common laser and arc-discharge sources.

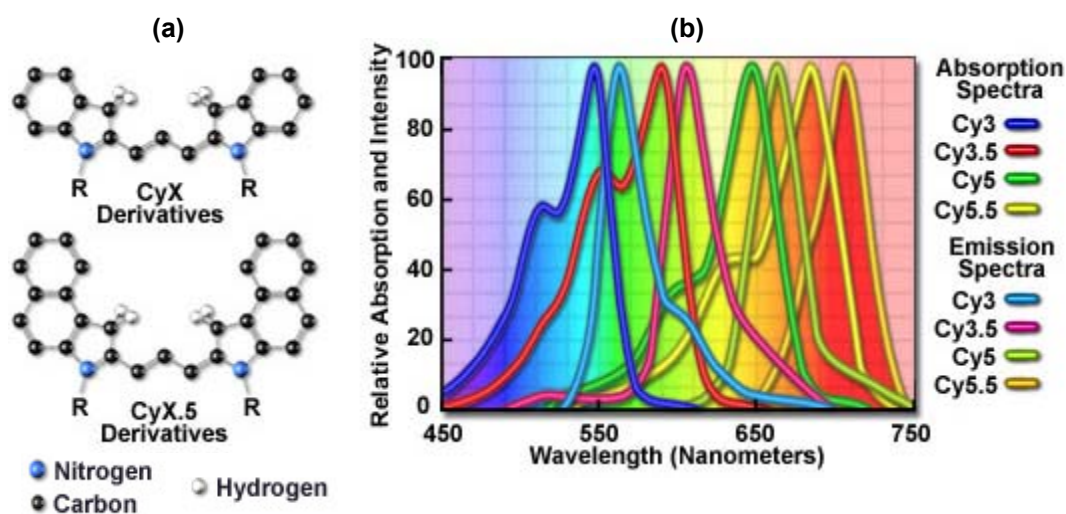


Figure 2: Properties of cyanine dyes (taken from Ref. 32)

a) molecular structure

b) spectral profiles

An alternative type of fluorescent labels are so-called molecular beacons which are able to signal the presence of unlabeled complementary analyte DNA strands (Ref. 33). They consist of a recognition sequence which is flanked on both sides by two short complementary strands (see Figure 3 a). Based on the FRET effect (fluorescent resonance energy transfer; Ref. 34), the ends of the entire sequence are labeled with a donor fluorophore (e.g. EDANS) on one side and an acceptor chromophore (e.g. DABCYL) on the other. In the absence of analyte DNA complementary to the recognition sequence, the short complementary strands on both ends hybridize and the molecular beacon remains in a bended hairpin shape with the donor and acceptor in close vicinity. Due to the strong $1/r^6$ dependence of the donor-acceptor

energy transfer (Ref. 34), the fluorescence of the donor is quenched by the acceptor in this configuration. Upon hybridization of a complementary analyte DNA strand to the recognition sequence, the beacon opens and the donor fluoresces uninhibited by the acceptor (see Figure 3 b). By this mechanism, unlabeled DNA can be detected, which is a simpler and faster approach that circumvents possibly problematic purification, amplification and labeling steps. Though compatible to any surface based detection method (see e.g. Ref. 35), molecular beacons can also be used to analyze DNA within homogeneous sample volumes (Ref. 33).

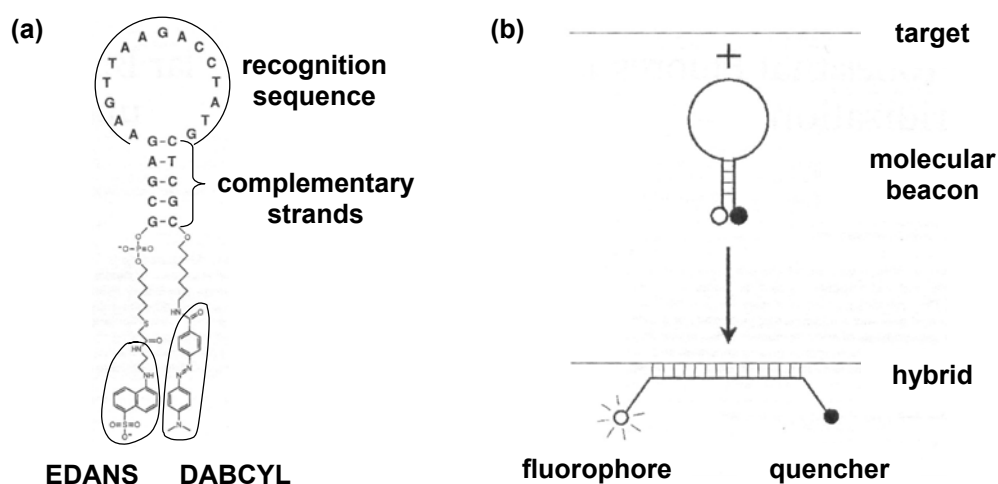


Figure 3: Molecular beacons (taken from Ref. 33)

a) structure

b) target DNA detection mechanism

Lately, advances in the controlled fabrication of semiconductor nanocrystals like CdSe or ZnS led to new improved fluorescent labels (Ref. 24). Because of their small size of only a few nanometers that is comparable to the bulk Exciton Bohr radius, the electron states in nanocrystals are quantized, which is why this class of materials is also called quantum dots. The spacing of the quantized energy levels depends on the size of the crystal, with smaller particles showing larger energy gaps. As a consequence, the band gap of semiconductor nanocrystals can be tailored by adjusting their size and shape (Ref. 36). This results in controlled optical properties through the mechanism of electron excitation and relaxation across the bandgap by photon absorption and emission. In principle, any photon with an energy larger than the band gap is capable of exciting an electron, so the adsorption spectrum is rather continuous up to a limiting wavelength (Ref. 37). Electron relaxation, however, mainly occurs near the edge of the bandgap, so the photon emission spectrum displays a sharp peak at a crystal size dependent wavelength (see Figure 4 b). Therefore, different colored nanocrystals can be excited with comparable efficiency by the same source (normally a laser in the ultraviolet), which is a clear advantage compared to organic fluorescent dyes. Furthermore, semiconductor nanocrystals also suffer less from photobleaching (Ref. 38), so they promise to be nearly ideal fluorescent markers if they can be functionalized effectively by biomolecules. Even though direct synthesis of semiconductor nanocrystals in aqueous solutions is possible, the size distribution and quantum yield for particles grown in organic solvents like TOPO (trioctylphosphine oxide) is superior (Ref. 38). The surface of the latter nanocrystals is hydrophobic, which makes them insoluble in the aqueous solutions required for biological applications. The easiest way to overcome this problem is to exchange the

original TOPO shell with bifunctional surfactant molecules that are hydrophilic on one end (e.g. carboxyl groups) and bind to the nanocrystals on the other end (e.g. via thiol groups). A more laborious but more stable method involves silanization of the particles (Ref. 38). At the surface of the silan shell, reactive crosslinker molecules like carboxyl (COOH) or amine (NH₂) can be attached that ensure covalent binding to biological conjugates (see Figure 4 a). With the problem of bioconjugation solved, semiconductor nanocrystals will most probably replace organic dyes for in vitro applications in the future due to their improved fluorescent properties (Ref. 24). However, their in vivo use remains problematic due to the toxicity of the semiconductor nanocrystal materials.

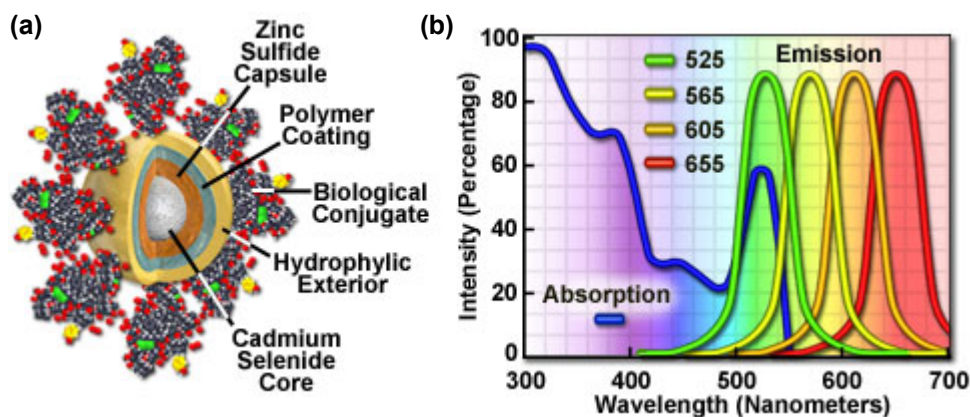


Figure 4: Properties of CdSe nanocrystal labels (taken from Ref. 32)

a) typical structure

b) absorption and emission spectra

In any case, currently available commercial DNA microarray systems still employ organic dyes as fluorescent labels. Their characteristics depend on a number of factors, the most important one being the type of experiment the array is used for. Possible applications include resequencing and mutational analysis (Ref. 39) or genetic disease diagnostics. However, the most important DNA microarray application at present is still expression profile analysis in biological research or drug discovery. Crucial issues in this respect include the amount of starting mRNA required, the total number of detectable genes per array, the discrimination of related genes and the dynamic range of the sensor. These quantities are affected by a number of issues, of which the final detection method for hybridized pairs is only but one. Therefore, it is only possible to compare the characteristics of complete systems. In the following, some of the presently most favorite commercial DNA microarray systems incorporating fluorescent detection units are presented.

The current market leader both in the fields of gene expression and mutational analysis is Affymetrix with the GeneChip™ system (Ref. 27). Other than cDNA microarrays which assemble probe DNA samples by microarray spotters, Affymetrix directly synthesizes arrays by photolithography and solid-phase chemistry which contain hundreds of thousands of oligonucleotide probes packed at extremely high densities. Each oligo consists of 25 nucleotides, and 11-16 of these oligos (called perfect match probes) specifically encode a certain gene (Ref. 40). By combining the signals from different probes, it is possible to obtain the same specific information as with cDNA microarrays, where each single spot represents an entire gene and contains the respective cDNA sequence with a length between 0.6 and 2.4 kb (Ref. 41). For reference purposes, the Affymetrix concept also includes single mismatch

Chapter 1: Introduction

oligo probes, so that an entire gene is represented by pairs of 11-16 oligonucleotides. The GeneChip™ is available for parallel analysis of up to 61.000 genes on one array, and it can reliably detect starting mRNA concentrations in the 1 pM range (Ref. 27). Another popular system is Nanogen's Nanochip™ (Ref. 28). Due to the limited number of 100 test sites on a single chip, it is used preferentially for mutational analysis. However, it involves a clever concept which draws functionalized probe DNA strands to single test sites by applying a voltage to that pad. Once the DNA arrives at the test site, it binds covalently to the surface through biotin-streptavidin bonds. Thus, a Nanochip™ can be prepared by the user without the need of a microarray spotter. Following probe DNA assembly, the labeled analyte molecules are hybridized across all pads, and the signals are read out by a fluorescence scanner. Due to the possibility of applying forces to the target molecules by putting a voltage across the pad, single base mismatches can be discriminated even after hybridization.

At the research level, there are several approaches to further improve sensor sensitivities, required starting material amounts and hybridization times of fluorescent biochips. One of the most advanced methods uses arrays of fiber optics to transmit the excitation light and the fluorescent signals from the labels. In these systems, each fiber can be functionalized with an individual oligonucleotide sequence at the distal end, while excitation and detection take place at the proximal end of the fiber. Advantages of these systems compared to arrays on glass slides include high density sensor packing, low sample volumes and fast hybridization. Initial work was on rather large low density arrays (7 fibers with a diameter of 200 μm each), in which the individual fibers were functionalized with oligonucleotides by separate immersion into an appropriate solution (Ref. 42). In this case, the detection limit for hybridizing complementary oligonucleotides was about 10 nM. However, much smaller optical fibers can be fabricated (e.g. with diameters of 3.5 μm; Ref. 43), thus enabling larger and more closely packed arrays (e.g. 6000 fibers in a bundle with a diameter of 500 μm; Ref. 43), but the question is how such small fibers can be functionalized individually. A demonstrated solution is to etch small wells into their distal ends and trap individual homogeneous microspheres with a little smaller diameter within these holes (see Figure 5).

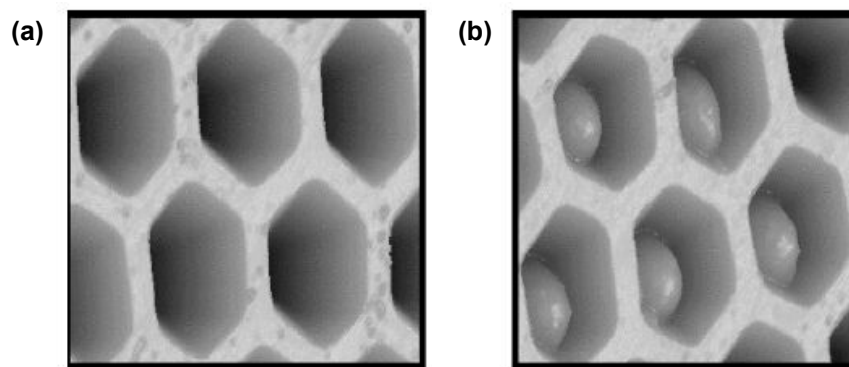


Figure 5: SEM micrographs of etched fiber bundles with a diameter of 3 μm (taken from Ref. 44)
a) empty fiber array
b) wells filled by suitably sized microspheres

The microspheres can easily be functionalized individually with desired oligonucleotide sequences, but since their distribution in the wells is random, they have to carry an additional label which can be read out afterwards to generate a map which relates individual fibers to the sequence carried by the microspheres loaded

within (Ref. 43). Therefore, the total number of different oligonucleotide sequences possible in such a microfiber array is determined by the number of distinguishable labels attached to (or within) the microspheres. So far, the discrimination of 25 sequences has been demonstrated on an array consisting of 6000 fibers (Ref. 43). Thus, hundreds of fibers carry the same sequence, which increases the signal to noise ratio of the measurements. However, a minimum number of fluorescent labels on each marker is necessary to obtain high enough signal levels from each individual fiber, so for detecting very low analyte concentrations, a compromise between good signal to noise ratio and measurable absolute signals has to be found. Walt et al. achieved reliable detection of 20-mer oligonucleotides down to concentrations of 100 aM in a total sample volume of 10 μ l, which corresponds to a number of only about 600 analyte DNA molecules totally and is amongst the best sensitivities reported so far (Ref. 45). Anyhow, to be of practical use in expression analysis, the total number of different detectable sequences has to be increased, which, due to the random nature of the array, is a non-trivial task.

1.2.1.2. Nanoparticle based detection

Related to fluorescent sensing schemes are methods that aim at detecting specifically bound metal nanoparticles directly through their optical characteristics. Because they are easily synthesized, chemically stable and readily attached to thiol functional groups of biomolecules, gold nanoparticles are the most prominent choice for this type of application. They are coupled to the target either directly before DNA hybridization (Ref. 46), or indirectly by ligand-receptor groups after DNA hybridization (Ref. 47).

Due to their large extinction coefficients (Ref. 48), it is possible to directly detect the number of bound particles on transparent substrates by optical absorbance measurements for high target concentrations (> 1 nM; Ref. 49). Lower analyte concentrations can be detected by the same instrumentation through the method of autocatalytic deposition of silver metal onto the gold nanoparticle seeds (Ref. 50). In this process, the substrate is immersed into a solution containing silver salt and hydroquinone, and the surface-bound nanoparticles catalyze the reduction of silver metal onto their surfaces, causing the particles to grow and the substrate to become increasingly more light absorbing. By this method, reliable detection of analyte DNA concentrations down to the fM range has been demonstrated (Ref. 51).

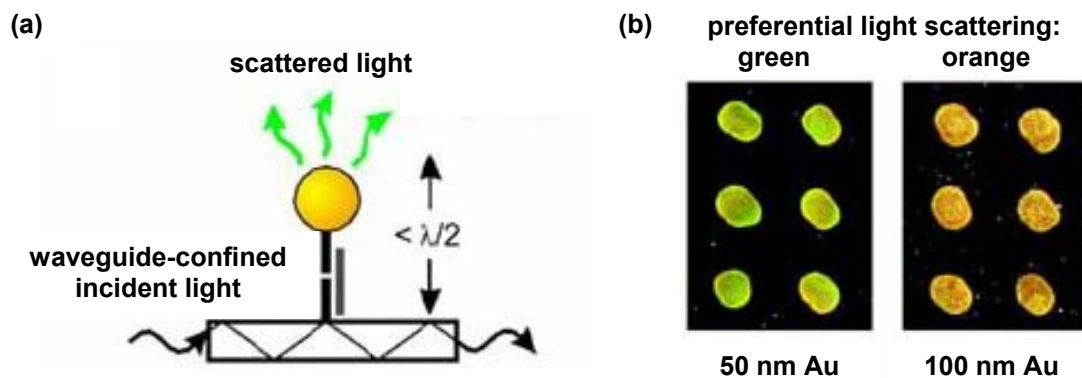


Figure 6: Evanescence light reflection by metal nanoparticles (taken from Ref. 51)

a) setup

b) reflected light from different sized gold nanoparticles

Another optical approach to detect surface bound nanoparticles is based on light scattering rather than absorbance. When light is injected into an array glass slide, it can be used as an internally reflecting waveguide (Ref. 52). Metal nanoparticles bound within the evanescent field of the waveguide scatter the light and can be imaged by standard microscopy (see Figure 6 a). Due to the limited range of the evanescent field (approximately half the wavelength of the employed incident light), only particles bound to the surface are detected by this method, thus allowing real-time measurements of analyte hybridization. Because the scattering spectrum of metal nanoparticles is size-dependent, multi-color labeling is also possible by this method (see Figure 6 b).

Apart from the mentioned methods, metal nanoparticles can also be detected by surface plasmon resonance (SPR; Ref. 53) or electrochemically (Ref. 54). SPR is described in more detail in chapter 1.2.2.3, and electrochemical detection is subject to the following section. In summary, metal nanoparticles provide a very sensitive and versatile method for analyzing biomolecules, and several companies are already offering or developing kits based on this approach (e.g. Nanosphere (Ref. 55) or Invitrogen (Ref. 56)). Thus, nanoparticle based DNA assays can be regarded as a serious competitor to the established fluorescent detection scheme.

1.2.1.3. Electrochemical detection

Apart from fluorescence, electrochemical detection is another popular method to analyze DNA sequences due to its simplicity, low instrumentation costs and high sensitivity. It is based on sensing an electrical redox current at the working electrode which originates from electron transfer to and from electroactive labels that bind to hybridized DNA pairs. The simplest protocol uses electroactive hybridization indicators such as cationic metal complexes (e.g. $[\text{Co}(\text{phen})_3]^{3+}$; Ref. 57) or planar aromatic organic compounds (e.g. daunomycin; Ref. 58) which preferentially interact with double stranded DNA only. Thus, their concentration at the electrode surface and, associated with that, the redox current increases proportionally to the amount of hybridized analyte DNA. By this method, a detection limit down to 1.8 fmol has been demonstrated (Ref. 59).

However, all of these hybridization indicators are not able to perfectly discriminate between double stranded and single stranded DNA, resulting in a rather large background signal proportional to the amount of immobilized probe DNA. Thus, it is advantageous to specifically link the electroactive labels to the analyte DNA alone before or after hybridization. These labels can be redox enzymes (e.g. soybean peroxidase; Ref. 60) or metal compounds like ferrocene. Figure 7 shows the principle of Motorola's eSensor™ (Ref. 61), which is based on electrochemical detection of target sequences by ferrocene labels on suitable signaling probes (Ref. 62). A thiol terminated self-assembled monolayer is coated onto the gold electrode that includes capture probe sequences on alkane linkers, oligophenylethynyl molecules as conductors between the electrode and the labels ('molecular wires') and insulating alkanes terminated by ethylene glycol to block access of redox species in solution to the electrode (see Figure 7 a). An electrochemical signal is obtained by specifically binding a ferrocene labeled signaling probe to the hybridized target sequence. Mediated by the molecular wires, electrons from the labels can flow to the electrode (Figure 7 b), and the dependence of the magnitude of the oxidation current on the potential at the working electrode (voltammogram) gives a signal proportional to the amount of hybridized target DNA. In Figure 7 c), the solid curve shows the response to 1 μM of target DNA and 2.5 μM of signaling probe, while the dashed line

represents the reaction to the same amount of signaling probe alone. The current obtained in the latter case is purely capacitive and misses the characteristic faradaic peak. It arises from oxidation of the hybridized labels, and its height is a measure of the target DNA concentration. On Motorola's eSensorTM, up to 16 different sequences can be detected in one cartridge, and the reader itself is capable of analyzing 48 cartridges at a time (Ref. 61). The system is rather inexpensive and has proven to be quite successful on the biochip market. Because no large optical equipment is necessary, there is also the potential to fabricate a portable device, which is currently under development at Motorola (Ref. 63).

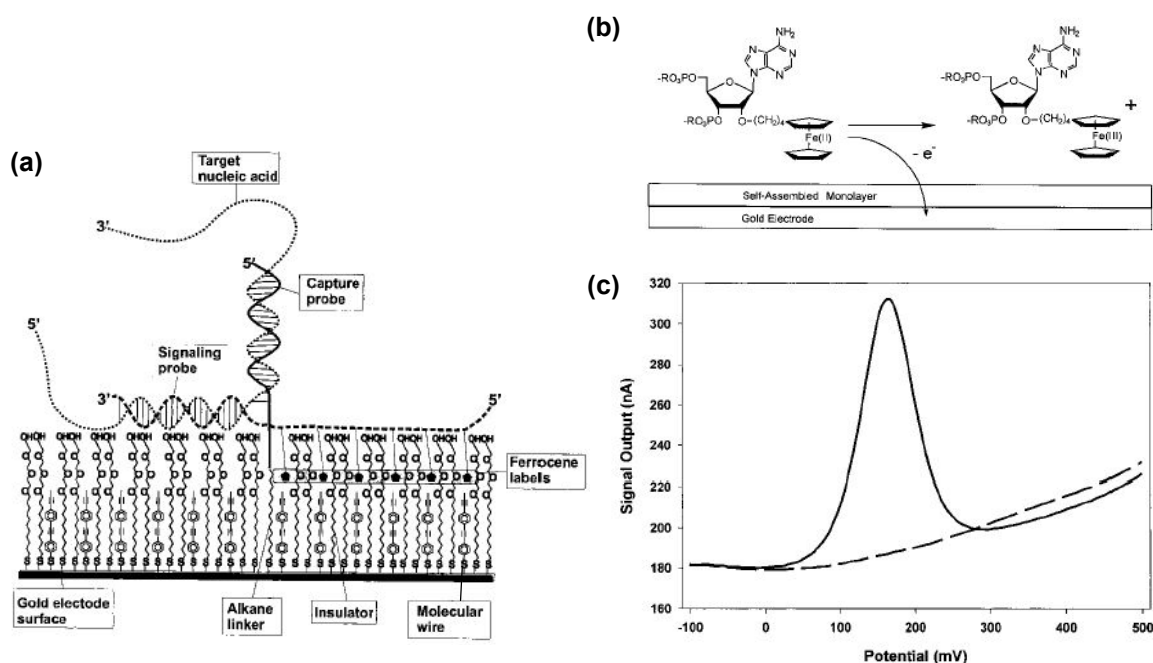


Figure 7: Electrochemical detection of DNA by the Motorola eSensorTM (taken from Ref. 62)

a) schematic diagram of the interface

b) sketch of the oxidation process at the working electrode

c) typical voltammograms with (solid) and without (dashed) target DNA present

Another type of electroactive label are metal nanoparticles, which can be dissolved into aqueous metal ions by a suitable etchant solution (e.g. HBr/Br₂). Next, the ions are sensed electrochemically at the working electrode (Ref. 51). The method is called anodic stripping voltammetry (Ref. 64), and has been used traditionally for trace metal measurements. Due to the large signal obtained from even single labels, the detection limit can be pushed down to the fM domain by this method, which is amongst the best sensitivities reported so far (Ref. 65).

Another approach is to induce absorption of insoluble molecules onto the working electrode surface, thus causing measurable changes in the faradaic electrochemical impedance. Generally, the electronic transport through a working electrode can be described by the equivalent circuitry shown in Figure 8 a), where R_s is the ohmic resistance of the electrolyte, Z_w denotes the Warburg impedance which results from the diffusion of ions from the bulk electrolyte to the electrode interface, C_{dl} is the double layer capacitance and R_{et} stands for the electron transfer resistance of the redox probe (Ref. 66). These factors can be quantified by measuring the impedance at different frequencies and plotting its imaginary part Z_{im} over the real part Z_{re} in a so-called Nyquist diagram, which typically consists of a semicircular region followed by a straight line (see Figure 8 b). The semicircular region is observed at higher

frequencies where the current is limited by the electron transfer process, whereas the linear part is characteristic to lower frequencies with a diffusion-limited current. In such a diagram, the diameter of the semicircle is equal to R_{et} , and C_{dl} can be obtained from the characteristic frequency $\omega_0=1/(C_{dl}R_{et})$ that is reached at the maximum value of Z_{im} in the semicircular region (Ref. 66). Relative to an unmodified electrode surface, any adsorbed insulating layer causes an increase of C_{dl} and R_{et} , which translates into a larger semicircle in the Nyquist diagram. To produce measurable signals, the group of Itamar Willner catalyzed the precipitation of insoluble phosphates onto the electrode by the use of enzymes which are attached specifically to the hybridized target DNA (Ref. 67). The corresponding impedance measurements before (dots) and after (triangles / squares) addition of a 27-mer target oligonucleotide (5 μ M) are shown in Figure 8 b) for different phosphate complex formation methods. The large signals which can be obtained that way allow reliable detection of analyte DNA down to a concentration of about 50 fM (Ref. 67).

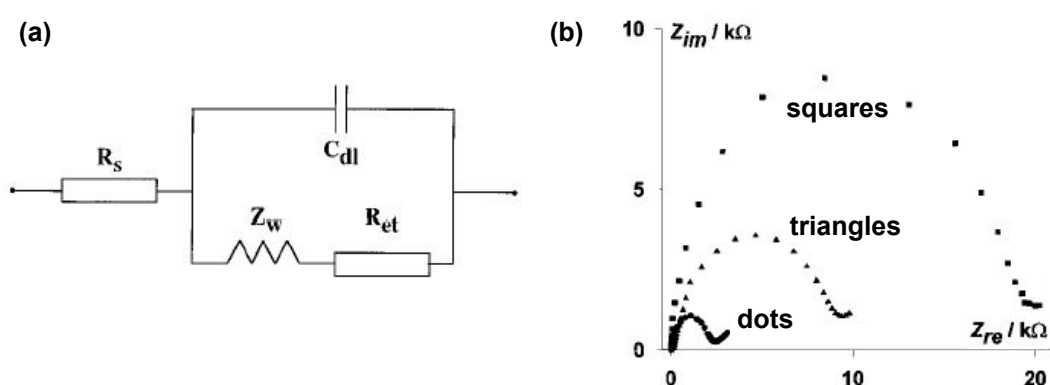


Figure 8: Faradaic impedance spectroscopy at electrode surfaces

a) equivalent circuit (taken from Ref. 66)

b) exemplary Nyquist diagrams (taken from Ref. 67)

Apart from the described methods, there is also the possibility to directly oxidize the guanine bases within the analyte DNA at the electrode surface without the need of any labels. This alternative is discussed in chapter 1.2.2.4.

1.2.1.4. Radioactive detection

Radioactive labels have a long history in bioanalysis, which is mainly due to the fact that they are readily integrated into biomolecules and can be detected quite sensitively by simple methods. Unlike all other types of labels, probe molecules which are chemically identical to unlabeled species can be constructed from radioactive isotopes (e.g. ^3H , ^{14}C , ^{33}P or ^{35}S), thus avoiding any distortions in intermolecular recognition reactions like hybridization. This principle has been applied long before the introduction of microarrays in the so-called Southern and Northern blotting analysis to identify the sequence of certain DNA and RNA bands after gel electrophoresis. In these methods, the DNA bands are denatured and transferred from the gel onto a nitrocellulose paper, resulting in immobilized single-stranded sequences at the respective band positions on the paper. Next, radioactively labeled probe DNA is hybridized and visualized by autoradiography, revealing the position of the band with a sequence complementary to the probe (Ref. 68).

Radioactively labeled DNA can be obtained directly during the transcription process from mRNA in expression analysis applications by building the cDNA from radioactively substituted nucleotides like ^{35}S -dATP or ^3H -dCTP (Ref. 69).

Alternatively, polynucleotide kinase can be used to label the 5'-end of completed DNA strands with radioactive nucleotides like ^{33}P -dATP (Ref. 70). In any case, strong radioactive signals are possible by massive labeling without affecting the biochemistry of the molecules.

For not too demanding applications with respect to parallelism, relatively simple nylon macroarrays with 50-2000 different probe spots can be employed in expression profile analysis using radioactively labeled target DNA and phosphor imagers or even X-ray films for image acquisition (Ref. 71). This method is quite cheap and gives good sensitivity values comparable to more elaborate fluorescent detection schemes (Ref. 72). In principle, it could be improved further to generate radioactive microarrays with superior detection limits (Ref. 72) and multi-analyte capability by employing different radioactive labels and energy-sensitive readers (Ref. 69). However, radioactive labels are potentially hazardous to the health of the user and also costly to dispose, which makes them rather unsuitable for the mass market. Anyhow, this detection method is still valuable for some demanding high sensitivity applications and continues to be under research.

1.2.2. Marker-free detection methods

Label-free strategies are generally suitable for in-situ realtime measurements and lead to simple operation protocols, which is attractive from an application point of view. Furthermore, they eliminate undesirable effects like steric impediments, binding biases or instabilities of markers. However, since analyte and probe DNA generally are of the same nature, any signal derived from them directly is also already present for single stranded DNA and only changes incrementally upon hybridization. In order to still ensure sensitive measurements, the operational requirements are generally more limiting than for methods employing labels, and the cost of the necessary instrumentation is higher (Ref. 63). This is why most current DNA chips use fluorescent or electrochemical methods, even though there are a number of promising label-free detection methods under development.

1.2.2.1. Mass sensitive detection

A rather obvious measurand for direct hybridization detection is the surface mass loading, which increases linearly with increasing number of hybridized target DNA. Ultra sensitive mass measurements are possible by measuring the resonance frequency of a quartz crystal microbalance (QCM, e.g. SiO_2 or ZnO ; Ref. 73), which is commonly of the order of tens of megahertz. By immobilizing probe DNA on one side of the QCM and immersing it into a solution containing the target DNA sequences, the resonant frequency changes according to the mass density of hybridized DNA (Ref. 74). By this method, sub-nanogram mass changes can be detected in realtime, which makes it a powerful way to determine binding and dissociation rate constants (Ref. 63). Furthermore, reliable detection of perfect match as to single base mismatch targets has been demonstrated by the QCM method (Ref. 75), and a sensitivity limit of about 60 nM has been shown for the specific detection of a 31-mer oligonucleotide (Ref. 76). Though some work on expanding this method into a multi-array format has been reported (Ref. 77), the number of independent measuring probes is currently too small to be used in highly parallel gene expression analysis, so the QCM method will most probably stay limited to a small number of specialized applications.

1.2.2.2. Charge sensitive detection

The phosphorous backbone of single DNA strands carries one electron charge per base (Ref. 68), which makes charge sensitive detection methods another way to directly sense DNA. Generally, this is done by hybridizing the target DNA to the surface of semiconductor field effect devices in an electrolyte solution and employing electrochemical methods to sense changes in the flatband potential of the semiconductor (Ref. 78). In its simplest version, a semiconductor-insulator structure is taken as the working electrode. With the insulating layer brought in contact with the electrolyte solution, such a system behaves similarly to a metal-oxide-semiconductor (MOS) device (Ref. 79). In particular, the flatband potential of the semiconductor (i.e. the bias voltage at which the semiconductor is electrically neutral) is quite susceptible to charges accumulating at the insulator surface. It is obtained by measuring the complex impedance of the device at varying bias voltages with a small superimposed high frequency excitation (around 100 kHz for typical systems). Figure 9 a) shows a sketch of the resulting real (Z_p) and imaginary (Z_q) impedance components as a function of potential against the reference electrode (Ref. 79). For the imaginary part, there are three distinct regions which correspond to well-known operational states of the MOS device, i.e. the accumulation (inversion) regime for positive (negative) potentials and the depletion regime at intermediate potentials, which shows up as a strong decrease of Z_q . From this curve, the flatband potential V_{fb} can be determined by extrapolating the slope of Z_q in the depletion regime to the applied potential axis (Ref. 79). If the charge at the insulator-electrolyte interface is modified, the underlying semiconductor compensates for this modification by a new charge distribution inside its space charge layer to maintain electrical equilibrium. Thus, a change in the flatband potential is induced, which is reflected by a displacement of Z_q along the potential axis. This is demonstrated in Figure 9 b), which shows the expected shifts due to accumulation of additional charge with hybridization of complementary analyte DNA. By denaturing the hybridized pairs, the additional charge is removed again and the original curve is restored (Ref. 79). By this method, detection limits down to about 100 pmol of analyte DNA have been demonstrated (Ref. 80).

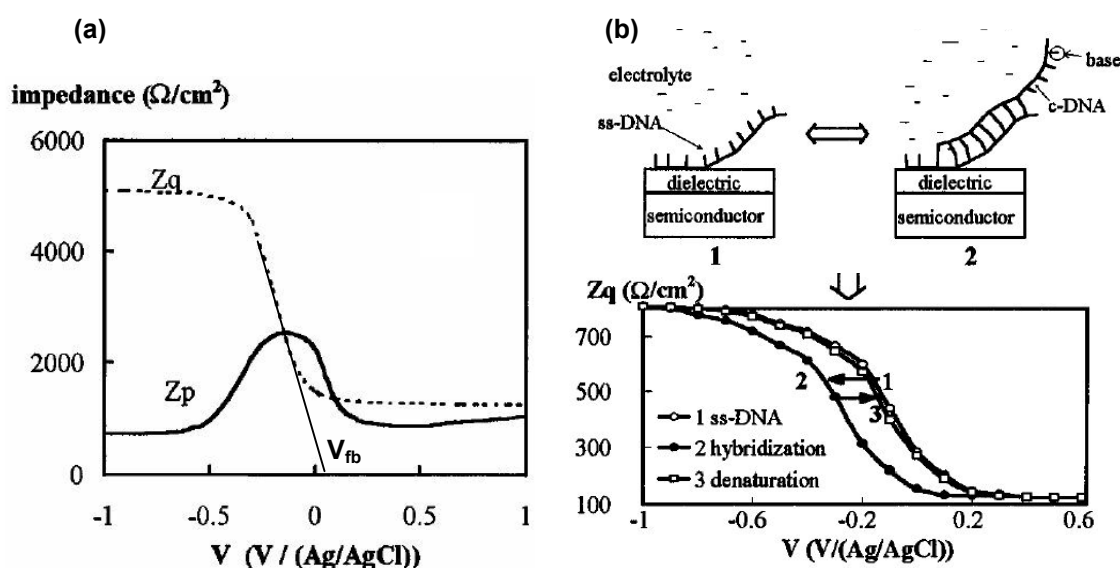


Figure 9: Impedance measurements at Si/SiO₂/electrolyte surfaces (taken from Ref. 79)
 a) typical shape of the real (Z_p) and imaginary (Z_q) impedance as a function of potential
 b) actual measurements for hybridization and denaturation of complementary analyte DNA

These impedance measurements can be extended by using field effect transistors (FETs), the mode of operation of which is sketched in [Figure 10 a](#)). Compared to a standard FET, the metallic gate contact is replaced by the electrolyte, and its potential V_{gs} relative to the source contact is controlled by the reference electrode of the potentiostat ([Ref. 81](#)). In the constant current mode, V_{gs} is regulated to maintain a stationary value of the source-drain current. Thus, the FET essentially provides access to the same information one obtains from the impedance measurements, i.e. shifts in the flat-band potential of the semiconductor body ([Ref. 79](#)). However, its advantage is that it enables direct observation of these shifts by recording V_{gs} . In [Figure 10 b](#)), an exemplary measurement is shown for the in-situ hybridization of 30 pmol of a 1 kb analyte DNA sequence ([Ref. 79](#)). This method provides direct translation of molecular detection into electronic signals, and the fabrication of high density arrays is straightforward. However, from a biological point of view it is not a very versatile method because up to now, it only gives good results under harsh restrictions on the applicable electrolytes ([Ref. 82](#)). Furthermore, the reported detection limits even under favorable conditions (nM range; [Ref. 83](#)) are rather high, which further limits the use of these systems.

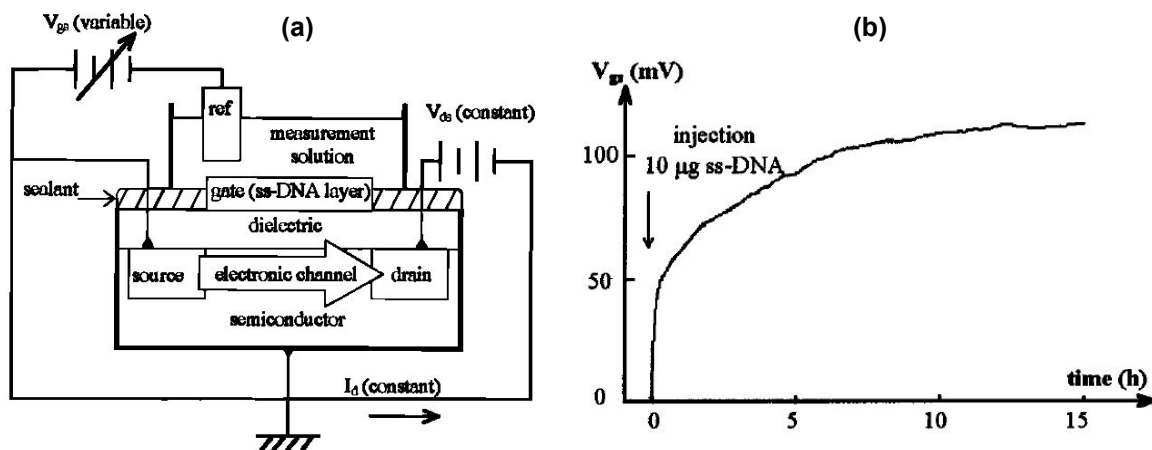


Figure 10: DNA hybridization detection using field effect transistors

a) mode of operation (taken from [Ref. 81](#))

b) reaction to the hybridization of 30 pmol of target DNA (taken from [Ref. 79](#))

1.2.2.3. Refractive index sensitive detection

The most widespread label-free molecular detection method makes use of slight differences in the refractive indices between surface layers of single stranded and double stranded DNA. By surface plasmon resonance (SPR) imaging, changes of less than 10^{-4} in the refractive index of thin surface layers can be detected in realtime with a spatial resolution of about $2 \mu\text{m}$ ([Ref. 84](#)), which makes this method a very promising array technology for the analysis of all kinds of molecular interactions, including DNA hybridization.

A plasmon is an electron density wave in an electrical conductor (e.g. metal layers like Au or Ag) which can be excited, for example, by reflecting photons from its surface. Due to energy and momentum conservation, it is only possible to excite plasmons by photons that incite onto the metal layer from a medium with a dielectric constant higher than that of the metal, thus excluding air as a feasible medium ([Ref. 85](#)). A practicable geometry for generating surface plasmons is shown in [Figure 11](#)

a). The photons are coupled onto the gold layer through a glass prism, which is generally referred to as the ATR (attenuated total reflection) configuration. Other possible coupling methods include optical waveguides and diffraction at metal gratings (Ref. 86). On the far side of the metal layer (usually around 50 nm in thickness; Ref. 84), the plasmons generate an exponentially decaying evanescent light wave, the extend of which depends on the refractive indices and thicknesses of the materials at the interface. This relation can be observed by measuring the dependence of the reflectance on the angle of the incident light (see Figure 11 b), which shows a distinct minimum at the angle corresponding to the surface plasmon resonance condition (Ref. 86). When a larger portion of the evanescent wave experiences a greater refractive index, the SPR shifts to higher angles. Usually, a fixed angle with a large reflectance derivative is chosen, and spatial variations of the optical properties at the interface show up as different light intensities at the CCD camera (Ref. 84).

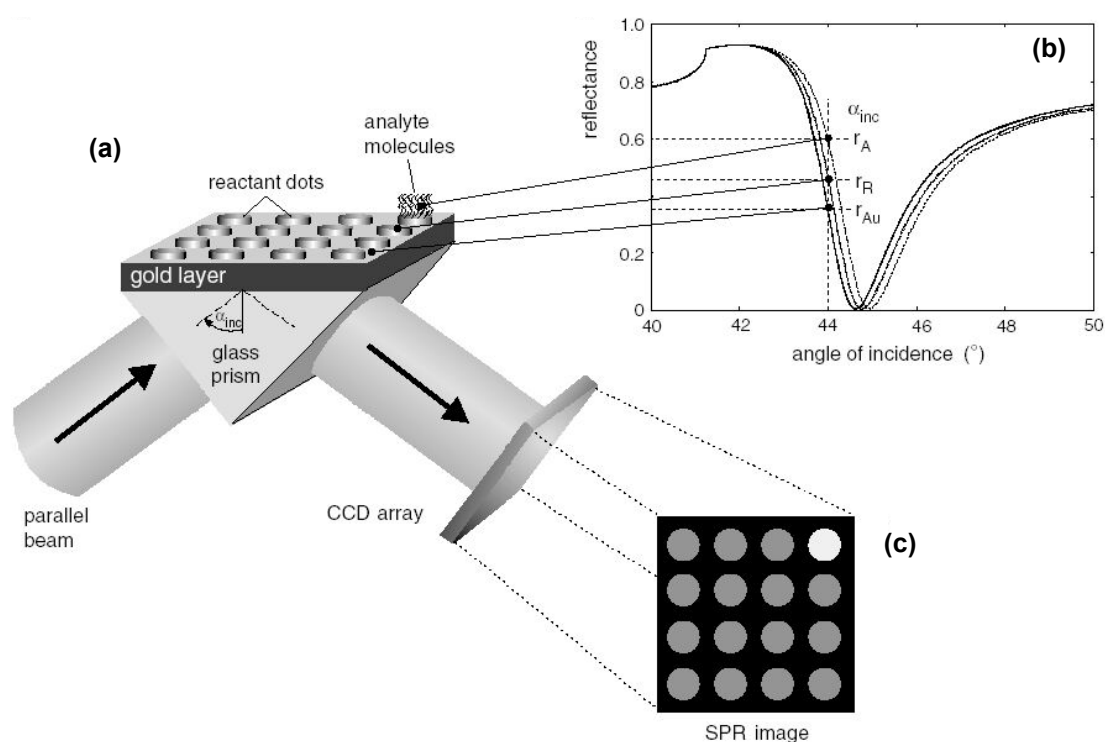


Figure 11: Surface plasmon resonance (SPR) imaging (taken from Ref. 84)

a) experimental setup

b) calculated SPR reflectance curves for the three different surfaces

c) SPR image as recorded by the CCD camera for the indicated angle of incidence

Arrays consisting of 100 probe DNA spots have been successfully hybridized with an unlabeled target DNA mixture and analyzed using SPR imaging, revealing a signal strong enough to discriminate single base mismatches (Ref. 87). IBIS Technologies BV offers a commercial SPR imaging instrument that allows the simultaneous label-free in-situ detection of up to 15000 different sequences (Ref. 88), while GWC Instruments supplies a high sensitivity system capable of detecting molecular film thickness variations of less than one Angstrom (Ref. 89). Still, direct label-free hybridization detection of oligonucleotides is presently limited to a concentration of about 10 nM by this method (Ref. 90), but by employing gold nanoparticles as labels, the sensitivity can be pushed down to about 10 pM (Ref. 91).

1.2.2.4. Electrochemical oxidation of guanine bases

Electrochemical analysis can also be used directly to quantify the abundance of hybridized analyte DNA. One method makes use of the enhanced reactivity of the nucleotide guanine, which can be transferred into its oxidized state electrochemically. Even though the immobilized probe DNA already contains guanine, its oxidation current decreases upon target insertion. This happens because after hybridization the bases are on the inside of the double helix, and their oxidation is hindered sterically by the surrounding sugars (Ref. 92). The method can be improved by employing modified probe DNA in which the guanine bases are replaced by inosine (Ref. 93). While still forming a base pair with the target cytosine, the oxidation of inosine occurs at a voltage well separated from the guanine peak. Therefore, direct detection of DNA hybridization can be accomplished through the appearance of the oxidation current of the target guanine bases (see Figure 12 a). Furthermore, the signal can be greatly amplified by adding redox mediators like $[\text{Ru}(\text{bpy})_3]^{3+}$ (Ref. 94) which help to transfer charge between the guanine bases and the electrode (see Figure 12 b). By combination with carbon nanotube electrode arrays, label-free detection of down to about 1000 target molecules has been reported by this method (Ref. 95), which is comparable to the detection limit of laser-based fluorescence but requires much less complex instrumentation.

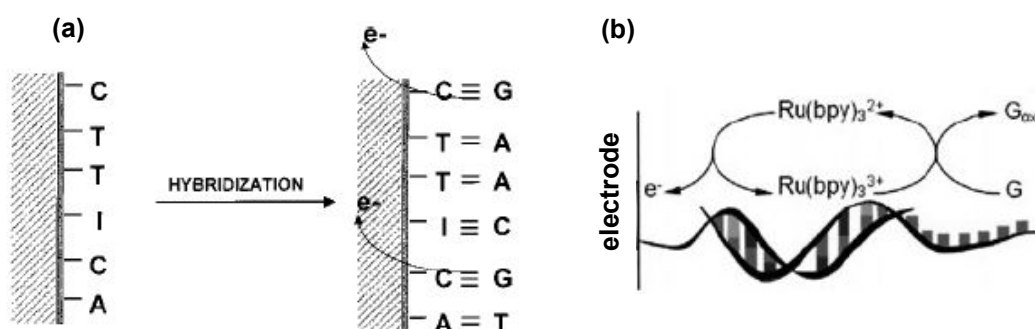


Figure 12: Direct electrochemical detection by guanine oxidation
 a) immobilized probe DNA with guanine (G) replaced by inosine (I) guarantees oxidation of target DNA guanine only (taken from Ref. 94)
 b) enhanced electron transfer by the redox mediator $[\text{Ru}(\text{bpy})_3]^{3+}$ (taken from Ref. 95)

1.3. Magnetic biosensors

With the introduction of functionalized magnetic microparticles for the separation of desired molecules from an arbitrary solution by Dynal Biotech in 1986 (Ref. 96), there has been growing interest in employing such particles also directly as labels to detect molecules. Magnetic markers have a number of advantages, the most important one being the fact that all other components in the sample solution are essentially non-magnetic, thus eliminating interference effects and minimizing the background signal (Ref. 97). Furthermore, their magnetic properties are stable over time (no photobleaching like encountered for example in many types of fluorescent dyes) and their surface is easily functionalized with suitable receptors, which simplifies specific binding to desired biomolecules. Last but not least, the possibility to apply local forces on the markers by generating magnetic gradient fields with on-chip current lines opens up the additional option of manipulating the labels (e.g. drag them to

desired positions or discriminate between perfect match and single base mismatch DNA hybridization).

Employing magnetic particles as labels requires the development of suitable magnetic transducers that translate their abundance into an electronic signal. The first type of magnetic transducer was introduced in 1996 by Kriz et al. (Ref. 98). It relies on determining the magnetic permeability of a sample by inductance measurements in a Maxwell bridge setup. The analyte is labeled by magnetic markers and allowed to settle at the bottom of a vial, and the sediment is introduced into the measuring coil. By this method, specific detection of a single analyte was demonstrated down to a concentration of about 250 nM (Ref. 97). Since it also requires large amounts of material, the sensitivity of this approach is quite limited. Still, it is a fast and robust way for detecting molecules and can easily be integrated into portable devices for point-of-care usage (Ref. 97).

Another type of magnetic transducer is based on measuring the remanence of single-domain magnetic nanoparticles bound to surface-immobilized biomolecules (Ref. 99). Compared to unbound particles which can rotate freely after removal of a magnetizing field (Brownian relaxation), the magnetization of an ensemble of surface-bound particles decreases according to the Néel relaxation time, which is much slower for suitable nanoparticle sizes. Therefore, by measuring the remanence of the sample after an appropriate relaxation time, it is possible to deduce the amount of surface bound particles. Maximum sensitivity is obtained by using a SQUID magnetometer (superconducting quantum interference device) for the remanence measurements, which has been demonstrated in an immunoassay application to possess a detection limit as low as about 50000 antibody functionalized nanoparticles that are bound to immobilized antigen targets (Ref. 100). So far, no single or multi-analyte DNA hybridization measurements have been reported by this method, and the cost of instrumentation as well as the necessity of cryogenics is a serious disadvantage of any SQUID based technique.

Magnetic transducers that incorporate Maxwell bridges or SQUID magnetometers can only detect one or at best a few different analytes at a time and are not suitable for integration into high density chip based systems. However, there are a number of different magnetic transducers that can be fabricated on chip by standard lithography methods, namely Hall sensors, giant magnetoimpedance (GMI) devices and magnetoresistive (MR) sensors. All of these transducers are capable of detecting stray fields of magnetic markers and translating them into an electronic signal, and suitable sensor sizes can easily be produced on the micrometer scale. Silicon Hall sensors (Ref. 101) and planar Hall sensors (Ref. 102) with junction areas in the micrometer range have been demonstrated to detect single magnetic microspheres with a superior signal to noise ratio, but so far, realistic analyte hybridization experiments are missing. The same is true for GMI devices, in which the impedance of high-permeability wires or thin films shows a strong dependence on the applied magnetic field at high frequencies (normally around 10 MHz) due to the skin effect (Ref. 103). They are expected to possess a better sensitivity than MR sensors, but so far, there are only rather crude reports on the detection of unspecified amounts of ferrofluids (Ref. 104) or magnetic microspheres (Ref. 105) which, at least so far, are not yet connected to molecular immobilization and recognition reactions.

More advanced results have been obtained with transducers based on magnetoresistive (MR) sensors. The pioneering work in this field was carried out by scientists of the Naval Research Laboratory (NRL) (Ref. 15; Ref. 16), who developed the first prototype magnetoresistive biosensor called BARC (Bead Array Counter). It consists of eight separate arrays, each incorporating eight single rectangular (5 x 80

μm^2) GMR based sensor elements per probe DNA spot. An element is capable of detecting a single micron-sized magnetic marker (Dynal Inc., M-280, mean diameter 2.8 μm ; [Ref. 96](#)) in an out-of-plane geometry for magnetizing the particles. They have shown good selectivity and sensitivity (ten times better than the unspecific signal) for hybridization of a 10 nM oligonucleotide concentration ([Ref. 106](#); [Ref. 107](#)). Recently, they introduced a second generation BARC design in which a single meander-shaped GMR based sensor element covers the entire area of a probe DNA spot (around 250 μm in diameter). The chip incorporates 64 sensor elements plus two references, and a detection limit of about 10 microparticles (M-280, see above) on a single sensor element has been shown ([Ref. 108](#)). However, no application of this new design to molecular detection experiments has been demonstrated so far.

A first model for the detection of magnetic markers by GMR-type magnetoresistive sensors was published by Tondra from NVE Inc. ([Ref. 109](#)). He concluded that single magnetic markers of any size can be detected as long as the sensor has about the same size as the marker and the insulating protection layer is thin enough.

Freitas et al. introduced integrated on-chip manipulation and detection of various types of markers by magnetic gradient fields ([Ref. 110](#); [Ref. 111](#)). They are using 2 x 6 μm^2 spin-valve type MR sensor strips and an in-plane geometry for magnetizing the particles and have shown detection of single magnetic labels with a diameter of 2 μm . For smaller particles, they calculated that the signal to noise ratio of their sensor design is sufficient to detect single labels with a diameter of 250 nm, but the experimental results are not yet decisive ([Ref. 112](#)). They specifically attached the labels to the sensor surface by biotin-streptavidin bonds, but biologically relevant molecular detection experiments have not been carried out so far ([Ref. 113](#)). Due to the small size of the sensor and the possibility to manipulate the markers, the approach followed by Freitas et al. is more suitable for single molecule detection than for large scale microarray methods.

The same is true for the spin-valve sensors by Wang et al., which are of similar size and structure ([Ref. 114](#); [Ref. 115](#)). Just like the Freitas group, they have also shown detection of single micron-sized markers, but their sensing geometry is somewhat different and combines in-plane and out-of-plane magnetization of the labels. So far, only direct detection of magnetic markers has been demonstrated by this group. In this context, another paper has been published by Kim et al. ([Ref. 116](#)) which further establishes detection of magnetic microspheres by MR spin-valve sensors, but contains little new aspects.

Apart from GMR and spin-valve structures, ring-shaped micron-sized elements based on the anisotropic magnetoresistance (AMR) have been proposed as possible biosensors ([Ref. 117](#)). Their diameter is adjusted to the size of the marker, and the particles are magnetized into the out-of-plane direction, resulting in a radial geometry of their in-plane stray fields (see chapter [3.2.1](#)). When centered above a ring structure, the stray field of a marker rotates the magnetization of the ring from the initial circumferential into a radial orientation, resulting in a measurable AMR signal. Such devices could be used as on/off type particle counters in a high density array, which would provide the optimum platform for any type of biosensor application. In this respect, a similar system is possible by combining MRAM cells and magnetic markers, and experiments on this topic have been reported by scientists from our laboratory ([Ref. 118](#)).

In this thesis, the approach followed is based on a single large-area MR sensor element per probe DNA spot, which is similar to the second generation BARC design from the NRL group ([Ref. 108](#)). Sensors based on both the GMR and the TMR effect are presented, and their characteristics for detecting magnetic markers are

compared. Due to the large surface area of each sensor element, detection of single markers is not possible, but the average surface coverage of magnetic labels on the MR sensor is measured. Thus, possible applications of the presented sensor systems are for example in cell expression analysis or in clinical diagnostics, but not in single molecule detection. Still, TMR based sensor systems for this purpose are currently under development at our research group (Ref. 118).

Figure 13 displays the different steps involved in DNA detection by the magnetoresistive biosensor developed within this thesis. Firstly, samples of probe DNA are spotted onto the sensor surface and get immobilized via epoxy groups embedded into the top polymer layer. Secondly, the biotin-labeled analyte DNA is added and hybridizes to complementary probe DNA. In the final step, the hybridized pairs are detected by introducing streptavidin coated magnetic markers that bind specifically to the biotin of the analyte DNA. After each step, washing removes unbound DNA or markers. The markers are magnetized by an external field and their magnetic stray fields are detected as a resistance change in the MR sensor embedded underneath each probe DNA spot.

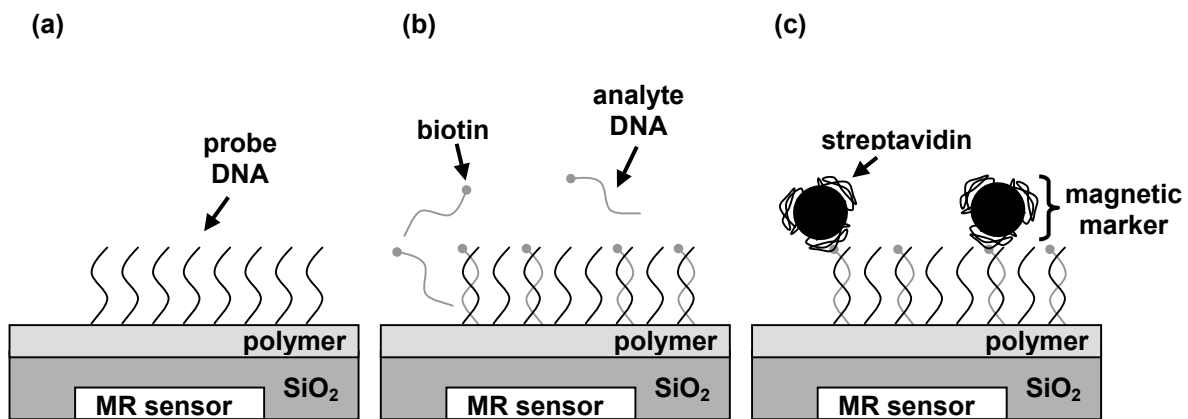


Figure 13: Principle of the molecular detection process followed in this thesis

a) immobilization of the probe DNA

b) hybridization of the analyte DNA

c) binding of the magnetic markers and detection of their stray field by the embedded MR sensor

1.4. Summery

Due to its numerous possibilities and the widespread integration into commercially available microarrays, optical detection systems presently are the gold standard to which every competing method has to be compared (see chapter 1). Also widely accepted is electrochemical detection, which can also be integrated into microarray formats. Both techniques can be designed to be highly sensitive for the detection of fM analyte concentrations (Ref. 51; Ref. 59), but electrochemical systems do not require the large and expensive equipment that is necessary for optical methods. Thus, they represent the most promising candidate for the detection unit of future lab-on-a-chip devices, and rivaling magnetoresistive biosensors have to offer some decisive advantages to compete against the established electrochemical systems. One of these factors is definitely the possibility to manipulate molecules via magnetic forces applied to their magnetic labels, which opens up new applications that are hardly possible to realize at this level of flexibility by other approaches. Furthermore, the electron transfer from the labels to the electrode is often inhibited in

Chapter 1: Introduction

electrochemical biosensors, which requires sophisticated chemical engineering to guarantee electronic communication ([Ref. 119](#)). Once oxidized, immobilized labels normally cannot be reduced again at the working electrode, which prevents repetitive measurements. Contrary to that, the stray field of magnetic markers is always present as long as they stay magnetized by an external field, and it can be reestablished at any time. Thus, magnetic biosensors are more robust than electrochemical ones, require less expensive and bulky equipment than optical methods, and are more flexible than both competing detection schemes, which makes it well worth to investigate their properties in detail.

2. Preparation and analytical tools

The magnetoresistive sensors are built from different stacks consisting of metallic and insulating layers, with individual layer thicknesses in the range of roughly 1-100 nanometers. The stacks are deposited by magnetron sputtering onto thermally oxidized silicon wafers in UHV chambers. Subsequently, they are patterned into a number of separate sensor elements by numerous steps of lithography. The resist patterns are transferred to the layer stacks either by deposition of additional films and lift-off (positive lithography) or by ion beam etching (negative lithography). In the case of an etching process, the mask consists of the resist itself or a layer of patterned tantalum. After completion, individual sensor elements are characterized by magnetoelectronic transport measurements.

Following is a short description of the employed preparation and analytical tools. The physical principle underlying each method and detailed specifications of the instrument's properties can be found in the respective references.

2.1. Film deposition

Thermally oxidized <100> silicon wafers from CrysTec ([Ref. 120](#)) with 100 nm of amorphous SiO₂ and a total thickness of 525 μm are being used as substrates for the magnetoresistive layer stacks, which are deposited in magnetron sputtering systems from Leybold Vakuum GmbH ([Ref. 121](#)).

The layer system for TMR sensors is deposited at a power of 115 W and an argon process pressure of $1.3 \cdot 10^{-3}$ mbar in a CLAB 600 system equipped with six four-inch magnetron sputter sources. Prior to deposition, a base pressure $< 3 \cdot 10^{-7}$ mbar is reached. Attached to the CLAB 600 sputtering chamber is a 2.46 GHz remote electron cyclotron resonance (ECR) oxygen plasma source from Roth & Rau GmbH ([Ref. 122](#)), which is used to create a tunneling barrier by oxidizing a previously deposited aluminum layer. The dependence of the quality of the tunneling barrier on the oxidation parameters of this system was analyzed by Thomas ([Ref. 123](#)). According to his results, the parameters for oxidizing a 1.4 nm thick aluminum layer are best at an oxygen pressure of $3 \cdot 10^{-3}$ mbar, an actual microwave power of 275 W and a DC bias voltage at the sample relative to the chamber of -10 V. Due to the different base layer stack, the oxidation time is reduced from the original value of 100 s in the work of Andy Thomas to only 70 s in this case. With these parameters, the aluminum layer transforms into amorphous Al₂O₃, while the subjacent layers remain free of oxygen.

Similarly, the layer system for GMR sensors is deposited at an argon process pressure of $2.8 \cdot 10^{-3}$ mbar in a LAB 560 system equipped with four four-inch magnetron sputter sources. The power is 94 W for copper layers and 102 W for permalloy (Py = Ni₈₀Fe₂₀) layers. Prior to deposition, a base pressure $< 6 \cdot 10^{-7}$ mbar is reached.

A proprietary developed UHV chamber with four 1.5-inch magnetron sputter sources is used to deposit interconnect lines and other supplemental layers at an actual power of 25 W and an argon process pressure of $2.3 \cdot 10^{-3}$ mbar. Prior to deposition, a base pressure $< 4 \cdot 10^{-6}$ mbar is reached. Additionally, insulating SiO₂ layers are deposited in this system by RF magnetron sputtering from a stoichiometric silica glass target at a gas mixture of $2.3 \cdot 10^{-3}$ mbar argon and $1.1 \cdot 10^{-4}$ mbar oxygen with a RF-generator from Hüttinger Elektronik GmbH ([Ref. 124](#)).

2.2. Vacuum furnace

One of the two ferromagnetic electrodes of the TMR sensor system is exchange-biased to a layer of the antiferromagnet $\text{Mn}_{83}\text{Ir}_{17}$. In order to set up the linear exchange anisotropy, the sample is heated above the blocking temperature of the $\text{Mn}_{83}\text{Ir}_{17}$ layer and cooled back to room temperature in a homogeneous uniaxial field. For this purpose, a proprietary developed vacuum furnace is employed which is able to heat the sample up to 550°C at a pressure below $1 \cdot 10^{-7}$ mbar. Typically, a temperature of 275°C is maintained for one hour, and the following cooling cycle back to room temperature takes about 20 min. During the entire process, a spatially homogeneous magnetic field of 80 kA/m is applied by a permanent magnet, thus defining the direction of the linear exchange anisotropy.

2.3. Lithography

2.3.1. Resists and processing chemicals

Table 1 gives an overview of the employed resists and processing chemicals, all of which are supplied by ALLRESIST GmbH (Ref. 125). The resist AR P 535 forms a special undercut profile after developing, which simplifies lift-off processes. Thus, the feature sizes of patterns written with this kind of resist are about $1 \mu\text{m}$ wider than what is specified by the design file. After spin-coating, the resist films are annealed on a standard hotplate.

	electron-beam	optical
resist number	AR P 610.03	AR P 535
type	positive	positive
spin-coating	60 s at 2000 rpm	30 s at 4000 rpm
resist thickness	130 nm	$1 \mu\text{m}$
annealing	17 min at 150°C	30 min at 95°C
developing	AR 600-55, 2 min	AR 300-35 2:1 H_2O , 30 s
removing	AR 300-70, 15 min at 80°C in ultrasonic bath	

Table 1: Overview of the employed resists and processing chemicals

2.3.2. Electron-beam lithography

Generally, electron-beam lithography is employed for feature sizes around or below $1 \mu\text{m}$. We are using a LEO series 1530 field emission electron microscope (Ref. 126) with a Raith ELPHY Plus lithography system (Ref. 127). The nominal resolution of the microscope is 1 nm at an accelerating voltage of 20 kV, which can be varied between 100 V and 30 kV. The minimum feature size is limited by the employed resist and proximity effects of backscattered electrons, and generally reaches about 50 nm in our case.

2.3.3. Optical lithography

For multi-step processes, we are using a laser lithography system from Heidelberg Instruments GmbH (Ref. 128) with a 4 mm write head and a built-in camera for alignment to preexisting patterns. It is a direct-write system that systematically scans given sample positions by an interferometer-controlled precision stage with an accuracy of 40 nm. With our photoresist, we can achieve a minimum feature size of

1.2 μm . The system's laser is from Melles Griot (Ref. 129), which has a nominal output power of 90 mW at a wavelength of 442 nm.

In the case of simple one-step exposures consisting of rather large patterns ($> 10 \mu\text{m}$), a UV-mask-lithography system from Thermo Oriel (Ref. 130) is used. It consists of a spatially homogeneous UV light source with controlled exposure times or dosages.

2.4. Etching

Pattern transformation into preexisting layers is carried out by Ar-ion beam etching with an UniLab system from Roth&Rau AG (Ref. 131). A base pressure of $5 \cdot 10^{-5}$ mbar is reached, while the Ar-pressure during etching is $1.2 \cdot 10^{-3}$ mbar. The discharge voltage of the ion source is set to 55 V, the beam voltage is 400 V, and the accelerator voltage is 30 V. The beam with a current of 7 mA is scanned in the plane perpendicular to its propagation by x- and y-deflector plates. At the same time, the sample is rotated, so that a circular area of homogeneous etching with a diameter of about 30 mm is created. To avoid re-deposition of ablated material at the edges of the sample patterns, its normal is tilted at an angle of 30° relative to the ion beam. End point detection of the etching process is done by integrating the electrical current through the sampleholder, which is a measure of the ion dosage deposited at the sample.

2.5. Energy dispersive X-ray sensor (EDX)

A supplemental device of the electron microscope is an EDX sensor from Oxford Instruments (Ref. 132). The lithium-drifted silicon sensor detects the energy of incoming x-rays generated by the high-energy electrons impinging into the sample material through generating electron-hole pairs within its volume. Since the energy of the x-rays is characteristic for the irradiated material, the sensor signal reveals the relative atomic composition of the sample down to a penetration depth of about 1-2 μm for 20 keV electrons. In this work, EDX analysis is used to check for the correct end point of etching processes.

2.6. Film thickness measurement system

A Nanospec Model 210 automatic film thickness measuring system from Nanometrics Inc. (Ref. 133) is applied to check SiO_2 film thicknesses on Si wafers during various steps in the fabrication process of GMR and TMR based sensor systems. It illuminates the sample and measures its wavelength dependent reflectivity by a spectrophotometer head in the range from 370 to 800 nm. A computer compares the measured spectrum with a reference spectrum from a pure Si surface and calculates the resulting thickness of the SiO_2 layer, which is accurate within 2 \AA in a measurement range from 50 to more than 1000 nm.

2.7. Atomic force microscope (AFM)

Surface analysis of the magnetoresistive sensors are carried out with an AFM from Veeco Instruments Inc. (formerly Digital Instruments, Ref. 134). Matching tips are supplied by Olympus (Ref. 135). All scans are taken in the Lift-ModeTM.

2.8. Magneto-transport measurements

Various proprietary developed setups are used to measure the in-plane magnetoresistance of the samples produced within this work. All of them apply conventional 2- or 4-probe DC measurement techniques and are computer-controlled (Ref. 123; Ref. 136). The voltage drop across the sample is set in a range from -2 to $+2$ V and maintained thereafter by adjusting the current accordingly, which is measured by an electrometer with six amplifier settings, ranging from $1 \mu\text{A}$ to 100 mA (maximum values of each amplifier setting). The output of the electrometer is measured by a Keithley Model 2000 digital multimeter (Ref. 137). The magnetic fields are produced by coils, either with or without ferrite rods. In the former case, the sample is placed in the air gap of the otherwise closed ferrite rod, and the magnetic field is induced by two collinear coils on both sides of the air gap. It is measured at the sample position by a Bell Tesla meter (Ref. 138), and can reach up to 280 kA/m . In the latter case, the magnetic field is applied by two orthogonal pairs of Helmholtz coils, thus allowing in-plane rotation of the field. Since no core is present, the strength of the field can directly be calculated from the applied current through the coils (after an initial calibration using the same magnetic field meter described above). The maximum field magnitude is 40 kA/m in one direction and 24 kA/m in the orthogonal direction.

In order to detect superparamagnetic markers by the magnetoresistive sensor elements, a magnetizing field has to be applied to produce a measurable magnetic moment. To minimize the direct effect of this magnetizing field onto the sensor itself, it is applied perpendicular to the plane of the sensor (see chapter 3.2.1). Within the scope of this thesis, a setup similar to the ones described above is designed (see Figure 14). It allows the application of both in-plane and out-of-plane magnetic fields while measuring and comparing the output signals of different magnetoresistive sensor elements. The fields are produced by two orthogonal pairs of Helmholtz coils, and their maximum magnitudes are 40 kA/m in the out-of-plane direction and 24 kA/m in the in-plane direction. The Helmholtz coils relative angles to the sample plane can be set independently by two fine thread screws, thus allowing to adjust the out-of-plane field to point perfectly orthogonal to the sample surface.

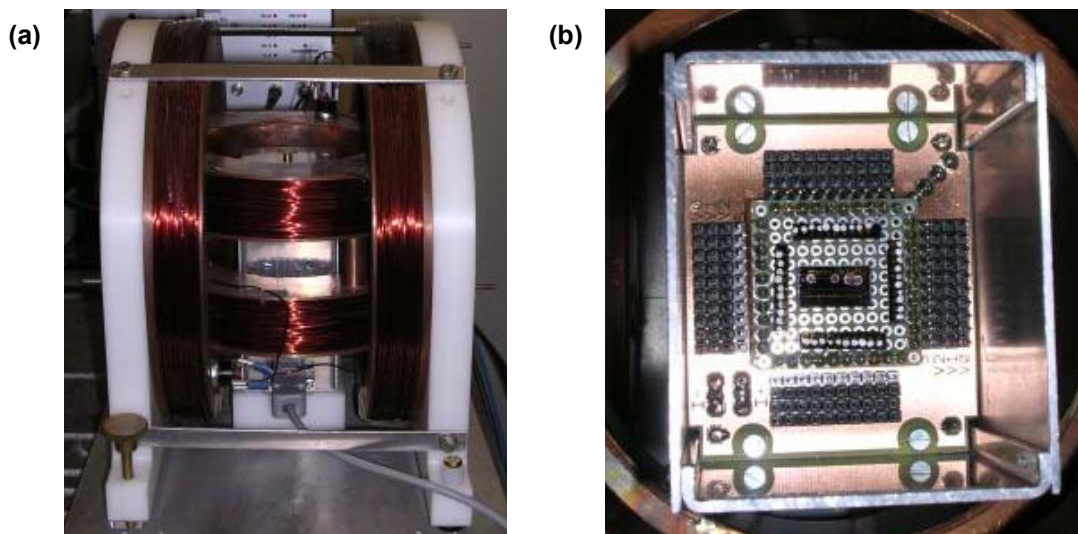


Figure 14: Photographs of the setup built for detecting magnetic markers
a) measurement box positioned in the middle of the Helmholtz coils
b) close-up of the sample position within the measurement box

The electronics for detecting magnetic markers is displayed in [Figure 15](#). It consists of two independent branches measuring one sensor element each. Usually, one of them is covered by markers, while the other one is an uncovered reference. For both branches, a common constant voltage is set across the respective sensor element ($V_0 = 2 \text{ mV}$, 10 mV , 50 mV , 200 mV , 1 V or 5 V), and the resulting current is measured by an IV-converter (LTC 1150) with five separate amplifier settings specified by the chosen current resistor ($1 \text{ k}\Omega$, $10 \text{ k}\Omega$, $100 \text{ k}\Omega$, $1 \text{ M}\Omega$ or $10 \text{ M}\Omega$). The current-proportional voltages are compared by a differential amplifier (INA 131), which amplifies the voltage difference by a constant factor of 100. The output is measured by a Keithley digital multimeter ([Ref. 137](#)), which converts the measured voltages into digital format and sends them to the computer.

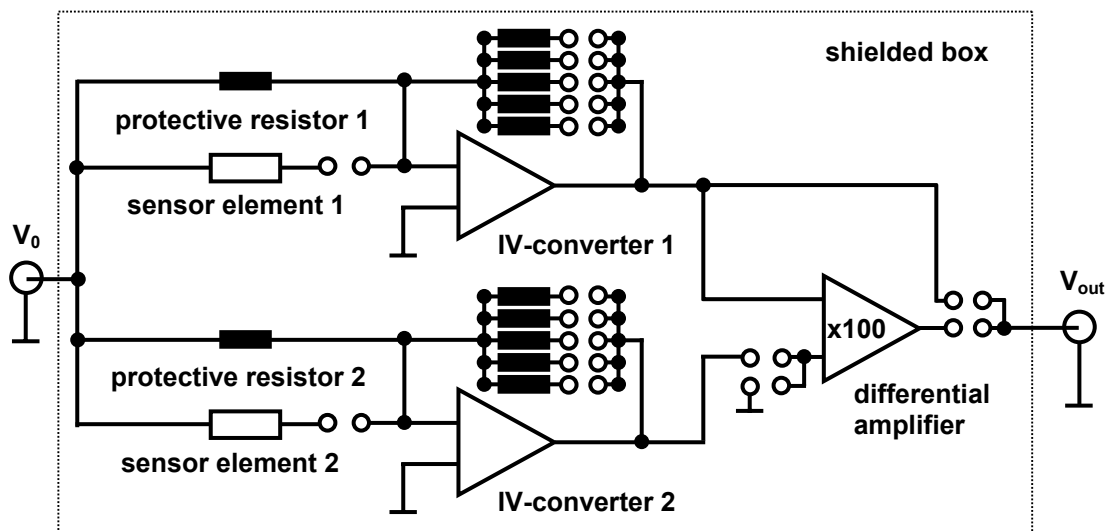


Figure 15: Measurement electronics for detecting magnetic markers

To protect delicate sensor elements from undefined electrical states during switching from one element to the next, a $1 \text{ k}\Omega$ protective resistor can be added in parallel. All the electronics and the sample are mounted within a closed aluminum box of $6 \times 7 \times 14 \text{ cm}^3$, which efficiently prevents noise pickup from the environment. Due to the limited space within the box, switching of sensor elements and amplifier settings is not done in an automated way using relays, but rather by manual switches and jumpers. They are indicated in [Figure 15](#) by small circles. The second measurement branch and the differential amplifier can be bypassed by appropriate jumper settings to enable single measurements of specific sensor elements.

The entire box is placed in the middle of the two pairs of Helmholtz coils, so that the sample as well as the electronics are exposed to the applied magnetic fields. This could be problematic if the operational amplifiers would be influenced somehow by the presence of these fields. To test this, several spiral-shaped structures identical in shape to the GMR based sensor elements (see chapter [5.2](#)) are fabricated by electron beam lithography. They consist of a $\text{Ta}_{5\text{nm}}\text{Au}_{25\text{nm}}$ bilayer, so no magnetic signal from the test patterns themselves is expected. The electrical resistance of such a test pattern is about $6 \text{ k}\Omega$, which is roughly half the resistance of a GMR sensor element. The case of an out-of-plane magnetic field is displayed in [Figure 16](#). In part a), the output is shown for a single measurement with a current resistor of $100 \text{ k}\Omega$ and $V_0 = 200 \text{ mV}$. In this setting, the resolution of the Keithley's AD-converter is $10 \mu\text{V}$, and the steps can be clearly observed in the data. The maximum noise amplitude is about 3 AD steps (or $30 \mu\text{V}$), corresponding to only $0.01 \text{ m}\%$ of the total

signal. The slight drift can be attributed to warming effects. No dependence of the output signal on the applied magnetic field is observed, which is also true when adding the second branch and the differential amplifier (see Figure 16 b). Now, the output signal is proportional to the difference in the conductance values of the two sensor elements. The measured noise level is about 3 mV, corresponding to 30 μ V at the inputs of the differential amplifier, which agrees to the single measurements. Similar behavior is found in the case of in-plane magnetic fields (not shown here), so that placing the entire electronics within the Helmholtz coils has no negative influence on the sensor measurements.

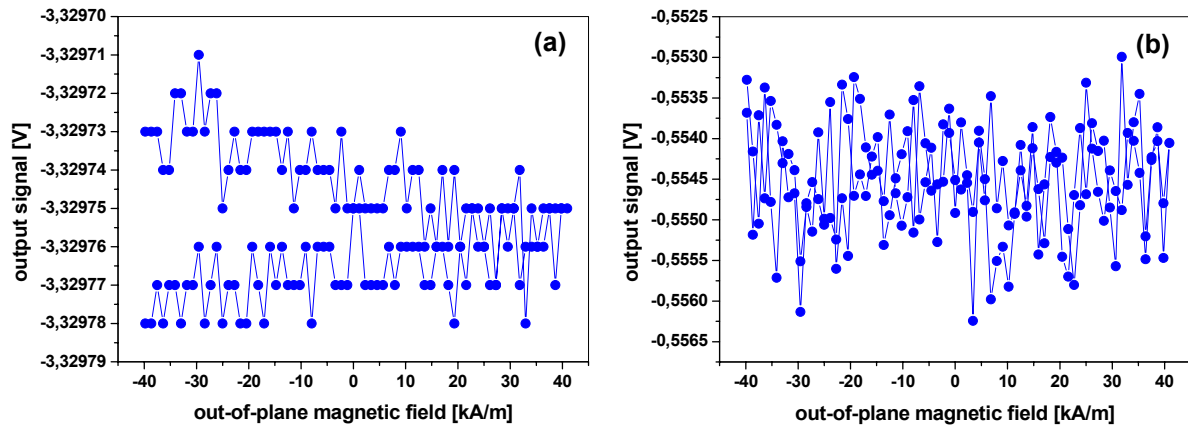


Figure 16: Reaction of the measurement electronics to an out-of-plane magnetic field
a) single measurement
b) differential signal

2.9. Alternating gradient magnetometer (AGM)

To measure the total magnetic moment of different microsphere samples, an alternating gradient magnetometer (AGM) from Princeton Measurement Corporation is used (Ref. 139). It has a maximum sensitivity of 10 pAm² and an accuracy of 2%. The magnetic field is applied by an electromagnet, and reaches a maximum value of 1120 kA/m at an air gap width of 12 mm.

3. Magnetic markers

3.1. Basic requirements for magnetic markers in biosensors

In order to be used in biosensor applications, magnetic markers have to satisfy a number of requirements. First of all, the ability to bind specifically to the target molecules is most important. We are making use of the high-affinity binding between biotin (vitamin H, ligand group of the analyte DNA) and the protein streptavidin (see chapter 3.2.2.1), thus requiring a large amount of functional streptavidin (i.e. in its correctly folded state) on the marker surface. Furthermore, the marker has to show a low affinity to the sensor surface in order to prevent unspecific binding, which could be due to electrostatic interactions, van der Waals forces or hydrogen bonds.

Another important factor is the overall size of the marker. Tests of our coworkers in the biology department (Ref. 140) with different sized similar streptavidin-coated markers (Bangs 1.4 μm , 0.86 μm and 0.35 μm) suggest that the ability to bind specifically to the analyte DNA's biotin increases rapidly with decreasing marker size. The analysis is carried out by measuring the marker coverage of equimolar biotin-labeled probe DNA spots. The decreased binding of larger markers can be attributed to steric hindrance at the sensor surface and increased flow resistance during washing steps.

Concerning the detection of markers, the magnetic moment per particle should be as large as possible in order to produce a magnetic stray field of sufficient magnitude to be measured by the magnetoresistive sensor. Even though the magnetization of the ferrimagnet magnetite is lower by a factor of 2-3 than for ferromagnetic materials (e.g. cobalt or iron), it is the main material of choice due to its biocompatibility and stability in aqueous solutions. Therefore, a high content of magnetite within the marker is desirable. Thus, larger markers would create larger magnetic moments and would be preferable from this point of view, so that a compromise has to be found between good binding and easy magnetoresistive detection of the markers.

To make different measurements comparable to each other, the magnetic markers should also be uniform in shape and narrow in size distribution. However, the larger the number of markers on a single sensor, the less important this criteria becomes, since differences between the particles are being averaged statistically.

3.2. Structure and common applications of magnetic microspheres

Magnetic particles are already widely employed in the biosciences. Initially, they were developed by Dynal Biotech (Ref. 96) to separate desired molecules from an arbitrary solution by binding them specifically to the particle surface and pulling them out of the bulk solution by magnetic gradient fields. This concept proved very successful, and by now, a large number of companies offer these so-called magnetic microspheres or beads, and they are available in a wide range of sizes, functionalities and magnetic properties.

According to their main purpose, magnetic microspheres generally have a large active surface covered by application-specific receptors, including for example streptavidin, carboxyl, amin or aldehyd. In order to avoid conglomeration of the microspheres, they need to display paramagnetic or superparamagnetic behavior, so that no attractive magnetic force between the particles is present with no external magnetic field applied. Usually, this is achieved by embedding small superparamagnetic magnetite particles into a polymer matrix, which magnetically isolates the individual particles from each other and shapes the microsphere (Ref.

141). Figure 17 shows a sketch of the structure common to most commercially available microspheres.

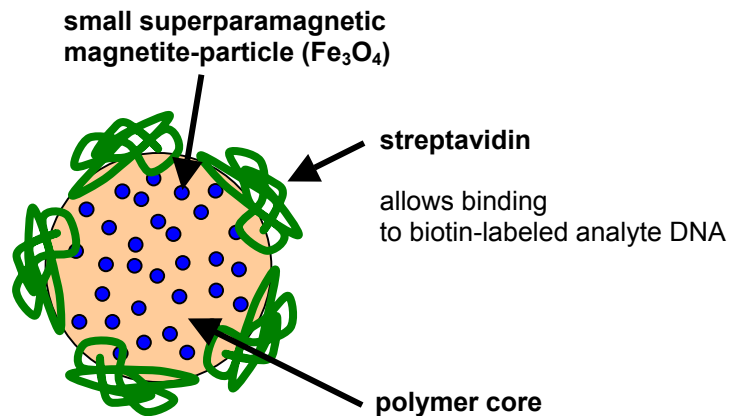


Figure 17: Common structure of superparamagnetic microspheres

Concerning the use of magnetic microspheres as markers in biosensor applications, they are ideal with respect to their inherent selectivity in binding to the target molecules (in our case the analyte DNA). Even though there is still room for improvements concerning size, magnetite content and particle homogeneity, magnetic microspheres are a natural choice as markers in initial magnetic biosensor experiments due to their availability and widespread use. So far, all groups dealing with magnetic biosensors rely on microspheres as markers, and our choice out of the numerous available types is motivated in chapter 3.2.2. However, even though they provide a good starting point, microspheres do not yet represent the ideal magnetic marker for biosensor applications. Possible developments towards this goal are discussed in chapter 3.3.

3.2.1. Principles of magnetic microsphere detection

Since all magnetic microspheres display superparamagnetic behavior, an external magnetic field has to be applied in order to magnetize the particles and to obtain measurable magnetic stray fields in biosensor applications. In principle, two distinctly different setups are thinkable: the magnetizing field could be applied perpendicular or parallel to the film plane of the magnetoresistive sensor.

However, it is important that the magnetizing field does not affect the sensitivity of the magnetoresistive sensor elements. Both our GMR- and TMR-type sensors consist of ferromagnetic layers with thicknesses between 3 and 8 nm, which, compared to the lateral dimensions of 1-50 μm , can be approximated as being infinitely thin. Thus, the demagnetizing field H_d in the direction perpendicular to the plane of the ferromagnetic layers can be expressed as $H_d = N_d \cdot M \cong M$, since the demagnetizing factor N_d reduces to $\cong 1$ in the case of infinite layer thinness (Ref. 142). The sense layer of our magnetoresistive devices consists of permalloy (Py), which is a common material in sensor applications due to its high permeability, low coercivity and vanishing magnetostriction (Ref. 143). With the room temperature saturation magnetization of Py being 860 kA/m (Ref. 143), a demagnetizing field of about the same magnitude hinders the magnetization of the sense layer to align perpendicular to its plane. Therefore, it is possible to apply a rather large magnetic field in the out-of-plane orientation of the magnetoresistive sensor, thus magnetizing the magnetic microspheres without affecting the magnetization configuration of the sense layer.

Since all of our fabricated magnetoresistive devices are highly sensitive at or near zero in-plane magnetic bias, most of the measurements presented in chapter 1,1 and 1 are obtained by applying a perpendicular magnetizing field. Such a setup was initially introduced by scientists from the Naval Research Laboratory (Ref. 15) and got adopted later by most other research groups active in the field of magnetic biosensors.

Applying the magnetizing field in the plane of the sensor is not completely out of the question, but it either requires magnetoresistive devices with sensitive regions at rather large in-plane fields or ferromagnetic markers. Otherwise, the magnetic moment of the microspheres is insufficient to produce measurable stray fields. Additionally, the presence of the microspheres would affect all the measurements, since they would always display the same magnetic moment in the crucial sensitive field range of the magnetoresistive sensor. Contrary, the microsphere's magnetic moment can be 'turned on and off' by varying the magnitude of the magnetizing field in the out-of-plane setup without affecting the magnetoresistive sensor itself. Thus, the same sensor element can also act as a reference, which efficiently eliminates inconsistencies due to variations in the magnetic or electrical transport properties from one sensor element to another.

Next, a brief calculation of the stray fields within the sense layer generated by a magnetized microsphere is presented. A uniformly magnetized sphere with volume V and magnetization M can be approximated as an ideal magnetic dipole placed in the sphere's center with a total magnetic moment of $m=VM$ (Ref. 144). Even though magnetic microspheres are composed of homogeneously dispersed small superparamagnetic particles embedded in a polymer matrix, they can be treated the same way, with an effective saturation magnetization $M_S=M_{mag} \cdot V_{mag} / V_{ms}$ due to symmetry. V_{mag} is the total volume of all individual magnetite particles in the microsphere, V_{ms} the total microsphere's volume and M_{mag} the saturation magnetization of the magnetic material. The stray field generated by a single magnetized microsphere with moment \vec{m} centered at the origin at a position \vec{x} has dipole-character and is given by (Ref. 144):

$$\vec{B}(\vec{x}) = \frac{\mu_0}{4\pi} \frac{3\vec{n}(\vec{n} \cdot \vec{m}) - \vec{m}}{|\vec{x}|^3} \quad \text{with } \vec{n} = \frac{\vec{x}}{|\vec{x}|} \quad \text{Equation 1}$$

The resulting stray field components within the sense layer are illustrated in Figure 18, both for the microsphere's magnetic moment lying parallel and perpendicular to the sense layer. Here, d is the vertical distance between the center of the microsphere and the sense layer. Though stronger in the perpendicular moment orientation, the out-of-plane stray field components do not play an important role due to the large demagnetizing field in this direction. Thus, the local magnetization configuration of the sense layer is mostly affected by the in-plane stray field components.

In the case of parallel moment orientation, the in-plane stray field in the vicinity of the marker is rather homogeneous in direction and points opposite to the microsphere's moment, with a maximum value directly underneath the microsphere. For perpendicular directions, the in-plane stray field is radially symmetric around the microsphere's center and reaches a maximum at a horizontal distance from the center of $d/2$. This can be seen from the stray field components along the x-axis, which are also displayed in Figure 18. Analytically, they are given by:

Chapter 3: Magnetic markers

\vec{m} out-of-plane: in-plane strayfield component: $B_x(\xi) = B_0 \cdot \Gamma(\xi)$

out-of-plane strayfield component: $B_z(\xi) = B_0 \cdot \Delta(\xi)$

\vec{m} in-plane: in-plane strayfield component: $B_x(\xi) = B_0 \cdot \Omega(\xi)$

out-of-plane strayfield component: $B_z(\xi) = B_0 \cdot \Gamma(\xi)$

Equation 2

with $B_0 = \frac{\mu_0 m}{4\pi d^3}$, $\xi = \frac{x}{d}$

and $\Gamma(\xi) = \frac{3\xi}{[1+\xi^2]^{5/2}}$, $\Delta(\xi) = \frac{2-\xi^2}{[1+\xi^2]^{5/2}}$, $\Omega(\xi) = \frac{2\xi^2-1}{[1+\xi^2]^{5/2}}$

Even though the geometry and relative magnitude of the induced in-plane magnetic stray field is favorable for the parallel compared to the perpendicular moment orientation, it is not possible to achieve high moments without saturating the sensor by the magnetizing field in the in-plane setup for our magnetoresistive devices. Therefore, we are using the out-of-plane setup for our measurements.

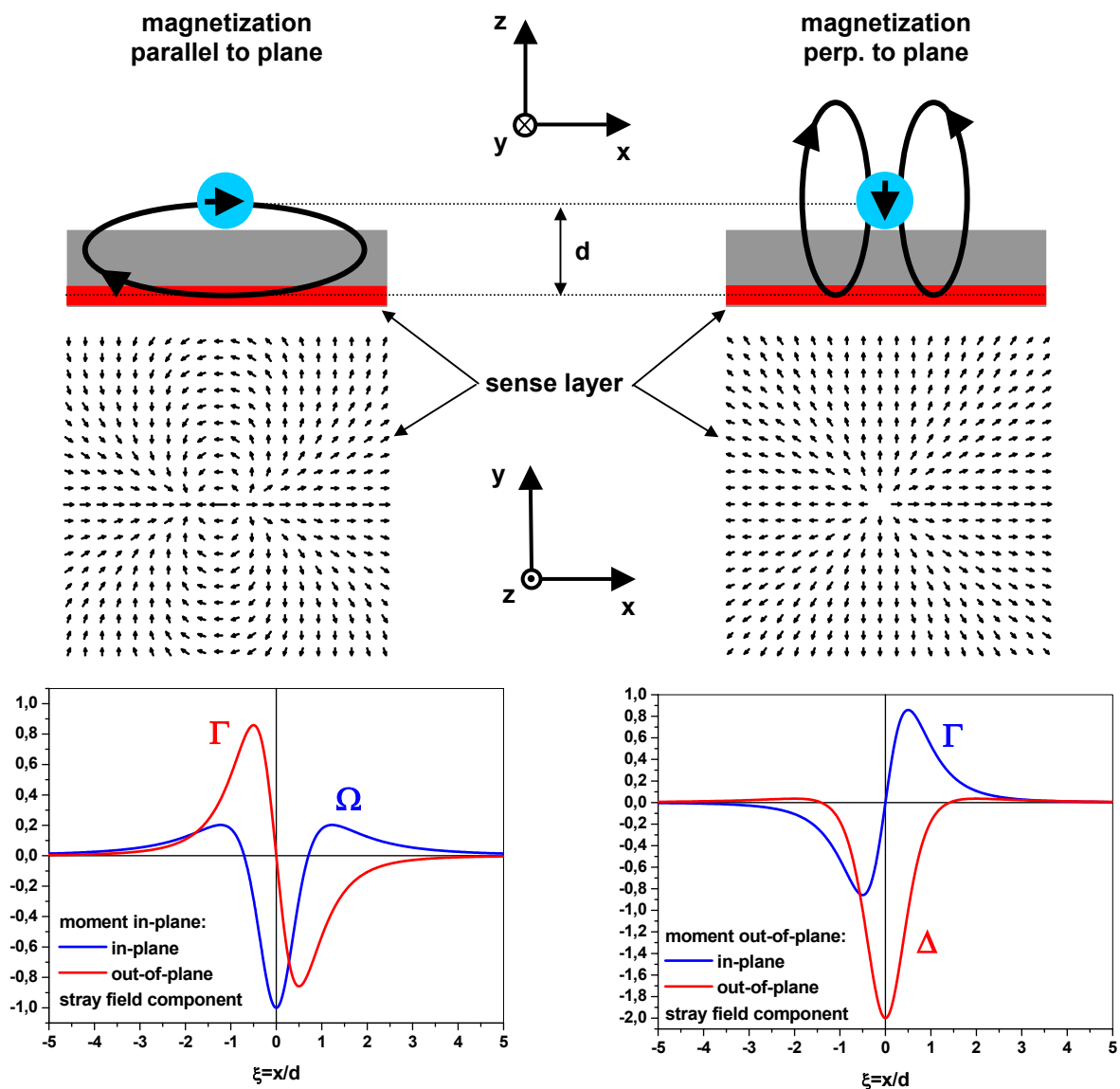


Figure 18: Magnetic stray field of a magnetized particle
top: configuration middle: stray field pattern in the sense layer
bottom: stray field component amplitudes along the x-axis for y=0

3.2.2. Choosing microspheres as magnetic markers

Of the many different kinds of magnetic microspheres that are commercially available from various manufacturers, we have to choose the ones that are most suitable as markers for our magnetic biosensor application. As described in chapter 3.1, there are a number of requirements which have to be fulfilled by these markers. Since we are using biotin as a ligand group of the analyte DNA, we limit our choice to magnetic microspheres with streptavidin receptor shells. There are very homogeneous spherical microspheres available from a number of vendors, but generally, it seems that this property goes along with large particle diameters and low magnetite contents. One of the smaller versions of homogeneous microspheres is offered by Spherotech (Ref. 145), but the magnetite content is quite low. On the other hand, the microspheres from Bangs Laboratories (Ref. 146) have a large magnetite content and are offered with mean diameters down to 350 nm, but their size distribution is rather broad. Similar microspheres are also offered by Chemagen (Ref. 147), but with a different polymer matrix. All four investigated microsphere types are spherical in shape, and their properties are summarized in Table 2.

	Bangs 0.35 μm	Bangs 0.86 μm	Chemagen	Spherotech
product number	CM 01 N, Lot 5062	CM 01 N, Lot 5030	M-PVA SAV 1	SVM-10-10
polymer	polystyrene		polyvinyl alcohol	polystyrene
magnetic material	Fe_3O_4 particles		Fe_3O_4 particles	$\gamma\text{-Fe}_2\text{O}_3$ coating
fraction of magnetic material	47% by weight <i>15% by volume</i>	45.8% by weight <i>14.7% by volume</i>	50-60% by weight <i>20-27% by volume</i>	<i>40% by weight</i> 12% by volume
mean diameter	0.35 μm	0.86 μm	0.9 μm	1.31 μm
mono-disperse	no	no	no	yes
particle density	$2.66 \cdot 10^7 / \mu\text{g}$	$1.82 \cdot 10^6 / \mu\text{g}$	$2.2 \cdot 10^6 / \mu\text{g}$	$4.05 \cdot 10^5 / \mu\text{g}$

Table 2: Properties of the four favorite microsphere types

Concerning the fraction of magnetic material, the given values from the manufacturer are in normal letters, whereas the calculated transformation is in italic print. It has been carried out using the material densities given in Table 3. If the densities of two materials are denoted by ρ_1 and ρ_2 , the relative weight fraction x of material 1 in a combination of material 1 and 2 is related to its volume fraction y by:

$$y = \frac{1}{\frac{1}{x} \frac{\rho_1}{\rho_2} - \left(\frac{\rho_1}{\rho_2} - 1 \right)} \quad \text{Equation 3}$$

	density in g/cm^3	reference
magnetite (Fe_3O_4)	5.18	Ref. 148
maghemite ($\gamma\text{-Fe}_2\text{O}_3$)	5.24	
polystyrene	1.06	Ref. 149
polyvinyl alcohol	1.30	

Table 3: Densities of microsphere materials

The information about the size distribution of the microspheres is based on our own SEM images, examples of which are shown in Figure 19. In general, the companies do not give this type of information, at least not quantitatively in terms of diameter standard deviation. Spherotech states that their microspheres have a diameter ranging from 1.0 to 1.4 μm , while the microspheres from the other companies are obviously much more disperse (see Figure 19).

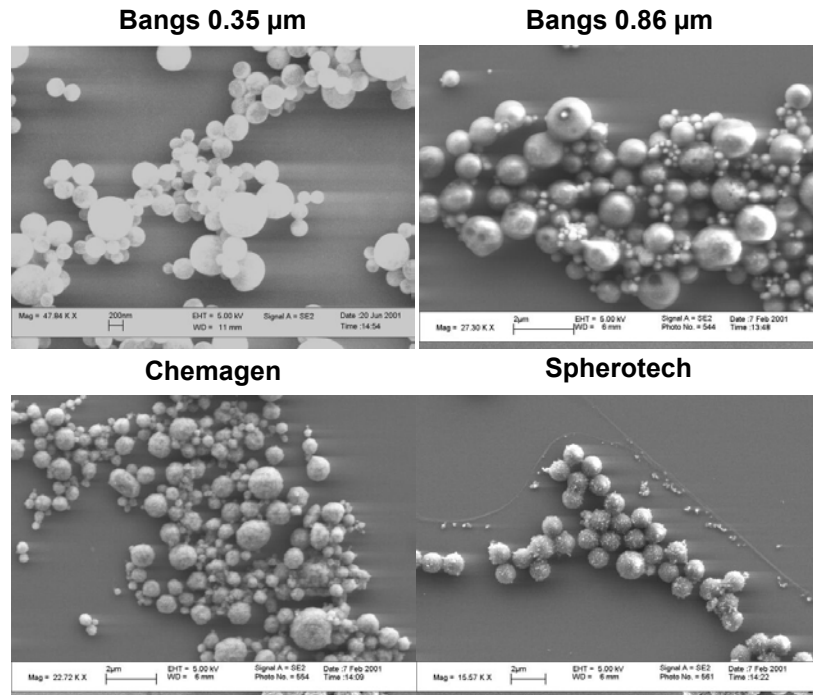


Figure 19: SEM images of the four different microsphere types used as labels

3.2.2.1. Molecular recognition to biotin-labeled test DNA

Molecular recognition between magnetic microspheres and the target molecules is based on high affinity binding between the protein streptavidin on the surface of the markers (receptor) and the coenzyme biotin, which is covalently coupled to the target molecules (ligand).

Biotin consists of a ring-like core and a freely movable $(\text{CH}_2)_4$ -tail called Valerat side-chain (see Figure 20). In biological systems, the carboxyl group at the end of the side-chain frequently binds covalently to amino-groups of enzymes, so that biotin helps in catalytic carboxylation reactions as a coenzyme (Ref. 150).

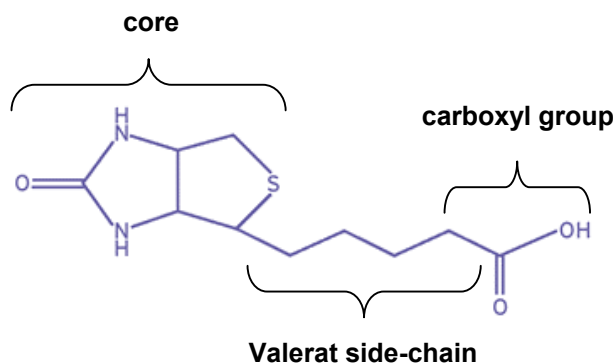


Figure 20: Molecular structure of biotin (taken from Ref. 150)

Streptavidin is a tetrameric protein, i.e. it integrates four identical and separate protein subunits into one protein molecule. Each subunit consists of a polypeptide chain incorporating 125-127 amino acids, has a molecular weight of about 14 kDa and folds into a tertiary structure of approximately $5 \times 5 \times 10 \text{ nm}^3$ (Ref. 151). The folding

pattern of the entire protein's backbone is shown in Figure 21, with each identical subunit displayed in a different color (Ref. 152; Ref. 153). The polypeptide chains start at the amino group of the first amino acid (N) and end at the carboxyl group of the last amino acid (C). Secondary protein structures (β -sheets and α -helices) are sketched as broad bands. Within each subunit, there exists a folding pan which can bind one molecule of biotin by a combination of various hydrogen bonds as well as hydrophobic and van der Waals interactions (Ref. 154). Therefore, one molecule of streptavidin can bind up to four molecules of biotin. Their positions within the folding pans of the protein subunits are also shown in Figure 21. The magnification shows the hydrogen bonds between the streptavidin's amino acid side-chains and the biotin molecule. The dissociation constant of the streptavidin-biotin compound is extremely low ($K_d \cong 10^{-15}$ mol/l), resulting in exceptionally stable linkage. Additionally, the binding is very specific to biotin, and streptavidin preserves its folding pattern under most conditions. Thus, the ligand-receptor pair biotin-streptavidin is ideal for applications requiring strong but exclusive binding between the two partners.

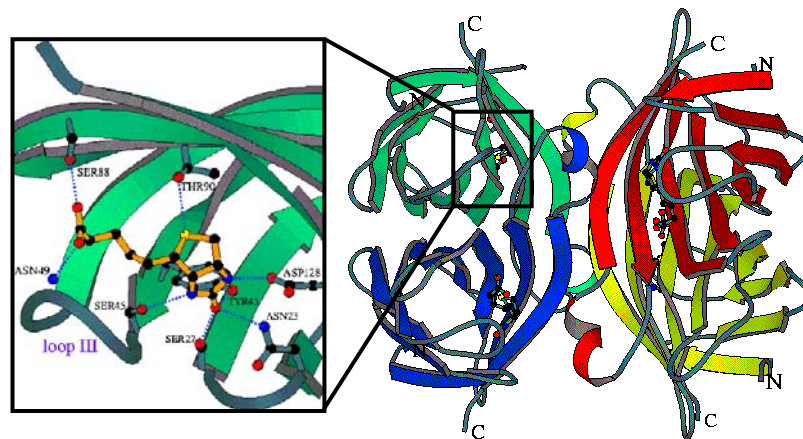


Figure 21: Folding pattern of Streptavidin including four bound biotin molecules (taken from Ref. 152)

In order to probe the molecular recognition of different types of streptavidin-coated magnetic microspheres, they are directly coupled to equimolar spots of biotin-labeled test DNA immobilized on polymer-coated wafer surfaces by our coworkers in the biology department (Ref. 140, see chapter 4.2 for the immobilization procedure). The same particle concentrations (1 % particle weight / volume) and binding conditions (1 hour incubation at 37-42 °C in moist atmosphere) are used for all types of microspheres. Afterwards, unspecifically bound microspheres are removed by washing with a solution containing 50 mM Na_2HPO_4 , 10 mM Tris-Base, 5 mM EDTA, 0,1 % SDS, 0,01 % Sarkosyl, 0,01 % Tween 20, 0,01 % Triton X100, 0,1 M NaCl, and 0,5 % PEG 4000. The pH of the solution is buffered to a value of 8.5. The resulting surface coverages of the microspheres on the biotin-labeled DNA spots are observed either by an optical microscope or by electron microscopy. The images are analyzed quantitatively by a proprietary-developed software, which detects the surface coverage of particles by taking the sum of all pixels above a certain grayscale value (see chapter 5.4.2). Generally, all four types of microspheres show good specific binding, but the surface coverage of the markers increases with decreasing particle size. An example is shown in Figure 22, which compares the surface coverage of Bangs 0.35 μm and Bangs 0.86 μm microspheres on a test DNA spot. In

this case, the smaller particles show a surface coverage 57% higher than their larger versions.

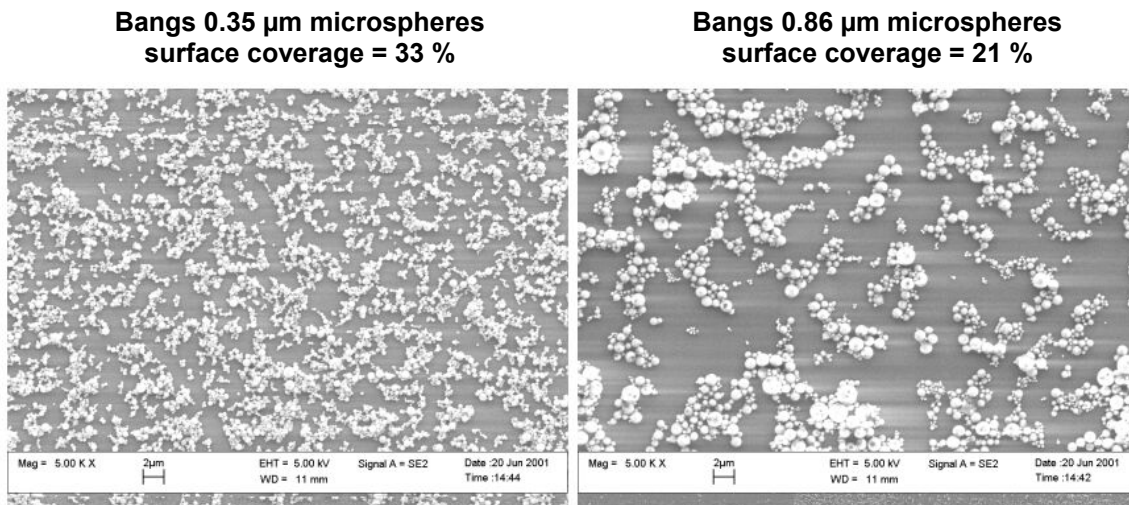


Figure 22: Molecular binding of different sized Bangs microspheres to biotin-labeled test DNA

3.2.2.2. Magnetic properties

The magnetic moments of the microspheres are measured at room temperature with the AGM described above (see chapter 2.9). For all four types of microspheres, drops with a particle solution volume of 2 μl are put onto two separate quadratic pieces of a 500 μm thick silicon wafer with 3-4 mm side length, resulting in controlled amounts of either 10, 20 or 50 μg of microspheres on the substrates (depending on the concentration of the solution). The magnetic moments of both samples are measured by the AGM up to a magnetizing field of 1120 kA/m, which is applied parallel to the plane of the wafer. Variations in the resulting saturation moments are most probably due to slightly differing drop volumes and particle concentrations (see Table 4). The differences of the individual measurements relative to their mean values are also given. Even though the number of independent measurements for each microsphere type is too small to deduce a meaningful standard deviation, this percentage gives some idea about the reliability of the measurements. Since the source of error is essentially the same for all of the microspheres, it is save to assume that all four mean values are only accurate within no less than 15%, which is the maximum difference recorded for an individual microsphere type.

The mean values of the AGM measurements are normalized per microsphere using the particle densities supplied by the manufacturers (see Table 2) and displayed in Figure 23. Part a) shows the complete cycle up to saturation, and part b) is a zoom around zero magnetizing field. While all the other microspheres show perfectly superparamagnetic behavior, the particles from Spherotech are obviously somewhat ferromagnetic, with a substantial coercive field of about 5.5 kA/m. Since they are supposed to be superparamagnetic as well, it is likely that our batch of microspheres is defective and does not agree with the specifications set out by Spherotech, at least concerning the magnetic properties. According to Spherotech's technical notes (Ref. 155), their magnetic microspheres are prepared by coating a layer of maghemite onto polystyrene cores. Apparently, this coating happens to be patched instead of

particulate in our case, resulting in ferromagnetic behavior. This should be kept in mind when comparing measurements of different magnetic markers in later chapters.

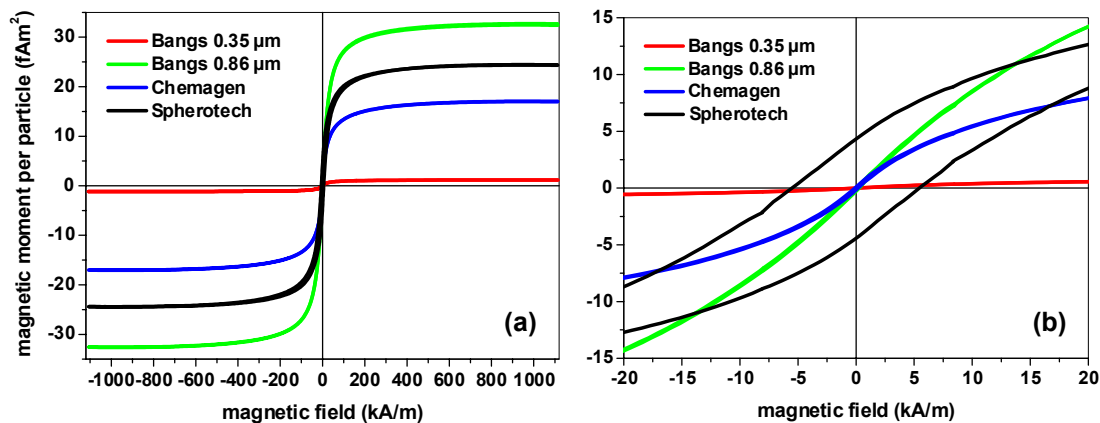


Figure 23: AGM-measurements of different microspheres, normalized per particle
 a) entire cycle to saturation
 b) zoom around zero field

Returning to Table 4, the expected magnetic saturation moments per microsphere are also calculated from the company's specifications of mean particle diameter and magnetic material type and content. The employed saturation magnetizations are 480 kA/m for Fe₃O₄ and 410 kA/m for γ -Fe₂O₃ (Ref. 156). In the following line, the differences between the measured and the calculated magnetic saturation moments are displayed relative to the measured values. For the microspheres from Bangs Laboratories, these differences are more or less consistent to what is expected from the variation of the individual moment measurements, but the magnetic saturation moments calculated for the microspheres from Chemagen and Spherotech are much larger than the measured ones. In the case of Chemagen microspheres, it is somewhat doubtful that the company's specification of the medium particle size is correct. On their web site (Ref. 157), Chemagen suggests that the diameter of M-PVA SAV 1 microspheres ranges from 0.5 to 1.0 µm. However, judging from our own SEM images (see Figure 19), it seems that the size distribution is much broader and particularly includes a lot of microspheres with diameters less than 0.5 µm. Therefore, the mean particle diameter is most probably smaller than what is stated by Chemagen, which would explain the discrepancy. For the microspheres from Spherotech, the difference between measured and calculated saturation moment is also very large. However, we already observed that the magnetic properties of those particles do not agree with Spherotech's specifications (see Figure 23).

	Bangs 0.35 µm	Bangs 0.86 µm	Chema- gen	Sphero- tech
sat. moment/µg (sample 1) [nAm ² /µg]	29.7	50.0	38.5	8.97
sat. moment/µg (sample 2) [nAm ² /µg]	31.8	67.9	36.0	10.7
sat. moment/µg (mean) [nAm ² /µg]	30.8	58.9	37.3	9.85
sat. moment difference in % of mean value	3.4 %	15 %	3.4 %	8.6 %
sat. moment/particle (mean) [fAm ²]	1.16	32.4	16.9	24.3
sat. moment/particle (calculated) [fAm ²]	1.62	23.5	43.1	57.9
difference between calculated and measured saturation moment in % of measured value	40 %	27 %	155 %	138 %
moment/particle at 40 kA/m (mean) [fAm ² /µm ²]	0.75	20.6	10.5	16.1

Table 4: Magnetic properties of the investigated microsphere types

In order to get an idea about the expected signals from each microsphere type, their in-plane stray field components are calculated according to Equation 2 for the out-of-plane moment orientation, which represents the common setup in this thesis. Since a maximum out-of-plane field of 40 kA/m is applied during measurements, the measured moment of the particles at this magnetizing field is used for the calculation (see last line in Table 4). The vertical distance d between the microsphere center and the magnetoresistive sense layer is the sum of the microsphere radius, the total thickness of the passivation layer (220 nm, see chapter 4.1), and half the thickness of the sense layer (20 nm in the case of GMR multilayers, see chapter 5.2). Figure 24 shows the results of the calculation. The field is radially symmetric, and its maximum value always occurs at a vertical distance $r_{\max}=d/2$ from the center of the microsphere. The calculation is carried out until the field strength decays below 40 A/m. This threshold field is obtained by assuming a minimum relevant resistance change of the GMR-sensor system of 0.01 % (see chapter 5.2), which, according to Equation 17, corresponds to an angle of 175.8° between the magnetizations of adjacent magnetic layers (or a rotation of 4.2° relative to the original antiparallel configuration). Comparing the respective antiferromagnetic exchange coupling energy difference between the ferromagnetic layers (see Equation 10 and chapter 5.2) to the Zeemann energy difference of a homogeneous in-plane field perpendicular to the original magnetization vectors, a field strength of 40 A/m is required to produce such a resistance change.

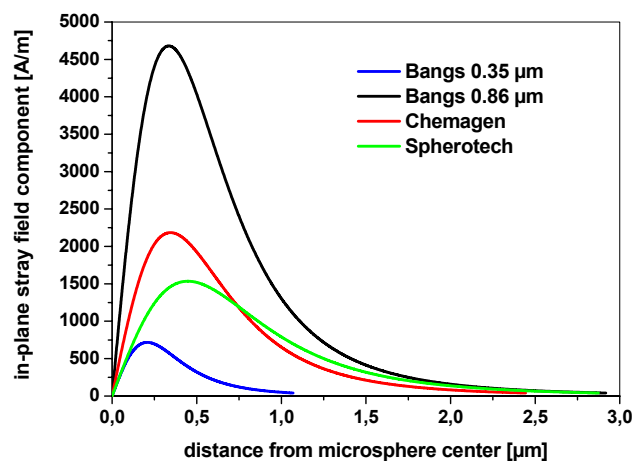


Figure 24: In-plane stray field components of the different markers within the sense layer

The threshold field defines the border of the range of influence for each microsphere type. Since they extend well beyond the radii of the particles, they interfere with each other when the markers are packed too closely on the surface of the sensor. In this case, their total effect on the magnetization configuration of the sense layer is reduced due to the radial symmetry of the stray fields in the out-of-plane configuration.

In order to calculate the total effectivity of the particles' stray fields, they are integrated across the circular area of influence up to the threshold radius, and the results of the calculations are shown in line 3 of Table 5. As the radius of influence is reduced for smaller markers, a larger number of labels fits onto a given sensor area without experiencing saturation effects due to stray field overlapping. Therefore, the integrated field strength is normalized to the area of influence of each particle type and displayed in line 4 of Table 5. With respect to this specific field strength, the Bangs 0.35 μm particles are comparable to the other markers, even though their total

moment is much smaller (see Table 4). Thus, they are also suitable concerning their magnetic properties and can be employed as labels in magnetic biosensor applications.

	Bangs 0.35 μm	Bangs 0.86 μm	Chemagen	Spherotech
vertical distance d [nm]	415	670	690	895
radius of influence [μm]	1.07	2.92	2.44	2.87
integrated field strength [$\mu\text{m}^2\text{A/m}$]	732	14232	8782	7828
specific field strength [A/m]	204	531	470	303

Table 5: Influence of different marker types on the sense layer

3.2.2.3. Conclusions

The comparison of the properties of different types of magnetic microspheres shows that these particles are generally suitable to be used as magnetic markers in biosensor applications. They bind with sufficient selectivity to biotin-labels immobilized at the surface of flat substrates, but the reduced steric hindrance and flow resistance of small-diameter particles makes Bangs 0.35 μm microspheres superior to larger particles in this respect. However, their magnetic moment is much lower than the one of the other microsphere types (by a factor of 15-28), which makes their detection by the magnetoresistive sensor more difficult. Still, since more particles fit onto the same sensor surface in the case of smaller particles, their overall stray field effectivity is still comparable to other larger particles. Therefore, we choose Bangs 0.35 μm microspheres as our most prominent marker type.

3.3. Outlook: ferromagnetic nanoparticles as magnetic markers

Even though magnetic microspheres are a good starting point for magnetic biosensor applications, they are not the most ideal markers possible. As mentioned earlier, they are still too large to bind efficiently to immobilized ligands, and their overall magnetic volume is too small to produce strong stray fields (cf. Table 2). The reason for this, of course, is their dominant use as separators in volume applications, where steric hindrance and unspecific binding at surfaces are of no concern. Also, the overall magnetic moment of the microspheres is not especially relevant for those tasks as long as the particles settle onto a permanent magnet within reasonable time.

With respect to magnetic biosensor applications, the ideal markers would be small single-domain ferromagnetic nanoparticles with a large magnetic moment and a suitable receptor shell, which are nevertheless stable in an aqueous solution and do not accumulate. In fact, due to a great variety of possible applications (e.g. in magnetic data storage or medical applications), the self-assembly of magnetic nanoparticles has been a very active field of research in the past years. In the case of data storage, small crystals of hard magnetic materials such as Co (Ref. 158; Ref. 159) and FePt (Ref. 160) are synthesized in non-polar organic solvents to prevent oxidation. Furthermore, the particles are stabilized within their carrier fluid by a shell of non-polar long chain fatty acid molecules, which counterbalance the attractive interparticle magnetostatic and van der Waals interactions by steric repulsion.

In medical applications, however, the nanoparticles should consist of biocompatible materials such as magnetite or maghemite, and the carrier fluid has to be aqueous (i.e. polar). In this case, the nanocrystals are stabilized by surfactants, which exhibit electrostatic repulsion forces between the particles due to charges adsorbed at their

surfaces (Ref. 161). A number of different approaches have been followed to synthesize iron oxide nanoparticles. They rely on co-precipitation from a solution of Fe(II) and Fe(III) salts (Ref. 162), and the particle's size distribution can be narrowed by following a microemulsion approach (Ref. 163). After synthesis of the nanocrystals, they can be coated by a silica layer. It forms from hydrolysis of TEOS (tetraethyl orthosilicate) into silicic acid, which undergoes polymerization and coats the particles (Ref. 164). The silica layer serves as a biocompatible and versatile group for further biomolecular functionalization. For example, avidin or streptavidin can be immobilized onto the silica layer simply by electrostatic attraction, thus resulting in a solid iron oxide nanoparticle with a receptor shell for biotin (Ref. 165). Even though such functionalized magnetic nanoparticles for bioapplications are not yet commercially available, they are already in a quite elaborate state of research and can be expected on the market soon.

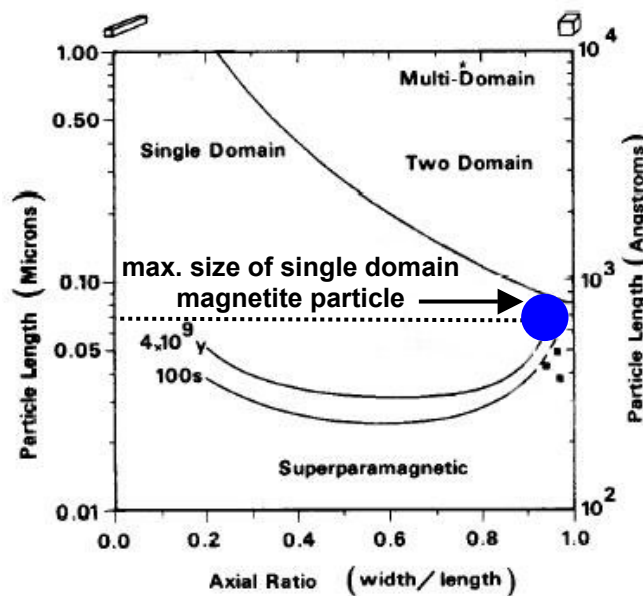


Figure 25: Single-domain stability field diagram of magnetite (taken from Ref. 166)

It is also possible to employ such functionalized magnetic nanoparticles as markers for magnetic biosensors. Ideally, they would be ferromagnetic and single-domain to produce maximal stray fields. According to Figure 25, which shows a calculated single-domain stability field diagram for magnetite (Ref. 166), spherical single-domain particles with diameters of up to 70 nm would be possible, resulting in a calculated magnetic saturation moment per particle of 0.086 fAm² ($M_S = 480$ kA/m, Ref. 156). Since such particles would be ferromagnetic and single-domain, their moment would be permanent, and no magnetizing field would be required like in the case of superparamagnetic microspheres. However, it would not be possible anymore to do reference measurements without markers on the same sensor element, since 'turning off' their moment is no longer an option. Therefore, measurements would have to be carried out in-situ, which implies that during hybridization of the magnetic nanoparticles to the analyte DNA, the resistances of the magnetoresistive sensor elements are monitored continuously. Like sketched in Figure 26, the effective signal would be the difference between the initial resistance before introducing the nanoparticles and the final resistance after the last washing step. An advantage of such an in-situ measurement is that the magnetic markers are effectively drawn towards the analyte DNA by the magnetic stray field gradient originating from the

current through the magnetoresistive sensor. Since the particles can rotate freely in the solution, their magnetizations would align parallel to the direction of the current's magnetic stray field, thus creating a stray field pattern of an in-plane magnetized particle perpendicular to the direction of the current in the magnetoresistive sensor (compare to chapter 3.2.1). The maximum in-plane stray field for such a single particle positioned at a vertical distance of 240 nm above the sense layer would be 330 A/m, which is still almost half the maximum value for out-of-plane magnetized Bangs 0.35 μm microspheres. Since detecting Bangs 0.35 μm microspheres in the out-of-plane setup is quite possible (see chapter 5.4.3), there should be no problem to sense such magnetic nanoparticles as well, while, at the same time, their small size should greatly improve specific binding to the hybridized analyte DNA.

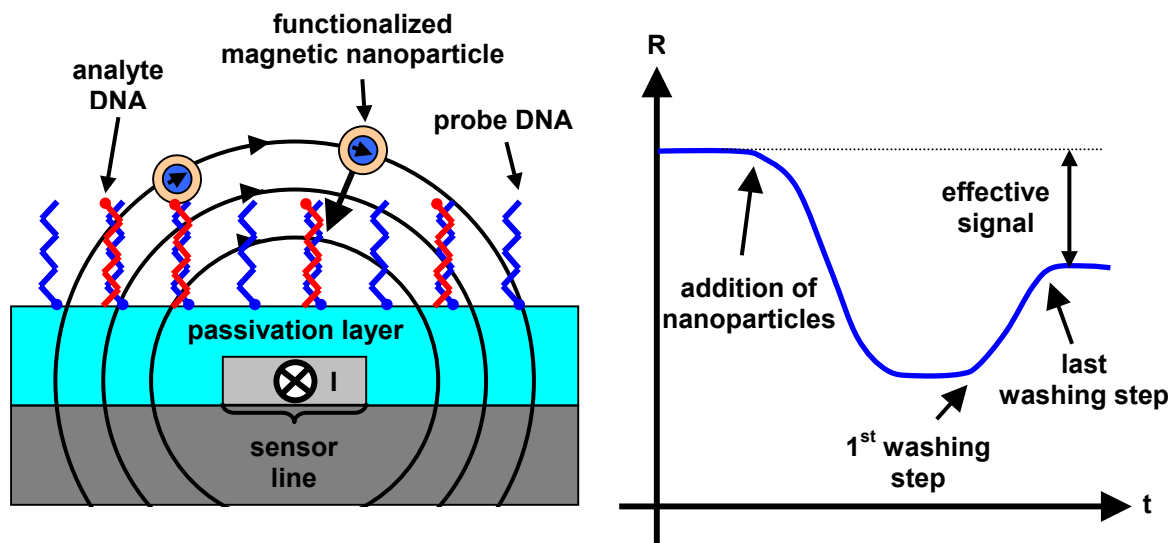


Figure 26: Measurement scheme for the in-situ detection of magnetic nanoparticles

4. The surface of the magnetic biosensor

4.1. Passivation of the sensor

In order to prevent oxidation, the sensor has to be passivated by a suitable protection layer. It should be as thin as possible to ensure large magnetic stray fields of the markers (compare to [Equation 2](#)), but solid enough to give reliable protection of the sensor from the various biological solutions employed during DNA immobilization and hybridization. Following is a list of the most important steps applied by our coworkers in the biology department ([Ref. 140](#)):

Probe DNA immobilization

1. Addition of probe DNA in spotting solution (containing 29 % DMSO and 1 % TEMED to adjust a pH of 10)
 2. Incubation in humid atmosphere at room temperature for 30 min
 3. Drying of the probe DNA spots at 37°C for 15 min
 4. Further drying on a hotplate at 100°C for 5 min
 5. Irradiation with 50 mJ of UV light
 6. Several washing steps
 7. Incubation in 1 M NaAc and 2.5 % PEG4000 (pH 5.0) at 55°C for 1 h (deactivation of remaining unbound epoxy groups)
 8. Several washing steps
- } binding of the probe DNA

Analyte DNA hybridization

9. Incubation of the analyte DNA solution in saturated water-vapor at 55°C for 1 h
10. Incubation together with hybridization solution (containing 35 % formamide and several detergents) at 42°C for 12 h
11. Several washing steps

Binding of the markers

12. Incubation of the marker solution in a humid atmosphere at 37-42°C for 1 h
13. Several washing steps

It is crucial that no liquid reaches the sensor elements during all these steps, because otherwise, their metallic layer structure would start to oxidize. Since some of these steps take place at elevated temperatures, the thermal expansion coefficient of the protection layer should match the one of the sensor material in order to prevent mechanical stress that could cause the destruction of the protection layer. Also, the protection layer should adhere well to the sensor material, and, naturally, it has to be electrically insulating to avoid shorting the sensor elements. All of these requirements are met by combining a thin layer of tantalum with an insulating layer of SiO₂.

The tantalum film has a typical thickness of 3-10 nm (depending on the type of sensor), and is sputter deposited as a final layer together with the sensor stack. Thus, it gets patterned into the same shape as the sensor elements, so that no short cutting metallic connections exist between them. The insulating SiO₂ passivation is added at the end of the sensor fabrication process and covers the entire chip (with the exception of the contact pads). It is sputter deposited to a thickness of about 150

nm in an argon/oxygen plasma mixture, resulting in the formation of a thin tantalum-oxide layer at the interface which assures good adhesion (Ref. 167).

The thermal expansion coefficient of tantalum ($6.6 \cdot 10^{-6}/K$, Ref. 156) is in-between the ones of typical sensor materials like iron or copper ($12..17 \cdot 10^{-6}/K$; Ref. 168) and the expansion coefficient of SiO_2 ($0.45 \cdot 10^{-6}/K$, Ref. 168), thus reducing the mechanical stress at the interface. It is further decreased by a thin polymer layer on top of the SiO_2 . Together, these two layers form laminated glass, which is less brittle than SiO_2 alone. The polymer is spin-coated from a 2.5 % (by weight) dioxane solution at 4000 rpm, resulting in a thickness of about 70 nm. Its exact composition is discussed in the following subchapter. The entire sensor passivation is sketched in Figure 27.

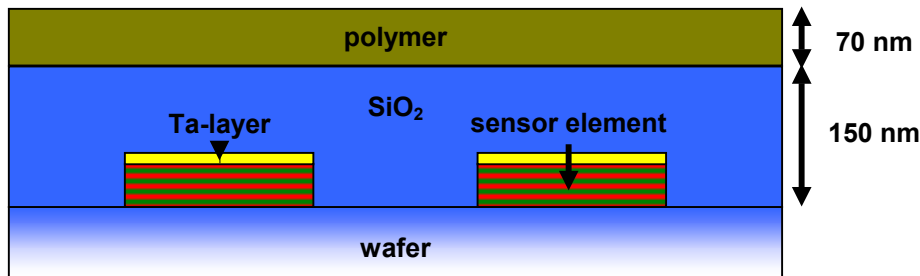


Figure 27: Cross-section of the sensor passivation

The passivation can only protect from oxidation if there are no residual particles on the sensor surface prior to the deposition of the protection layer. Otherwise, it is not tight enough and liquid can enter through the imperfections. Dust and other unintentional particles (like metal shreds after lift-off processes) are avoided by careful treatment and processing in a cleanroom. However, there is always the possibility of resist remnants at the edges of exposed patterns (both for our optical and e-beam resists), and these residues can also cause leakage through the passivation layer. This is demonstrated in Figure 28, which shows the partial oxidation of a TMR sensor element after leakage of solvents through imperfections in the passivation layer. The resist residues display a bright contrast, and the oxidized parts of the sensor element appear dark due to reduced secondary electron generation compared to the metallic parts.

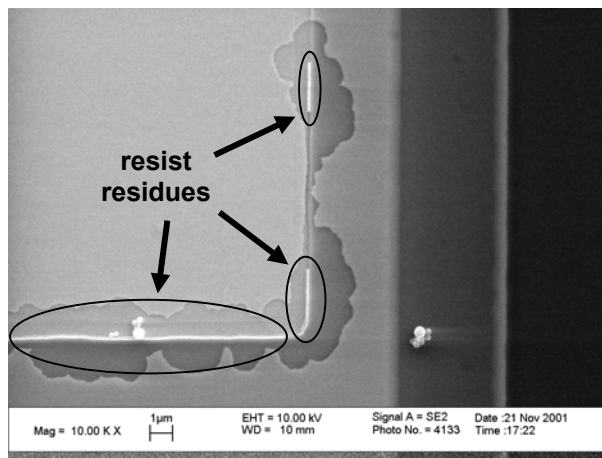


Figure 28: Oxidation of a TMR sensor element after leaking of liquids through imperfections caused by resist residues

Chapter 4: The surface of the magnetic biosensor

Mainly, such residues are generated when employing the resist itself as a mask for ion beam etching. Since the sample is rotating and tilted relative to the incident beam, the resist at the edges of the patterns is directly exposed to the beam throughout its entire thickness. Apparently, the energy deposited into the resist by the Ar-ions causes a chemical transformation of the polymer (most probably chain crosslinking) which prevents its subsequent removal. These remnants at the pattern edges are almost impossible to get rid of, which is demonstrated by the series of images in [Figure 29](#), each showing the same spot after various attempts to remove the residues. Even prolonged exposure to an oxygen plasma does not remove the remnants completely, and such a harsh treatment is certainly not desirable concerning the sensor properties. Lift-off processes, on the other hand, are less susceptible to this problem, and the resist residues can be removed by not too harsh treatments with the designated chemicals. An exception is SiO₂ lift-off, which also produces quite stable residues along the pattern edges.

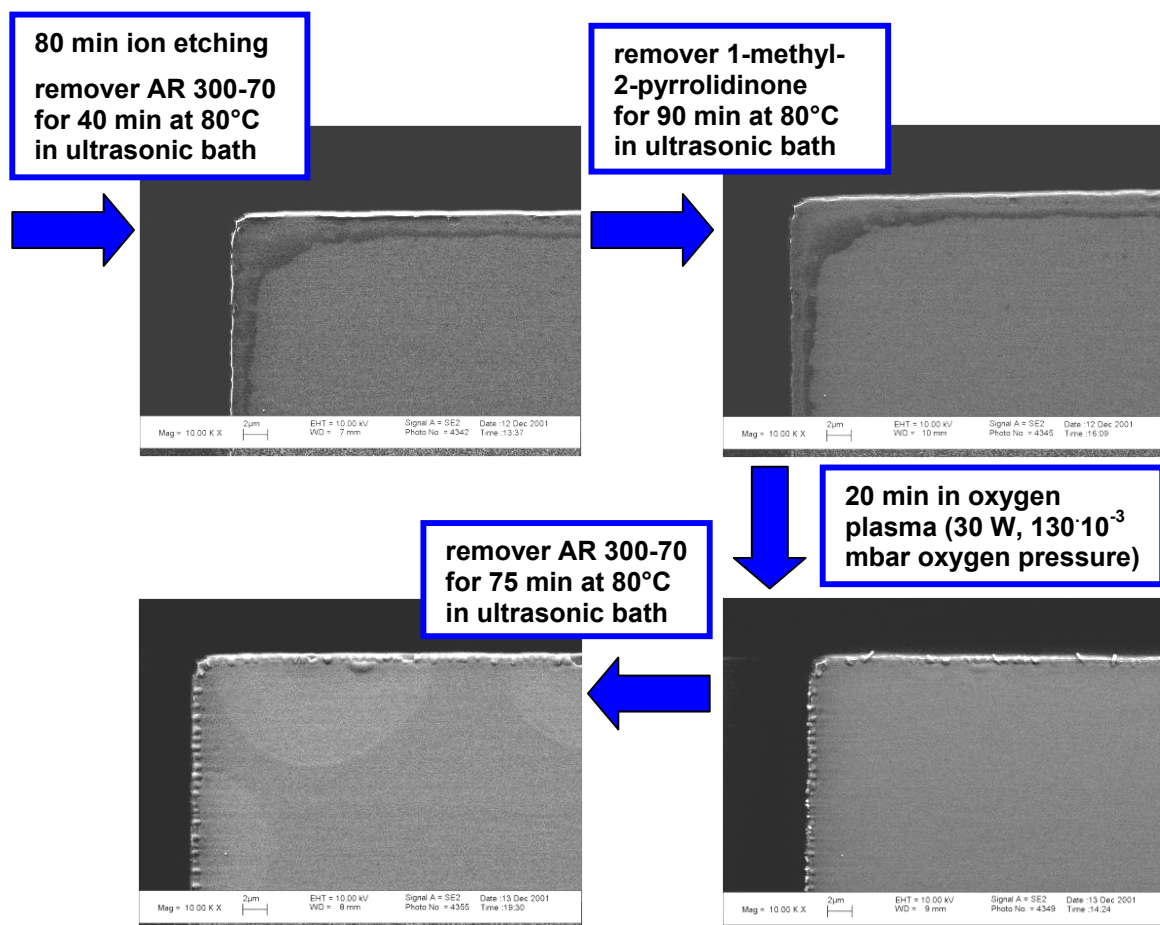


Figure 29: Resist remnants after various attempts to remove them

To avoid the problem of resist remnants, all processes involving etching steps are carried out using tantalum hard masks instead of the resist itself. This makes lithography somewhat more complex, since the thickness of the hard mask has to be tuned to the required etching dosage. Otherwise, the mask will either remain in parts on the sensor pattern, or the top layers of the sensor stack will be etched away. The conceptual difference between the two methods is sketched in [Figure 30](#).

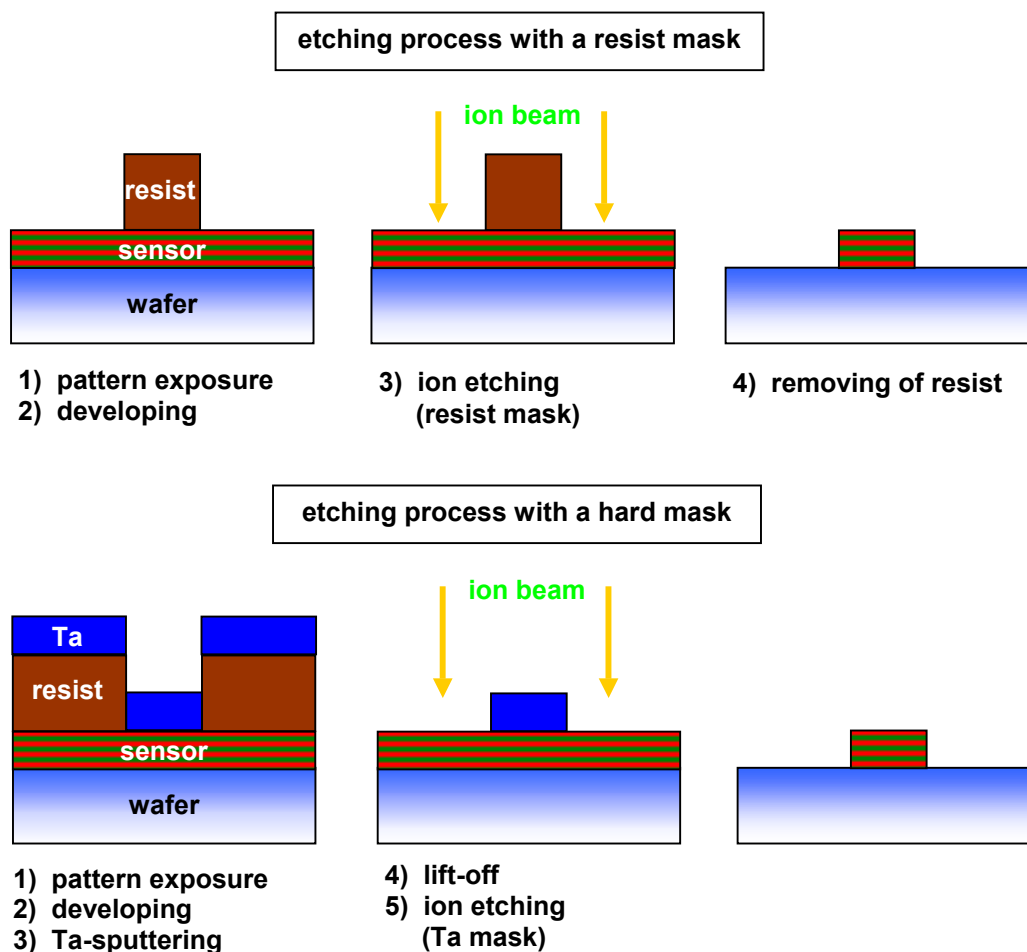


Figure 30: Steps of negative lithography using a resist mask or a hard mask

4.2. Probe-DNA immobilization

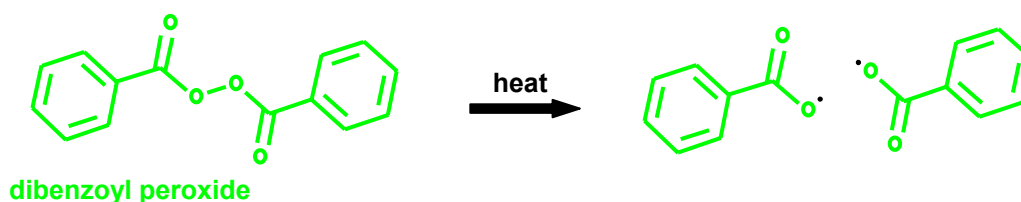
This chapter describes work that is carried out by our coworkers in the biology department (Ref. 140). However, due to the strong interconnection, it is also mentioned here for clarity.

Individual probe DNA samples are transferred onto the sensor surface in small drops in a contact free manner either by a piezo microarray spotter (typical drop volume 0.3 nl) or manually by a pipette (typical drop volume 0.2 μ l). Apart from the DNA strands, the spotting solution contains 29 % DMSO and 1 % TEMED to adjust a pH of 10. It denaturates the double stranded probe DNA into individual single strands to which the analyte DNA can hybridize in a subsequent step. After deposition of the spots, the probe DNA strands are immobilized onto the surface by forming covalent bonds. In initial experiments, the passivation layer consisted of SiO₂ alone, which was functionalized by epoxy-silan groups to enable covalent binding of the probe DNA's amino groups. By introducing the polymer as the final passivation layer, these epoxy sites are directly contained within the polymer network as active side groups. Even though the polymer was introduced initially as an additional protection of the sensor, it turned out that it is capable of binding much greater amounts of probe DNA than a plain silanized glass surface. In fact, comparative tests show that the fluorescent signals from Cy3 markers coupled to immobilized biotin-labeled probe DNA are about

5 times larger in the case of a polymer surface, which is probably due to larger amounts of accessible epoxy groups, thus causing enhanced binding of probe DNA. Synthesis of the polymer is carried out in a 1,4-dioxane solution containing 0.5 M glycidyl methacrylate (GM) and 20 mM of symmetric ethylene glycol dimethacrylate (EGD) monomers. The GM monomers contain the epoxy groups and polymerize into linear chains, while the EGD monomers provide chain crosslinking. The process is started by adding dibenzoyl peroxide at 80°C, causing homolytic scission of the dibenzoyl peroxide that leaves benzoyloxy radicals as initiators for the polymerization. It is allowed to propagate for two hours and terminated by adding ethanol. A sketch of the polymerization process is shown in Figure 31. After centrifugation, the polymer pellet is re-dissolved in 1,4-dioxane at a concentration of 2.5 % (weight / volume) and spin-coated at 4000 rpm onto the SiO₂ surface of the sensor.

1. Initiation

free radical creation by dissociation



2. Polymerization

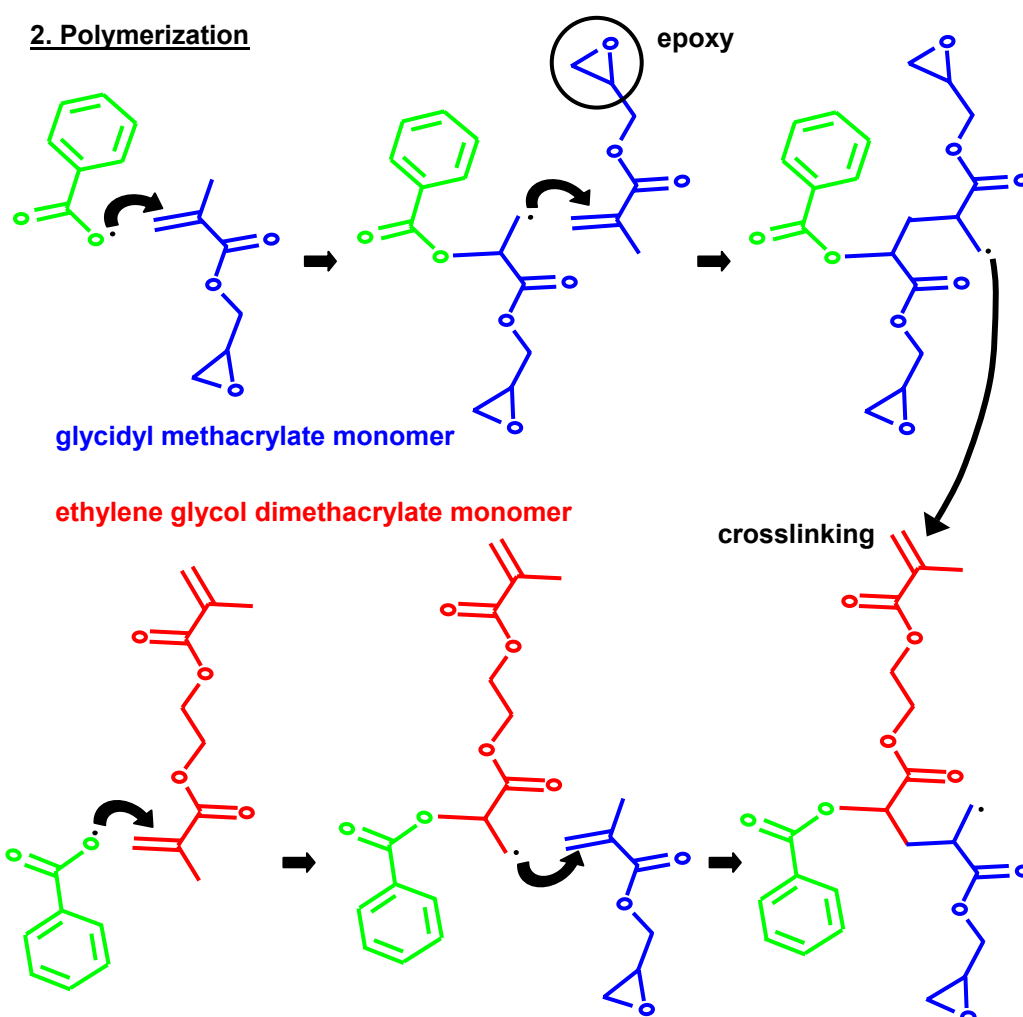


Figure 31: Sketch of the polymerization process

Chapter 4: The surface of the magnetic biosensor

Following probe DNA assembly, the drops are incubated in a humid atmosphere at room temperature for 30 min to allow formation of covalent bonds between the DNA's amino groups and the epoxy groups in the polymer. Afterwards, the spots are dried at 37°C for 15 min and at 100°C for 5 min on a hotplate. Additional covalent binding is achieved by irradiation with 50 mJ of UV light. Non-immobilized probe DNA is removed by several washing steps, and the remaining empty epoxy groups are inactivated by incubation in 1 M NaAc plus 2.5 % (weight / volume) PEG4000 solution (pH 5.0) at 55°C for 1 h. After another washing cycle, the probe DNA immobilization is finished, and the sensor is ready for analyte DNA hybridization.

5. GMR-type magnetic biosensor

5.1. GMR theory

Giant magnetoresistance in ferromagnetic layers separated by thin metallic non-ferromagnetic spacers is basically due to spin-dependent scattering of the conduction electrons at the ferromagnetic layers (Ref. 169). For ferromagnetic electrodes with their magnetization direction parallel (antiparallel) to the spin of the conduction electrons, the scattering probability is low (high), thus leading to a small (large) electrical resistance. Because spin-flip scattering can be neglected in most systems, spin-up and spin-down electrons can be regarded as two independent conduction paths parallel to each other (Ref. 170). In the case of antiparallel orientation of the magnetizations of adjacent ferromagnetic layers, both conduction paths encounter high and low scattering probabilities, thus leading to a relatively large total resistance. However, if the magnetizations of the ferromagnetic layers are aligned parallel to each other, the conduction path with the electron spins parallel to the magnetization directions experiences low scattering, while the electrons of the other path are constantly scattered with a large probability. This leads to a decreased total resistance relative to the antiparallel orientation. Thus, if a system of ferromagnetic layers separated by spacers can be tailored into an antiparallel ground state, it is possible to decrease its electrical resistance by applying external magnetic fields which force the system into parallel alignment. The mechanism which can create such an antiparallel configuration in the case of magnetic multilayer systems is the interlayer exchange coupling, which is discussed in the following chapter.

5.1.1. Interlayer exchange coupling

5.1.1.1. Introduction

Antiferromagnetic interlayer exchange coupling was first observed by Grünberg for Fe/Cr multilayers in 1986 (Ref. 4). Shortly afterwards, Parkin discovered that the coupling oscillates between the ferromagnetic and the antiferromagnetic configuration as a function of spacer thickness (Ref. 171). Initial experimental investigations revealed a unique oscillation period of about 10 Å for almost all non-magnetic 3d, 4d and 5d transition metals investigated as spacer materials (Ref. 172). But soon, it was discovered that things are more complicated than that, since some materials like Os showed larger oscillation periods (Ref. 173). Also, the period turned out to be dependent on the specific growth orientation of the crystal (Ref. 174). Furthermore, experiments with improved crystal qualities showed that there is not only one but several oscillation periods for different spacer materials like Cr or Mn (Ref. 175). These effects can be understood by looking at the actual Fermi surface of the spacer material, since the observed periods are related to the magnitudes of the extremal spanning wavevectors of the Fermi surface. For example, this relationship has been carried out in great detail by Stiles (Ref. 176). Even though these wavelengths are much shorter than the observed periods (around 3 Å compared to 10 Å), this discrepancy can be solved by taking into account the atomic discreteness of the interlayer thickness (see e.g. Ref. 177).

There are basically two strategies to study the interlayer exchange coupling theoretically, namely total energy calculations and perturbative methods. In total energy calculations, the magnetic coupling is determined by calculating the energy difference between the ferromagnetic and the antiferromagnetic configuration of the

entire multilayer system as a function of the spacer thickness. There are three different approaches to this method: ad initio calculations (Ref. 178), tight-binding calculations (Ref. 179) and quantum well calculations (Ref. 176; Ref. 180). The first two methods are straightforward, but quite difficult to perform since the obtained energy difference between the two states is several orders of magnitude smaller than the total energy itself. To obtain sufficient numerical accuracy within reasonable computation times, these methods are restricted to systems with small spacer thicknesses and do not appear to be well suited for the investigation of long-period oscillatory coupling. However, these models are most probably the only ones that could correctly predict the strength of the interlayer exchange coupling, since all other approaches are characterized by various approximations and simplifications. In quantum well models, for example, the actual band matching at the layer interfaces is simply replaced by step-like potentials. Still, such calculations have proven quite successful in the description of the period and phase of various multilayer systems. A more thorough discussion of this method follows in chapter 5.1.1.2.

Another approach to the problem of interlayer exchange coupling is followed by various perturbative methods, which attack the problem by formulating an additive Hamiltonian which is supposed to result in the observed coupling mechanism. Since the additional energy due to the interlayer exchange coupling is small compared to the total energy of the system, such an approach is justified. A mechanism proposed from early on uses the long known RKKY coupling (Ref. 1; Ref. 2; Ref. 3) between magnetic impurities in a nonmagnetic host metal. This indirect interaction is being transmitted by spin-polarization of the conduction electrons in the host metal. Looking at one magnetic impurity, the conduction electrons try to screen its magnetic moment by spin-polarizing around the impurity. But since it is not possible for the conduction electrons to form a localized screening, they do the closest possible alternative, which is a concentric spherical shell of opposite alignment around the impurity. This shell overcompensates the impurity, so an additional shell of parallel alignment is formed further away, and so on (Ref. 181). Another impurity then interacts with the first one via the polarized conduction electrons. The RKKY interaction is oscillatory in nature and can be taken as a basis for explaining the interlayer exchange coupling by superposing the coupling of each magnetic atom with every other magnetic atom in the system. The first extension of the RKKY theory to magnetic multilayers has been carried out by Yafet (Ref. 182), and is now generally accepted as the underlying mechanism of the interlayer exchange coupling. It correctly predicts the period of the oscillatory coupling for most systems, but fails to explain its phase and amplitude (strength). A more generalized approach applies the Anderson model of local state conduction-electron mixing (Ref. 183) to the problem of magnetic multilayers. It leads to a RKKY-like interaction in the case of low-energy spin-excitations, but also produces an additional superexchange for high-energy virtual charge excitations which corrects the phase of the oscillatory exchange interaction (Ref. 184). The prediction of its amplitude, however, remains problematic, and only seems to be accessible by total energy calculations from first principles.

5.1.1.2. Quantum well model

In this chapter, the quantum well model of the interlayer exchange coupling is presented. It relies on quantum interferences in the spacer material due to spin-dependent reflections of the conduction electrons at the interfaces between the spacer and the magnetic layers. These reflections modify the density of states in the spacer and give rise to a change of the system's energy. Because the reflection

coefficients depend on the orientation of the spin of the conduction electrons relative to the magnetizations of the ferromagnetic layers, the change of energy takes on different values for a ferromagnetic and an antiferromagnetic magnetization alignment. Due to the oscillatory nature of quantum confinement, the type of coupling oscillates as a function of spacer thickness, depending on which energy is lower for a given thickness. Amongst others, this model has been applied by Mathon (Ref. 169; Ref. 185), Jones (Ref. 181), Stiles (Ref. 176) and Bruno (Ref. 180). In particular, it has been worked out in great detail by Stiles and Bruno, and other approaches like the RKKY model have been connected to the quantum well theory in a self-consistent way (Ref. 176). Here, the approach by Bruno as described in Ref. 180 is followed.

First of all, lets consider a simple 1dim problem like the one sketched in Figure 32. The spacer layer has a thickness D and is situated between two sandwich layers of the same material. Here, the band matching at the interfaces leads to a potential well with a depth V , so that bound states with discrete energies exist within the spacer. Since the sandwich layers are approximated as being infinitely thick, the reflection coefficients at the two interfaces are equal to one for $E < V$, and the density of states in the spacer is given by a set of δ -functions. The wavefunctions for $E > V$ are also affected by the presence of the potential well, since they are reflected with an energy dependent reflection coefficient $r_{A/B}(E)$ at the two interfaces. This results in resonances at specific energies, and, therefore, an increase in the probability density. At other energies, the interference between the incident and reflected wave is destructive, so the probability density decreases. Since the amplitude of the reflected wave decreases rapidly with energy, the change of the probability density as a function of energy has the form of a damped oscillation for $E > V$. This change of the probability density compared to a continuous bulk metal also leads to a change in the density of states within the spacer.

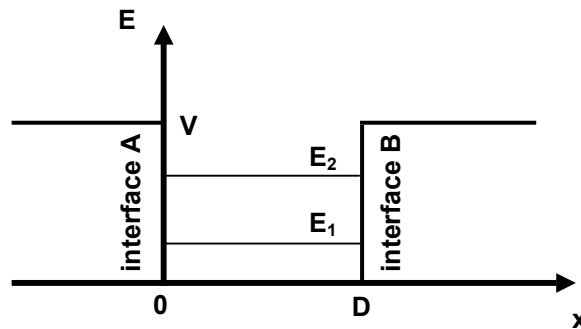


Figure 32: 1dim quantum well model of the interlayer exchange coupling

Bruno has developed a quantitative description of the modification of the density of states due to the formation of a quantum well. Using a general approach by calculating the Green's function of the system, he gives the following result for the change of the integrated density of states ΔN within the spacer layer relative to bulk material:

$$\Delta N(E) = -\frac{2}{\pi} \text{Im} \left(\ln \left[1 - r_A(E) r_B(E) e^{2ik_{\perp}(E)D} \right] \right) \quad \text{Equation 4}$$

Here, $k_{\perp}(E)$ describes the dependence of the electron wavevector component perpendicular to the plane on its energy. In our 1dim model, it is identical to the full wavevector $k(E)$. For 3dim problems, the same expression holds true, but integrated

over all possible parallel wavevector components. The integrated density of states N is simply the density of states n integrated up to a certain energy E :

$$N(E) = \int_0^E dE' n(E') \quad \text{Equation 5}$$

Bruno does not explicitly give the change of the density of states itself, but taking the derivative of the integrated form results in the following expression. The energy derivative of the reflection coefficients was neglected compared to the energy derivative of the exponential factor, which is a valid approximation for large spacer thicknesses.

$$\Delta n(E) = \frac{d(\Delta N(E))}{dE} = \frac{4}{\pi} D r^2(E) \frac{dk(E)}{dE} \frac{\cos[2k(E)D] - r^2(E)}{1 - 2r^2(E)\cos^2[2k(E)D] + r^4(E)}$$

with $k(E) = \sqrt{\frac{2m_E E}{\hbar^2}}$ and $r(E) = \begin{cases} 1 & \text{for } E \leq V \\ \left(\frac{\sqrt{E} - \sqrt{E-V}}{\sqrt{E-V} - \sqrt{E}} \right)^2 & \text{for } E > V \end{cases}$ Equation 6

To get an idea about the actual form of the density of states modification, [Figure 33](#) shows $\Delta n(E)$ for exemplary values of $V = 3$ eV and $D = 2$ nm. Here, the band structure of the spacer is neglected, so the electron mass m_E is set equal to the free electron mass. For $E < V$, the bound states show up as δ -like functions, and the corresponding energies are marked by small arrows. The bound states are modified by the bulk density of states (blue curve in [Figure 33 a](#)), which has a $1/\sqrt{E}$ dependence for 1dim systems. For $E > V$, one gets the expected oscillations in the change of the density of states (see [Figure 33 b](#)), the details of which depend on the barrier properties and the spacer width. However, if the parameters are such that an increase of the density of states occurs around the Fermi level E_F , this configuration is strengthened, while the opposite is true for a decrease of the density of states around the Fermi level.

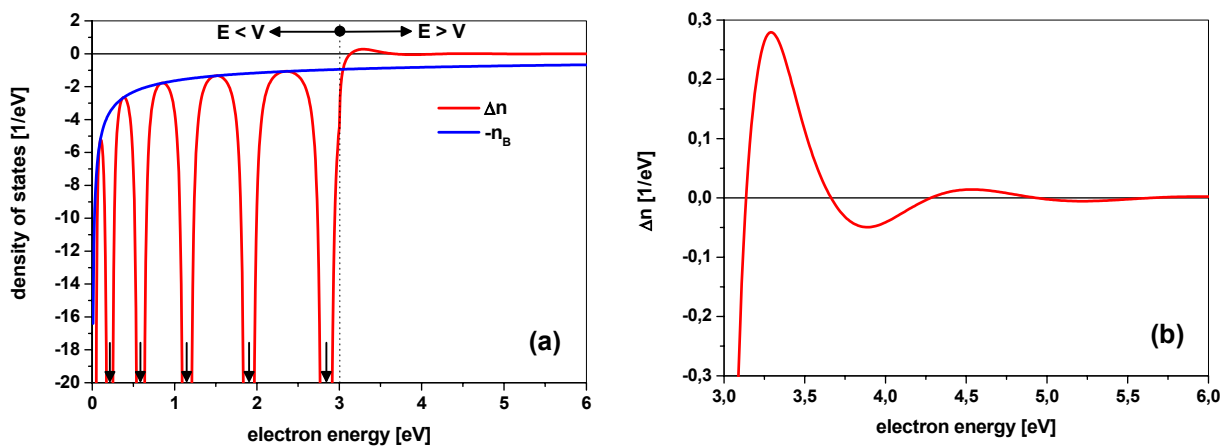


Figure 33: Density of states modification Δn due to the formation of a quantum well
a) comparison to bulk DOS n_B ; arrows indicate bound energy states
b) zoom of Δn for $E > V$

From the change of the density of states Δn , the change of energy ΔE in the spacer layer can be derived according to:

$$\Delta E = \int_0^{\infty} dE (E - E_F) \Delta n(E) f(E) \stackrel{T=0}{=} \int_0^{E_F} dE (E - E_F) \Delta n(E) \stackrel{P.I.}{=} - \int_0^{E_F} dE \Delta N(E) \quad \text{Equation 7}$$

In order to assure conservation of the number of particles, the grand canonical ensemble has been used. Furthermore, the calculation is for $T=0$, so that the Fermi-distribution is given by $f(E) = \Theta(E_F - E)$. Upon partial integrating, one gets the integral over the integrated change of the density of states. Plugging in the expression for $\Delta N(E)$ from Equation 4, the result for the change of energy in the spacer due to the formation of a quantum well is:

$$\begin{aligned} \Delta E &= \frac{2}{\pi} \text{Im} \int_0^{E_F} dE \ln \left[1 - r_A(E) r_B(E) e^{2ik(E)D} \right] \\ &= \frac{2}{\pi} \int_0^{E_F} dE \arctan \left(\frac{r_A(E) r_B(E) \sin[2k(E)D]}{r_A(E) r_B(E) \cos[2k(E)D] - 1} \right) \end{aligned} \quad \text{Equation 8}$$

When the sandwich layers are ferromagnetic, the reflection coefficients at the two interfaces A and B depend on the relative orientation of the electron spin to the magnetization vector. This dependence can be implemented in the above model by introducing a potential shift Δ (Ref. 176). If the electron spin is parallel (antiparallel) to the direction of the magnetization in the ferromagnetic layer, the electron 'sees' a smaller (greater) barrier height $V_{\text{par}} = V - \Delta$ ($V_{\text{anti}} = V + \Delta$). The situation is shown in Figure 34 for ferromagnetic and antiferromagnetic alignment of the magnetic layers. The reflection coefficient at the barrier V_{par} (V_{anti}) is denoted by r (R), and the arrows indicate the magnetization directions in the magnetic layers.

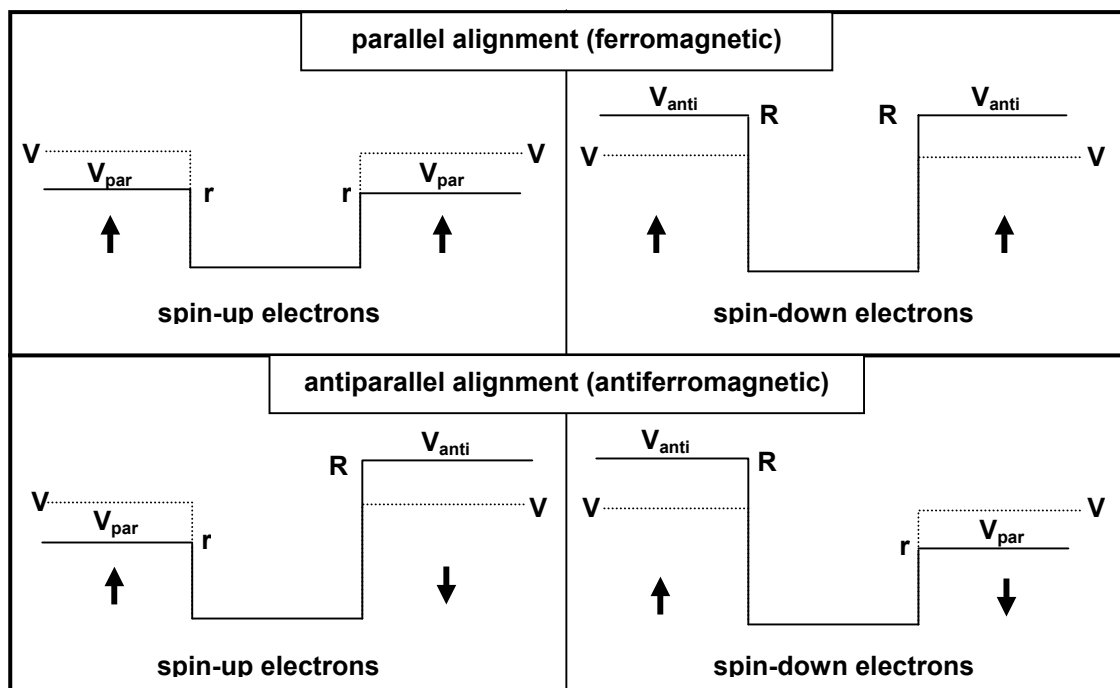


Figure 34: Comparison of the barrier heights for ferromagnetic and antiferromagnetic alignment of the magnetic layer magnetizations

The change of energy is now given by the average of the spin-up and the spin-down channel, and the interlayer exchange coupling J is defined as the energy difference between the parallel (ΔE_{par}) and the antiparallel (ΔE_{anti}) magnetization configuration:

$$J = \Delta E_{\text{par}} - \Delta E_{\text{anti}}$$

$$\text{with } \Delta E_{\text{par}} = \frac{1}{\pi} \text{Im} \int_0^{E_F} dE \left(\ln \left[1 - r^2(E) e^{2ik(E)D} \right] + \ln \left[1 - R^2(E) e^{2ik(E)D} \right] \right) \quad \text{Equation 9}$$

$$\text{and } \Delta E_{\text{anti}} = \frac{2}{\pi} \text{Im} \int_0^{E_F} dE \ln \left[1 - r(E) R(E) e^{2ik(E)D} \right]$$

Due to this definition, a positive (negative) value of J means that the antiferromagnetic (ferromagnetic) alignment is energetically favorable, and the system relaxes into the corresponding state. [Figure 35](#) shows the results for ΔE_{par} , ΔE_{anti} and J according to [Equation 9](#) for exemplary values of $V = 3$ eV, $\Delta = 1$ eV and $E_F = 7$ eV. To solve these equations, the energy integral has been transferred into a sum over 5000 equally distributed discrete energies from zero to E_F for each value of the spacer thickness. The Fermi level of 7 eV corresponds to copper as spacer material, which is frequently used in GMR multilayer systems.

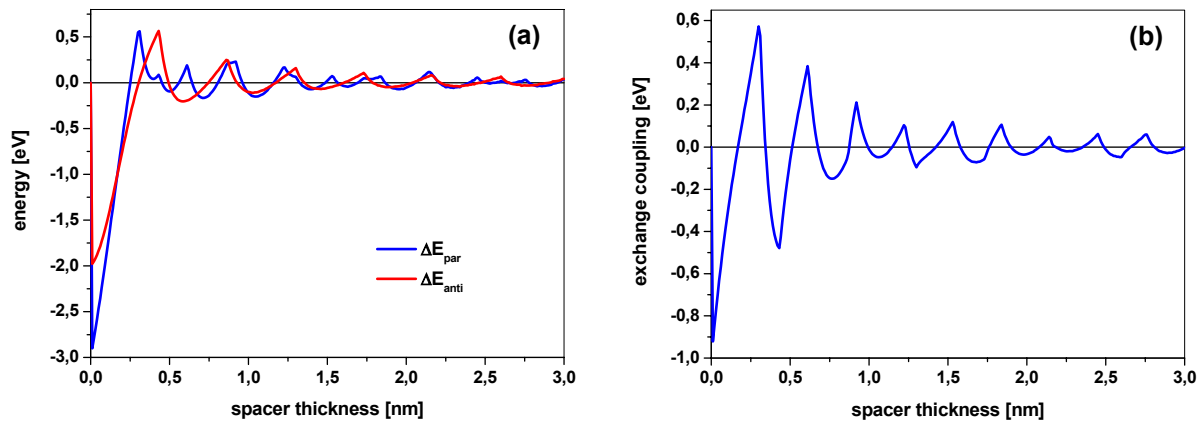


Figure 35: Results of the calculation of the exchange coupling
a) energy differences ΔE in the spacer relative to bulk material
b) interlayer exchange coupling

Looking at part a) of [Figure 35](#), it is apparent that the energy difference relative to bulk material favors either a parallel or an antiparallel magnetization configuration, depending on the exact thickness of the spacer layer. Thus, the interlayer exchange coupling ([Figure 35 b](#)) oscillates between negative and positive values with an oscillation period of 0.30 nm. Compared to the Fermi-wavelength of our free electron model of 0.46 nm (for $E_F=7\text{eV}$), this value agrees more or less to the theory that the oscillation period is determined by the extremal spanning vectors of the Fermi surface. As expected, the coupling is ferromagnetic in the limit of zero spacer thickness. This is required since the two magnetic layers become one in this case and share a common magnetization direction.

Even though this simple model gives a relatively good value of the oscillation period in this case, this cannot be expected in general. For example, the free electron model is oversimplified, and one has to take into account the band structure for the specific materials involved. By doing so, the dispersion relation $k(E)$ changes, and with it also

the oscillation period, since it depends on the wavevector components perpendicular to the plane of the layer interfaces.

In addition, the problem really has to be treated three dimensional. By doing this, an integration over the wavevectors parallel to the interfaces is added, and generally, both the reflection coefficients and the perpendicular wavevector components depend on the parallel wavevectors. Thus, both the period (it depends on the perpendicular wavevector component) and the strength of the coupling (it depends on the reflection coefficients) change when treating the problem three dimensional. Combined with realistic band structures, this also reveals several oscillation periods, since there is more than only a single extremal spanning vector for a realistic three-dimensional Fermi surface.

Another assumption of this model is an infinite thickness of the magnetic layers, which cannot be true for realistic systems. A pretty obvious effect of a finite magnetic layer thickness is a change in the reflection coefficients, since in this case, there is also transmission for $E < V$. This results in a decrease of the reflection coefficient and, therefore, a decreased coupling strength. Furthermore, there are also oscillations in the coupling with respect to the magnetic layer thickness due to the formation of resonances in the magnetic layers.

Still, the simple model presented here gives some insight into the mechanism of the interlayer exchange coupling, and it can easily be extended to more realistic situations, as it was done (amongst others) by Bruno (Ref. 181) and Stiles (Ref. 176). By doing so, a large degree of agreement is reached between experimental results and predictions of the quantum well model, so this theory is generally accepted by now.

5.1.1.3. Phenomenological model

The coupling between two ferromagnetic layers can be described phenomenologically in terms of energy contributions. Generally, there is also a biquadratic coupling term which leads to a 90° orientation between the magnetizations of adjacent ferromagnetic layers. The origin of this term is also linear exchange coupling, but non-ideal circumstances like interface roughness (Ref. 186) and intermixing of free magnetic atoms in the spacer layer (“loose spin” mechanism, Ref. 187) lead to frustrations of the linear exchange, which give rise to an effective quadratic coupling. When θ denotes the angle between the magnetization vectors \vec{M}_1 and \vec{M}_2 of two ferromagnetic layers separated by a spacer layer, the interlayer energy contribution E_{int} due to the bilinear coupling J_L and the biquadratic coupling J_Q is given by (Ref. 186):

$$E_{\text{int}} = -J_L \frac{\vec{M}_1 \cdot \vec{M}_2}{|\vec{M}_1| \cdot |\vec{M}_2|} - J_Q \left(\frac{\vec{M}_1 \cdot \vec{M}_2}{|\vec{M}_1| \cdot |\vec{M}_2|} \right)^2 = -J_L \cos \theta - J_Q \cos^2 \theta \quad \text{Equation 10}$$

5.1.2. Giant Magnetoresistance

Soon after the discovery of the interlayer exchange coupling by Grünberg in 1986 (Ref. 4), it was observed by Baibich (Ref. 5) that the electrical in-plane resistance of such a system depends on the relative magnetization configuration of the ferromagnetic layers, which could be altered by applying an appropriate magnetic field. This new type of magnetoresistance was named giant magnetoresistance (GMR) due to the large magnitude of the resistance change compared to the previously known anisotropic magnetoresistance (AMR). In the meantime, devices which are based on the GMR effect found their way into a number of different applications like for example read heads in hard disk drives (Ref. 8).

Theoretically, the GMR effect can be derived by a simple resistor network model. It relies on negligible spin flip scattering, so that the conduction paths of spin-up and spin-down electrons can be treated independently as two channels parallel to each other (Ref. 170). The model was initially developed by Edwards in 1991 (Ref. 188), while the description here follows the work by Mathon from Ref. 169.

In ferromagnetic transition metals, the densities of states for majority and minority d electrons are split. Therefore, the resistivities for the two spin channels are also different from each other, which is due to their proportionality to the density of states at the Fermi level for elastic scattering processes (the higher the density of states, the more states exist for the electron to scatter into, and the larger the resistivity, Ref. 170). Thus, an electron which transverses a magnetic multilayer superlattice experiences alternating resistivities which depend on the orientation of its spin relative to the local magnetization vectors. The distribution of these local resistivities is sketched in Figure 36 as a bar diagram for spin-down and spin-up electrons transversing a unit cell of a magnetic multilayer superlattice. Here, ρ_H (ρ_L) denotes the high (low) resistivity state which occurs in ferromagnetic layers (abbreviated by FM) for antiparallel (parallel) spin and magnetization, while ρ_N stands for the spin-independent resistivity of the non-magnetic spacer layer (abbreviated by NM).

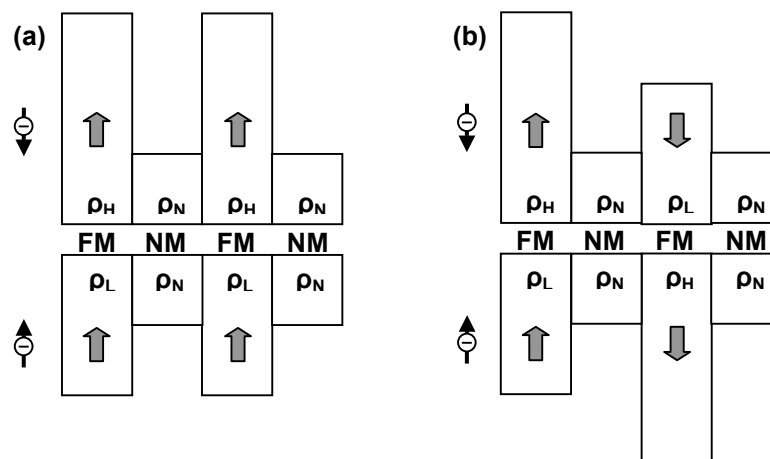


Figure 36: Sketch of the local resistivities for spin-up and spin-down electrons transversing a magnetic superlattice (after Ref. 169)

a) ferromagnetic configuration
b) antiferromagnetic configuration

An initial antiferromagnetic configuration of the magnetization vectors of the ferromagnetic layers can be transferred into a ferromagnetic configuration by applying a sufficient magnetic field, and the relative change of resistivity of the system is given by the GMR-ratio:

$$\text{GMR} = \frac{\Delta R}{R_{\min}} = \frac{R_{\uparrow\downarrow} - R_{\uparrow\uparrow}}{R_{\uparrow\uparrow}} \quad \text{Equation 11}$$

Thus, by calculating the resistances for those two configuration within our model, we can predict the respective magnetoresistance ratio of the system. Since the entire multilayer system can be constructed out of the blocks shown in [Figure 36](#), it is sufficient to calculate the resistance of those unit cells only. In the system of interest, the current is applied in the plane of the layers, so an appropriate rule for adding up the resistivities of the individual layers has to be found. Generally, this is only possible within a microscopic description, but there are two limits in which the superlattice can be approximated by macroscopic terms.

In the first limit, the mean free path of the electrons is much shorter than the thicknesses of the individual layers. This case leads to negligible intermixing of electrons originating from adjacent layers, so the total resistivity is simply given by adding all single layer resistivities in parallel. In [Figure 36](#), this would correspond to a parallel circuit of all eight individual resistivities (four from each spin channel), resulting in identical total resistivities of the parallel and antiparallel configuration and no magnetoresistance.

The opposite limit is reached when the mean free path of the electrons is much larger than the thicknesses of the individual layers. In this case, the conduction electrons transverse many consecutive layers before being scattered and experience an average resistivity ρ_{av} . For a superlattice consisting of N components with an individual resistivity ρ_n and a layer thickness t_n , it is given by:

$$\rho_{\text{av}} = \frac{t_1\rho_1 + t_2\rho_2 + \dots + t_N\rho_N}{t_1 + t_2 + \dots + t_N} \quad \text{Equation 12}$$

Since the mean free paths in metals are of the order of tens to hundreds of interatomic distances, magnetic multilayer systems with layer thicknesses in the nanometer range typically fall into this category, and we can use [Equation 12](#). For a unit cell with length L and width W consisting of ferromagnetic layers with a thickness t_M and non-magnetic layers with a thickness t_N , the total resistances of individual spin channels in the different magnetization configurations are given by:

ferromagnetic configuration :

$$\begin{aligned} \text{spin-down electrons: } R_{\uparrow\uparrow}^{\downarrow} &= \frac{L}{2(t_M + t_N)W} \frac{2t_M\rho_H + 2t_N\rho_N}{2(t_M + t_N)} \\ \text{spin-up electrons: } R_{\uparrow\uparrow}^{\uparrow} &= \frac{L}{2(t_M + t_N)W} \frac{2t_M\rho_L + 2t_N\rho_N}{2(t_M + t_N)} \end{aligned} \quad \text{Equation 13}$$

antiferromagnetic configuration :

$$\text{spin-down / spin-up electrons: } R_{\uparrow\downarrow}^{\downarrow} = R_{\uparrow\downarrow}^{\uparrow} = \frac{L}{2(t_M + t_N)W} \frac{t_M\rho_L + t_M\rho_H + 2t_N\rho_N}{2(t_M + t_N)}$$

Assuming that the two spin channels can be treated independently, the total resistance of the unit cell in each magnetization configuration is given by a parallel circuit model:

ferromagnetic configuration :

$$R_{\uparrow\uparrow} = \frac{R_{\uparrow\uparrow}^{\downarrow} R_{\uparrow\uparrow}^{\uparrow}}{R_{\uparrow\uparrow}^{\downarrow} + R_{\uparrow\uparrow}^{\uparrow}} = \frac{L}{2(t_M + t_N)^2 W} \frac{(t_M \rho_H + t_N \rho_N)(t_M \rho_L + t_N \rho_N)}{t_M \rho_L + t_M \rho_H + 2t_N \rho_N}$$

Equation 14

antiferromagnetic configuration :

$$R_{\uparrow\downarrow} = \frac{1}{2} R_{\uparrow\downarrow}^{\downarrow} = \frac{1}{2} R_{\uparrow\downarrow}^{\uparrow} = \frac{L}{8(t_M + t_N)^2 W} (t_M \rho_L + t_M \rho_H + 2t_N \rho_N)$$

Following Equation 11, the GMR ratio in this model is given by:

$$GMR = \frac{R_{\uparrow\downarrow} - R_{\uparrow\uparrow}}{R_{\uparrow\uparrow}} = \frac{(\alpha - \beta)^2}{4 \left(\alpha + \frac{t_N}{t_M} \right) \left(\beta + \frac{t_N}{t_M} \right)} \quad \text{with } \alpha := \frac{\rho_H}{\rho_N} \quad \text{and } \beta := \frac{\rho_L}{\rho_N}$$

Equation 15

As a result, the most important factor for a large GMR ratio within this model is a strong spin asymmetry ratio $\alpha/\beta = \rho_H/\rho_L$. Its dependence is shown in part a) of [Figure 37](#) for $t_N/t_M=1$ and $\beta=1$. The latter parameter corresponds to equal densities of states of the majority d electrons in the magnetic layer and the d electrons in the spacer layer at the Fermi energy, which is true for example in Cu/Co multilayers ([Ref. 189](#)). For values of $\alpha > 2$, the GMR ratio increases almost linearly with increasing α . In Cu/Co multilayers, a typical value is $\alpha=8$ ([Ref. 169](#)). This parameter was used to calculate the dependence of the GMR ratio on the thickness fraction t_N/t_M , the result of which is displayed as the blue curve in [Figure 37 b](#)). For large spacer thicknesses, the GMR ratio falls off as $1/t_N^2$, which is a consequence of the increased shunting. In order to judge the results of this simple model, some of the low temperature measurements of Parkin ([Ref. 190](#)) on Cu/Co multilayers with varying spacer layer thickness are also shown in [Figure 37 b](#)). Because an antiferromagnetic ground state has been assumed, the model can only describe the envelope of the data which oscillates as a function of spacer thickness. This envelope, however, agrees pretty well to the model for the 2nd and 3rd antiferromagnetic coupling maximum. For the 1st maximum, the predicted GMR ratio is too high in this case, but optimized superlattices with a large number of multilayers are reported to reach a GMR ratio of up to 115 % at 4.2 K in the 1st maximum ([Ref. 191](#)).

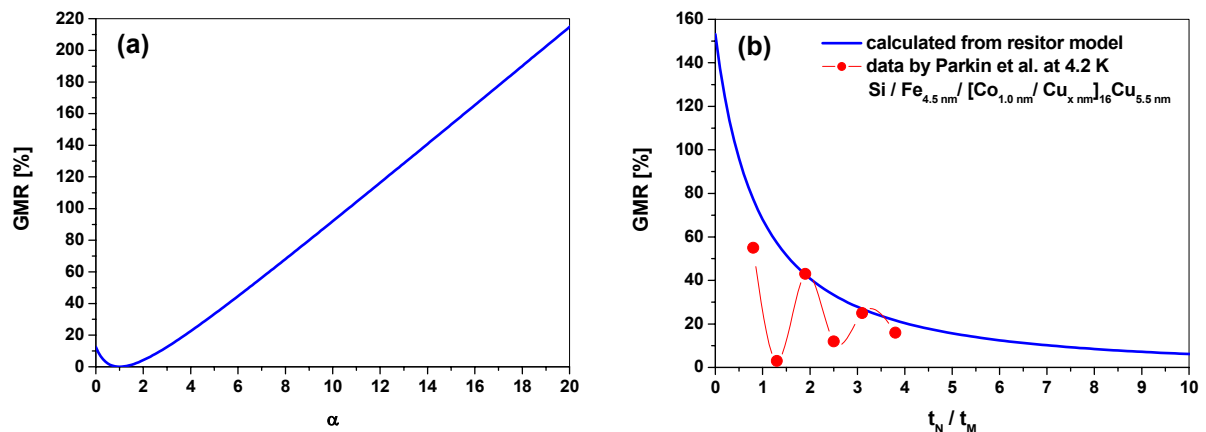


Figure 37: Calculated GMR ratios according to the resistor network model
a) dependence on the spin asymmetry ratio $\alpha/\beta=\alpha$ for $\beta= t_N/t_M=1$
b) dependence on the relative spacer thickness t_N/t_M for $\alpha=10$ and $\beta=1$

Even though a good degree of agreement to the data is reached by the resistor network model, there are some discrepancies due to its simplicity. For example, it is observed experimentally that the GMR ratio decreases exponentially with increasing spacer thickness (Ref. 192). Within the model, this decay should be proportional to $1/t_N^2$. The difference can be attributed to the assumption of a long free path of the electrons compared to the layer thickness, which is no longer valid in the limit of large spacer thicknesses. Furthermore, measurements of the mean free path in Py multilayer systems revealed length scales comparable to the layer thickness (Ref. 193), so that this assumption seems to be questionable even in the limit of thin spacers. Also, the resistor network model produces the same GMR ratio no matter in which geometry the current is passed through the multilayer stack, but experimentally, the current perpendicular to plane (CPP) geometry shows substantially higher GMR ratios than the current in plane geometry (CIP). This is related to the different critical length scales: in the CPP geometry, every electron is forced to pass every single layer of the stack, so it is sufficient if the spin diffusion length is larger than the layer separation. On the other hand, the critical length scale in the CIP geometry is the much shorter mean free path, which is due to the fact that the electrons have to sample both magnetic layers before being scattered in order to display a magnetoresistance (Ref. 194). This differentiation is neglected in the resistor network model.

Due to these shortcomings, it is obvious that the resistor network model is oversimplified and has to be extended or supplemented by other approaches to correctly predict all aspects of the GMR effect. There are many different methods to treat this problem, and a comprehensive review can be found for example in Ref. 195. Basically, the various approaches can be classified according to the effort they put into the electronic structure of the multilayer system and, secondly, the electron transport mechanism through the superlattice. Concerning the electronic structure of the multilayers, the most basic approaches employ a free electron model (Ref. 196) or assume a single tight binding band (Ref. 197). Though oversimplified, these methods successfully reproduce some of the main features like the dependence of the GMR ratio on the thickness of the spacer and the magnetic layers or its enhancement with increasing multilayer number. However, these results are only qualitative, and a quantitative agreement requires the incorporation of the actual band structure of the superlattice, which is either calculated from first principles within the local density approximation (Ref. 198) or derived with the help of parameterized multiple tight binding bands (Ref. 199).

With respect to electron transport, the most common model uses the widely accepted versatile semiclassical Boltzmann theory (Ref. 200). In most multilayer systems, however, its applicability is limited, and a full scale quantum mechanical transport theory like the Kubo-Landauer formalism (Ref. 201) has to be used. Combined with realistic multiband structures, this is the best way to describe the GMR effect quantitatively.

5.2. Sensor layout and characteristics

Our GMR sensors consist of Cu/Py multilayers (Py = Ni₈₀Fe₂₀) in the second antiferromagnetic coupling maximum. In order to ensure good adhesion of the subsequent SiO₂ passivation, a thin tantalum layer is added to the top. The entire multilayer system has the following composition:

wafer / Py_{1.6nm} / [Cu_{1.9nm} / Py_{1.6nm}]₁₀ / Ta_{3nm}

Figure 38 shows the magnetoresistance response of a continuous unpatterned layer stack to an in-plane magnetic field. Its resistance decreases by 8 % at a saturation field of 4.6 kA/m, resulting in an overall sensitivity of about 1.7 % per kA/m. The response is linear almost up to saturation and shows no hysteresis. Thus, this magnetoresistive system is quite suitable for the detection of small magnetic fields.

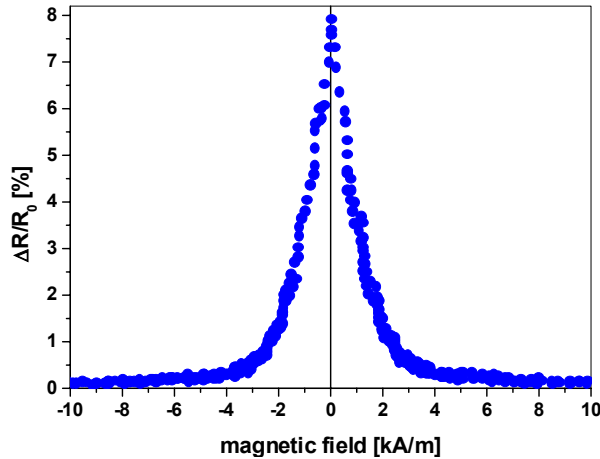


Figure 38: Magnetoresistance response of an unpatterned multilayer system

The strength of the bilinear and biquadratic coupling are determined from the magnetoresistance response of the continuous layer stack according to the fitting routine described in the diploma thesis of Sonja Heitmann (Ref. 202). It takes into account the Zeeman energy and the coupling energies (see Equation 10) and determines the respective coupling strengths by minimizing the energy sum. The resulting fitting function has the following form:

$$H(x) = \frac{4}{\mu_0 t_{Py} M_S} \sqrt{x} [4J_Q x - 2J_Q + J_L] \quad \text{Equation 16}$$

Here, x represents the alternative definition of the GMR-ratio which is normalized to the high resistive state and is also normalized to its full amplitude A . The Py-thickness t_{Py} is set to 1.6 nm, and its saturation magnetization is given by $M_S=860$ kA/m. For one branch of a typical magnetoresistance measurement, the corresponding fit is compared to the data in Figure 39.

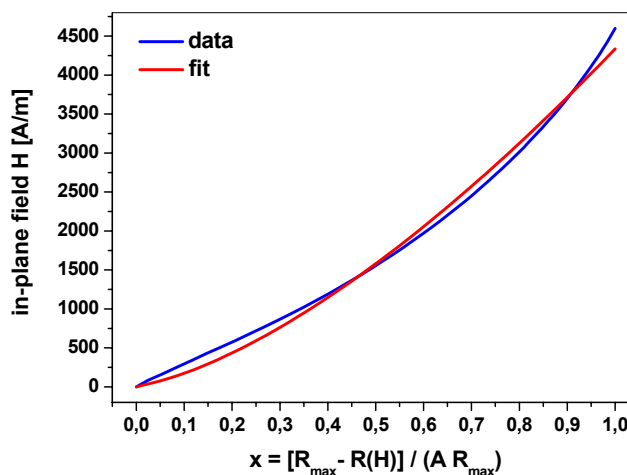


Figure 39: Data and corresponding fit for determining the coupling strengths

The fitting procedure gives the following results for the coupling coefficients from one magnetic layer to another (the fact that the coupling in infinite multilayers is given by twice that value is already included in the derivation of the fitting function):

$$J_L = 0.97 \mu\text{J}/\text{m}^2$$

$$J_Q = 0.46 \mu\text{J}/\text{m}^2$$

$$\text{effective af-coupling: } J_{\text{eff}} = J_L + 2 J_Q = 1.89 \mu\text{J}/\text{m}^2$$

The quadratic term agrees well to the data given in Heitmann's diploma thesis (Ref. 202), whereas the linear coupling strength only reaches about $2/3^{\text{rd}}$ of the value given in this reference. However, the samples analyzed in Heitmann's diploma thesis consisted of four times as many multilayers, and it is known that the coupling strength increases with increasing multilayer number due to enhanced growth (Ref. 202). Furthermore, the fitting procedure in Heitmann's diploma thesis has been carried out for samples which were prepared on thin glass slides. Samples on Si-wafer substrates, which have also been investigated in this reference, only show about half the saturation field, which leads to a decreased linear coupling strength. Thus, the origin of the discrepancy can be attributed to a combination of those two factors.

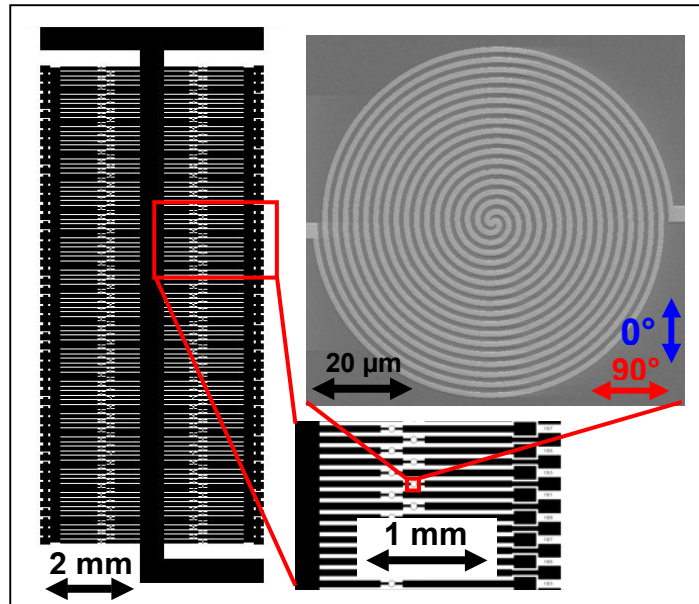


Figure 40: Layout of the GMR biosensor prototype

Individual sensor elements are patterned from the continuous stack by positive electron beam lithography and argon ion etching. A 17 nm thick tantalum layer is applied as a hard mask for the etching process to prevent resist remnants that could cause leaking sites in the subsequent protection layer (see chapter 4.1). The resulting sensor elements consist of lines with a thickness of 1 μm and a total length of about 1.8 mm which are wound into spirals with a total diameter of 70 μm and an electrical in-plane resistance at zero magnetic field of about 12 kΩ (see Figure 40). In order to prevent shortcuts between individual spiral windings, the etching process is continued into the underlying SiO₂. Additionally, about 3 nm of the Ta hard mask is left over to ensure that the GMR multilayer stack remains in its original state (no intermixing, oxidation, etc.). The section analysis of the AFM image shown in Figure 41 reveals a total height of the spiral windings of about 82 nm, which implies an etching depth into the substrate of approximately 40 nm.

An individual sensor element covers the entire area of a single probe DNA spot, which has a typical diameter of around 100 μm for standard piezo spotters. Thus, one sensor element measures the average signal of all the magnetic markers which are bound at one specific probe DNA spot. However, markers which are situated in the 1 μm wide spacing between the spiral windings only contribute a reduced signal. This effect is analyzed quantitatively in chapter 5.4.3. By putting a number of smaller sensors underneath each probe DNA spot, it would be easily possible to resolve the internal spatial marker distribution, but for typical microarray hybridization experiments only the average signal is relevant. Therefore, our sensor is optimized for such macroscopic molecular recognition reactions.

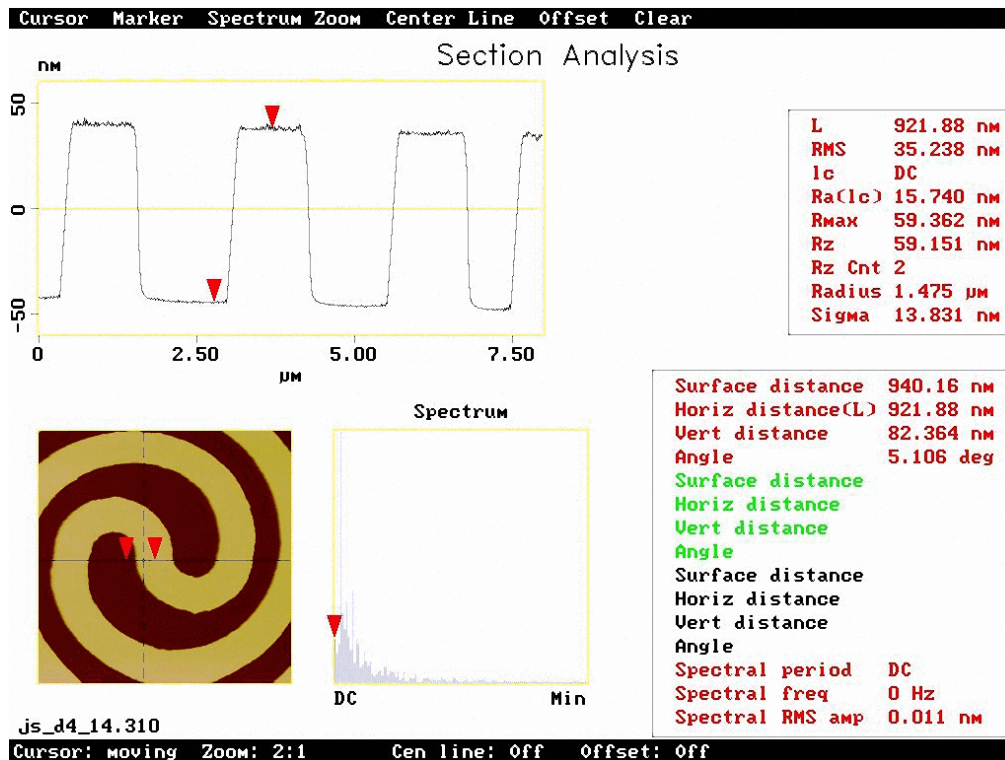


Figure 41: AFM analysis of the inner part of a spiral-shaped GMR sensor element

A total number of 206 separate sensor elements are integrated into a prototype magnetoresistive biosensor on a total area of 5 x 12 mm^2 . The contact pads and interconnect lines are made of a $\text{Ta}_{10\text{nm}}\text{Au}_{50\text{nm}}\text{Ta}_{10\text{nm}}$ sandwich structure and are patterned using positive photo lithography and lift-off. Keeping some elements uncovered for reference purposes, as many as 200 different probe DNA spots can be tested at the same time with this prototype.

The magnetoresistance response of a single spiral-shaped sensor element is displayed in Figure 42. Due to the isotropic design, the characteristic is the same no matter in which direction the external in-plane field is applied (the two displayed directions are oriented perpendicular to each other and are specified in Figure 40). However, there is still shape anisotropy along the individual windings of the spiral, which causes the magnetization to lie tangential to those windings. Furthermore, contour imperfections at the edges present an additional source of domain wall pinning, which gives rise to the observed hysteresis of about 270 A/m. Such a hysteresis is not observed in the case of an unpatterned layer stack.

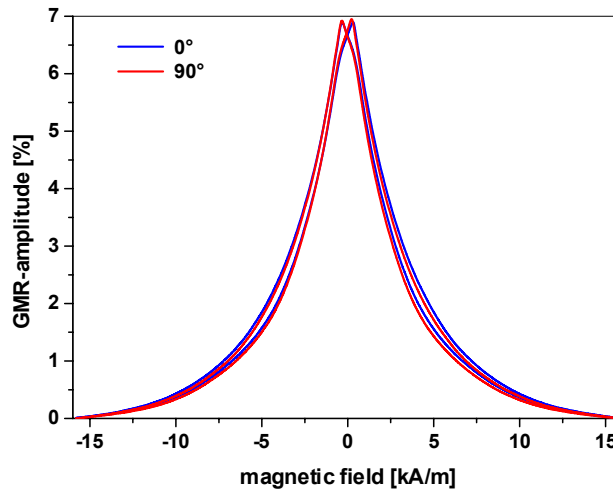


Figure 42: Isotropic magnetoresistance response of a spiral-shaped sensor element

5.3. OOMMF model

A micromagnetic simulation of our GMR type biosensor is developed on the basis of the public domain program “oommf” (Ref. 203), which solves a given problem by evolving it in terms of the Landau-Lifshitz-Gilbert equation (Ref. 204). Even though such calculations cannot predict results quantitatively in this case, they help to interpret the various measurements associated with this sensor type.

Due to the large size of a single sensor element, the transfer of the entire spiral area into the micromagnetic simulation would cause unacceptably long runtimes. Keeping the cellsize in the range of typical grain sizes (about 20 nm for our sputtering conditions), sensor areas of a few μm^2 can be simulated within reasonable runtimes (about one week) at current processor speeds (AMD Athlon 1.9 GHz). Thus, the magnetoresistance characteristic of an entire sensor element has to be mimicked by a model system no larger than a few μm^2 .

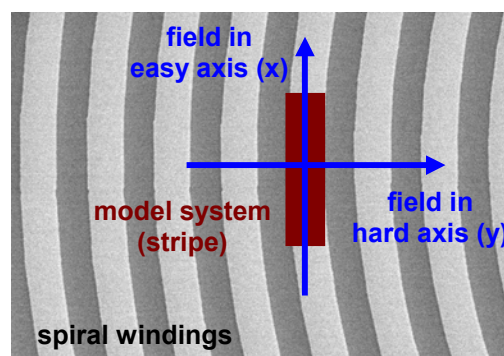


Figure 43: Model system for simulation purposes

Neglecting their curvature, individual spiral segments of a sensor element can be characterized in a crude way by straight lines, where each angular line orientation has the same probability of occurrence (see Figure 43). Following this approach, a line-shaped model system should display a magnetoresistance characteristic similar to an entire spiral if several of its GMR responses are averaged over various in-plane angles of the applied magnetic field. In fact, since the plane of the sensor is two-dimensional, it is sufficient to take only two linearly independent field directions. Here,

we choose the easy direction (field parallel to the long side) and the hard direction (field parallel to the short side) of our model system. Furthermore, we implement an additional simplification by simulating only two magnetic layers separated by a single non-magnetic spacer layer. Such a tri-layer model system produces the same GMR response like a multilayer stack if the effective af-coupling is doubled for simulation purposes (in an infinite multilayer system, each magnetic layer experiences af-coupling from two adjacent ferromagnetic layers).

A number of parameters enter the micromagnetic simulation. Straightforward are the thickness of the ferromagnetic layers (1.6 nm) and the saturation magnetization of Py (860 kA/m at room temperature, Ref. 143). The cellsize is set to $20 \times 20 \text{ nm}^2$, which corresponds to the size of a typical grain in a Py-layer. The standard six-neighbor exchange energy term is taken for the ferromagnetic coupling, and the exchange coefficient is set to its full value for Py (13 pJ/m, Ref. 143). Due to the reduction of our actual multilayer system to a tri-layer, the antiferromagnetic coupling strength is set to $3.8 \mu\text{J}/\text{m}^2$, which is twice the value derived in chapter 5.2. Further energy terms are the demagnetizing energy and the Zeeman energy, which can include both a spatially homogeneous external field of adjustable strength and direction and various dipole fields from magnetic particles. Even though Py does show a small crystalline anisotropy of $K_V = -0.4 \text{ kA/m}$ (Ref. 143), it is not included in this simulation due to its negligible magnitude and the fact that our magnetic layers are polycrystalline. In terms of simulation parameters, a total torque across all spins of the system of $dm/dt = 0.01 \text{ }^\circ/\text{ns}$ is chosen as a stopping criteria at each stage.

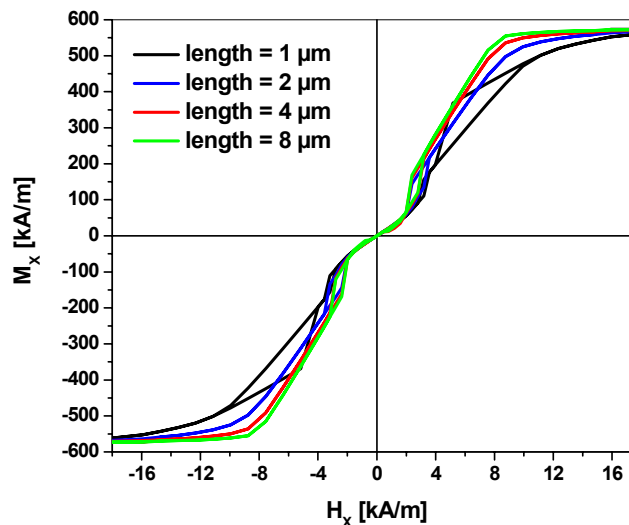


Figure 44: Projection of the total magnetization onto the long axis as a function of applied external in-plane field for different lengths of the model system

Another set of parameters comes from the dimensions of the line which is used as a model system in this simulation. According to the respective value of the spiral windings, its width is set to $1 \mu\text{m}$. Its length, however, is not determined that clearly. Looking at the mid-section of a spiral-shaped sensor element shown in Figure 43, one could say that a length of $4 \mu\text{m}$ approximates the tangential of a winding without too much error due to the neglected curvature. Another criteria is the shape anisotropy of the model system, which should be large in order to correctly resemble the situation within a spiral winding. Figure 44 shows the simulated field dependence of the total magnetization for different lengths of the model system. The field is applied in the easy axis (x-direction), and the respective magnetization component is calculated relative to the total volume of the model system (the spacer layer is set to

the same thickness as the magnetic layers, which is why the displayed saturation magnetization is only $2/3^{\text{rd}}$ of the Py-value). To increase computation speed, the cellsize is set to 200 nm for this test only. As expected, the saturation field becomes smaller with increasing shape anisotropy, but the difference between a length of 4 μm and 8 μm is only marginal. Thus, a stripe length of 4 μm is chosen to save some computation time.

No periodic boundary conditions are applied at either edge of the model system, which results in stray fields and diverted magnetization patterns at its borders. In a real spiral segment, this is not the case along the easy axis, since the windings are similar to closed loops. However, the oommf code is not designed for implementing periodic boundary conditions, so that additional edge effects have to be kept in mind when comparing simulated results to measurements.

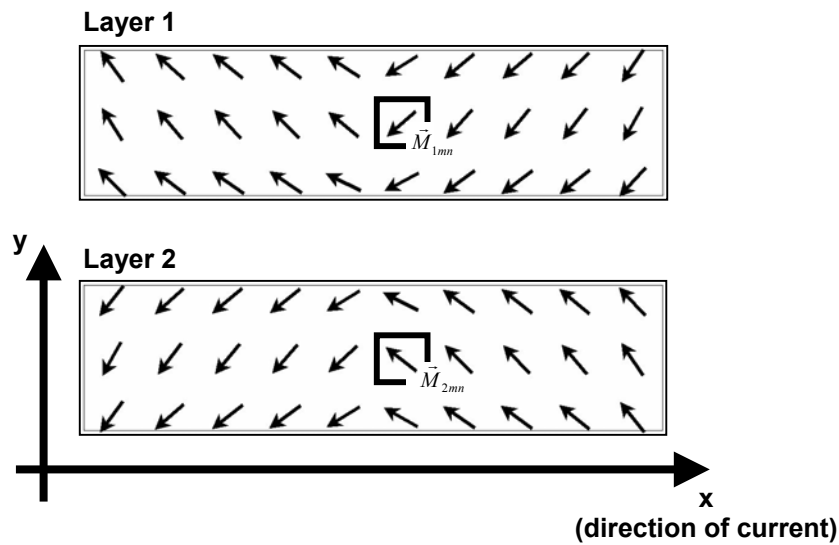


Figure 45: Sketch of the relative resistance calculation for the model system

The main output of the oommf simulation program is the local magnetization vector at every cell for each value of a stepped external homogeneous magnetic field. In order to compare these simulated results to measurements, the magnetization information has to be converted into magnetoresistance curves, i.e. relative electrical resistance over applied magnetic field. Since the current flows parallel to the spiral windings, it is taken to be oriented along the easy axis (x-axis, see Figure 45) of our model system. In order to calculate the total resistance of the model system, the relative resistances of all pairs of opposing cells are computed from the angles between their respective magnetization vectors. For cell number m,n in this two-dimensional array, its resistance r_{mn} is given by:

$$r_{mn} = r_0 \left[1 + \frac{A}{2} (1 - \cos \alpha_{mn}) \right] \quad \text{with} \quad \alpha_{mn} = \frac{\vec{M}_{1mn} \cdot \vec{M}_{2mn}}{|\vec{M}|^2} \quad \text{Equation 17}$$

Here, α_{mn} is the angle between the two magnetization vectors \vec{M}_{1mn} and \vec{M}_{2mn} , r_0 is the cell resistance in saturation (at $\alpha_{mn}=0^\circ$), and A is the full GMR amplitude. Next, the relative resistances of all possible conduction paths are calculated by summing the individual cell resistances along the x-axis (total number of M cells in each path). These conduction paths are parallel to each other, so that the total resistance R of

the model system for a particular magnetization configuration is obtained by taking the inverse sum of all conduction paths along the y-axis (N conduction paths). Relative to its saturation resistance R_0 , it has the following form:

$$\frac{R}{R_0} = \frac{N}{M} \sum_n \left(M + \frac{A}{2} \sum_m (1 - \cos \alpha_{mn}) \right)^{-1} \quad \text{Equation 18}$$

These calculations are carried out for each step of the external field, resulting in complete GMR curves that can be compared to the data. Strictly speaking, the construction of the relative resistance from the magnetization configuration is not entirely accurate, since in this model, there is no possibility of a current flowing in a diagonal direction. However, such paths have a larger total resistance and only contribute in a negligible way.

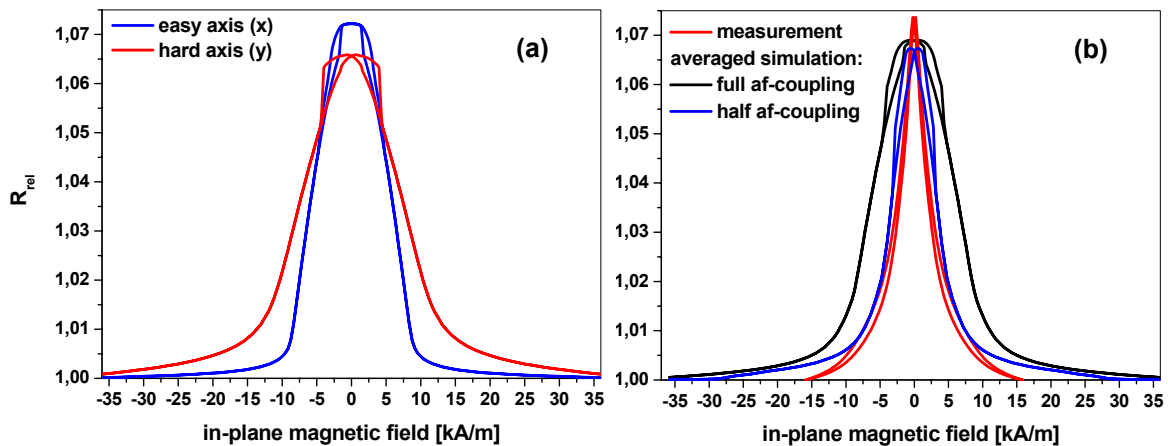


Figure 46: Relative magnetoconductance of the model system
a) simulated GMR characteristics along the hard and easy axis of the model system
b) comparison of average simulated and measured characteristics

Figure 46 displays GMR characteristics obtained from simulations of the described model system. The amplitude A is set to 7.4 %, which corresponds to the data taken for a real spiral-shaped sensor element. In part a), the individual magnetoconductance curves along the x- and y-axis are shown. Clearly, the saturation field is smaller when the field is applied in the easy direction. The reason why the amplitude does not reach its full value of 1.074 lies in the stray fields at the borders of the model system. These edge effects prevent a perfectly antiparallel alignment of the magnetization vectors of the two magnetic layers.

In Figure 46 b), the two individual simulated GMR characteristics are averaged and compared to a measured magnetoconductance curve of a spiral-shaped sensor element. Clearly, there is quite some disagreement in the saturation field, the behavior at small fields (the resistance is almost stationary in the simulated case) and the hysteresis. Such differences are to be expected due to the oversimplified model and the perfectly straight edges of the simulated rectangle, which tends to produce symmetric vortices around zero external field. These vortices are the reason for the almost constant characteristic at small fields, since they are pretty stable and need a comparably large field to break up.

Most of the parameters that enter the simulation are pretty fixed and cannot be varied without leaving the physical basis. The only exception is the ferromagnetic coupling, which could be smaller at the edges of grains due to crystal mismatches. However,

reducing the exchange coefficient does not affect the simulated GMR curves dramatically, and no better agreement to the measured characteristic can be obtained this way. Thus, it is left at its original value of 13 pJ/m. The saturation field mostly depends on the antiferromagnetic coupling coefficient, and a reduction to one half of its original value (1.9 instead of 3.8 $\mu\text{J}/\text{m}^2$) results in a much better agreement in this respect. Even though such a modification cannot be justified within the physical picture, it is undertaken for all subsequent GMR type oomf simulations in order to improve their quantitative quality. The values of all other parameters remain like they are stated above for all following oomf calculations.

Despite the adjustment of the af-coupling, the characteristics are still quite different at small fields, which effectively disables real quantitative comparisons to the measurements described below. However, the simulations within this model system are still valuable, since they help in interpreting the measurements qualitatively.

5.4. Detection of magnetic markers

As mentioned in chapter 3.2.1, the magnetic microspheres only produce a detectable stray field when magnetized by an external field. In order to prevent sensor saturation, the magnetizing field is applied in the out-of-plane orientation. In a typical measurement, the angle of the magnetizing field is adjusted initially so that it points perpendicular to the plane. The best alignment is achieved when the response of reference sensor elements (i.e. sensor elements not covered by any magnetic markers) is minimal. Next, the signals from all sensor elements are taken in dependence on the strength of the perpendicular field by the measurement setup described in chapter 2.8 at a bias voltage of 200 mV. The following chapter describes the response of reference sensor elements under those conditions.

5.4.1. Reference signal

Applying an aligned perpendicular field to an uncovered reference sensor element produces data like the one shown in Figure 47. Generally, those curves are parabolic, but with an additional linear term which depends upon the direction of the prior uniaxial in-plane saturation field applied to the sensor element. Furthermore, they display a certain amount of hysteresis.

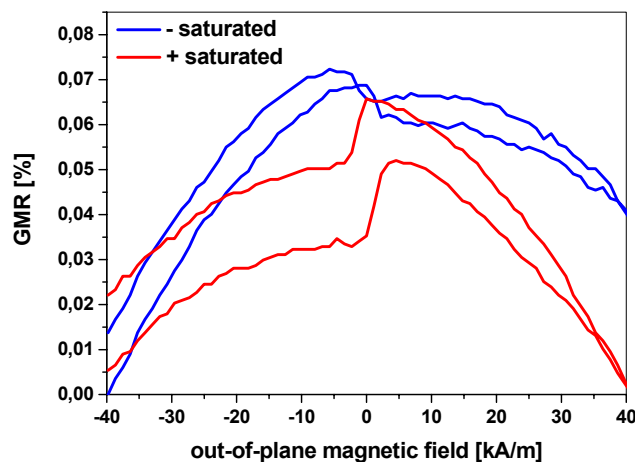


Figure 47: Typical dependence of the signal of a reference sensor element on a perpendicular magnetic field

The parabolic term can be understood as a slight rotation of the magnetization of the ferromagnetic layers into the perpendicular field direction. Since the initial magnetization configuration at zero external field is antiferromagnetic, the resistance decreases due to such a rotation which tends to align adjacent magnetizations parallel to each other. Following Equation 17, a typical resistance decrease of about 0.06 % relative to the maximum resistance would correspond to a rotation of about 5.2° of the magnetization vectors out of the plane of the sensor. In this case, the z-component of the magnetization at a perpendicular field strength of 40 kA/m would be approximately 9.1 % of its full value. Assuming a linear increase of the magnetization's z-component with increasing field strength, a saturation field of about 440 kA/m would be expected. However, the saturation field in the direction perpendicular to the plane of the magnetic layers should be close to the saturation magnetization of Py (860 kA/m, compare to chapter 3.2.1). This fact is also supported by results of oommf simulations of our model system for a perpendicular magnetic field, which show a linear increase of the magnetization's z-component with increasing field strength, no hysteresis, and a saturation field of approximately 870 kA/m (see Figure 48 a). Such a behavior is a result of the perfectly hard magnetic axis perpendicular to the film plane and produces a parabolic shape of the corresponding GMR-curve according to Equation 17. At the maximum field strength applied during measurements (40 kA/m), the z-component of the magnetization reaches about 4.7 % of its maximum value in the simulation, which corresponds to an angle of about 2.7° of the magnetization vectors relative to the plane of the sensor and a resistance decrease by about 0.016 %.

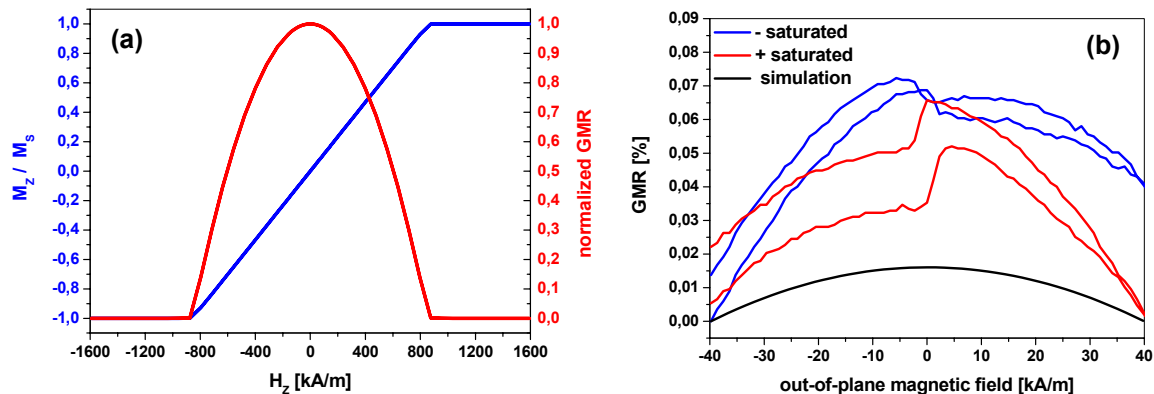


Figure 48: Response of the model system to a perpendicular magnetic field
 a) simulated system only under strong perpendicular fields up to saturation
 b) zoom around zero field and comparison to reference sensor element

The zoom to a maximum field strength of 40 kA/m of the simulated GMR-curve is shown in Figure 48 b) together with the corresponding measurements from Figure 47. Since the resistance change of the simulated curve is much smaller than the observed one and also lacks hysteresis and a linear component, it is apparent that a rotation of the magnetization vectors into the perpendicular direction alone cannot explain the measured reference signals.

Even after adjusting the orientation of the perpendicular field, a slight misalignment may remain which causes an additional in-plane component of the applied magnetic field. Such a misalignment leads to an increased resistance change and an additional linear dependence of the reference signal on the applied magnetic field, which originates from the hysteresis of the sensor system (compare to chapter 5.2) and is highlighted in Figure 49. Part a) shows a magnified major loop, while part b) presents

minor loops around zero field. Clearly, the response of the sensor system is almost linear for small in-plane fields and depends upon the direction of the prior saturation.

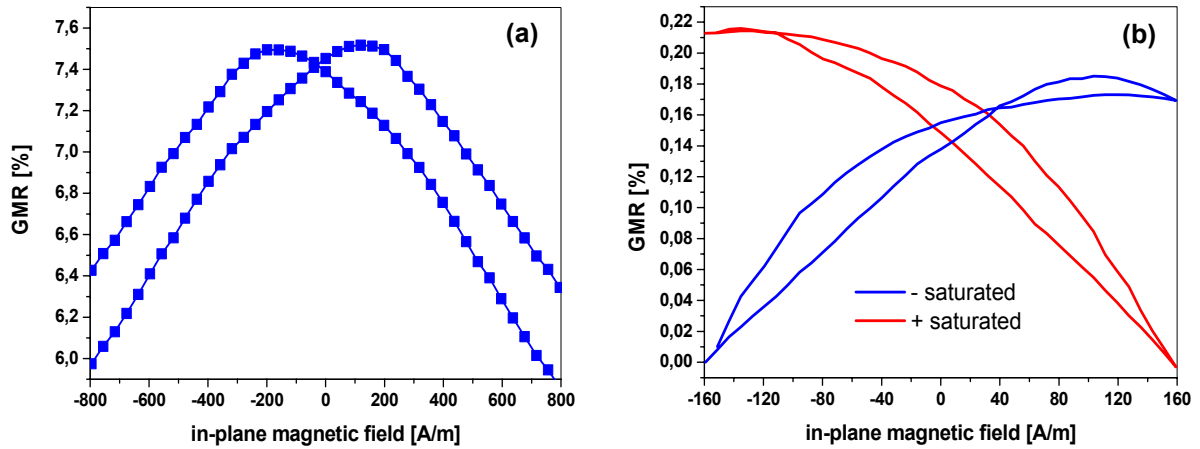


Figure 49: Measured GMR sensor response to an in-plane field
a) magnified major loop
b) minor loops

A similar behavior can be found for the out-of-plane characteristics shown in Figure 47. Comparing the magnitudes of the resistance variations, an in-plane field component of approximately 100 A/m can be assumed at a perpendicular field strength of 40 kA/m, resulting in a misalignment of the field angle of approximately 0.1° . The in-plane component of the perpendicular field is also the reason for the small hysteresis observed in Figure 47, since a rotation of the magnetization into the hard perpendicular axis can be assumed to be completely reproducible. Another possibility is a time-dependent resistance increase due to temperature drift. However, even after applying the same current value for more than 15 minutes, the measured curves are still the same, which rules out a time-dependent temperature drift contribution.

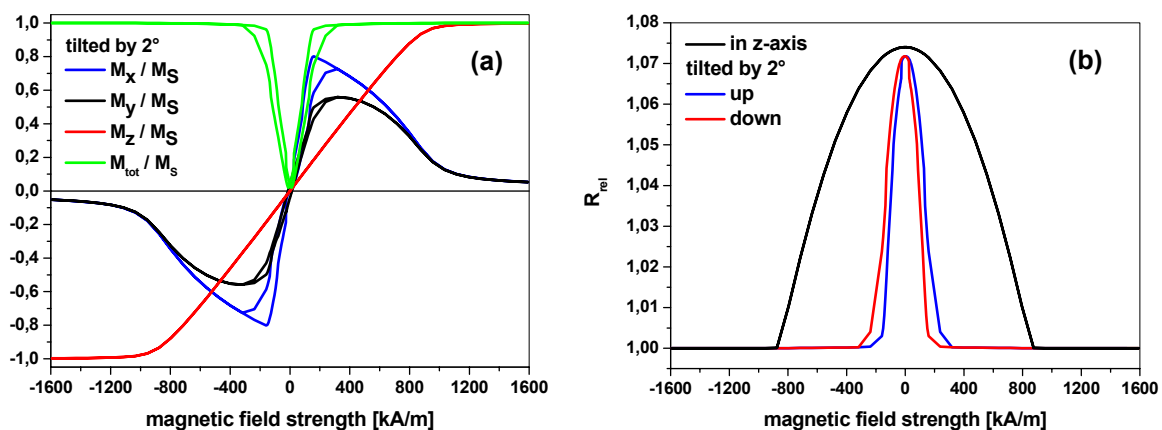


Figure 50: Simulated sensor response to a slightly tilted perpendicular field
a) magnetization curves of the lower Py-layer
b) corresponding GMR characteristics

In order to verify the effect of a slightly misaligned perpendicular field, another simulation is carried out with the applied field tilted by 2° out of the normal direction at an angle of 45° relative to the x-axis of the model system (see Figure 50). In this

case, an in-plane component with a magnitude of 3.5 % of the total field strength acts upon the sensor system and causes the magnetization to saturate at a much lower field of about 320 kA/m (see Figure 50 a). At this point, the magnetization vector almost lies in the plane of the sensor, while it constantly tilts towards the out-of-plane direction for higher fields. The corresponding GMR-characteristic is shown in Figure 50 b) together with the previous one for a field perfectly aligned in the z-axis.

Contrary to a perfectly aligned perpendicular field, there is an additional linear term to the otherwise parabolic shape of the sensor response in the case of a slightly tilted field (see zoom in Figure 51 a). Just like observed in the measurements (see Figure 51 b), the slope of this term depends on the direction of the prior in-plane saturation field and is a consequence of the hysteresis of the sensor system. Even though no in-plane saturation field has been applied explicitly in the simulation, the in-plane component of the large perpendicular field is sufficient to saturate the magnetization accordingly. Thus, the situation is in fact comparable to a real measurement in which the perpendicular field is only varied up to a strength of 40 kA/m, but an in-plane saturation field is applied prior to each measurement.

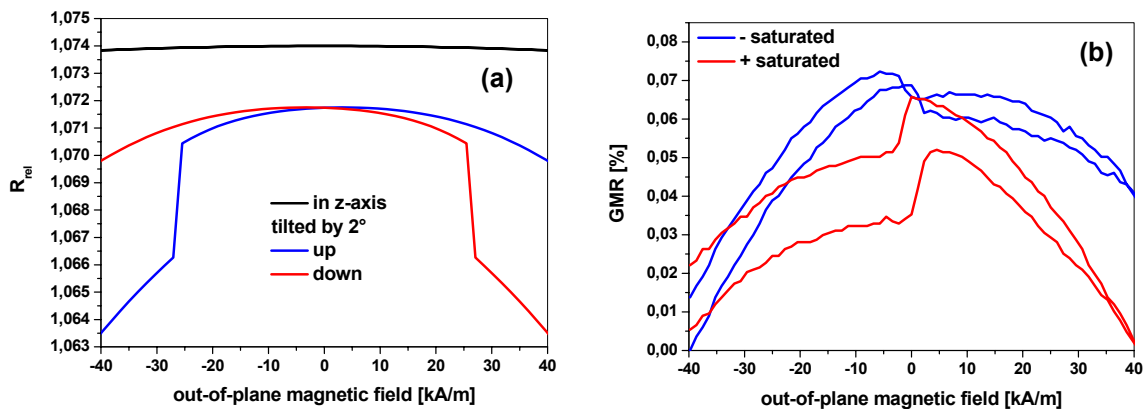


Figure 51: Comparison of reference sensor element signals
 a) oommf model (zoomed major loops)
 b) measurements (minor loops)

In the measured response, there is a hysteresis loop with minor amplitude around zero perpendicular field. Most probably, it is due to small magnetization rearrangements in the $3 \times 10 \mu\text{m}^2$ contact pads on either end of the sensor's spiral line which also consists of the magnetic multilayer structure. It certainly has nothing to do with the large jump observed in the simulated GMR characteristic at a perpendicular field of ± 26 kA/m, which originates from a domain wall reorientation from the diagonal direction imprinted at large fields to a natural Néel wall which separates two domains oriented along the easy axis at low fields (see Figure 52). This jump is unique to the simulated model system and has no correspondence to a real sensor element. Also, the chosen angle of misalignment in the simulation is much larger than for real measurements, so the magnitude of the resulting linear contribution to the resistance decrease is also much greater. Still, the simulation helps to understand the measurements qualitatively.

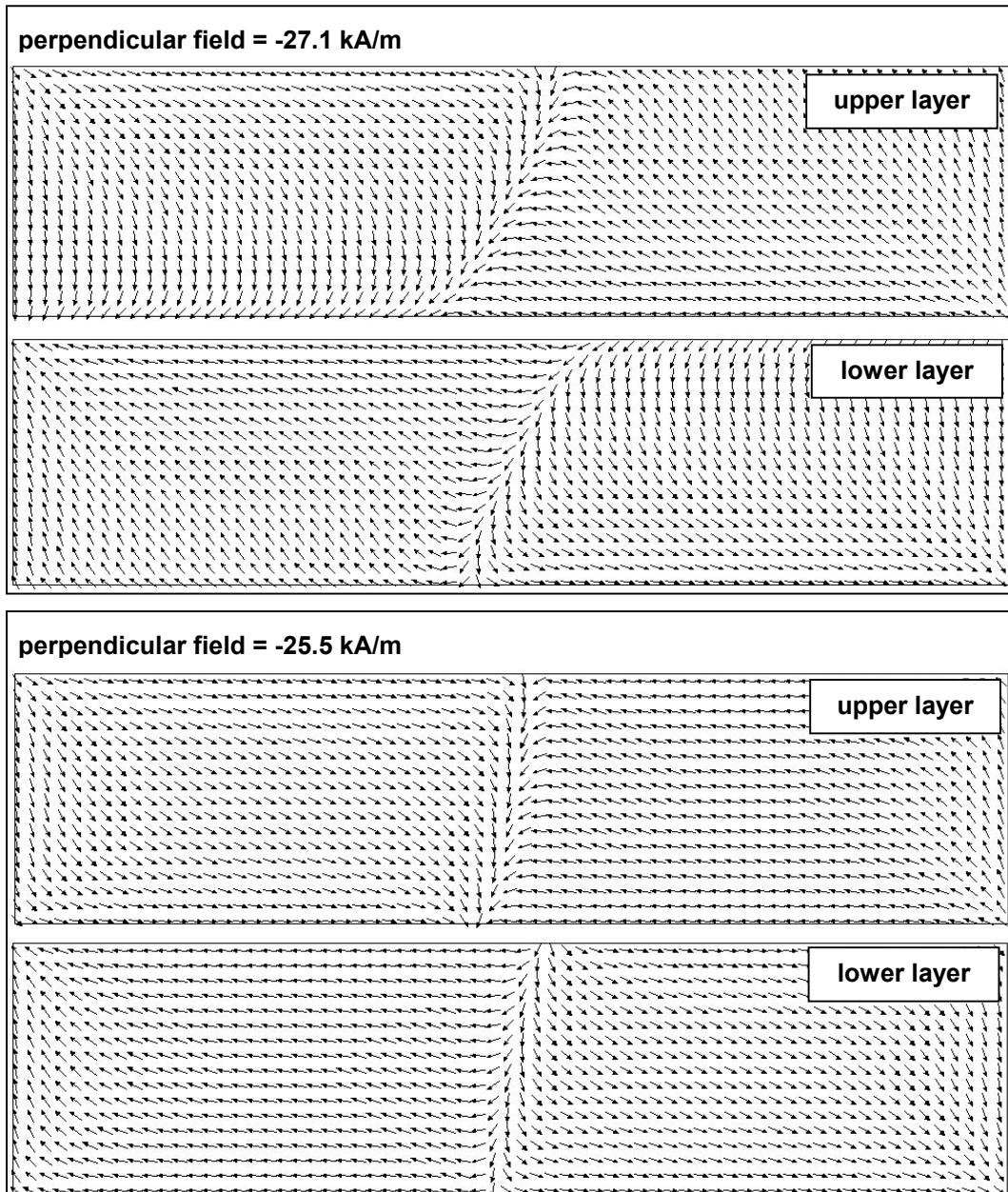


Figure 52: Magnetization configuration of the oommf model system at the observed jump in the GMR curve

5.4.2. Response to magnetic markers

After analyzing the response of reference sensor elements to a perpendicular field, the question is how the presence of magnetic markers on the surface of a sensor element affects its output signal. As mentioned in chapter 3.2.1, the markers get magnetized and produce a stray field. Within the markers' vicinity, their in-plane components cause a reconfiguration of the local magnetization vectors in the magnetic multilayer system. Since the magnetization vectors are aligned antiparallel at zero magnetic field, such a reconfiguration causes a resistance decrease. With increasing particle density, more and more of the sensor area gets affected by local stray fields. Thus, it is expected that the total sensor signal increases proportionally to the number of magnetic particles on its surface.

In order to determine the marker coverage on the surface of a specific sensor element, a proprietary developed image analysis program is used. For each sensor element of interest, a SEM picture (1024x768 pixels, 8bit grayscale, tagged image file format) is taken at constant microscope and imaging parameters (magnification = 3000x, acceleration voltage = 5 keV, working distance = 9 mm, aperture = 20 μm , in-lens detector with collector bias = 132 V, brightness = 80 %, contrast = 77 % and scan speed = 12). At those settings, the magnetic particles display a bright contrast, while the sensor in the background is dark and only barely visible. The histogram of a typical SEM raw image is shown in Figure 53. The markers are clearly identified as bright spots, so their corresponding place in the histogram is at large grayscale values. The other two distinct regions within the histogram belong to the sensor line and the background. Thus, just by looking at the grayscale of a certain pixel, it is possible to decide whether it belongs to a particle or not. Before running the image analysis software, the sensor area is cut from the total picture by filling the remaining region black. The image analysis program now scans through all the pixels of the image and adds the pixels above a certain adjustable grayscale value. In the example of Figure 53, this threshold value is set to a grayscale of 120. In an output image file which serves as a control, all the counted pixels above the threshold value are displayed black, while the uncounted pixels are white. This output file is also shown in Figure 53. Finally, the resulting area coverage of the markers on the entire image is normalized to the sensor area.

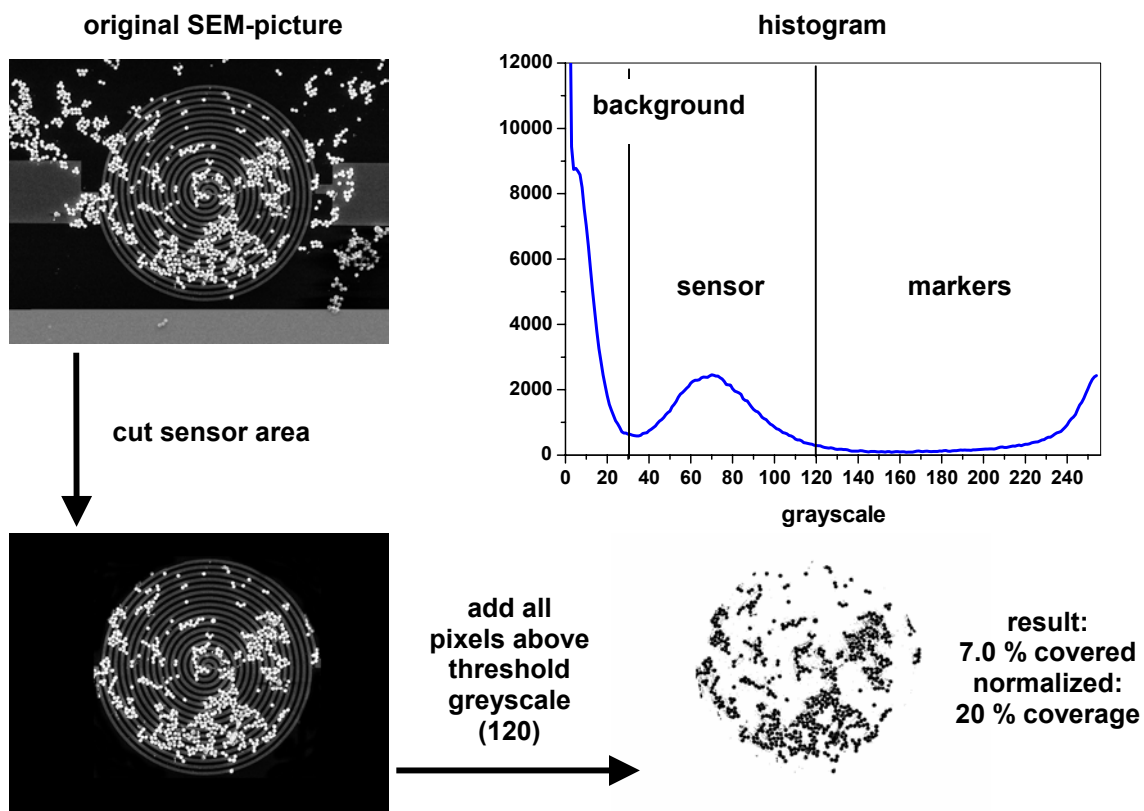


Figure 53: Determination of the marker surface coverage from SEM images

An exemplary sensor element with a 5.0 % surface coverage of Bangs 0.86 μm particles is shown in Figure 54 a). Using the setup described in chapter 2.8, single measurements of this sensor element are taken in dependence of the strength of the perpendicular magnetizing field. Prior to the measurements, the magnetization

configuration is set into a defined state by applying an in-plane saturation field in either the positive or negative direction. The resulting raw signals are displayed in Figure 54 b). Their principal characteristics are similar to the measurements obtained for reference sensor elements (compare to chapter 5.4.1), but while the linear contribution and the hysteresis are almost identical, the parabolic contribution is much larger. Since the origin of the linear contribution is a small in-plane component of the perpendicular field, it has the same effect on all sensor elements, whether they are covered by markers or not. Also, as a result of their local character and radial symmetry, the in-plane stray fields of the markers are not sufficient to cause a major irreproducible magnetization reconfiguration. Thus, they only have a minor effect on the hysteresis, which is still mostly a result of global in-plane field components of a not perfectly aligned perpendicular magnetizing field.

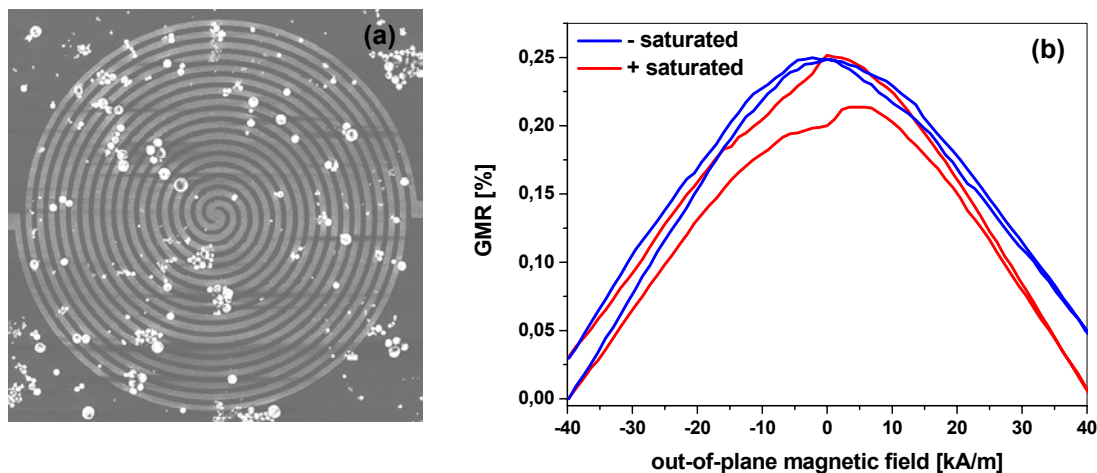


Figure 54: Sensor element with a surface coverage of 5 % of Bangs 0.86 μm particles
a) SEM image
b) single measurements of raw signals

The parabolic resistance decrease, however, can be attributed to a reproducible local rotation of the magnetization in the vicinity of each marker due the in-plane components of their stray fields. The out-of-plane components, though stronger, do not significantly alter the magnetization configuration due to the large demagnetizing field in the perpendicular orientation. Qualitatively, the results can be understood by looking at simulations of our model system.

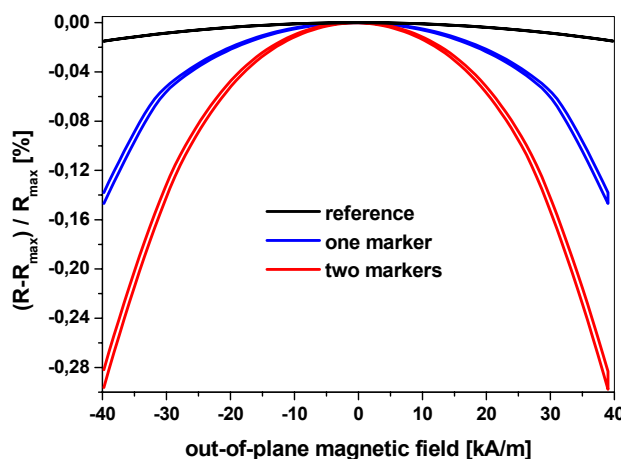


Figure 55: Simulated response of the model system to artificial Bangs 0.86 μm markers

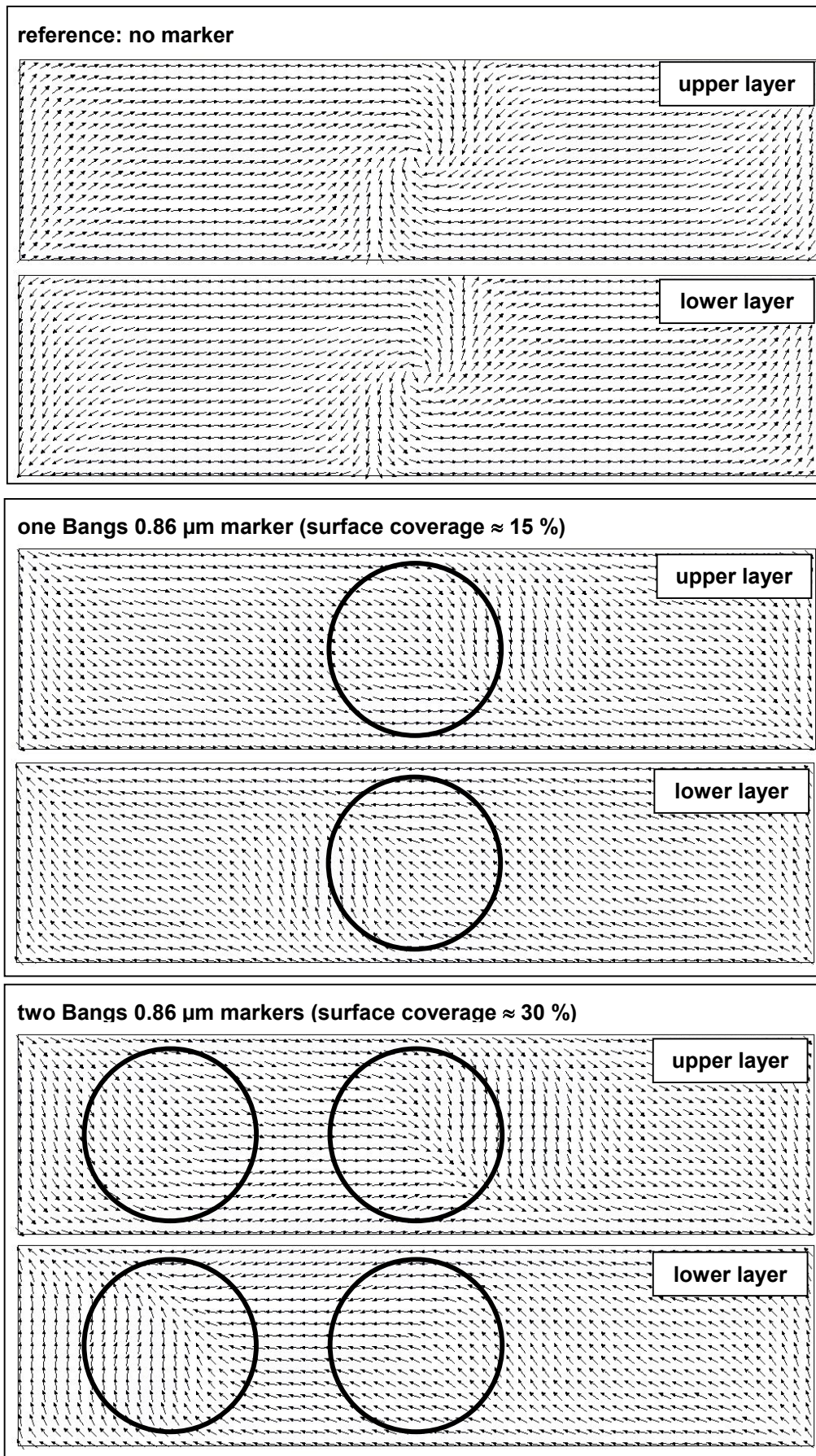


Figure 56: Magnetization configuration of the model system at a magnetizing field of $+40 \text{ kA/m}$

Figure 55 shows the resistance decreases relative to the maximum resistance in dependence of a perfectly perpendicular magnetizing field. Compared to the reference curve (same as in Figure 48), the simulations with markers show a much more distinct parabolic behavior and a slight hysteresis. As markers, Bangs particles with a diameter of $0.86\ \mu\text{m}$ are assumed. According to the real sensor system, a passivation layer thickness of $220\ \text{nm}$ is chosen. The magnetic moment of the markers is taken to behave like an ideal dipole. According to Table 4, its maximum value is set to $21\ \text{fAm}^2$, and is taken to vary linearly with the applied magnetizing field.

Figure 56 shows the corresponding magnetization configurations of the model system for the three different cases at the maximum magnetizing field of $+40\ \text{kA/m}$. In this orientation, the magnetic moments of the markers are directed upwards and produce a radially symmetric in-plane stray field that points towards the marker's center. A marker in the center of the model system causes a breakup of the original central vortex structure of the reference system. At first, this is a surprising result, since the symmetry of the marker's stray field generally favors the formation of vortices. However, such a vortex structure would have to be aligned parallel in both layers, which is prevented by the strong antiferromagnetic exchange coupling. Still, the resulting magnetization configuration has a larger fraction of partially parallel spin pairs in the vicinity of the marker, thus causing a stronger resistance decrease relative to the reference system. The sphere of influence of each marker is about twice its radius, and a second particle with sufficient distance to the first one roughly doubles the effect on the system's resistivity (see Figure 55). Thus, a linear rise of the resistance decrease can be expected with increasing marker coverage on the sensor surface.

Even though these simulations give a good qualitative insight into the mechanism of the measured signal, they cannot predict its magnitude quantitatively. First of all, a real sensor element does not relax into a vortex-like magnetization configuration like the reference system shown in Figure 56. Such a behavior is due to the oversimplified model and the perfectly straight edges of the simulated system (see chapter 5.3). In fact, the stability of such a vortex is also the reason for the comparably low resistance decrease of the simulated system of about $0.01\ \%$ per $\%$ of covered sensor area (see Figure 55), which is only about $1/5^{\text{th}}$ of the measured signal (see Figure 54). In reality, no vortices are formed, and the stray field of the markers has a greater effect on the sensors magnetization configuration. Also, the linear dependence of the marker's moment on the magnetizing field is only an approximation. For real markers, the initial slope is larger and decreases with increasing magnetizing field (see Figure 57 a). With the assumption of a linear behavior, the simulation produces a parabolic dependence of the resistance decrease on the magnetizing field (see Figure 57 b). Even though the response of the simulated model system to small in-plane fields does not quite match the characteristic of a real sensor element (see Figure 46), it seems that the deviation of the marker's moment dependence on the magnetizing field from a straight line compensates the parabolic resistance decrease observed in the simulation and leads to an almost linear resistance decrease with the applied magnetizing field for a real sensor system (see Figure 57 b). However, since it depends on the precise response of the sensor system and the specific characteristic of the magnetic moment of the markers, such a linear behavior can not be expected to be a general feature for any combination of markers and sensor systems. Still, it holds true in our case for GMR-based sensors.

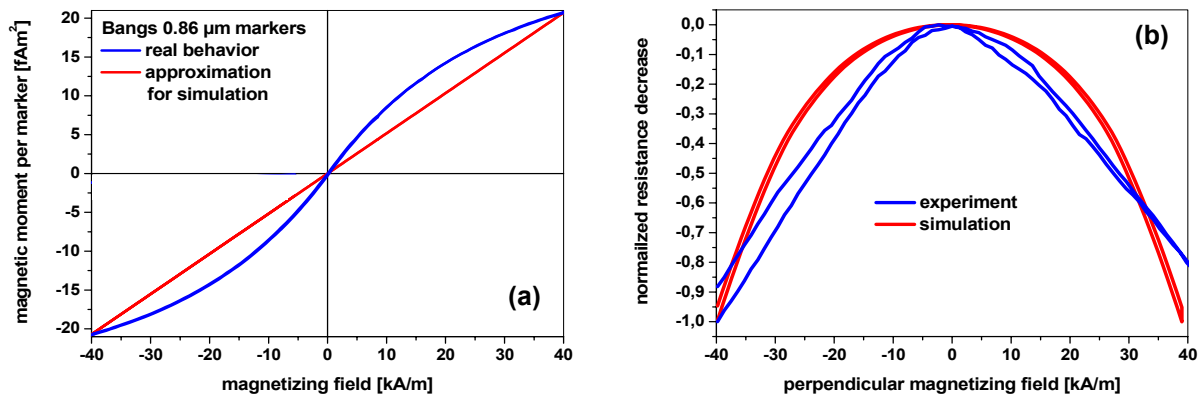


Figure 57: Comparison of the model system and a real sensor
a) dependence of the magnetic particle moment on the magnetizing field
b) normalized resistance decrease

In order to extract the signal originating from the magnetic markers from the effect of the perpendicular field, differential measurements are taken between a sensor element of interest and a reference sensor element which is not covered by any markers by the setup described in chapter 2.8. All the following data is taken in the 100 k Ω setting of the electrometer amplifiers in both branches, and a bias of 200 mV is applied. Figure 58 a) shows the resulting output of the differential amplifier when both sensor elements are not covered by any markers. Before taking the data, the sensor elements are put into a defined magnetic state by applying an in-plane saturation field in an uniaxial positive or negative direction. Clearly, the resulting output signals do not display any dependence on the out-of-plane magnetizing field since all of its perturbing effects are eliminated by the differential measurements. All that remains in this case is noise and a slight temperature drift. The output itself is different from zero since the absolute resistances of the two sensor elements divert by about 0.5 %. Also, the output signals vary depending on the direction of the prior in-plane saturation field, which is due to the fact that the sensor elements reach slightly different resistance ground states (i.e. magnetization configurations) for those two cases.

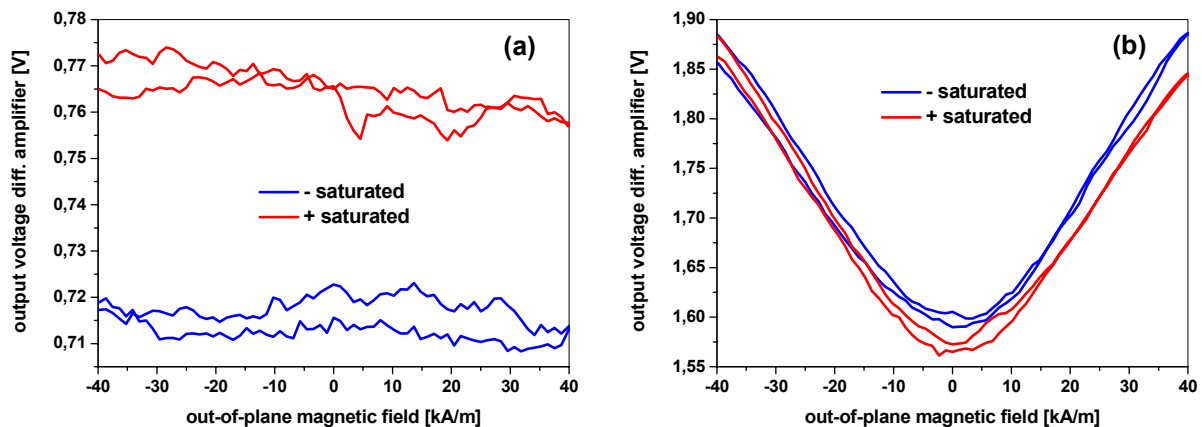


Figure 58: Measured differential raw signals
a) two reference sensor elements
b) reference sensor element – sensor element covered with 5 % of Bangs 0.86 μ m particles

In Figure 58 b), the differential signal between the reference sensor element from above and the sensor element shown in Figure 54 a) is displayed. As described before, the stray field of the magnetized particles causes a resistance decrease in the marker-covered sensor element, so that the current-proportional negative output of the electrometer amplifier in this branch increases in magnitude. At the same time, the current through the reference sensor element stays almost constant, so that the output signal of the differential amplifier rises with increasing moment of the markers. Again, the absolute voltage is a measure of the ground state resistance differences of the two elements. The dependence of the output on the magnetizing field is almost linear for each field direction at higher fields, which is analogue to the single measurements presented above.

Still, there is a slight difference in the signals between a prior positive and negative in-plane field saturation. As we have seen before, such a behavior can be attributed to in-plane field components of a not perfectly aligned out-of-plane field. However, due to the differential nature of the measurements, this effect should be canceled in the output. However, a slight spatial inhomogeneity of the Helmholtz-field or minor differences in the sensor characteristics due to small variations of the film thicknesses or lithographic properties could cause such a behavior. Since such inhomogeneities are expected to be largest at the edges of the sample, there should be a correlation between the relative positions of the sensor elements on the chip and the observed signal asymmetry between positive and negative in-plane saturation. The definition of the signal asymmetry is illustrated in Figure 59 a). For each direction of the saturation field, the difference between the signal at +40 kA/m and the average signal at -40 kA/m is taken. Thus, in the example from Figure 59 a), the difference Δ_{pos} is -156 mV, and the difference Δ_{neg} is 95 mV. Now, the signal asymmetry is defined as the magnitude of the difference $\Delta_{\text{neg}} - \Delta_{\text{pos}}$. It is calculated for a number of different measurements and plotted against the distance between the sensor elements in Figure 59 b). The different colors of the data markers represent different series of measurements on separate sensor chips covered by different types of markers.

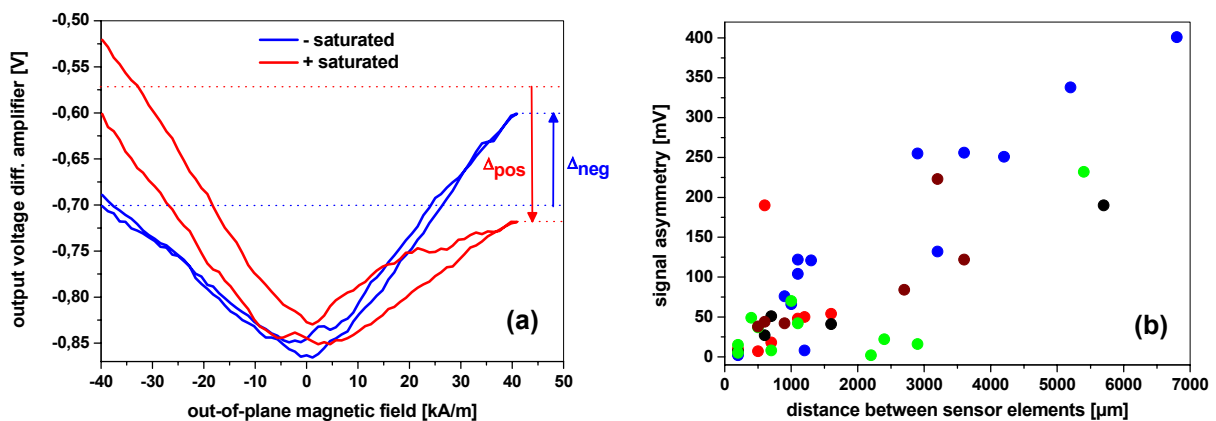


Figure 59: Asymmetry of the differential output signal

a) illustration of the asymmetry definition

b) dependence of the asymmetry on the distance between sensor elements

Even though the scattering of the data is pretty large, there is a clear tendency to larger asymmetries for greater distances between the sensor elements. A typical asymmetry of about 200 mV in the output of the differential amplifier corresponds to a variation of the resistance difference of the two sensor elements of about 0.06 %, which is approximately equal to the total signal of a single reference measurement

(see Figure 47). According to Figure 49, an in-plane field of about 100 A/m is required to produce such a resistance change.

In order to track down the origin of the asymmetry, the field of our Helmholtz coils is calculated by breaking up every single winding into 180 small pieces and adding all contributions according to the rule of Biot-Savart (Ref. 144). The results are displayed in Figure 60 in dependence on the radial direction for different z -values around the center of the coils (see inset of Figure 60 b)). Exactly in the center ($z=0$), there is no radial field component due to symmetry. Therefore, if spatially inhomogeneous radial field components were to cause the asymmetry, the sample would also have to be misaligned in its perpendicular coordinate. As the entire setup is build centered around the sample, such a misalignment can not exceed a few millimeters, but the respective radial field components for relevant sensor distances ($r < 7$ mm) never come close to the anticipated value of 100 A/m. Similarly, the variations of the perpendicular field components (below 0.1 % within the relevant area) are also insufficient to explain the observed asymmetry. Therefore, the origin of the asymmetry must be due to slightly differing sensor properties rather than inhomogeneities of the Helmholtz field.

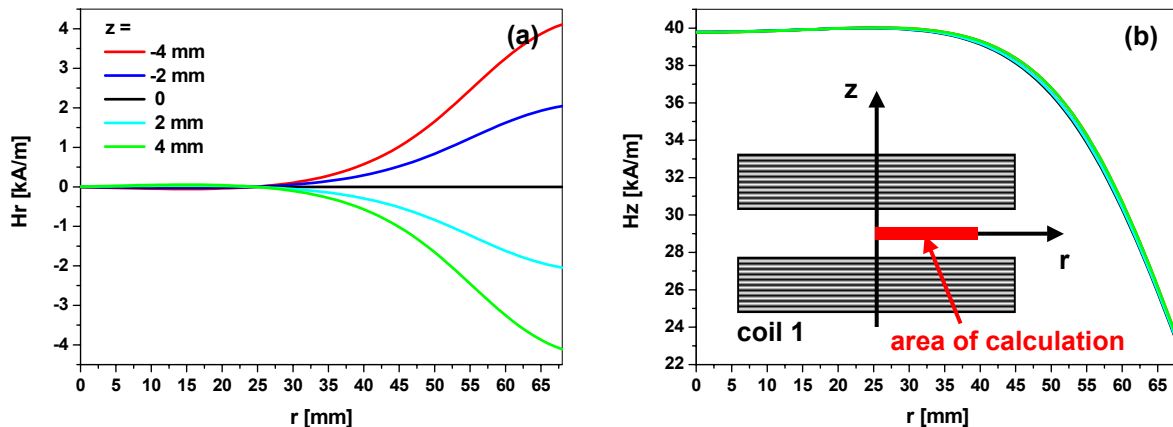


Figure 60: Calculated perpendicular field as generated by our Helmholtz coils
 a) in-plane components
 b) out-of-plane components; inset: sketch of the Helmholtz coils and the investigated space

In order to enable easy comparison of the data from different sensor elements, it has proven helpful to modify the differential output before further analysis. First, a time-dependent linear drift compensation is applied which balances the signal levels at the beginning and end of each measurement. The origin of the mismatch divides into a real magnetic hysteresis of the system and an actual temperature drift. Afterwards, the asymmetry between the signals at the positive and negative extremal perpendicular fields is leveled by a linear field-dependent compensation. As a result, a distinct total signal of each pair of sensor elements can be defined as the difference between the maximum and minimum output signals of the perpendicular field-dependent measurements. Due to the compensations, such a total signal no longer depends upon the direction of the prior in-plane saturation field, which makes measurements from different sensor elements comparable to each other. Exemplarily, this is displayed in Figure 61, which compares the raw signals from Figure 58 to the compensated data. Clearly, the adjusted curves show a much better consistency. It must be noted, however, that those adjustments do not only cancel parasitic effects of the magnetizing field and temperature drifts, but also remove some of the magnetic information contained in the hysteresis of the curves. Thus, it

should be considered as nothing more than a suitable tool to gain effective comparable data from the raw measurements. These adjustments are carried out for all measurements with a fixed protocol and could easily be integrated into an automated signal analysis for an actual product.

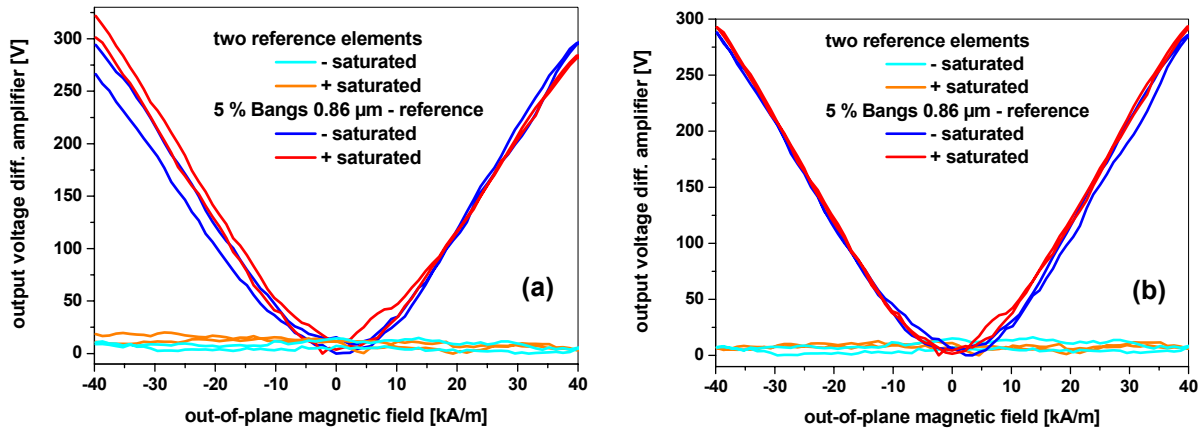


Figure 61: Comparison of initial and compensated differential signals
 a) differential raw signals
 b) compensated differential signals

5.4.3. Dependence of the sensor signal on the marker coverage

Since each magnetic microsphere has only a limited range of influence, a linear increase of the total output signal of the sensor is expected as the surface coverage of markers is increased and more and more of its area gets affected by the particles' stray fields. Such a linear dependence is already observed for our GMR model system (compare to Figure 55), but the question remains whether this is also true for real sensor elements.

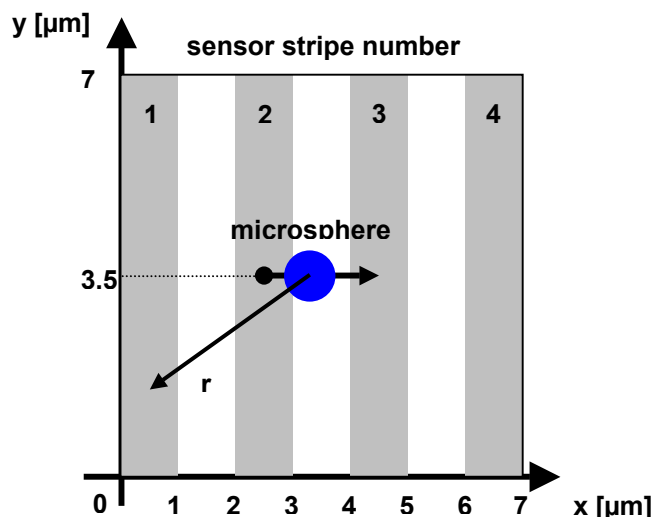


Figure 62: Sketch of the employed model for calculating the influence of the microspheres' position onto the induced signal

Due to the spacing of 1 μm between individual windings of the sensor's spiral structure, it is expected that the effect of a particle's stray field on the sensor's resistance depends upon its position relative to the sensor lines. To quantify this, a

simple model is developed that only takes into account the strength of the induced stray field and consists four straight sense lines only. According to the real system, the stripes have equal widths and spacings of 1 μm each. As sketched in Figure 62, the position of a single microsphere is varied between the centers of the two inner stripes. For each position, the average induced in-plane stray field is calculated within all four stripes. The total section area of $(7 \mu\text{m})^2$ is large enough to ensure that most of the marker's stray field is enclosed for all of its positions. The marker's moment m is assumed to be dipole-like with its origin at the microsphere's center. It is oriented out-of-plane and has a magnitude according to line 8 of Table 4. Thus, the average induced in-plane magnetic field \bar{H} in stripe number i is given by:

$$\bar{H}_i = \frac{1}{A_i} \int dA_i H(A_i) \quad \text{with} \quad H = \frac{1}{4\pi} \frac{m}{d^3} \frac{3\xi}{[1+\xi^2]^{5/2}} \quad \text{and} \quad \xi = \frac{r}{d} \quad \text{Equation 19}$$

Here, A_i denotes the area of sensor line number i , r resembles the horizontal distance between the microsphere's center and an integration point in one of the sensor lines, and d is the vertical distance between the center of the microsphere and the plane of the sensor. The latter value depends on the mean diameter of the particle, which was chosen according to the values given in line 5 of Table 2 and the thickness of the passivation layer (see chapter 4.1). The integration across the sensor stripes for the different microsphere positions was carried out with the help of a MATLABTM program with a mesh size of $(20 \text{ nm})^2$. The distance between the different microsphere positions is also set to 20 nm.

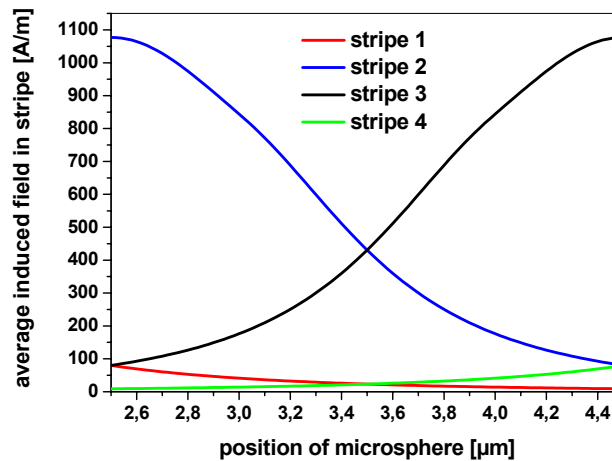


Figure 63: Average induced in-plane fields in the four different stripes for a Bangs 0.86 μm particle in dependence of its position

The results for a single Bangs 0.86 μm particle are shown in Figure 63. As the microsphere is moved from the center of stripe 2 to the right, the average induced stray fields in stripes 1 and 2 decrease, while the opposite is happening for stripes 3 and 4. Due to symmetry, the signals are identical for stripe 2 and 3 at the extremal particle positions, which is also true for stripes 1 and 4. Obviously, the contribution of the outer stripes is relatively small (less than 10 % of the inner stripes), which justifies the choice of a limited integration area. The average fields across all four stripes are displayed in Figure 64. Part a) shows the absolute values, while part b) presents the same curves normalized to their respective maximum values.

While the magnetic moments of the microspheres determine the magnitude of their induced stray fields, their size governs the dependence of the signal on their position. For larger markers, the signal stays at a higher level when they are positioned within the gap between the sensor lines, which is related to the increased range of their magnetic stray field relative to smaller particles. From the data in Figure 64 b), one can obtain the average signal of each microsphere relative to its maximum as it is moved across the sensor area (see Table 6). Since each position of a microsphere on top of a spiral-shaped sensor element has the same probability, these values represent correction factors when comparing the surface coverage of each microsphere type.

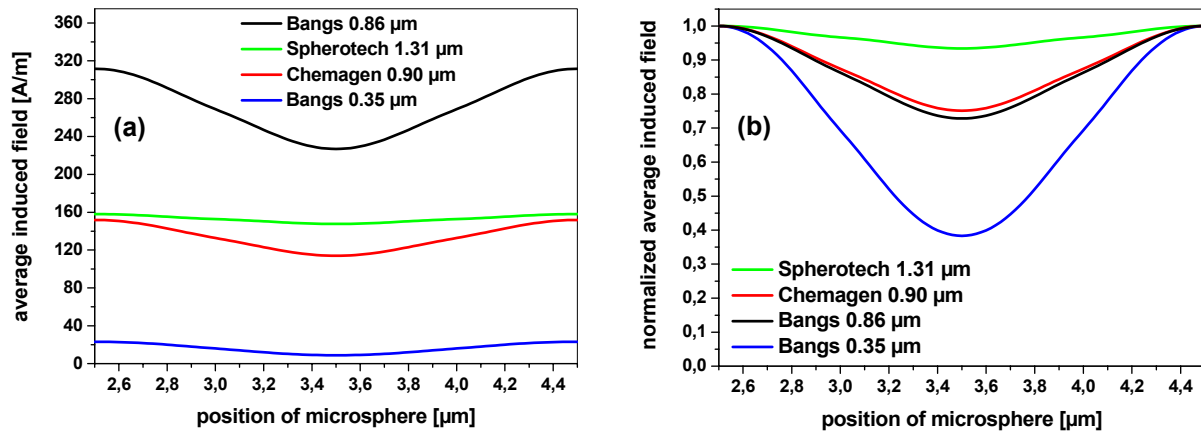


Figure 64: Average induced stray fields of all four stripes for the four different microspheres
 a) absolute values
 b) relative values

	Bangs 0.35 μm	Bangs 0.86 μm	Chemagen	Spherotech
average rel. signal	0.70	0.87	0.88	0.97

Table 6: Average signals of the different microspheres as their position on the sensor is varied

According to the method described in chapter 5.4.2, the response of the different types of magnetic markers is investigated in dependence of their surface coverage. For each single measurement, the described compensation of drift and asymmetry is carried out. Afterwards, the maximum difference in the output signal is taken and plotted versus the marker coverage of the specific sensor element (Figure 65 a). Error bars in the y-direction are given by the standard deviation of 6-8 independent measurements of the same element, while the error bars in the x-direction represent 10 % of the corresponding surface coverage, which is a typical error for the image analysis method described in chapter 5.4.2 (it is obtained from the range of the resulting coverage values when the threshold grayscale value is varied). The shaded area represents the maximum signal obtained from reference elements with zero marker coverage, which is always less than 40 mV. At coverages not too close to saturation, a linear increase of the sensor signal on the marker coverage is observed, as more and more of the sensor area gets affected by the induced stray fields. The corresponding slopes of the linear regressions to the data are shown in line 1 of Table 8. The fit is carried out with the boundary condition that the signal at zero coverage is equivalent to the average reference signal level of 30 mV. Deviations from the linear regression can be attributed to conglomerations of markers in specific regions of a sensor element, which effectively decreases the signal as the areas of influence of different markers overlap. Furthermore, there is also a certain degree of piling especially for the smallest markers at high coverages, which is an additional

source of error for these types of measurements as the markers are being spotted directly onto the sensor surface (compare to chapter 8.2).

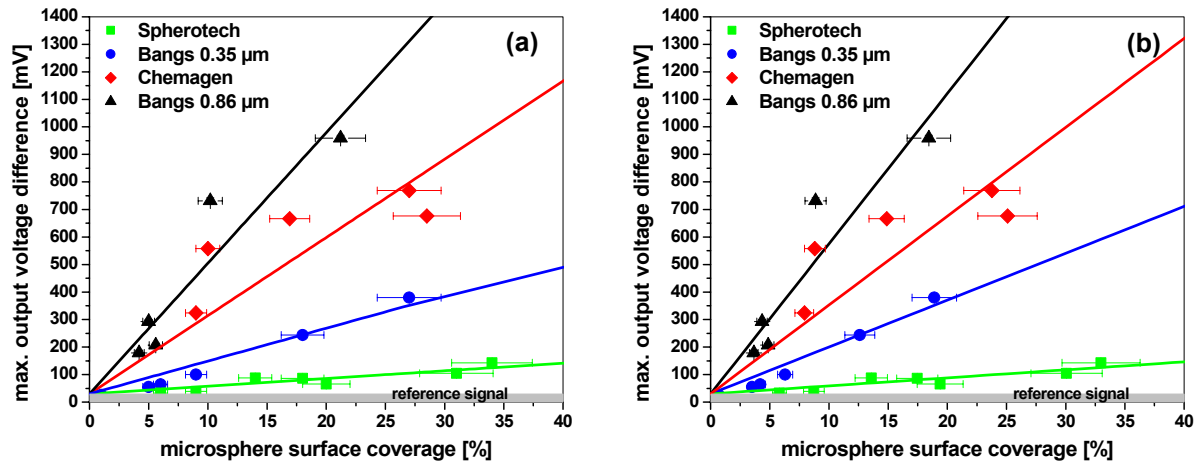


Figure 65: Dependence of the maximum output voltage difference of the differential amplifier on the surface coverage of magnetic markers

a) original data

b) data adjusted according to the range of influence of each marker type

An estimate of the minimum detectable number of markers on the surface of a sensor element is obtained by assuming a limiting output voltage of the differential amplifier of 80 mV, which is twice the maximum reference signal. From the linear regressions to the data, the corresponding surface coverage is shown in line 1 of Table 7. Line 2 displays the respective part of the total sensor area (3850 μm²) which is covered by markers, while line 3 represents the corresponding number of particles, which is calculated based on the average size of each marker type (Table 2). Due to the small size of the Bangs 0.35 μm particles, their minimum detectable number is comparably large.

	Spherotech	Bangs 0.35 μm	Chemagen	Bangs 0.86 μm
surface coverage [%]	18.0	4.1	1.8	1.0
surface area [μm ²]	692.7	157.8	69.3	38.5
number of markers	514	1640	109	66

Table 7: Estimate of the minimum detectable number of markers

In part b) of Figure 65, the coverage of the markers on the sensor surface has been modified according to the correction factors presented in Table 6, which take into account the limited effectivity of markers situated within the gaps between individual spiral windings. This leads to an increased slope of the linear regression to the data (see line 2 in Table 8), which is especially true for the smallest markers. Even though the real applicable signals for this type of sensor is represented by the uncorrected diagram, the modified characteristic can be used to compare the electrical response of the system to the corresponding magnetic data of the markers. Since the origin of the sensor signals lies in the number and magnitude of local magnetic stray fields on its surface, the slopes in line 2 of Table 8 should be correlated to the specific field strengths of the markers as calculated in Table 5. Ignoring the data of the Spherotech markers for the moment, the magnetoresistive and the magnetic data relative to the respective values of the Bangs 0.35 μm microspheres agree within an error of 20 %. Due to the uncertainties in the characteristics of the various particle

types (average size for Chemagen particles and magnetic behavior for Spherotech markers, see chapter 3.2.2.2), deviations should be expected as those values enter the calculation of the specific field strength. In particular, the Spherotech particles do not show a consistent behavior. Most probably, this is due to their abnormal magnetic characteristic, since a closed shell of ferromagnetic material effectively prevents the creation of a significant stray field.

		Spherotech	Bangs 0.35 μm	Chemagen	Bangs 0.86 μm
slope of $V_{\text{out}}(\text{A})$	original [mV / %]	2.79	11.71	28.41	47.45
	adjusted [mV / %]	2.91	17.03	32.28	54.55
	relative	-	1.0	1.9	3.2
specific field strength	absolute [A/m]	303	204	470	531
	relative	-	1.0	2.3	2.6

Table 8: Slopes of the linear regression to the data of sensor signal on marker coverage and comparison to AGM data of moment density

5.5. Conclusions

A magnetoresistive sensor on GMR basis is developed and fabricated which covers a circular area with a diameter of 70 μm by a spiral-shaped sense line. Each chip consists of over two hundred individual sensor elements, each of which is capable of detecting one specific DNA sequence. The area of a single sensor element is chosen according to the diameter of a typical probe DNA spot.

In order to detect magnetic markers on the surface of a sensor element, a perpendicular field is applied to magnetize the markers. Their radially symmetric local stray fields cause a linear resistance decrease with increasing magnetizing field, while the resistance of uncovered reference sensor elements stays almost constant.

Various marker types are dispersed directly on the chip in different concentrations, and the corresponding output signal of each covered sensor element is taken in dependence on the out-of-plane magnetizing field relative to an uncovered reference sensor element in a differential setup. Since every single marker mainly affects the sense line in its immediate vicinity, the total output signal of each sensor element rises linearly as the density of markers on its surface is increased. Depending on the type of marker, a minimum number of about 100 magnetic particles can be detected with this type of sensor.

6. TMR-type magnetic biosensor

6.1. TMR theory

6.1.1. Introduction

Tunneling between two conducting electrodes through a potential barrier is one of the oldest known quantum phenomena and has already been recognized in the 1930's (Ref. 205). Still, it continues to be an active field of research and has even reached the engineering level due to ever decreasing size scales in the microelectronics industry.

The first observation of spin-dependent tunneling was carried out on Al-Al₂O₃-Ni sandwich structures by Tedrow and Meservey in 1971 (Ref. 206). As shown before by the experiments of Giaever (Ref. 207), the dependence of the tunneling current from a normal metal into a superconductor on the applied voltage V across the barrier is a direct map of the BCS quasiparticle density of states (DOS) of the superconductor (see Figure 66 a/b). When a magnetic field with strength H below the critical field of the superconductor is applied in the plane of the sandwich structure, the quasiparticle states in the superconductor experience Zeemann splitting by $2\mu_B H$, resulting in four separate peaks in the tunneling conduction curve (see Figure 66 c/d). In the case that the electrons originate from a normal metal, the density of states at the Fermi energy is equal for both spin orientations, resulting in equal values of the relative conduction peak heights $\sigma_4 - \sigma_2$ and $\sigma_1 - \sigma_3$ for the minority and majority electrons. For a ferromagnetic electrode, however, the relative conduction peaks are weighted by its corresponding spin polarization. Thus, the technique of spin polarized tunneling into a superconductor allows for conclusions on the tunneling spin polarization of the ferromagnetic electrode at the Fermi energy according to:

$$P(E_F) = \frac{(\sigma_4 - \sigma_2) - (\sigma_1 - \sigma_3)}{(\sigma_4 - \sigma_2) + (\sigma_1 - \sigma_3)} \quad \text{Equation 20}$$

However, the spin polarizations obtained by this technique are all positive (for a summary of the values, see e.g. Ref. 209), which is in contradiction to the negative spin polarization of the bulk band structures of Co and Ni (Ref. 210). This apparent inconsistency was solved by Stearns (Ref. 211) by noticing that the tunneling conductance does not only depend on the densities of states of the two electrode materials, but also on the tunneling probability through the barrier. Since the localized d-electrons of the 3d ferromagnets have a strong minority weight at the Fermi energy, they contribute most to the bulk spin polarization. However, due to their large effective mass, their tunneling probability is small compared to the nearly free 4s electrons. Thus, the tunneling current is mainly mediated by 4s electrons which show a larger weight of majority electrons at the Fermi energy. Therefore, despite a negative bulk spin polarization, the total tunneling spin polarization is positive for sufficient barrier thicknesses. Still, even though Stearns model presents a major advance in understanding spin polarized tunneling, it does not account for the influence of the barrier and bonding at the ferromagnet-insulator interface. These issues are currently under investigation (see e.g. Ref. 212), and up to now, no unitary theory has been developed which could explain every aspect of spin polarized tunneling.

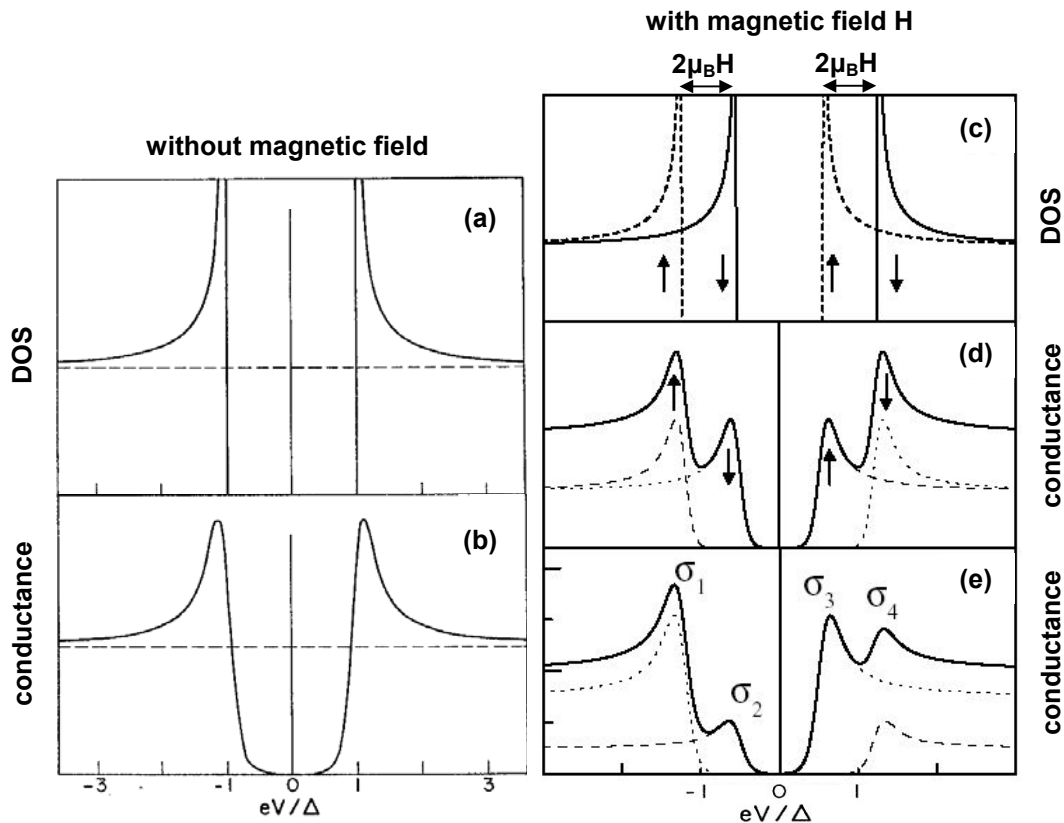


Figure 66: Tunneling in metal / insulator / superconductor sandwich structures as a function of applied voltage V across the barrier (after Ref. 208; Ref. 209)

a) superconducting DOS

b) corresponding conductance through the barrier

c) a magnetic field with strength H in the plane of the sandwich structure causes a Zeemann split of $2\mu_B H$ of the peaks in the superconducting DOS

d) corresponding conductance for a normal metal with equal spin distribution

e) corresponding conductance for a ferromagnet with 50 % spin polarization

The observation of spin polarized tunneling led to the idea of using a second ferromagnetic layer instead of a superconductor as spin detector. In this case, the tunneling current through the sandwich structure should depend on the relative orientation of the magnetization vectors of the two ferromagnetic electrodes, thus giving rise to a tunneling magnetoresistance (TMR). Such an effect was first observed by Jullière in 1975 (Ref. 6). He also developed a simple model for the TMR effect based on tunneling spin polarizations of the two ferromagnetic layers. Though only phenomenological, this model is still frequently used to estimate the expected TMR effect of a given sandwich structure.

Jullière's results stimulated much future research, but it took almost two decades until a sizable TMR effect at room temperature could be realized experimentally (Ref. 7). In retrospect, this breakthrough was due to improved fabrication techniques and the introduction of Al_2O_3 barriers. Compared to the previously employed magnetic oxide barriers, these insulators prevent significant spin-flip scattering which reduces the maximum achievable TMR effect. By now, the fabrication of magnetic tunnel junctions is a standard technique, and devices based on the TMR effect are starting to become commercially available (e.g. MRAM, Ref. 12).

6.1.2. Tunneling through a barrier

Following is a brief description of electron tunneling through a barrier as it is needed within the scope of this work. A thorough discussion of the topic can be found for example in the review by Wolf (Ref. 213).

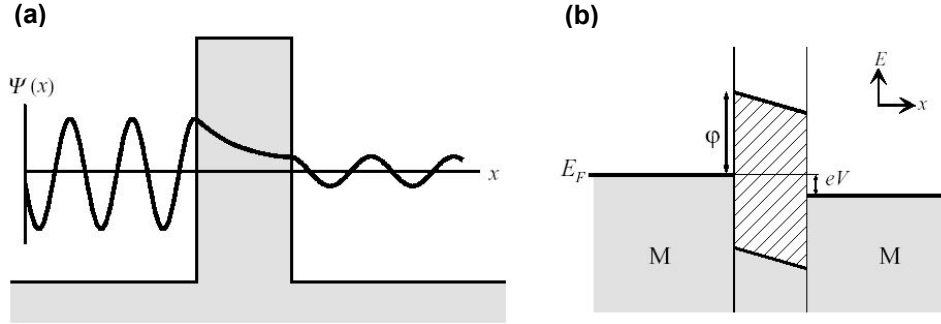


Figure 67: Sketch of an electron tunneling process between two metallic electrodes through an insulating barrier (taken from Ref. 209)

a) electron wave functions

b) energy levels

Figure 67 a) sketches an electron wave function as it encounters a potential barrier larger than the electron's energy. Within the insulator, the wave function decays exponentially, and for thin enough barriers, some intensity remains on the other side (the reflected wave function is not shown here). Thus, even though classically impossible, there is some small probability for the electron to tunnel through the barrier. In part b) of Figure 67, the potential diagram for the metal / insulator / metal sandwich structure is shown with a bias voltage V applied across. The occupied energy states are shaded gray, and the hatched region marks forbidden states within the barrier. The current of electrons with an energy E tunneling from the left to the right electrode is determined by the number of occupied states in the left electrode, the number of vacant states in the right electrode, and the square of the tunneling probability T through the barrier. The electron energy on each side is measured from the respective Fermi level E_F . By integrating over all possible electron energies, the total tunneling current from the left to the right electrode is proportional to:

$$I_{l \rightarrow r} \propto \int_{-\infty}^{\infty} dE \rho_l(E) f(E) |T(E)|^2 \rho_r(E + eV) [1 - f(E + eV)] \quad \text{Equation 21}$$

Here, ρ denotes the density of states (DOS) and f stands for the Fermi-Dirac distribution. Similarly, the total tunneling current from the right to the left electrode is proportional to:

$$I_{r \rightarrow l} \propto \int_{-\infty}^{\infty} dE \rho_r(E) f(E) |T(E)|^2 \rho_l(E - eV) [1 - f(E - eV)] \quad \text{Equation 22}$$

The total current which tunnels through the barrier is the difference between the two currents:

$$I_{\text{tot}} = I_{l \rightarrow r} - I_{r \rightarrow l} \quad \text{Equation 23}$$

In order to evaluate those general expressions, one has to calculate the transition matrix element T . This problem has been tackled by several different simplified models (e.g. Ref. 214; Ref. 215). Here, we focus on the work of Brinkman (Ref. 216), who used the WKB approximation (Ref. 217) to numerically calculate the dependence of the tunneling conductance on the applied bias voltage for asymmetrical barriers like the one sketched in Figure 68. It is characterized by its average height ϕ , the asymmetry $\Delta\phi$, and its thickness d .

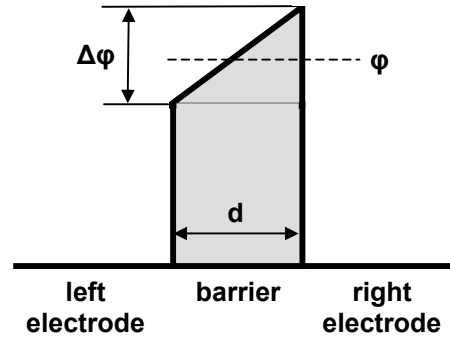


Figure 68: Barrier model applied by Brinkman (Ref. 216)

As a result, Brinkman concluded that the dependence of the area specific tunneling conductance G on the bias voltage V can be fitted by a 2nd order polynomial function.

$$G = \frac{dI_{\text{tot}}}{dV} = A(\phi, d) V^2 + B(\phi, \Delta\phi, d) V + C(\phi, d) \quad \text{Equation 24}$$

The parameters A , B and C depend on the parameters of the model barrier. Thus, by fitting the experimentally obtained area specific tunneling conductance curve by a 2nd order polynomial, it is possible to deduce the barrier parameters from the three constants:

$$\begin{aligned} \phi^2 &= \frac{e^2 C}{32A} \ln^2 \left(\frac{\hbar^3}{\sqrt{2\pi} e^3 m_{\text{eff}}} \sqrt{AC} \right) \\ d &= -\frac{\hbar}{2\sqrt{2m_{\text{eff}}}\phi} \ln \left(\frac{\hbar^3}{\sqrt{2\pi} e^3 m_{\text{eff}}} \sqrt{AC} \right) \\ \Delta\phi &= -\frac{12\hbar B}{\sqrt{2m_{\text{eff}}} e C} \frac{\phi^{3/2}}{d} \end{aligned} \quad \text{Equation 25}$$

Here, m_{eff} is the effective mass of the tunneling electrons, which is generally set to $0.4 \cdot m_E$ (Ref. 218). Even though Brinkman's model is oversimplified, it gives realistic values for the barrier thickness, as can be checked for example by tunneling electron microscopy. Thus, it is used in this work to characterize the barrier properties.

However, the application of a free electron model for calculating the transition matrix elements leads to a cancellation of the DOS of the two electrodes in the expression for the tunneling current in Equation 23. If this were true, there could be no TMR effect. In order to accurately calculate the tunneling current, more sophisticated models have to be applied. For example, Mathon (Ref. 219) developed a unified theory both for CPP GMR and TMR structures by applying the Kubo-Landauer

formalism (Ref. 201) to a single-orbital tight-binding band structure model. Even though the characteristic features are reproduced much better by this approach, the absolute value of the TMR is still greatly overestimated.

6.1.3. Tunneling magnetoresistance

As already mentioned in the introduction, the dependence of the tunneling current on the density of states of the adjacent electrodes can be exploited to fabricate a device for which the conductance through the barrier depends on the relative orientation of the magnetization vectors of the ferromagnetic layers on both sides of the barrier. If spin-flip scattering is avoided in the tunneling process, the total conduction of the electrons can be divided into separate spin-up and spin-down channels parallel to each other. Thus, Equation 23 can be rewritten as:

$$I_{\text{tot}} = I_{l \rightarrow r}^{\text{up}} + I_{l \rightarrow r}^{\text{down}} - I_{r \rightarrow l}^{\text{up}} - I_{r \rightarrow l}^{\text{down}} \quad \text{Equation 26}$$

In the simplest case for $T=0$, the only electrons which can cross the barrier are those from occupied states in the left electrode which tunnel into empty states in the right electrode, and their energies range from $E_F - eV$ to E_F . For sufficiently small bias voltages V , the DOS ρ and the tunneling matrix element T can be approximated as constant over this energy range, with their values replaced by those at the Fermi energy. Due to $f(E) = \Theta(E_F - E)$ at $T=0$, Equation 26 simplifies to the following form for the two extreme cases of parallel and antiparallel alignment of the electrode's magnetization vectors:

$$\begin{aligned} \text{parallel:} \quad I_{\text{tot}} &\propto (\rho_l^{\text{up}} \rho_r^{\text{up}} + \rho_l^{\text{down}} \rho_r^{\text{down}}) |T|^2 V \\ \text{antiparallel:} \quad I_{\text{tot}} &\propto (\rho_l^{\text{up}} \rho_r^{\text{down}} + \rho_l^{\text{down}} \rho_r^{\text{up}}) |T|^2 V \end{aligned} \quad \text{Equation 27}$$

The tunneling matrix element is assumed to be identical for both spin orientations. Thus, differences in the currents are only due to relative differences in the DOS for the parallel and antiparallel magnetization alignment. Following the most common definition of the TMR effect, it can be expressed solely by the DOS in the left and right electrode for the two spin channels:

$$\text{TMR} = \frac{R_{\uparrow\downarrow} - R_{\uparrow\uparrow}}{R_{\uparrow\uparrow}} = \frac{I_{\uparrow\uparrow} - I_{\uparrow\downarrow}}{I_{\uparrow\downarrow}} = \frac{(\rho_l^{\text{up}} \rho_r^{\text{up}} + \rho_l^{\text{down}} \rho_r^{\text{down}}) - (\rho_l^{\text{up}} \rho_r^{\text{down}} + \rho_l^{\text{down}} \rho_r^{\text{up}})}{(\rho_l^{\text{up}} \rho_r^{\text{down}} + \rho_l^{\text{down}} \rho_r^{\text{up}})} \quad \text{Equation 28}$$

Here, $I_{\uparrow\uparrow}$ and $I_{\uparrow\downarrow}$ denote the respective tunneling currents for parallel and antiparallel magnetization orientation. The spin polarization in each electrode is defined as the asymmetry in the DOS of the majority and minority electrons:

$$P = \frac{\rho^{\text{up}} - \rho^{\text{down}}}{\rho^{\text{up}} + \rho^{\text{down}}} \quad \text{Equation 29}$$

Inserting this definition in Equation 28, the TMR effect can be related to the spin polarization of the two electrodes according to:

$$\text{TMR} = \frac{2P_l P_r}{1 - P_l P_r} \quad \text{Equation 30}$$

This is the original result for the TMR effect derived by Jullière (Ref. 6). Since most tunneling spin polarizations are positive, the actual resistance of the junction is lower in the parallel magnetization configuration than in the antiparallel state. Even though only phenomenological, the model agrees pretty well to experimental low temperature results at near-zero bias voltage when employing tunneling spin polarizations as measured by tunneling experiments into superconductors with identical barriers (Ref. 209). By doing so, all further influences on the tunneling magnetoresistance (e.g. tunneling probability for electrons from different bands and effects of the barrier and the interfaces) are included in the measured tunneling spin polarization values, so the good agreement of this simple equation with just two parameters to the experimental data is not very astonishing. In order to understand the dependence of the TMR ratio on other parameters like temperature or bias voltage, more elaborate theories have to be employed (see e.g. the reviews in Ref. 220; Ref. 221). Still, the model of Jullière remains a valuable basis for estimating the TMR ratios for new materials like “half-metallic” ferromagnets with an expected spin polarization of 100% (e.g. the Heusler alloys NiMnSb and Co₂MnSi).

Generally, the relative resistance of a magnetic tunnel junction can be expressed as a function of the enclosed angle θ between the magnetizations of the two ferromagnetic electrodes as (Ref. 222):

$$\text{TMR}(\theta) = \text{TMR}_{\max} \frac{1 - \cos \theta}{2} \quad \text{Equation 31}$$

Here, TMR_{\max} denotes the maximum resistance difference between the antiparallel and the parallel state, normalized to the parallel resistance.

For practical purposes, TMR junctions have to be fabricated in which the relative orientation of the magnetizations of the two ferromagnetic layers can be aligned both into stable parallel and antiparallel states by an external magnetic field. The simplest method to meet this requirement is to use two ferromagnets with different coercive fields, i.e. a hard and a soft magnetic material. The resulting TMR characteristic with applied in-plane magnetic field is sketched in Figure 69 a). The arrows indicate the magnetization vectors of the respective ferromagnetic layers, where the upper layer is the softer material and switches its magnetization at a lower field than the hard magnetic material. Thus, a stable antiparallel high resistive orientation is reached in-between the parallel saturation states. However, concerning promising applications like MRAM cells, it is a necessity that a two-fold resistance state exists at zero applied field. This can be achieved by exchange biasing one of the ferromagnetic electrodes to an antiferromagnetic material (either natural or artificial, see chapter 6.1.4). In Figure 69 b), the TMR characteristic for a system with the lower electrode exchange biased in the negative field direction is sketched. If no further coupling mechanisms are present, the upper free electrode switches its magnetization direction symmetrically around zero field, while the exchange coupled magnetic layer has its hysteresis loop shifted in the positive field direction by the magnitude of the pinning field. Therefore, a two-fold resistance state is reached around zero field. Though this is not an essential requirement for magnetic biosensor applications, only exchange biased magnetic tunnel junctions (MTJ) are employed in this work.

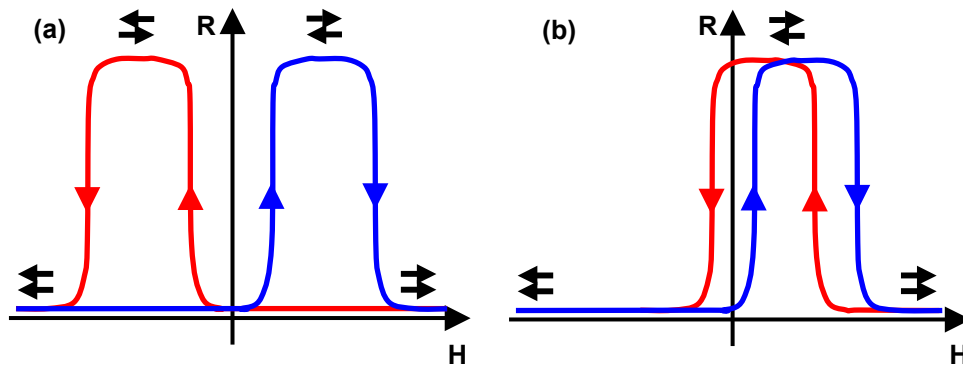


Figure 69: Schematic representation of TMR loops

a) hard-soft MTJ

b) exchange biased MTJ

6.1.4. Exchange bias

The phenomena of an exchange bias between a ferromagnet and an antiferromagnet in immediate contact to each other was initially observed for fine Co particles by Meiklejohn and Bean in 1956 (Ref. 223). Due to oxidation, there existed a thin layer of the antiferromagnet CoO around the particles, which had been field cooled from above the Néel temperature of CoO (293°K) to liquid nitrogen temperature (77°K). As a consequence, the hysteresis loop of the particles showed a distinct shift of almost 150 kA/m, which was attributed to a unidirectional exchange anisotropy arising from the interaction at the interface.

Schematically, the functionality of the antiferromagnet-ferromagnet exchange coupling is displayed in Figure 70 (Ref. 224). In part a), the sample is annealed at a temperature between the Néel temperature T_N of the antiferromagnet and the Curie temperature T_C of the ferromagnet. Thus, the magnetization of the ferromagnetic layer aligns parallel to the external magnetic field H , while the spin configuration of the antiferromagnet remains random. From this initial state, the temperature is decreased below T_N with the magnetic field still present (part b). In the case of an uncompensated interface, the spins of the antiferromagnet at the interface orient parallel to the magnetization vector in the ferromagnet due to direct exchange interaction, while the subsequent planes follow the antiferromagnetic order to produce zero net magnetization. When a magnetization curve is taken in this state with the applied field aligned parallel to the original cooling field, the ferromagnet follows its hysteresis curve, but with its center shifted by the magnitude of the exchange field H_{EB} (part c-d). It arises due to the interfacial interaction with the antiferromagnet, which remains essentially unchanged due to its very large anisotropy energy. Experimentally, it is observed that the magnitude of the exchange bias decreases with increasing temperature and vanishes at the blocking temperature T_B with $T_B \leq T_N$.

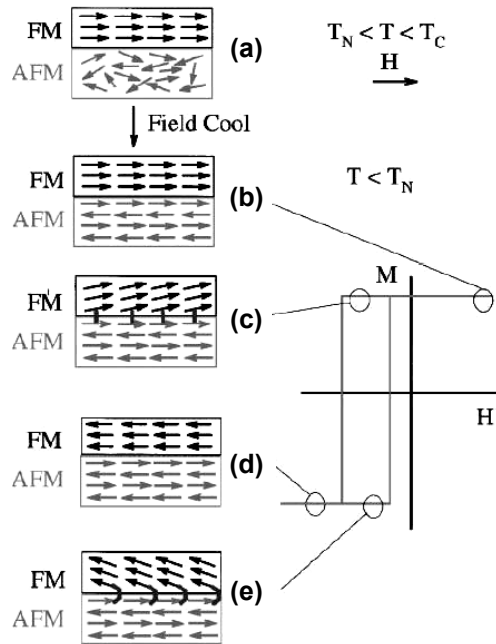


Figure 70: Sketch of the spin configuration of an exchange coupled antiferromagnet-ferromagnet system (taken from Ref. 224)

The magnitude of H_{EB} can be estimated by the following consideration (after Ref. 225). Neglecting all other contributions, the total energy E of the system is the sum of the anisotropy energy E_{EB} and the Zeemann energy E_Z :

$$E = E_Z + E_{EB} = -\mu_0 m H \cos \theta - K_{EB} \cos \phi \quad \text{Equation 32}$$

Here, θ is the angle between the applied magnetic field H and the magnetization M , and ϕ denotes the angle between the exchange bias anisotropy (equivalent to the direction of the cooling field) and the magnetization. When the hysteresis measurement is taken in the direction of the cooling field, the magnetization of the ferromagnet remains antiparallel to the applied field and parallel to the anisotropy direction until the field strength H_{EB} is reached. At this stage, the magnetization switches into the field direction. Setting the total energies of the system in those two states equal to each other results in an exchange bias field of:

$$H_{EB} = \frac{k_{EB}}{\mu_0 M_S t_{FM}} \quad \text{Equation 33}$$

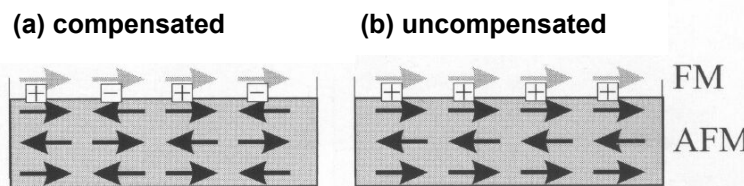


Figure 71: Spin configuration at a smooth ferromagnet-antiferromagnet interface (taken from Ref. 225)

- a) compensated moment structure
- b) uncompensated moment structure

Here, the area-specific anisotropy energy constant $k_{EB} = K_{EB} / A$ is employed, and t_{FM} is the thickness of the ferromagnet. In order to predict the magnitude of the exchange bias, the anisotropy constant should be expressed in terms of microscopic quantities, which requires to take a look at the spin configuration at the interface. [Figure 71](#) illustrates the two major possibilities for a perfectly smooth model interface. For a compensated moment structure, the exchange couplings between neighboring ferromagnet and antiferromagnet moments are favorable (+ sign) and unfavorable (- sign) in alternating order. Therefore, the macroscopic interface exchange coupling vanishes and no exchange bias exists. However, for an uncompensated surface, all moment pairs are either favorable or unfavorable, which yields different interface exchange coupling energies and a total specific anisotropy energy of:

$$k_{EB} = \frac{N}{A} J_{INT} \quad \text{Equation 34}$$

N/A is the total number of spin pairs per area, and J_{INT} is the coupling energy per ferromagnet-antiferromagnet spin pair. Thus, the exchange bias field H_{EB} is given by:

$$H_{EB} = \frac{1}{\mu_0} \frac{N}{A} \frac{J_{INT}}{M_S t_{FM}} \quad \text{Equation 35}$$

However, using typical values of J_{INT} , the exchange biases obtained by this equation are larger by 2-3 orders of magnitude than the observed fields ([Ref. 224](#); [Ref. 225](#)). One of the reasons for this discrepancy probably lies in the interface roughness, which is neglected in the above picture. By introducing a certain roughness, some spin pairs experience partially unfavorable coupling even for uncompensated interfaces ([Ref. 225](#)), thus reducing the total exchange coupling. Anyhow, despite more than four decades of research, the microscopic understanding of the exchange coupling effect is still not fully established, and various attempts to solve this problem can be found in the cited review articles ([Ref. 224](#); [Ref. 225](#); [Ref. 226](#)).

6.1.5. Orange peel coupling

When two magnetic layers are separated by a non-magnetic spacer layer and show correlated roughness, there exists an effective ferromagnetic exchange coupling which is induced magnetostatically by the formation of magnetic poles at the interface. It was first described by Néel in 1962 ([Ref. 227](#)) and is, therefore, also called Néel coupling. In his original work, the ferromagnetic layers are assumed to be infinitely thick. This model was refined by Zhang ([Ref. 228](#)) by introducing finite film thicknesses and developed further by Kools in 1999 ([Ref. 229](#)).

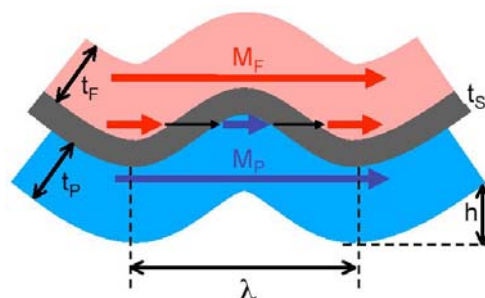


Figure 72: Sketch of the mechanism of orange peel coupling (taken from [Ref. 123](#))

Figure 72 sketches the principle mechanism of this kind of coupling. In the model, it is assumed that the roughness of the layers is completely correlated and can be described by a sinusoidal function with a wavelength λ and an amplitude h . The magnetization M of the lower ferromagnet with thickness t is fixed in space (for example by exchange coupling to an antiferromagnet, see chapter 6.1.4) and is called the pinned layer (subscript P). The non-magnetic spacer is identified by the subscript S, and the free ferromagnet carries the subscript F. Because the magnetization of the pinned layer is fixed, it introduces magnetic poles at the interface which are the origin of magnetostatic fields that tend to align the magnetization of the free magnetic layer ferromagnetically to the pinned layer. Following the description of Kools (Ref. 229), the strength of this type of coupling can be expressed by an effective unidirectional pinning field H_P with a magnitude of:

$$H_P = \frac{\pi^2 h^2 M_P}{\sqrt{2\lambda} t_F} \left[1 - \exp\left(-\frac{2\pi\sqrt{2}t_F}{\lambda}\right) \right] \left[1 - \exp\left(-\frac{2\pi\sqrt{2}t_P}{\lambda}\right) \right] \exp\left(-\frac{2\pi\sqrt{2}t_S}{\lambda}\right) \quad \text{Equation 36}$$

Due to the respective (1-exp) term, the pinning field increases with increasing thickness of the pinned layer up to a maximum value for infinite thickness, which is related to the formation of a larger number of poles. Similarly, more poles of the free layer can react to the induced stray fields for larger values of t_F (represented by the respective (1-exp) term), but due to the limited range of the stray fields, the pinning field also decreases with $1/t_F$. The latter is also the reason for the exponential decrease of H_P with increasing spacer thickness. Since its formulation, the model of Kools has been confirmed by various experiments (e.g. Ref. 230).

6.2. Sensor layout

Our TMR sensor system comprises the layer structure shown in Figure 73. Highlighted by a rectangle is the functional group which consists of the magnetic layers and the barrier. The film stack is deposited in the CLAB 600 sputtering system, and the barrier is fabricated by oxidizing a 1.4 nm thick aluminum layer by an ECR assisted oxygen plasma source (see chapter 2.1). In order to ensure a stable antiparallel magnetization state of the two ferromagnetic layers facing the barrier, the lower $\text{Co}_{70}\text{Fe}_{30}$ layer is exchange biased to the antiferromagnet $\text{Mn}_{83}\text{Ir}_{17}$ by field annealing the sample in the vacuum furnace according to the description in chapter 2.2. $\text{Mn}_{83}\text{Ir}_{17}$ is chosen due to its excellent thermal reliability (Ref. 231), the large exchange bias (Ref. 232) and a reasonable blocking temperature (Ref. 233).

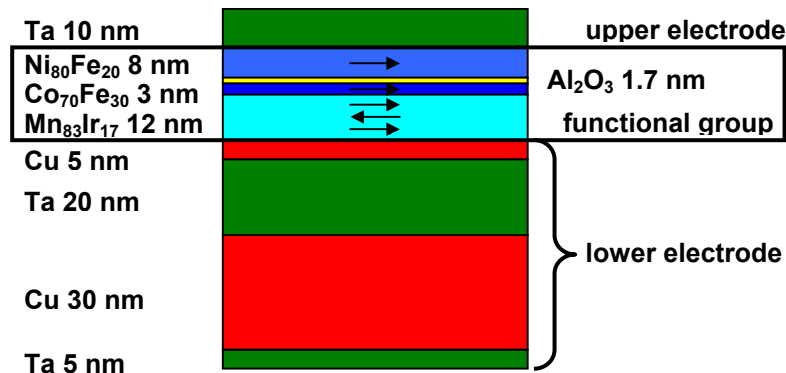


Figure 73: Layer stack of the TMR sensor system

The remaining layers form the upper and lower electrode and serve as electrical contact. Whereas the upper electrode consists of a single film of tantalum which prevents oxidation of the layers underneath, the lower electrode is a tantalum copper sandwich structure that is required due to the subsequent lithography process. The initial tantalum layer serves as an adhesion promoter to the SiO₂ wafer surface, while the thick copper layer is required to ensure good electrical conductance to a specific TMR element through the lower electrode.

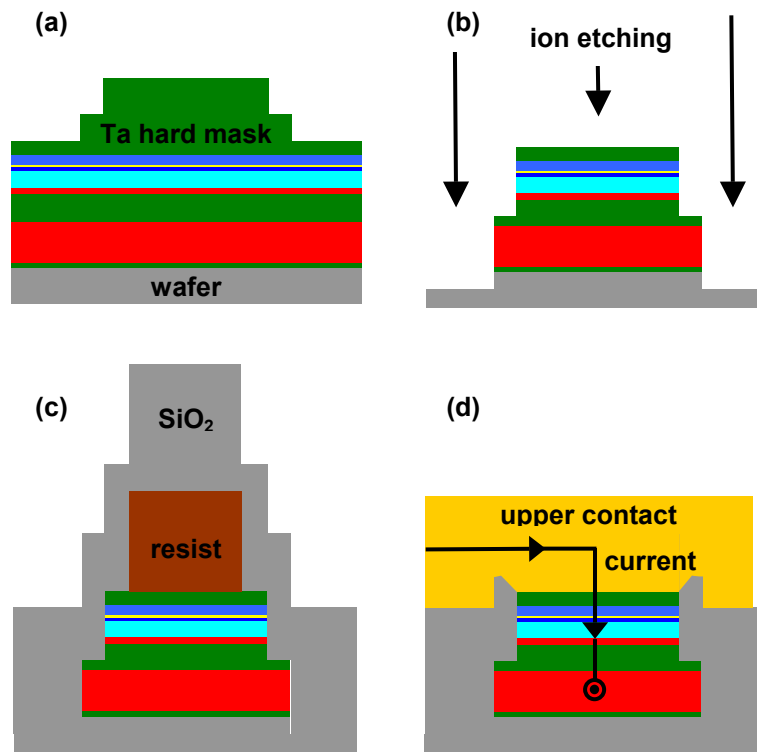


Figure 74: Sketch of the lithography process

a) a Ta hard mask is applied in a two step lithography process to define the lower electrode and the TMR elements

b) Ar-ion etching process

c) a third lithography process leaves resist caps above each TMR element and an insulating SiO₂ layer is deposited across the entire sample

d) lift-off of the resist caps leaves a conduction path to the top electrode of each TMR element which is contacted via a fourth lithography step by conducting lines

The entire lithography process is sketched in a cross-section view in [Figure 74](#). Initially, two subsequent optical laser-lithography steps (see chapter [2.3.3](#)) define long base lines which serve as a common contacts to the lower electrode and a number of separate small areas that form the individual TMR sensor elements. A number of different sizes and shapes has been realized during this work, but in its final version, each TMR sensor element is defined as a circular region with a diameter of 50 μm. Thus, it covers the same actual area as the spiral-shaped sense line of a GMR sensor element (see chapter [5.2](#)). After each exposure, a Ta layer with appropriate thickness is deposited as a mask for the subsequent Ar-ion etching step (see chapter [2.4](#)), which is carried out until a total dosage of 3600 mC has passed through the sampleholder. As a result of the etch, the layer stack in the unprotected areas of the sample is completely removed. Additionally, 30-40 nm of the originally 100 nm thick SiO₂ layer on the wafer are also removed in those areas, thus assuring

perfectly insulating behavior. The remaining SiO₂ thickness on the wafer is checked by reflectivity measurements (see chapter 2.6).

In the area which is protected by the first Ta mask with a thickness of about 20 nm, the etching is carried out through the barrier into the lower electrode and stops in the middle of the second Ta layer from the bottom. These regions form the common contact to the lower electrode of each TMR element. Due to the slow etching rate of Ta and the large thickness of this layer, the end point of the etching step is always reached within this so-called stopping layer, even if other conditions are slightly varying (i.e. mask thickness, thickness of the total layer stack, etching rate). Additionally, the remaining Ta surface of this layer acts as an adhesion promoter for the subsequent insulating SiO₂ layer. The thin Cu layer on top is needed as a seed for the growth of the Mn₈₃Ir₁₇ antiferromagnet.

The region which is protected both by the first and second Ta mask (the thickness of the second mask is about 27 nm) defines the individual TMR elements. As a result of the etching process, both masks are ablated, but the entire original layer stack of the TMR system is still present. Figure 75 displays two x-ray spectrums as measured by EDX (see chapter 2.5) after the etching process, one on top of the lower electrode and the other on a TMR sensor element. The SEM image to the left clarifies the respective scanning positions, but does not represent the actual sample (the scans are taken from a later TMR chip with circular sensor elements). In case the entire film stack is still present, peaks from all elements can be observed due to the large penetration depth of roughly 1 μm for electrons with an energy of 20 keV. In particular, Ni from the topmost layer is visible in the spectrum, which assures that the etch has not been carried out too deep. On the lower electrode, however, only Ta and Cu show up in the spectrum, thus assuring that the etch has been carried out through the barrier into the lower contact layers in those regions. An especially characteristic feature are the two MnKα¹ and Kα² lines at 5.899 and 5.888 keV. They overlap and show up clearly in the spectrum on top of a TMR element, but are missing for the scan on the lower electrode. Since the antiferromagnet Mn₈₃Ir₁₇ is situated well below the barrier, the disappearance of this peak is characteristic for the correct endpoint of the etch.

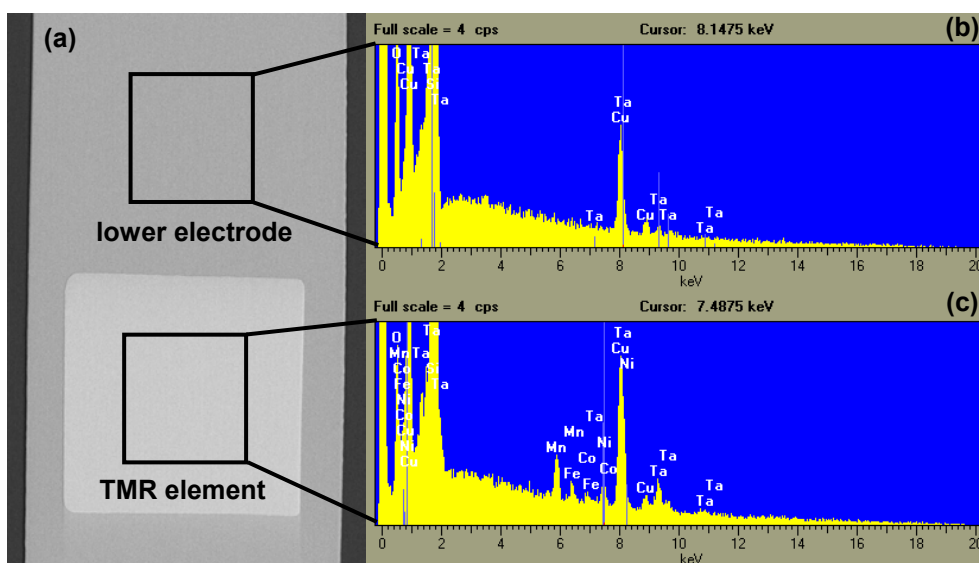


Figure 75: EDX spectra of two 10x10 μm² spots on the sample after the etching process
a) exemplary SEM image of the respective scanning positions
b) scan on the lower electrode
c) scan on a TMR sensor element

Following the etch, a third optical lithography step is carried out which leaves spherical resist caps with a diameter of 30 μm centered on top of each TMR element (Figure 74 c). Afterwards, a 100 nm thick SiO_2 layer is sputter deposited in the proprietary developed UHV chamber described in chapter 2.1 which acts as an electrical insulator between the bottom and top electrodes. In order to ensure electrical conduction from individual contact lines to the top electrodes of the TMR elements, the resist caps are removed subsequently, resulting in small circular holes in the surrounding glass layer.

In case the sensor chip is going to be used to detect DNA, the holes through the glass layer are obtained in an alternative way which circumvents the SiO_2 lift-off step. This is necessary since this step tends to result in resist remnants which cause leaking sites in the subsequent protection layer (see chapter 4.1). In this approach, the SiO_2 is sputter deposited first across the entire sample. Subsequently, it is removed again on top of the TMR elements only by an etching step through holes in a Ta hard mask. Sensor chips have been produced successfully by this approach, and they proved to resist the biological solvents in the DNA hybridization procedure. However, the etch through the glass layer into the top electrode of the TMR elements carries a great risk of destroying the barrier if not every single parameter is controlled precisely. Thus, the less critical procedure described above is used in order to fabricate sensor chips which test the reaction of TMR elements to magnetic markers alone.

Next, contact lines are patterned by optical lithography which connect bonding pads to the top electrode of each TMR element via the holes in the glass layer. The lines consist of the sandwich structure $\text{Ta}_{10\text{nm}}\text{Au}_{50\text{nm}}\text{Ta}_{10\text{nm}}$ and are deposited by the proprietary developed sputtering machine described in chapter 2.1. The Ta films ensure good adhesion to the glass layer below and the protection layer above (see chapter 4.1). In order to allow wire bonding, the contact pads only are covered by an additional layer stack of $\text{Ta}_{3\text{nm}}\text{Au}_{120\text{nm}}$.

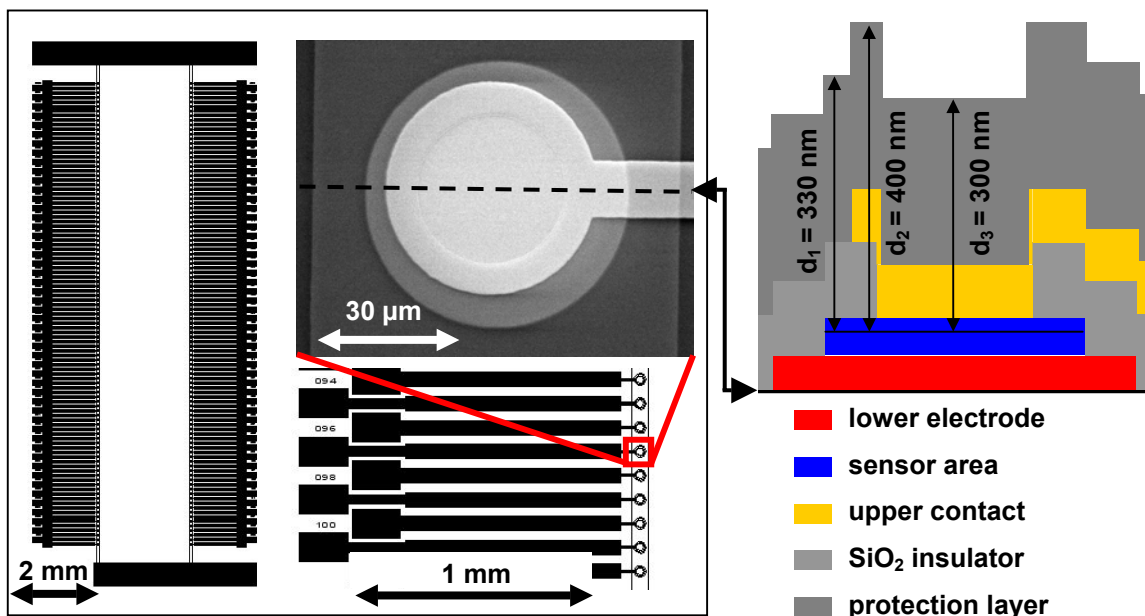


Figure 76: Layout of the TMR sensor chip

Just like in the case of a GMR sensor, a TMR chip incorporates a total number of 206 sensor elements which are arranged in two rows, each of which is situated above a 70 μm wide lower electrode with a length of 12 mm. The lower electrodes are also

connected to large contact pads through holes in the insulating glass layer, so that two-point measurements of single TMR elements can be carried out between the common lower electrode and a specific upper electrode contact. The entire sensor layout is shown in [Figure 76](#). To the right, the topography across a single sensor element is explicitly displayed along the dashed line above the SEM micrograph. In order to bring the free magnetic layer as close as possible to the fluid interface, the hole in the insulating glass layer is expanded over as much of the sensor surface as allowed by lithographic restrictions. But apart from that middle area with a diameter of 30 μm , there are also two rings with larger distances of the free magnetic layer to the fluid interface (width = 5 μm each). The subdivision of the total sensor area to the three different distances is shown in column 2 of [Table 9](#), which leads to an area weighted average distance of 339 nm. As the strength of a marker's stray field in the sense layer strongly depends on this distance ([chapter 3.2.1](#)), the signal produced by a marker depends on its respective position on the sensor surface. This is illustrated in column 3 of [Table 9](#) for the maximum in-plane stray field component of a Bangs 0.86 μm particle with an out-of-plane magnetic moment of 20.6 fAm^2 . At the largest distance, the stray field only reaches about $2/3^{\text{rd}}$ of the maximum value for a particle situated in the sensor's center. For smaller markers, those differences get even larger. In an optimized sensor design, such topography variations should be avoided.

distance interface-sense layer [nm]	sensor area at this distance [μm^2]	maximum stray field of a Bangs 0.86 μm marker [A/m]
300	707	3620
330	707	3210
400	550	2470

Table 9: Subdivision of a sensor for the different distances of the sense layer to the interface

6.3. Sensor characteristics

First of all, the insulating barrier of a typical sensor element is investigated by looking at its conductance dependence on the applied bias voltage. In part a) of [Figure 77](#), the area-specific current is shown for parallel alignment of the magnetizations of the two ferromagnetic electrodes (IV-curve taken at an in-plane field of 160 kA/m). It displays a slight deviation from purely ohmic behavior, which shows up more clearly when looking at the derivative (the area-specific differential conductance) in [Figure 77 b](#)). The parabolic shape with a linear component agrees to what is expected within the model of Brinkman ([Ref. 216](#)), and the respective barrier parameters can be derived from a 2nd order polynomial fit to the data according to [Equation 25](#). With an effective electron mass of $0.4 \cdot m_E$ ([Ref. 218](#)), the results are:

$$\begin{array}{ll}
 A = 132\text{e}3 \text{ A}/(\text{V}^3\text{m}^2) & \Leftrightarrow \quad \varphi = 3.14 \text{ eV} \\
 B = 3.91\text{e}3 \text{ A}/(\text{V}^2\text{m}^2) & \quad \quad \quad d = 1.66 \text{ nm} \\
 C = 115\text{e}3 \text{ A}/(\text{V m}^2) & \quad \quad \quad \Delta\varphi = -0.42 \text{ eV}
 \end{array}$$

Assuming that all the aluminum gets transformed into Al_2O_3 , the original Al layer thickness of 1.40 nm should increase by a factor of 1.3 to 1.82 nm after oxidation (calculated from the bulk densities of Al (2.7 g/cm^3) and Al_2O_3 (4.0 g/cm^3) as well as the atomic mass numbers of O (16 g/mol) and Al (27 g/mol); values taken from [Ref. 168](#)). If this were true, the barrier thickness obtained from the Brinkman fit is too small. However, it is possible that other oxides with a lower oxygen content are partially formed within the barrier, and the densities of the thin amorphous layers can

be different from the bulk values. Also, uncorrelated roughness contributions at the interface lead to thinner barriers at some localized spots. Due to the exponential thickness dependence of the tunneling current, those thinner regions dominate the transport and lead to an effectively thinner barrier. The same reasoning holds true for metallic impurities within the barrier, which present islands for the tunneling electrons. Concerning the barrier height, the bandgap of Al_2O_3 is about 8.7 eV (Ref. 234). Since the Fermi energy in undoped insulators is situated in the middle between the valence and the conduction band, the maximum barrier height is half the bandgap, i.e. 4.35 eV in this case. According to the Brinkman fit, it only reaches 72 % of this maximum value for our barriers, which can be due to a number of reasons. First of all, the cited bandgap is for crystalline Al_2O_3 , which is certainly not the case for our barrier. Its structure is amorphous, which leads to a reduced bandgap. Also, the simplified model of Brinkman does not take into account the effect of image forces on the tunneling electrons, which round off the corners of the barrier and make it lower and narrower (Ref. 214; Ref. 216).

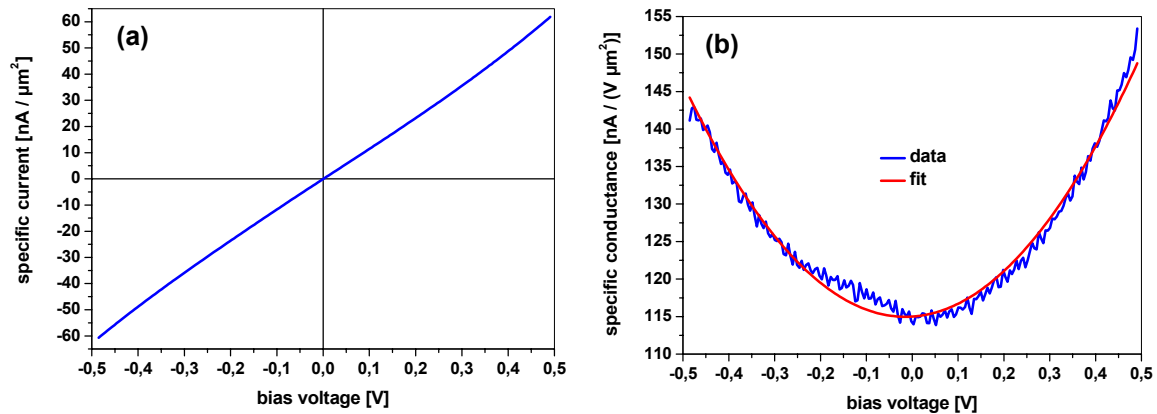


Figure 77: Electrical characterization of the tunneling barrier

a) specific current curve

b) specific conductance curve

In any case, the values for the height, thickness and asymmetry of the barrier agree pretty well to the references for optimum barriers from other work on similar systems (Ref. 123; Ref. 235; Ref. 236). With respect to the resistances and TMR ratios, a group of 15 individual elements on a sensor chip is analyzed at a bias voltage of 10 mV. The area resistances range from 8.71 to 9.75 $\text{M}\Omega\mu\text{m}^2$ in the parallel state (mean: 9.20 ± 0.36 $\text{M}\Omega\mu\text{m}^2$), and the TMR ratios vary between 44.2 and 48.3 % (mean: 46.6 ± 1.4 %). The relatively large distribution of these values has its origin in spatial variations of the film properties across the sensor chip, where the TMR elements are situated within an area of $2 \times 10 \text{ mm}^2$. Still, the values agree to the expectations for this particular layer system (Ref. 123).

Exemplary magnetotransport measurements are shown in Figure 78. Part a) displays a major loop taken with the field applied parallel to the pinning direction. While the free Py layer switches its magnetization direction around zero field, the $\text{Co}_{70}\text{Fe}_{30}$ layer is pinned to the antiferromagnet $\text{Mn}_{83}\text{Ir}_{17}$ and has its hysteresis loop shifted by the exchange bias field H_{EB} , which has a magnitude of about 64 kA/m. Due to the large exchange bias, a stable antiparallel alignment of the magnetization vectors of the two ferromagnetic layers is reached between the parallel orientations, which guarantees that the sensor resistance varies by the full magnitude of the possible TMR ratio (respective magnetization vectors indicated by arrows). According to Equation 33, an exchange bias of 64 kA/m corresponds to an area specific

anisotropy energy constant k_{EB} of 0.40 mJ/m^2 ($M_S^{\text{CoFe}} = 1650 \text{ kA/m}$, Ref. 237), which agrees well to the respective literature (Ref. 238).

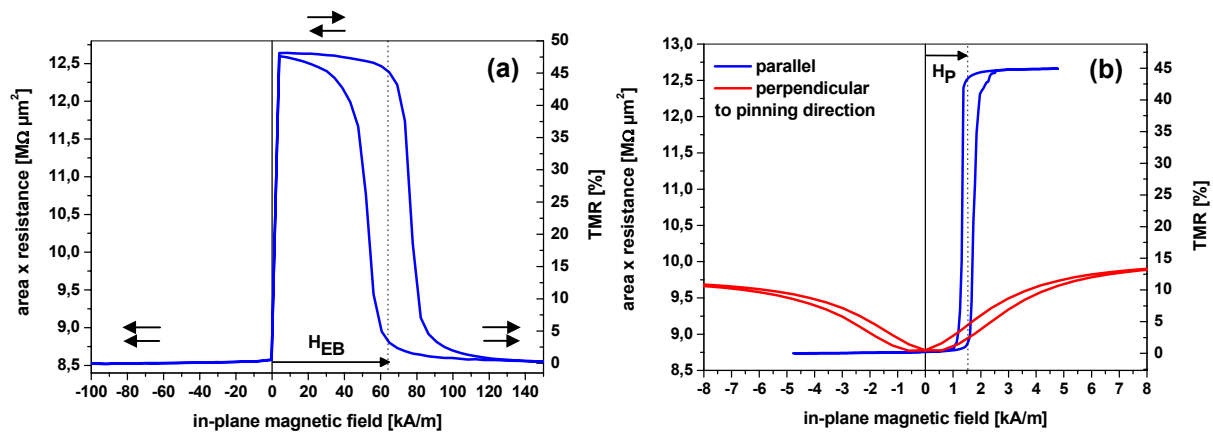


Figure 78: Magnetotransport measurements of spherical TMR sensor elements with a diameter of $50 \mu\text{m}$
 a) major loop
 b) minor loop

Part b) of Figure 78 shows corresponding minor loops of a sensor element. When the field is applied in the direction of the cooling field, the orange peel coupling causes a ferromagnetic pinning of the free Py layer to the exchange biased $\text{Co}_{70}\text{Fe}_{30}$ layer. In our case, the pinning field H_P has a magnitude of about 1.6 kA/m . Theoretically, the strength of H_P is given by Equation 36, a sketch of which is shown as a function of the free magnetic layer thickness t_F in Figure 79. Here, perfectly correlated sinusoidal roughness with an amplitude h of 0.4 nm and a wavelength λ of 20 nm is assumed (values taken from the measurements on similar systems in Ref. 123). The red curve represents the total pinning field H_P , which takes on a value of 1.5 kA/m at a free layer thickness of 8 nm , thus corresponding rather well to the experimental results.

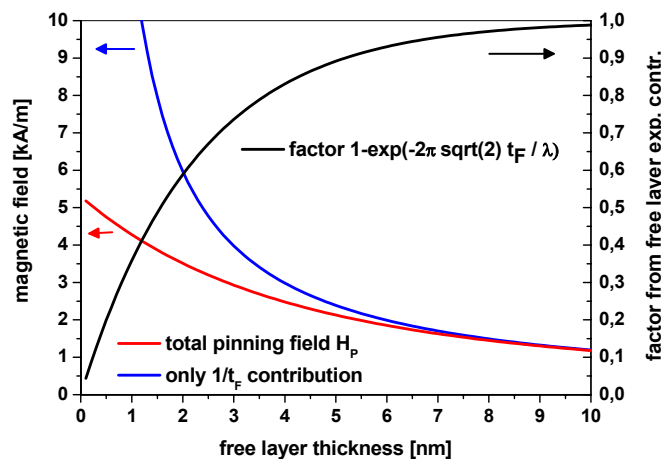


Figure 79: Dependence of the pinning field H_P on the thickness t_F of the free magnetic layer

In order to point out the different contributions in Equation 36 to the total pinning field, the blue curve in Figure 79 shows the $1/t_F$ prefactor and the black one the $1-\exp$ contribution. Even though the $1-\exp$ expression alone would cause an increase of H_P with increasing t_F , this effect is counterbalanced by the $1/t_F$ term, resulting in a monotonous decrease of H_P with increasing t_F . This dependence has also been observed experimentally by fabricating TMR sensors with different free layer

thicknesses. Although H_p can be compensated by an in-plane bias field, from an application point of view it is preferential that the sensitive region of the TMR characteristic is as close to zero field as possible. In this case, it might be possible to do without such an additional bias field when using those sensor systems for the detection of magnetic markers. Thus, the thickness of the free magnetic layer was chosen to be comparably large for our sensors (8 nm, see chapter 6.2).

Returning to part b) of Figure 78, the red curve shows the dependence of the sensor resistance on an in-plane field which is applied perpendicular to the pinning direction. In this case, half the maximum TMR value is expected if the magnetization of the free layer would follow the field while the magnetization of the hard layer would stay pinned to the antiferromagnet (see Equation 31 for $\theta = 90^\circ$). However, due to the anisotropy induced by the antiferromagnet, this field direction is the hard axis for both magnetic layers, so ideally, both magnetization components increase linearly with the magnitude of the perpendicular field. The only difference is the strength of the anisotropy (direct exchange coupling for the pinned layer and orange peel coupling for the free layer), which causes the magnetization of the free layer to rotate more quickly. Therefore, no perpendicular configuration is achieved, and the TMR ratio reaches a maximum below $\text{TMR}_{\text{max}} / 2$. For higher fields, the angle between the two magnetization vectors decreases again, and with it the TMR ratio.

In order to quantify this effect, a simple Stoner-Wohlfarth model (Ref. 239) of the free (index F) and the pinned (index P) layers with magnetic moments $m_{F/P}$ is applied. It only includes the Zeemann and the anisotropy energy terms:

$$E_{F/P}(H) = -\mu_0 m_{F/P} H \cos \theta - K_{F/P} \cos \phi = -\mu_0 m_{F/P} H \cos \theta - K_{F/P} \sin \theta \quad \text{Equation 37}$$

Here, H is the magnitude of the applied in-plane field (the respective directions and angles are sketched in the inlet of Figure 80 a). According to chapter 6.1.4, the area specific anisotropy energies $k_{F/P} = K_{F/P} / A$ can be expressed by:

$$\begin{aligned} k_F &= \mu_0 M_F t_F H_p \\ k_P &= \mu_0 M_P t_P H_{EB} \end{aligned} \quad \text{Equation 38}$$

For both ferromagnetic layers, the orientation of the magnetization vectors $M_{F/P}$ is obtained by minimizing the total energies $E_{F/P}$. As a result, the angles $\Theta_{F/P}$ between $M_{F/P}$ and H are given by:

$$\begin{aligned} \theta_F &= \arctan(H_p / H) \\ \theta_P &= \arctan(H_{EB} / H) \end{aligned} \quad \text{Equation 39}$$

As sketched in part a) of

Figure 80, Θ_F decreases much faster than Θ_P (values of H_p and H_{EB} chosen according to the data described above). The maximum difference between the two angles is obtained at a field around 10 kA/m, but reaches only a value of 72° . Therefore, according to Equation 31, the best TMR ratio achievable in this configuration is limited to 35 % of the maximum value. The simulated dependence of the TMR ratio on the strength of the field perpendicular to the pinning direction is compared to the measured values in part b) of

Figure 80. Within the scope of this simple model, the two curves agree well to each other. The hysteresis in the measured curve is most probably caused by a slight misalignment of the applied field from the hard direction.

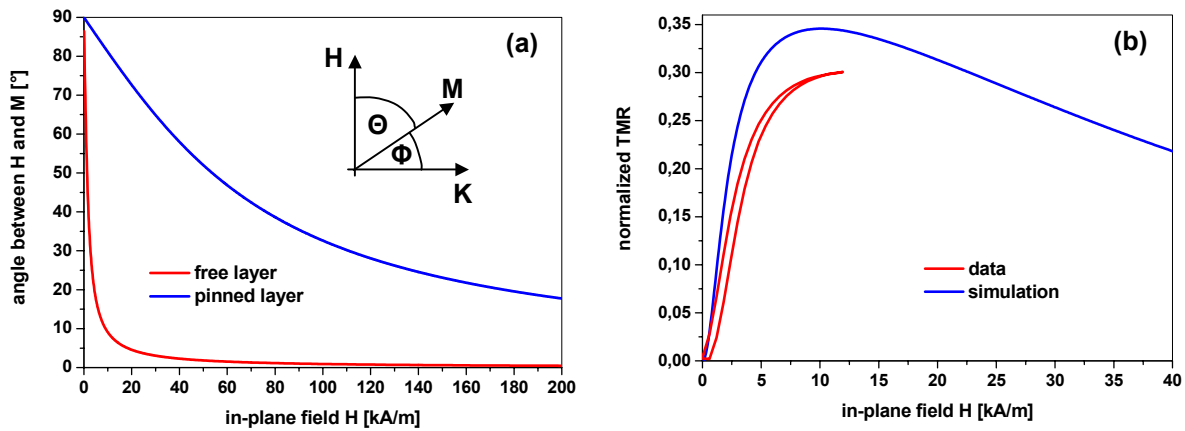


Figure 80: Stoner-Wohlfarth model for a TMR characteristic with the field applied perpendicular to the pinning direction

a) angles

b) comparison of the normalized TMR to the data

Since the in-plane stray fields of the magnetic markers are radially symmetric when magnetized perpendicular to the plane, the actual response of our TMR sensor can be regarded as the average between its characteristics parallel and perpendicular to the pinning direction. Thus, a signal is expected even without a bias field that compensates for H_p .

6.4. OOMMF model

Like in the case of GMR sensors, a model based on the oommf micromagnetic simulation code (Ref. 203) is employed which mimics the characteristics of our TMR sensor system. Due to the large exchange anisotropy induced by the antiferromagnet, the magnetization of the pinned magnetic layer is assumed to stay uniform and fixed in space at all times. Thus, it is sufficient to simulate the response of the free magnetic layer only. Because of computational limitations, it is not possible to include the entire sensor with a sufficiently small cellsize. Keeping the cellsize at 20 nm (the typical grain size for our sputtering conditions), a circular sensor with a diameter of 4 μm proved to be the maximum workable sensor area (runtimes below one week). Though much smaller than the actual TMR sensor, this model at least shares the same symmetry. According to the real sensor system, the simulated free magnetic layer is chosen to consist of Py with a thickness of 8 nm. ($M_S=860$ kA/m at room temperature, Ref. 143). The standard six-neighbor exchange energy term is taken for the ferromagnetic coupling, and the exchange coefficient is set to its full value for Py (13 pJ/m, Ref. 143). Further energy terms are the demagnetizing energy and the Zeeman energy, which can include both a spatially homogeneous external field of adjustable strength and direction and various dipole fields from magnetic particles. Even though Py does show a small crystalline anisotropy of $K_V = -0.4$ kA/m (Ref. 143), it is not included in this simulation due to its negligible magnitude and the fact that our magnetic layers are polycrystalline. The orange-peel coupling is considered in the simulation by introducing an additional bias

field along the magnetization direction of the pinned magnetic layer (negative x-axis) with a magnitude equal to the pinning field H_P (1.5 kA/m). Figure 81 a) shows the total in-plane magnetization components of the simulated free magnetic layer in dependence on the field strength parallel to the pinning direction. As sketched in Figure 81 b), the magnetization switches through a s-state, which is certainly not the case for the much larger real sensor system that allows formation of actual magnetic domains.

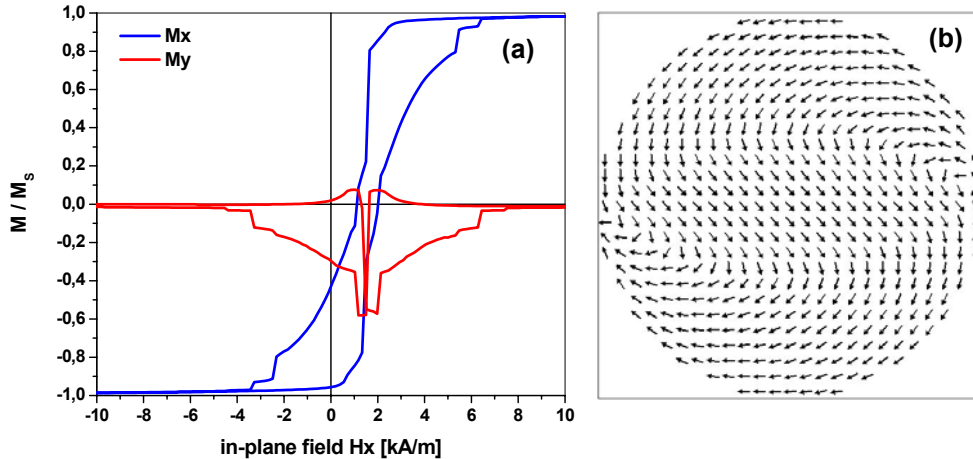


Figure 81: Characteristics of the TMR oommf model system
a) magnetization components
b) magnetization configuration at zero field (at sweep from negative to positive fields)

In order to directly compare the oommf simulations to the experimental data, the magnetization map of the free magnetic layer at every stage of the simulation has to be converted into magnetotransport data. This is done by calculating the relative resistances of all cells of the simulated model system (given by Equation 31) and summing over all individual resistance paths in a parallel circuit configuration. If the pinned magnetic layer stays magnetized homogeneously along the negative x-axis, the total resistance R of a system consisting of a free magnetic layer with N cells relative to the low resistance state R_0 (magnetizations of the free and pinned magnetic layer aligned ferromagnetically) is given by:

$$\frac{R}{R_0} = N \left(\sum_{i=1}^N \frac{1}{1 + \frac{A}{2} \left(1 + \frac{M_x^i}{M} \right)} \right)^{-1} \quad \text{Equation 40}$$

Here, A is the full TMR amplitude normalized to the low resistance state, which is set to 47 % according to chapter 6.3. M_x^i denotes the magnetization component of cell i along the x-axis in a specific free layer magnetization map. The above calculation is carried out for each stage of the simulation, resulting in relative magnetoresistance curves that can be compared to the experimental data. Though mostly similar in shape to curves that simply plot the total x-component of the free layer magnetization, there are magnetization configurations that lead to differences (see Figure 82 a), so the above calculation really is necessary to enable meaningful data comparison. Part b) of Figure 82 shows a minor loop comparison between our simulated system and a real sensor. Due to its reduced size, the simulated system

shows a stronger coercivity and a much larger saturation field, which is related to the different magnetization switching mechanisms (rotation through an s-state for the simulated system and domain formation and propagation for the real sensor device). Therefore, the simulated model system can only be expected to produce qualitative results, since a quantitative agreement would require equal magnetic behavior under all aspects. Still, some features observed for the detection of magnetic markers by real sensors are reproduced by the model system, which is analyzed in detail in the following chapter.

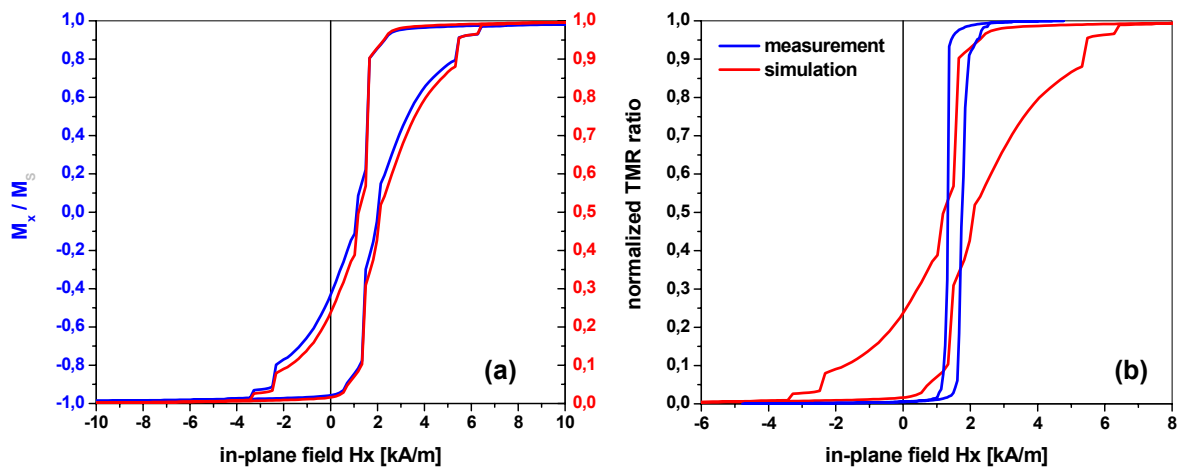


Figure 82: Comparison of the simulated minor loop to the experimental data
 a) relationship of the magnetization of the model system to the calculated resistance
 b) comparison of the simulated and measured normalized minor loops

6.5. Detection of magnetic markers

6.5.1. Perpendicular field method

Analogous to the standard magnetic marker detection method for GMR type sensors (see chapter 5.4), the sensor response is recorded in dependence on the strength of the perpendicular magnetizing field. Additionally, a constant in-plane bias field oriented along the pinning direction can be applied to move the operational point of the TMR sensor relative to the switching field of the free magnetic layer. It is always adjusted starting from the negative saturation field in order to ensure identical magnetic ground states prior to each measurement. Furthermore, the orientation of the perpendicular field is adjusted by minimizing the response of a central uncovered reference element before starting a set of measurements. All data are taken in a two probe geometry at a bias voltage of 10 mV. For higher bias voltages, the maximum TMR ratio decreases due to the energy dependent electronic structure of the ferromagnetic electrodes and magnon excitations (Ref. 209; Ref. 235).

Before coming to the response of the TMR sensor elements to magnetic markers, the signals obtained from uncovered reference sensors are examined. Figure 83 b) shows typical sensor responses to a sweeping perpendicular field at various in-plane bias fields (displayed in Figure 83 a). With increasing bias, the sensor resistance rises due to slight adjustments of the free layer magnetization configuration prior to its switching, but is almost independent of the perpendicular field strength. The difference in the sensor resistance between the scan and rescan is due to a slight induced voltage in the circuit loop, which remains despite a rather long waiting time

period of 200 ms between adjustment of the field strength and recording of the data. As the in-plane bias approaches the switching field of the free magnetic layer, a small magnetic hysteresis feature becomes visible around zero perpendicular field, which most probably arises due to small reversible rotations of some parts of the free layer magnetization out of their local anisotropy directions. Furthermore, a slight linear dependence of the sensor resistance on the perpendicular magnetizing field starts to become visible for in-plane bias fields close to the switching field (see red curve in Figure 83 b). Just like observed for GMR-type sensors, this can be attributed to a slight misalignment of the out-of-plane field, which results in an additional linear contribution for a tilt parallel to the pinning direction (compare to Figure 78).

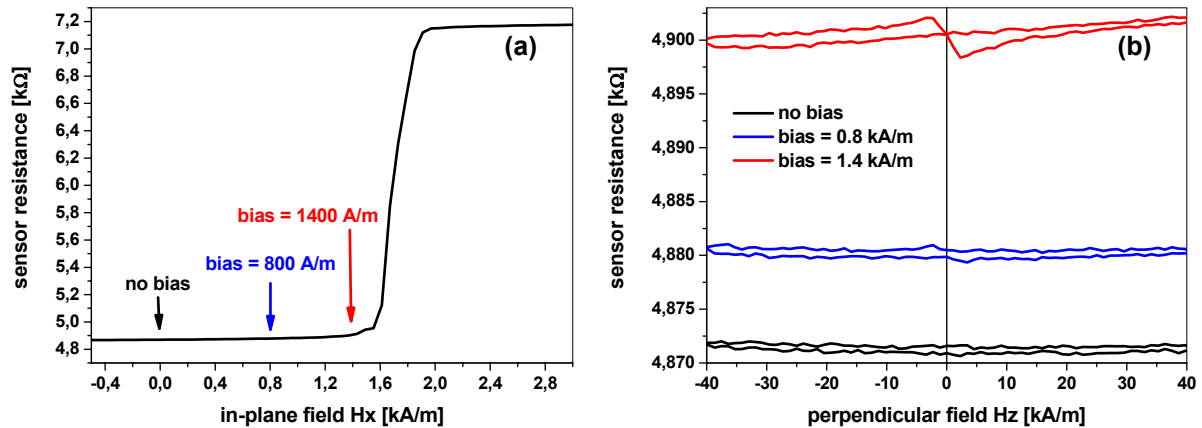


Figure 83: Measured TMR reference sensor signals

a) positions of the applied in-plane bias fields relative to the minor loop

b) sensor response in dependence on the perpendicular field strength for different in-plane bias fields

The response of a sensor element under those conditions is also simulated by our model system. Figure 84 a) shows the resulting magnetoresistance curve in comparison to the experimental data at an in-plane bias field of 800 A/m (TMR normalized to lowest resistance of each set of data). The parabolic shape of the simulated magnetoresistance curve is a consequence of the linear increase of the total magnetization's z-component with increasing perpendicular field strength (see Figure 84 b). Because the magnetization of the pinned magnetic layer is assumed to stay fixed in the simulation, the calculated TMR ratio (according to Equation 40) directly resembles the slight tilt of the free magnetic layer's magnetization induced by the perpendicular field. In reality, however, the magnetization of the pinned layer also follows the perpendicular field, thus reducing the observed parabolic behavior. Since the pinned $\text{Co}_{70}\text{Fe}_{30}$ layer has a larger saturation magnetization than the free Py layer (1650 kA/m (Ref. 237) compared to 860 kA/m (Ref. 143) at room temperature), its perpendicular magnetization component at a certain out-of-plane field is smaller, and a non-zero TMR ratio remains nonetheless. This is checked by a simple Stoner-Wohlfarth (Ref. 239) calculation that assumes a linear increase of the perpendicular magnetization component up to a limiting field given by the saturation magnetization of the respective ferromagnetic material. In each case, the magnetizations are assumed to be oriented perfectly parallel at zero out-of-plane field, and the TMR ratio is calculated according to Equation 31 (with $A = 47\%$) both for rotation of the free layer's magnetization only and for the case that both magnetizations follow the out-of-plane field (see Figure 84 a). As expected, the single layer Stoner-Wohlfarth calculation agrees well to the oommf simulation (differences are due to the non-zero y-component of the free layer magnetization in the oommf simulation), but the

calculation including both ferromagnetic electrodes closely resembles the small remaining parabolic dependence observed for the reference sensor measurements. Thus, the measured reference signals can be understood by a combination of perpendicular magnetization components, a slightly misaligned magnetizing field, parasitic induced voltages by the sweeping magnetic field and some minor local reversible magnetization rotations.

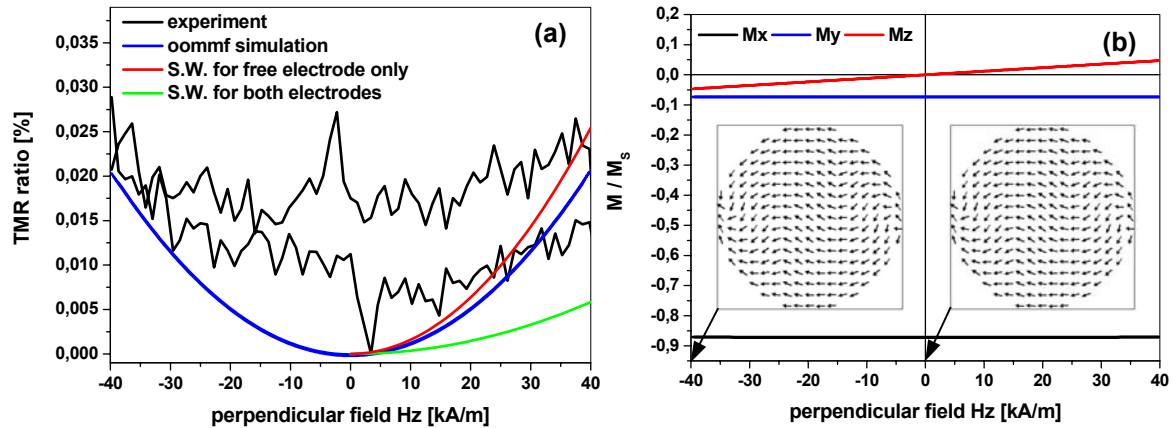


Figure 84: Simulated response to a perpendicular field at an in-plane bias field of 800 A/m
a) comparison of the experimental data to Stoner-Wohlfarth and oomf calculations
b) magnetization components; included maps show the magnetization configuration at the indicated perpendicular field strengths (-40 kA/m and zero).

Neglecting the comparably small bias field, markers on the sensor surface are mostly magnetized out-of-plane by the perpendicular field and produce radially symmetric stray fields round their center positions which cause distortions of the magnetization configuration within the free magnetic layer. With increasing magnetizing field, these distortions become stronger, thus leading to greater local tilts of the magnetization vectors out of their original alignment parallel to the pinned magnetic layer. Thus, the measured sensor resistance should increase with rising magnetizing field. This characteristic is observed for all the curves shown in Figure 85 c), which shows the response of the sensor element displayed in Figure 85 a) to perpendicular magnetizing fields at the various in-plane bias fields indicated in Figure 85 b). As the bias approaches the switching field, the magnetization configuration of the free magnetic layer starts to relax, and correspondingly, the overall resistance rises. Additionally, with the pinning field reduced, the in-plane components of the markers' stray fields cause greater local magnetization adjustments, so a larger relative resistance change is achieved for a given magnetizing field. Because the strength of the stray fields can be approximated to depend linearly on the magnetizing field (compare to chapter 3.2.2.2), the resistance also increases linearly with the magnetizing field for each polarity. Also, the response is symmetric, implying that radial stray fields pointing inward and outward have about the same effect on the original free layer magnetization configuration.

As shown below, it is possible to obtain signals proportional to the marker coverage on a sensor element under these measurement conditions. However, to that end the bias field must be kept well separated from the switching field (about 1650 A/m), because otherwise, irreversible partial switching of the free magnetic layer can be induced by the perpendicular magnetizing field (see the orange curve in Figure 85 d). Because of the instability of this process, it is no longer possible to extract meaningful data from such a curve, as the onset of the switching and also its amplitude are not

related to the surface coverage of magnetic markers. In fact, partial switching is also observed for uncovered reference sensor elements when the bias field is getting too close to the switching point, which is probably also caused by a non-vanishing in-plane component of the perpendicular field due to non-perfect alignment. To prevent these irreversible and hysteretic processes for all elements on an entire sensor without having to readjust the perpendicular field alignment, the bias field must be kept at a distance to the switching field of at least 400 A/m. Under this premise, reversible curves like the ones sketched in Figure 85 c) are obtained which show a total change of resistance proportional to the surface coverage of magnetic markers on each sensor element. However, under those conditions the sensor response is mainly due to the stray field components oriented perpendicular to the pinning direction, since the sensor's reaction to field components parallel to the pinning direction is much smaller at these bias fields (see Figure 78). Therefore, as switching processes have to be avoided, the actually applicable measurement regime of these TMR sensors is given by their characteristics perpendicular to the pinning direction. In contrast to the response to fields applied parallel to the pinning direction, larger saturation fields are required in this geometry, and the TMR amplitude also only reaches a reduced maximum value (compare to chapter 6.3). Thus, the usable sensitivity is greatly reduced compared to the expectations excited by the picture of a TMR loop with the field applied parallel to the pinning direction (more details are given in chapter 1).

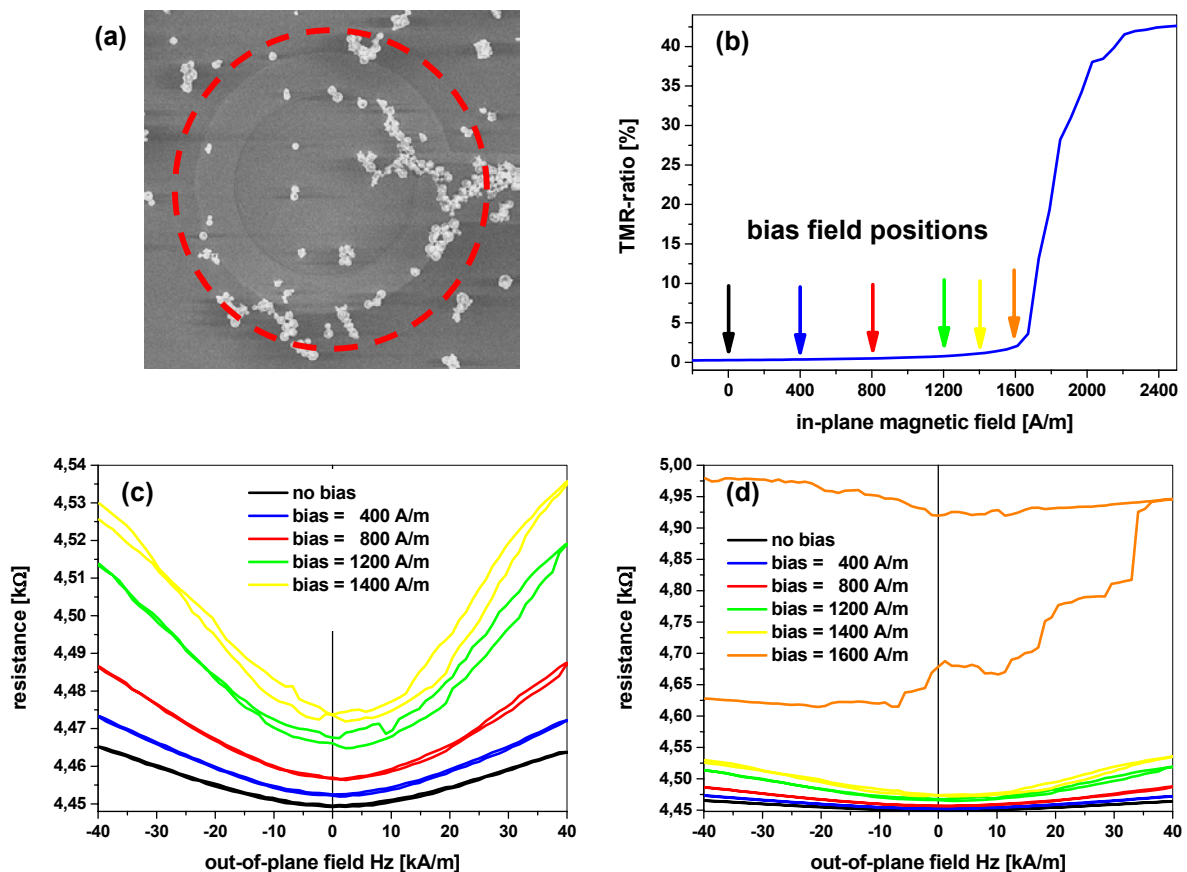


Figure 85: Exemplary response of a TMR sensor element to magnetic markers in the perpendicular geometry
a) sensor element (highlighted by red circle) with an 8% surface coverage of Bangs 0.86 μm microspheres
b) indication of the bias field positions relative to the sensor's minor loop
c)/d) response to a perpendicular field at different bias fields

The same situation is observed for our model system, in which different numbers of Bangs 0.86 μm markers are positioned above the sensor element. They are assumed to be situated in the central area of the sensor, so that the distance between the free magnetic layer and the surface is set to 300 nm (see Figure 76). The magnetic moment of the markers is taken to behave like an ideal dipole with a value of 21 fAm² at a magnetizing field of 40 kA/m (see Table 4). Its strength is approximated to vary linearly with the total field, and it is oriented parallel to the respective magnetic field vector (perpendicular bias field plus in-plane field). Figure 86 shows a comparison between experimental data and simulated results for sensor elements with similar marker coverage (two labels for the simulated system at the positions indicated in the red framed magnetization map). The TMR ratio is normalized to the lowest resistance recorded in each set of data. Just like observed in the respective experiments, there are also two different regimes for the simulated system which can be distinguished by the proximity of the applied bias to the switching field of the free magnetic layer. At sufficient distance, a reversible parabolic resistance increase with applied perpendicular magnetizing field is observed, the magnitude of which is comparable to the experimental data (see Figure 86 a). It originates from local reorientations of the free layer magnetization in the vicinity of the markers due to their dipolar stray fields (compare the magnetization maps with and without markers at maximum magnetizing field shown in Figure 86 a). Whereas the resistance increases linearly with applied magnetizing field in the experimental data at higher field magnitudes, the dependence is purely parabolic throughout the entire range of the magnetizing field for the simulated model system, which corresponds to the situation already observed in the case of GMR type sensors. Again, the reason for this deviation is probably found in the linear approximation of the dependence of the marker's moment on the magnetizing field in the simulated model system (see chapter 5.4.2).

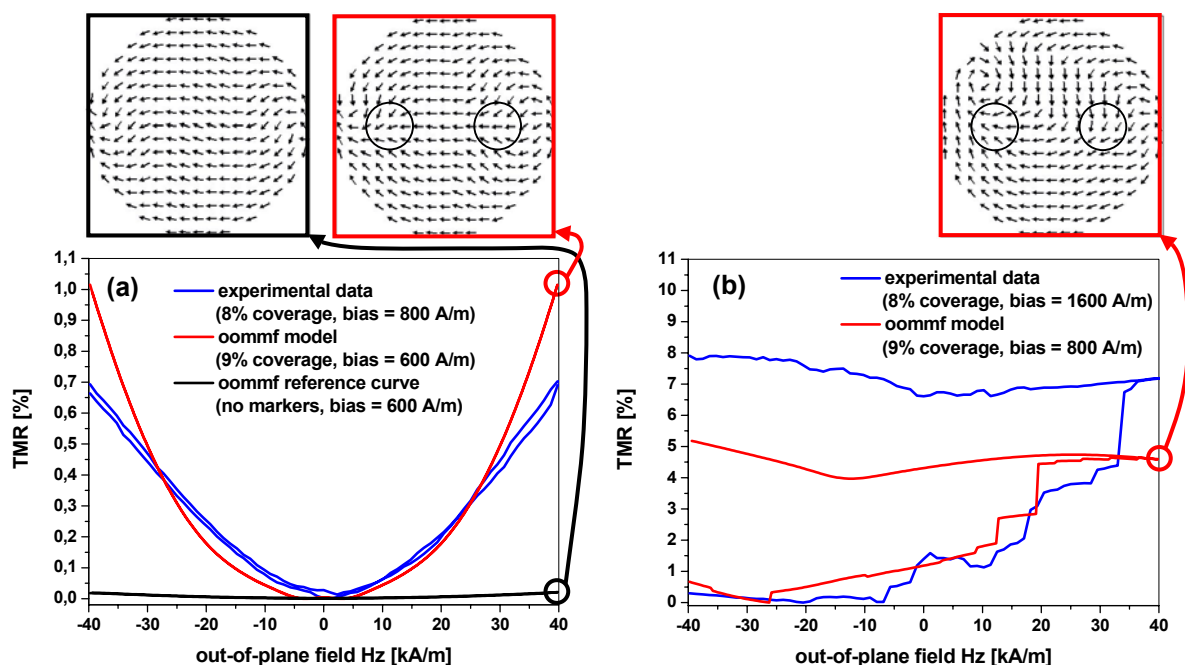


Figure 86: Comparison of simulated and experimental TMR signals at different bias fields
a) reversible regime
b) irreversible partial switching

When the bias approaches the switching field of the free magnetic layer, irreversible partial switching is also induced in the case of the simulated model system (see [Figure 86 b](#)). As magnetization reversal takes place over a much larger field range (compare to chapter 6.4), the onset of irreversible switching is situated at smaller bias fields than for the real sensor system, but other than that, the simulated curve shows characteristics similar to the experimental data. As the magnetizing field is applied perfectly perpendicular in the simulated model system, it is clear that irreproducible switching is in fact stimulated by the presence of magnetic markers and not so much by a possible misalignment of the out-of-plane field. The magnetization map displayed in [Figure 86 b](#)) shows that the free layer starts to switch through a vortex structure in the upper left part of the simulated sensor. This modification is induced by the presence of magnetic markers as an uncovered reference sensor does not display such a partially switched configuration (see [Figure 84 a](#)).

Still, at bias values sufficiently far from the switching field, the output signal of different TMR sensors depends linearly on the surface coverage of magnetic markers. This is shown in [Figure 87 a](#)) for two different values of the in-plane bias field. The magnetic markers (Bangs 0.86 μm microspheres) are directly spotted onto the surface of the sensor. Just like described in chapter 5.4.2, all measured TMR curves are adjusted for a time-dependent linear drift and a linear field-dependent contribution. Thereafter, the maximum TMR value (relative to the lowest recorded resistance of each measurement) is plotted versus the surface coverage of magnetic markers, which is again calculated by the image analysis procedure described in chapter 5.4.2. Uncovered sensor elements only contribute a total TMR ratio smaller than 0.04 % for both bias field values, which is indicated as reference level in [Figure 87 a](#)). Out of the ten different sensor elements, there are two which show a signal inconsistent with the linear dependency shared by the other ones (data points shaded by a striped pattern in [Figure 87 a](#)). These are situated at the very edge of the sensor area, but do not show any vastly different magnetoresistive characteristics or a special arrangement of markers on their surface (like conglomerations at certain positions). Thus, it is hard to tell why they do not comply with the results shared by the majority of sensor elements. In any case, they are excluded in the linear regression to the data, which gives the following results for the two different bias fields:

fitting function: $\text{TMR}(A) = 0.04 \% + c \cdot A$

with A given in % of total marker surface coverage

no bias: $c = 0.0406$

bias = 800 A/m: $c = 0.0880$

Equation 41

The ratio of the two slopes is 2.17. As the reference signal is almost independent of the bias field at this range (see [Figure 83](#)), higher sensitivities are obtained for larger bias fields. This, however, is only true up to the onset of irreversible partial switching, which starts to occur at a bias field of about 1200 A/m for some of the elements on the sensor.

Part b) of [Figure 87](#) shows the response of our oommf model system to different numbers of Bangs 0.86 μm magnetic markers in dependence on the perpendicular magnetizing field. The case of two markers and the reference curve are already familiar from [Figure 86 a](#)), and as expected, the response to a single label lies in between those two curves at maximum magnitude of the magnetizing field (the position of the single label corresponds to the left marker position indicated in the

red-framed magnetization map of Figure 86 a). However, the shape of the single-label curve is quite out of the ordinary, as the response is not symmetric to the polarity of the magnetizing field and has its minimum at +10 kA/m. This is probably attributed to the broken symmetry in this configuration, which causes the magnetization pattern to relax into a different local energetic minimum at zero field. By adding a second marker at the opposite position, the symmetry gets restored. For real small scale sensors, a dependence of the output signal on the actual position of the label has already been observed by simulating the marker's stray field with a MFM tip (Ref. 118). Concerning future single molecule detection schemes, such a behavior has to be avoided, which can be achieved by modifying the sensor design and the detection scheme. For our large scale sensors, however, such effects are not observed due to the larger sensor size and the greater number of markers on its surface.

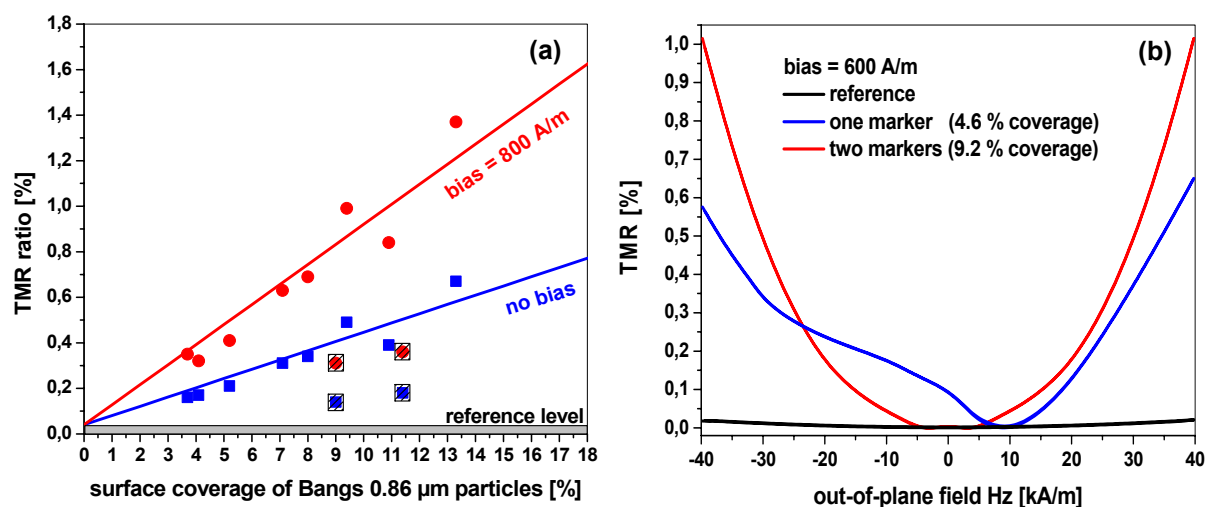


Figure 87: Dependence of the TMR signal on the surface coverage of magnetic markers
 a) experimental data for two different values of the in-plane bias field
 b) oommf simulation for zero, one and two markers on top of the model system

An estimate of the minimum detectable number of Bangs 0.86 μm markers on the surface of a sensor element is obtained by assuming a limiting TMR ratio of 0.08 %, which is twice the maximum reference signal. From the linear regressions to the data, the corresponding surface coverage is shown in line 1 of Table 10. Line 2 displays the respective part of the total sensor area (1963 μm^2) which is covered by markers, while line 3 represents the corresponding number of particles, which is calculated based on the average size of Bangs 0.86 μm markers (see Table 2).

	no bias	bias = 800 A/m
surface coverage [%]	0.98	0.45
surface area [μm^2]	19.2	8.8
number of markers	33	15

Table 10: Estimate of the minimum detectable number of Bangs 0.86 μm markers

6.5.2. Observation of the full free layer hysteresis curve

The difficulties encountered with irreproducible switching for the perpendicular field method make it necessary to put the operational point of the sensor system at a bias

field well apart from the switching field of the free magnetic layer. Thus, the signal obtained from the stray fields of magnetic markers under those conditions is mainly attributed to the sensor response to fields perpendicular to its pinning direction, which is a much less sensitive configuration than for fields applied parallel to the pinning axis (compare to chapter 6.3). To make use of the large resistance difference associated with switching of the free magnetic layer, another type of measurement setup has to be employed. In fact, the stray fields of magnetic markers should influence the shape of the free layer hysteresis curve, provided they possess a sufficient magnetic moment. This is assured by applying a large constant out-of-plane magnetizing field, resulting in radially symmetric stray fields round the markers' center positions within the free magnetic layer. Next, the in-plane minor loop is recorded for different values of the perpendicular magnetizing field. Compared to the method described in the previous chapter, full switching is achieved for every measurement, thus eliminating the irreproducible and uncorrelated partial switching processes induced by the perpendicular field in the prior setup.

Due to the radial symmetry of the markers' stray fields, no global shift of the hysteresis curve is expected for this measurement geometry. Nevertheless, the markers should cause distortions in the magnetization configuration of the free layer, thus requiring stronger in-plane fields to achieve saturation. Therefore, as sketched in Figure 88, the expected signal in this kind of measurement setup would be a shear of the minor loop. For a given marker coverage, the increase of the saturation field should be proportional to the strength of the out-of-plane magnetizing field (see black, blue and red curve). An increase of the marker coverage at a given magnetizing field, however, should leave the saturation field unchanged, since it is only governed by the maximum induced stray field strength. Instead, a higher marker coverage should lead to larger resistance modifications at any field in between the saturation states as a larger portion of the sensor area gets affected by the stray field induced magnetization changes (see green curve in Figure 88). Thus, a possible measurand for determining the surface coverage of magnetic markers on the sensor would be the relative resistance at the saturation field of the reference curve, which is also indicated in Figure 88. Since the markers only possess a negligible moment at the in-plane fields required to record minor loops, it should be possible to use a minor loop with no perpendicular bias applied as an intrinsic reference for each sensor element (whether covered by markers or not), thus eliminating possibly problematic comparisons between properties of different sensor elements.

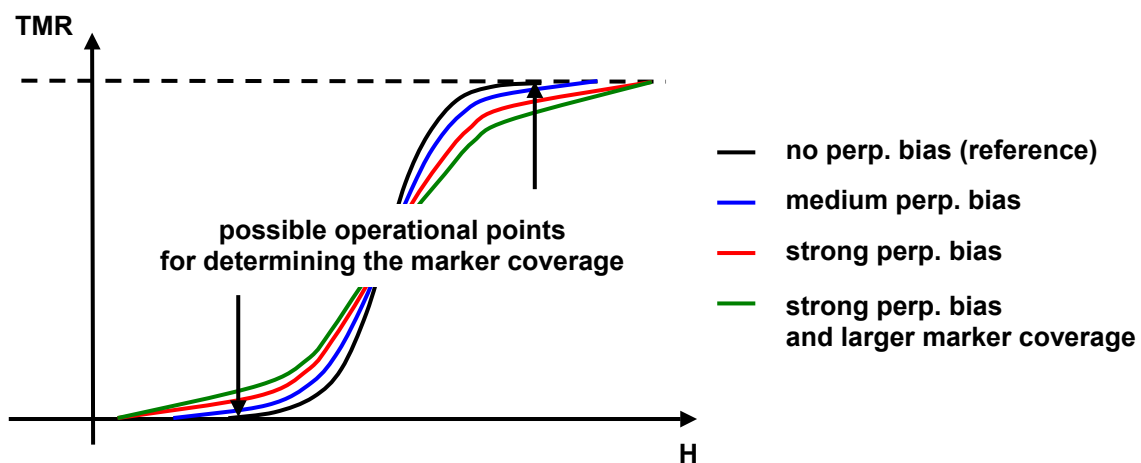


Figure 88: Expected modifications of a minor loop branch under the influence of perpendicularly magnetized magnetic markers

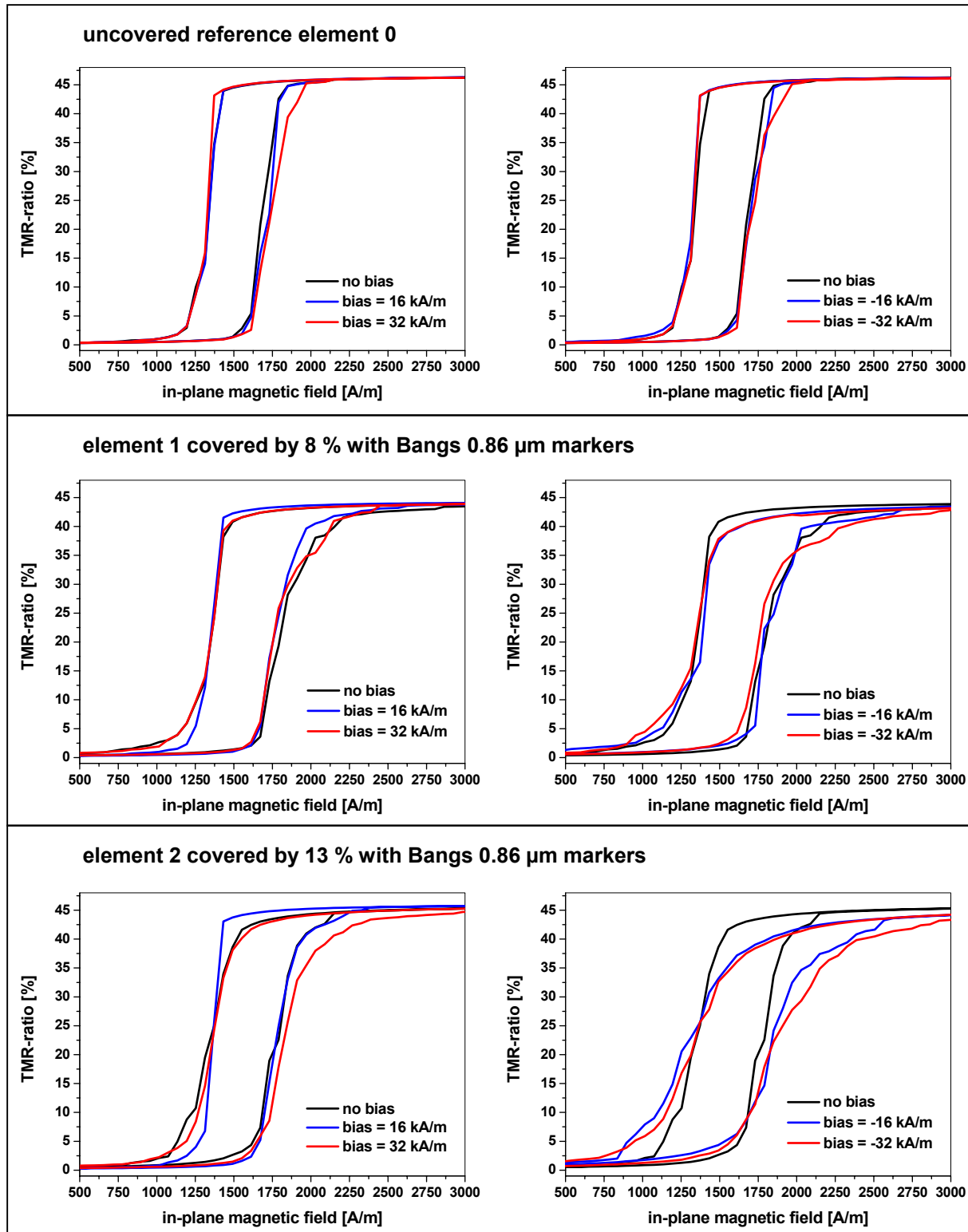


Figure 89: TMR minor loops of different sensor elements with varying perpendicular bias field

Figure 89 displays experimental data for different sensor elements covered by varying concentrations of Bangs 0.86 μm particles under the measurement conditions described above. According to Kerr microscopy on similar samples (not shown here), the switching mechanism for the free magnetic layer is given by the formation and propagation of stripe domains. Clearly, the minor loops of the uncovered reference element are essentially not affected by the presence of a constant perpendicular field, whereas the expected shearing is observed for marker

covered sensor elements (especially visible in the lower right graph). As the strength of the markers' stray fields increases with rising magnitude of the magnetizing field, the saturation field at both ends of the hysteresis loop should also go up. Actually, this correlation is observed in most cases, which corresponds to similar TMR-type measurements on arrays of artificial labels (i.e. ferromagnetic dots, see Ref. 240). Still, there are measurements which are not in agreement (for example element 1 for positive values of the perpendicular magnetizing field). Furthermore, most minor loops depend strongly on the polarity of the perpendicular magnetizing field, which implies different switching behavior of the free magnetic layer for radial stray fields pointing inward and outward. And most importantly, it is impossible to extract a measurand from the data which is clearly correlated to the surface coverage of magnetic markers on the sensor.

The same situation is observed for our model system, in which different numbers of Bangs 0.86 μm markers are positioned above the sensor element. They are assumed to be situated in the central area of the sensor, so that the distance between the free magnetic layer and the surface is set to 300 nm (see Figure 76). The magnetic moment of the markers is taken to behave like an ideal dipole with a value of 21 fAm² at a magnetizing field of 40 kA/m (see Table 4). Its strength is approximated to vary linearly with the total field, and it is oriented parallel to the respective magnetic field vector (perpendicular bias field plus in-plane field). and it is oriented parallel to the respective magnetic field vector (perpendicular bias field plus in-plane field). Unlike for real sensor elements, the magnetization of the free magnetic layer of the model system switches through a double-vortex state. In case of an uncovered reference sensor, the simulated minor loop in the presence of a perpendicular magnetizing field is essentially identical to the one without the out-of-plane field (see blue and black curve in Figure 90). As markers are added on top of the sensor, the field required to saturate the free layer magnetization increases, i.e. the minor loops experience a shear (see red and green curve in Figure 90). This is also visible by looking at the two simulated magnetization maps shown in Figure 90, which display the free magnetic layer at an in-plane field of 7.2 kA/m on the scan from negative to positive fields both for the reference sensor and the sensor with one marker on top (marker position indicated by circle on the second map). While the magnetization is already saturated for the reference sensor, a slight tilt remains in the vicinity of the marker as a consequence of its radially symmetric stray field that points towards the marker's center position.

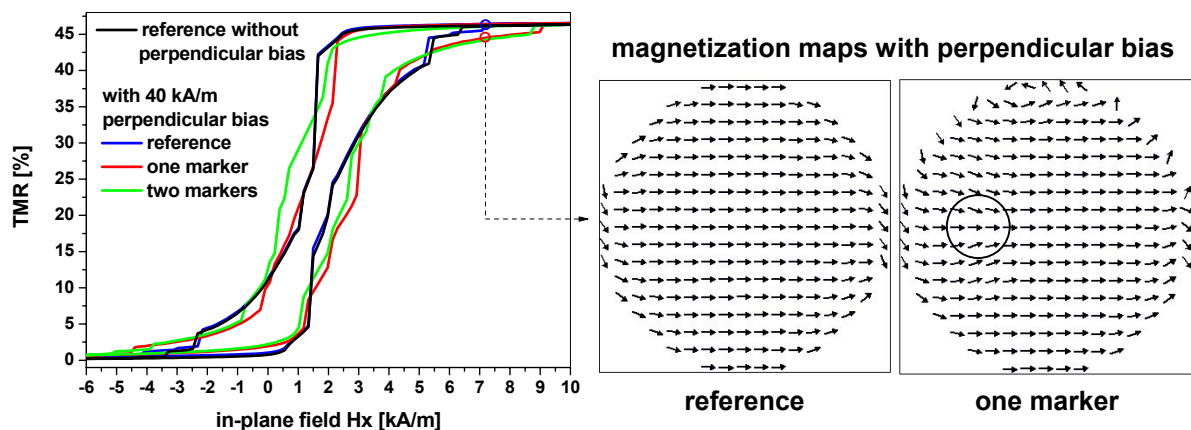


Figure 90: Simulated minor loops of the model system under different conditions

However, just like observed for the real sensor system, the relative resistance at the reference saturation field is not reliably related to the marker surface coverage, nor is any other characteristic feature of the minor loops. The reason for that lies most probably in the natural instability of magnetization switching processes, which are easily affected by minor variations of the initial conditions. These variations are caused by the markers' stray fields, but, at least in the case of a limited number of large labels, it is not necessarily true that a greater number of disturbances automatically leads to continuous variations in the minor loop properties. Instead, magnetization switching is either induced or not, and for that, other factors like the position of the markers on the sensor could to be more important than their actual number. Thus, this measuring setup is not well suited to analyze the abundance of our types of magnetic labels.

6.6. Conclusions

A magnetoresistive sensor on TMR basis is developed which covers a circular area with a diameter of 50 μm . A chip consists of over two hundred individual sensor elements, each of which is capable of detecting one specific DNA sequence. The area of a single sensor element is chosen according to the active area of the GMR type biosensor.

In order to detect magnetic microspheres, different measurement schemes are applied. The only conditions under which signals proportional to the surface coverage of magnetic markers are recorded is the perpendicular magnetizing field method at sufficient distance of the in-plane bias field to the switching field of the free magnetic layer. In this case, a linear dependence of the TMR ratio on the surface coverage of magnetic markers is observed, and a minimum number of about 20 magnetic particles can be detected with this type of sensor.

In order to effectively employ TMR type sensors for the detection of magnetic labels, the sharp switching characteristic of the current design should be replaced by double exchange biased junctions with the pinning directions oriented perpendicular to each other, for example. In such a device, there is no sharp irreversible transition, and the entire magnetoresistance range of the sensor can be employed for the detection of magnetic markers. Currently, this route is followed by colleagues within our research group.

7. Comparison of GMR- and TMR-type magnetic biosensors

As shown in chapter 5.4 and 6.5, both GMR and TMR type magnetic biosensors produce signals which depend linearly on the coverage of magnetic markers on the surface of a sensor element. In this chapter, the response and applicability of both biosensor types is compared.

Figure 91 displays the response of both GMR and TMR based sensor elements to global unidirectional in-plane fields. In part a), the magnetoresistance curves are plotted, whereas part b) shows a comparison of the corresponding sensitivities (i.e. the field derivatives of the magnetoresistance curves). Clearly, the TMR based sensor displays sharp sensitivity peaks of up to 0.3 % resistance change per A/m when the free magnetic layer switches its magnetization direction between parallel and antiparallel alignment to the pinning direction (blue curves). However, as demonstrated in chapter 6.5.1, it is not possible to actually use such a switching process for the detection of magnetic markers in our sensors, so the relevant sensitivity range for TMR type sensors is given more by its response to fields applied perpendicular to the pinning direction (black curves). In this configuration, the maximum sensitivity values are about two orders of magnitude lower (around 3 % per kA/m) and become comparable to the ones obtained for our GMR type sensor systems (red curves).

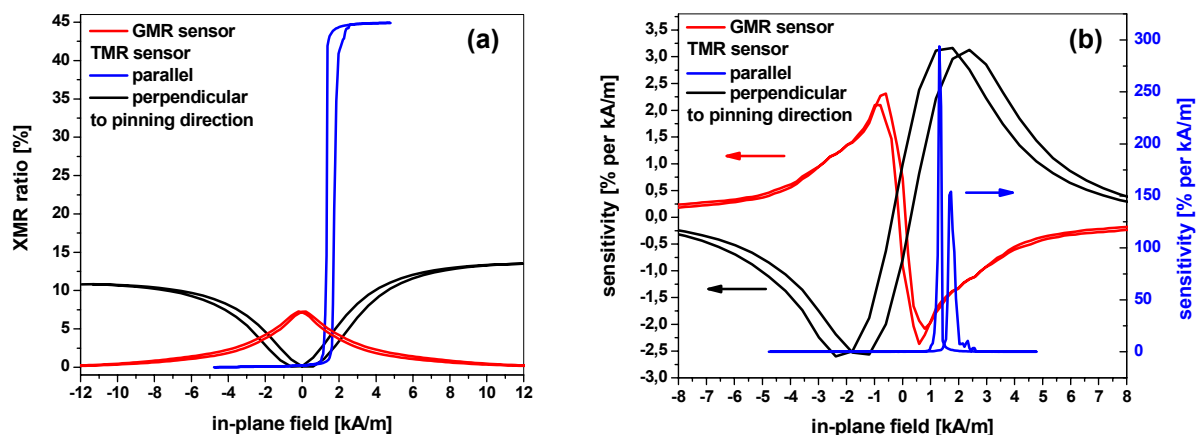


Figure 91: Comparison of the response of TMR and GMR sensor elements to unidirectional global in-plane fields

a) magnetoresistance ratio
b) sensitivity

However, as the TMR type sensors are operated at an in-plane bias field that results in almost maximum sensitivity in the perpendicular field direction (see chapter 6.5.1), their response to magnetic markers is still larger than for GMR type sensors, for which most measurements are taken at zero in-plane bias field due to practical considerations (see chapter 5.4.2). This is demonstrated in Figure 92, which compares the response of exemplary GMR and TMR type sensor elements to an approximately equal surface coverage of Bangs 0.86 μm magnetic markers (the corresponding sensor elements are shown at identical scale in the electron micrographs of Figure 92). Both signal responses are compensated for drift and asymmetry according to the description in chapter 5.4.2 and constructed as differential measurements by subtracting the response of an uncovered reference sensor. The same is true for the displayed reference curves, which show the differential response of two uncovered GMR and TMR type sensor elements,

respectively. The magnetoresistance effects are normalized to the original resistance state at zero perpendicular field for each sensor type. For the TMR type sensor, measurements are taken at an in-plane bias field of 800 A/m (compare to chapter 6.5.1). Due to the smaller total current in the TMR setup, the noise level is slightly higher, resulting in a little larger total reference XMR effect (0.0127 % compared to 0.0075 % for the GMR reference curve). Still, as the magnitude of the TMR sensor response to magnetic markers is about 3.6 times larger than for the GMR sensor, the sensitivity ratio (total signal normalized to the corresponding reference effect) reaches a value of about 32 for the TMR sensor and only approximately 15 for the GMR type sensor at this coverage of magnetic markers. Thus, our TMR sensor design is about twice as sensitive as our GMR type sensor under the applied measurement conditions.

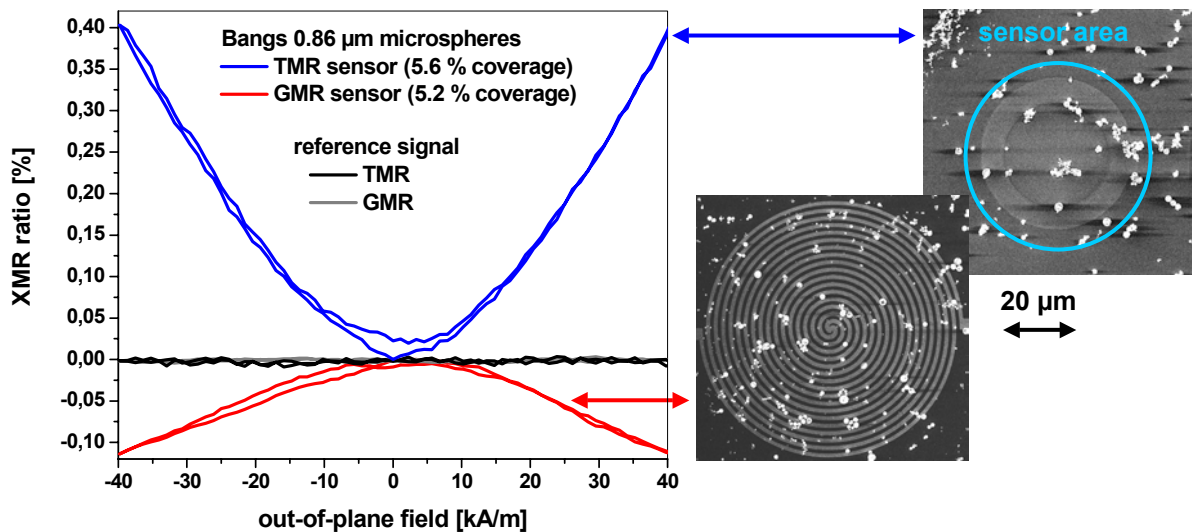


Figure 92: Comparison of the response of TMR and GMR type sensor elements to an approximately equal surface coverage of Bangs 0.86 μm magnetic microspheres

Still, due to the limitations of the applicable measurement regime (see chapter 6.5), our TMR type sensors are not that much more sensitive as implied by the huge sensitivity to global in-plane fields parallel to the pinning direction (see Figure 91). As GMR type sensors are much easier to fabricate, allow the application of higher currents, are more robust to harsh environmental conditions and effectively show a comparable sensitivity, they are chosen as the most prominent sensor type for gene expression type experiments, which require the simultaneous large scale detection of different DNA sequences at relatively high concentrations well beyond the single molecule regime. Here, the required sensor size is of the order of a typical probe DNA spot, which can be realized easily by suitable GMR type sensor designs, and corresponding molecular detection experiments are described in chapter 1.

While GMR type sensors are best applied for large scale molecular detection experiments, TMR sensors can be used for the detection of single molecules, which presents the ultimate objective both for medical and biotechnological applications as well as fundamental research. For magnetic biosensors, the goal of single molecule detection corresponds to the requirement of resolving the presence of single magnetic markers. This can be accomplished by shrinking the size of the sensor to the dimensions of the relevant labels (Ref. 109), i.e. to the sub- μm size scale. In this regime, it becomes increasingly demanding to build GMR type sensors with sufficient resistivity to allow an easy readout of the signals, which is due to the highly

conductive all-metallic structure of this sensor type and the resulting low resistance. Contrary, the resistance of TMR type sensors increases with decreasing area of the tunneling barrier, and elements with a resistance in the $k\Omega$ range have been demonstrated at sub- μm length scales for MRAM applications ([Ref. 241](#)). Thus, an ideal type of magnetic biosensor would consist of an array of small TMR sensor elements which give a logical yes/no type of output signal, depending on whether a single magnetic marker is present at the surface or not. By combining such sensors with small ferromagnetic labels in an in-plane sensing geometry (see chapter 3.3), it would be possible to actually use the large signals obtained from the switching of the free magnetic layer in single-pinned TMR junctions to generate this type of logical output signal. Combined with on-chip manipulation of molecules via magnetic gradient fields applied to their labels, such a system presents a very promising path towards the control of single molecules.

8. DNA-detection and comparison to fluorescent method

8.1. Outline of the experiment

In order to test the capability of our magnetoresistive biosensor, a comparison experiment with standard fluorescent DNA detection is carried out. Important questions in this respect are the biological sensitivity to small amounts of DNA and the dynamic range of the sensor, i.e. the difference in DNA concentration between a minimum detectable signal and saturation of the sensor.

To ensure a meaningful comparison, both the magnetoresistive sensor and the fluorescent chip have to be treated as identical as possible. Due to the better suitability for the detection of bulk amounts of DNA, our GMR-type magnetoresistive biosensor is employed. As fluorescent chip, a standard glass slide from TeleChem (Ref. 242) is used and coated with the same polymer layer as the magnetoresistive sensor (see chapter 4.2). Thus, the active surfaces of both devices are identical.

In a standard application, the concentration of probe DNA is chosen to be very large, so that little amounts of analyte DNA molecules find as many hybridization sites as possible. However, to test our sensor system it is more convenient to vary the concentration of the probe DNA on the chip down to small numbers and keep the concentration of the analyte DNA at a constant high level. In contrary to the standard method, such a procedure allows the simultaneous detection of various DNA concentrations of the same test sequence with only one sensor chip. Apart from being less intricate, it also enhances the comparability, since variations in the properties of different sensor chips or slightly varying binding and hybridization conditions are excluded.

Different concentrations of double stranded PCR-amplified DNA sequences with a length of 1 kb are used as specific probe, while the unspecific probe consists of double stranded salmon sperm DNA of the same length in a single but much larger concentration (see Table 11). In this experiment, the probe DNA spots are deposited onto the surface with a hand-held precision pipette. The total volume per spot is 0.2 μ l, and it disperses to spot diameters of about 1 mm. The resulting total number of probe DNA strands within each spot is calculated from the molar mass of double stranded 1 kb DNA (about 660 kg/mol; Ref. 150). Assuming a homogeneous distribution within the spot, the number of probe DNA strands on the surface of a single sensor element of the magnetoresistive chip is calculated by comparing its surface area with the DNA spot size.

	concentration	molarity	# DNA-strands per spot	# DNA-strands per sensor element
specific spot A	10 ng/ μ l	15 nM	1.9e9	9.1e6
specific spot B	2.0 ng/ μ l	3.0 nM	3.7e8	1.8e6
specific spot C	400 pg/ μ l	600 pM	7.3e7	3.6e5
specific spot D	80 pg/ μ l	120 pM	1.5e7	7.3e4
specific spot E	16 pg/ μ l	24 pM	3.1e6	1.5e4
unspecific spot F	100 ng/ μ l	150 nM	1.9e10	9.1e7

Table 11: Probe DNA concentrations employed in the comparison experiment

After deposition of the spots onto the surface, the probe DNA is immobilized and remaining coupling sites are inactivated according to the procedure described in chapter 4.2. In the next step, single stranded biotin-labeled (5' and internal) analyte DNA complementary to the specific probe DNA is hybridized at a concentration of 10 ng/ μ l by incubation in a 35 % formamide solution including detergents (0.2 % SDS,

0.1 % Sarkosyl, 0.05 % Tween 20) at 42°C for 12 hours. Subsequently, non-hybridized analyte DNA is removed by washing.

Only at this stage, as the markers are being added, the magneto-resistive biosensor and the fluorescent chip are treated differently. In the case of the magneto-resistive biosensor, streptavidin-coated Bangs 0.35 µm microspheres are bound to the biotin-labeled analyte DNA in a neutral solution at a mass concentration of 1 % for one hour at 37°C. Afterwards, unspecifically bound magnetic markers are washed away. For the fluorescence chip, Cy3 streptavidin markers are coupled to the biotin-labeled analyte DNA.

8.2. Comparison of the signals

The fluorescence of bound Cy3 markers on the glass chip is measured with a commercial laser scanner (Scan Array 4000, Perkin Elmer). Its sensitivity is adjusted to almost saturation for the highest specific DNA concentration, and the resulting images are shown in Figure 93. The fluorescence of each spot is taken relative to the average intensity of the unspecific DNA spots. For every specific probe DNA concentration, the average relative fluorescence of 7-8 spots and the corresponding standard deviation are calculated, the results of which are also displayed in Figure 93.

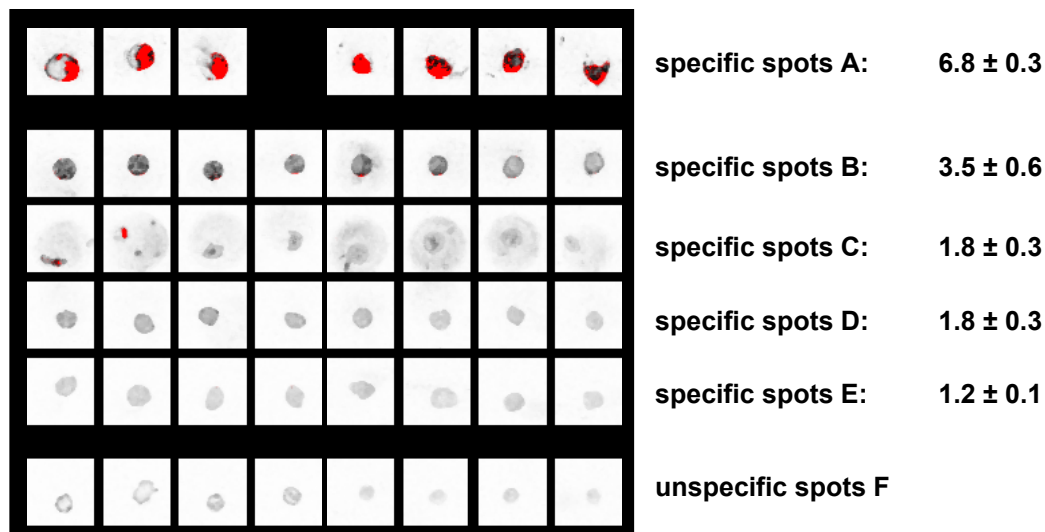


Figure 93: Fluorescent images from the glass chip and average intensities relative to unspecific average signals

The situation for the magneto-resistive biosensor is illustrated in Figure 94. The probe DNA spots are targeted over the rows of sensor elements, and each spot covers at least 2-3 sensor elements which are situated in central spot regions. Those sensor elements are chosen for measurement and contacted via Au-wire-bonding (Figure 94 a/b). The surface coverage of magnetic markers (white dots) is vastly different for specific and unspecific probe DNA spots. For example, it reaches 18 % for the sensor element underneath specific spot C (Figure 94 c), but only 0.2 % for the sensor element below the unspecific probe DNA spot of very large concentration (Figure 94 d). The unspecific marker coverage is identical to the background outside of the probe DNA spots. Some sensor elements in those regions are also contacted for reference purposes. Since no completely uncovered regions are present on the chip, these sensor elements determine the reference signal.

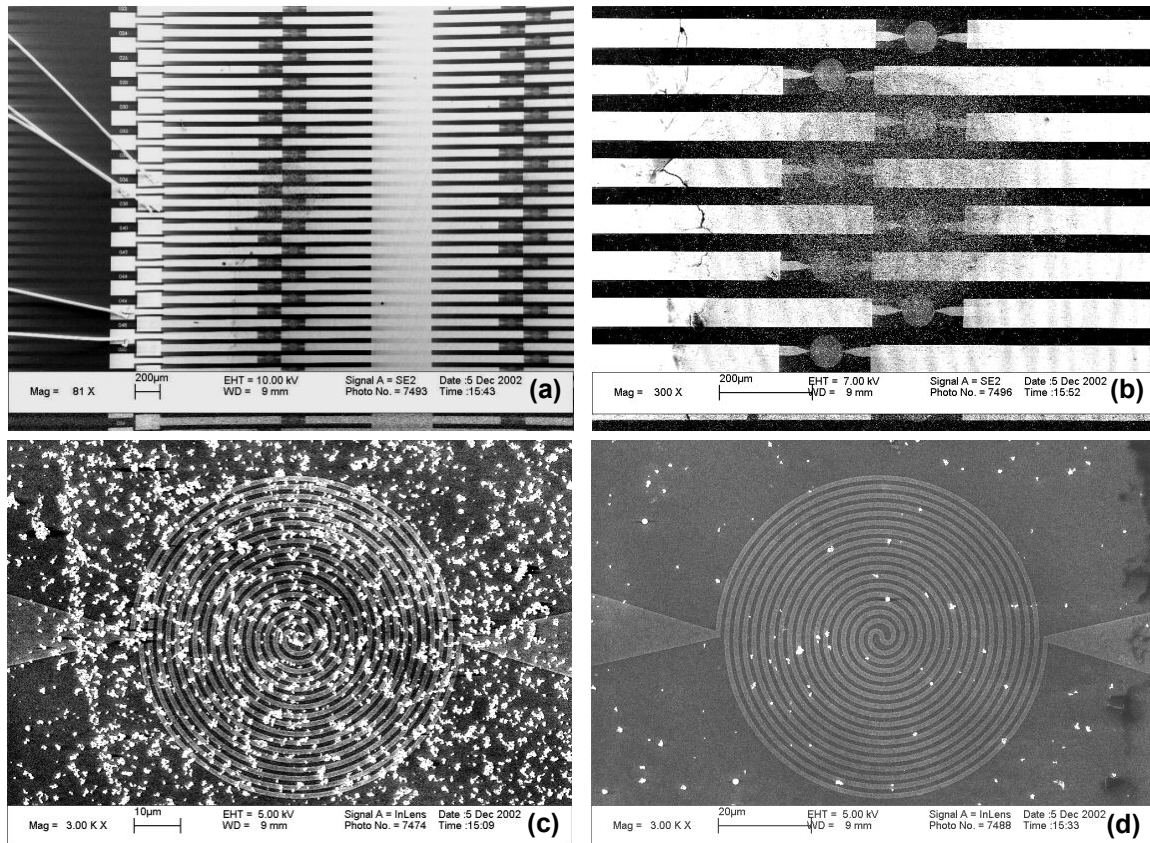


Figure 94: Magneto-resistive biosensor after binding of magnetic markers
a) overview
b) close-up of specific spot B
c) sensor element covered by specific spot C
d) sensor element covered by unspecific spot F

For each sensor element, the dependence of the output signal of the differential amplifier on the perpendicular magnetizing is taken relative to a reference sensor element with the setup described in chapter 2.8. As explained in chapter 5.4.3, a single value is obtained from this set of data by taking the maximum output signal difference. Just like shown before, the original differential data is compensated for drift and asymmetry before calculating the maximum output signal difference. These measurements and calculations are carried out six times for all contacted sensor elements. Since at least two different sensor elements belong to the same probe DNA concentration, the effective signal for each probe DNA concentration is the average of no less than 12 different measurements. Additionally, the standard deviation is calculated from the difference of the individual measurements to the average signal for each probe DNA concentration.

In order to compare the data from the magneto-resistive biosensor to the fluorescent detection method, the average signals of each probe DNA concentration are normalized to the average signal of the unspecific probe DNA sensor elements. Along with the data from the fluorescent chip and the corresponding standard deviations, those relative sensitivities are plotted over the corresponding probe DNA concentration in Figure 95. Apparently, both methods are sensitive to the whole range of probe DNA concentration, ranging from 16 pg/ μ l to 10 ng/ μ l, i.e. almost over a range of three orders of magnitude. At the high concentration region, both sensor types are saturated, whereas the sensitivity at the lower end is limited by unspecific signals. However, in the case of the magnetic biosensor, the density of bound

markers within unspecific probe DNA spots is the same as in regions outside of the DNA spots. Contrary to that, there is some additional background signal within the unspecific probe DNA spots in the case of fluorescent detection, which decreases the relative sensitivity. Therefore, in this experiment the sensitivity of the magnetic biosensor is superior to fluorescent detection at low probe DNA concentrations, for example by a factor of 2.7 at 600 pg/ μ l.

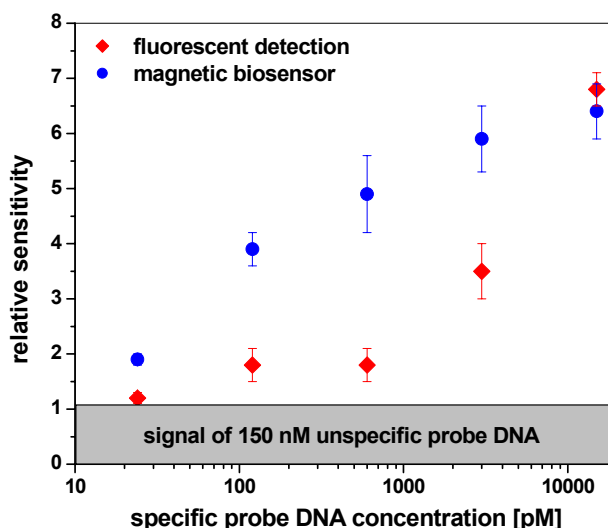


Figure 95: Relative sensitivities of the magneto-resistive biosensor and the fluorescent chip

Table 12 displays the total efficiency of analyte DNA hybridization and marker binding to immobilized probe DNA. At each concentration, the value is calculated from the average total marker coverage on the respective sensor elements (analyzed by SEM image analysis, see chapter 5.4.2), the average size of the employed markers (see Table 2), and the estimated number of probe DNA strands (see Table 11). At the lowest specific DNA concentration, a total binding efficiency of about 13 % is reached at the described circumstances of incubation time etc. This percentage could be improved by employing a piezo-spotter for more homogenous probe DNA spots and by using smaller markers to reduce steric problems. With increasing probe DNA concentration, the fraction of successful binding becomes smaller, as the marker coverage is getting closer to saturation. Because the marker coverage for spots A and B is already almost identical, saturation of marker binding is reached in the probe DNA concentration range from 0.6-3.0 nM.

	marker coverage [%]	# of markers per sensor	binding efficiency [%]
specific spot A	43.0	17200	0.19
specific spot B	42.7	16920	0,94
specific spot C	23.4	9360	2,60
specific spot D	13.3	5320	7,29
specific spot E	4.9	1960	12,8
unspecific spot F	0.2	80	0,000088

Table 12: Binding efficiency of analyte DNA and markers at the different probe DNA concentrations

The stationary marker surface coverage at higher probe DNA concentrations is one reason for the saturation of the magnetic biosensor's sensitivity observed in Figure 95. However, Figure 96 shows that also the dependence of the total output signal on the surface coverage of DNA-bound magnetic markers deviates from the straight line

observed for direct placement of markers onto the sensor elements (see chapter 5.4.3). Contrary to this previous set of data, the signals from markers that are immobilized to the surface by specific binding to the analyte DNA's biotin groups already saturate at medium surface coverage. The fitting of a straight line (red line in Figure 96) has been replaced by an asymptotic growth fitting function for the dependence of the output signal sig on the marker surface coverage A (values in %) according to:

$$\text{sig}(A) = 30\text{mV} + a(1 - e^{-A/b}) \quad \text{Equation 42}$$

Like before when linear fitting was applied, the constant level of 30 mV corresponds to the reference output at zero coverage. For $b > 0$, the fitting function of Equation 42 results in an asymptotic level of $30\text{mV} + a$ for $A \rightarrow \infty$. Its application to the data for bound markers gives the following values of the fitted parameters a and b (corresponding function shown as blue curve in Figure 96):

$$a = 218 \text{ mV} \quad \leftrightarrow \quad b = 15.8 \%$$

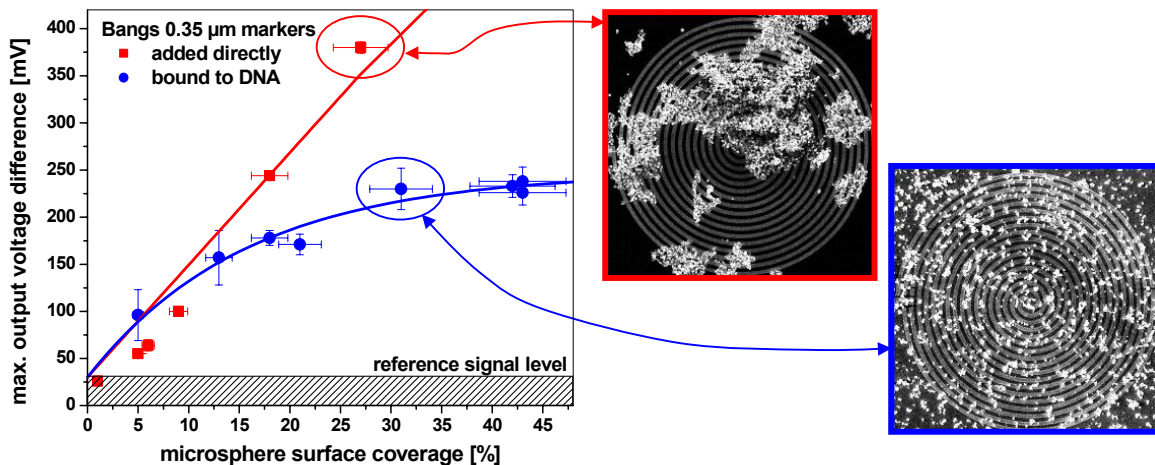


Figure 96: Comparison of the absolute differential signals of the magnetic biosensor to the measurements obtained previously for directly added magnetic markers

Saturation of the sensor signal at a sufficient surface coverage of magnetic markers is a natural and expected feature which is attributed to partial stray field compensation as the spheres of influence of adjacent markers start to overlap (see chapter 3.2.2.2). However, the question remains why this behavior is not observed in the investigated coverage range when magnetic markers are directly put on top of the magnetoresistive sensor. A comparison of the exemplary electron microscope images displayed in Figure 96 shows that the distribution of markers in the two cases is vastly different. While they are distributed evenly as single labels or small clusters when coupled to analyte DNA, they tend to form large localized batches when spotted directly onto the sensor. If they were forming a monolayer in these batches, the resulting signal should be even smaller than the one observed for DNA-coupled markers, as stray field overlapping would play an important role in that case. However, as the measured signal is much larger, the only conclusion is that the batches actually consist of more or less intense piles of markers which possess an increased magnetic moment density comparable to larger markers (see for example the signals of the larger Bangs 0.86 μm particles in Figure 65). In the red-framed

image displayed in [Figure 96](#), this can actually be seen from the varying electron backscattering intensities, which translate into differing ‘layer’ thicknesses of markers at different spots within the batches. Still, the presented image is only an extreme case, and most of the other sensor elements from the data sets displayed in [Figure 65](#) show a more uniform marker distribution. In fact, the signals obtained from the Chemagen particles (red data in [Figure 65](#)) could also be interpreted in terms of an asymptotic growth function, so this behavior is also detectable for markers that are directly dropped onto the surface. In particular, no significant piling of any marker type can be observed for smaller coverage values by SEM analysis, which can also be seen by the good agreement of the initial slopes of the two fitting curves displayed in [Figure 96](#). Thus, while the actual sensor response curves are best accessed by specifically binding the markers to the surface, the analysis carried out in [chapter 5.4.3](#) remains valid nonetheless.

In order to estimate the onset of sensor saturation and explain the form of the asymptotic growth function, a simple 1dim model is assumed in which the average in-plane stray field magnitude in between two markers (Bangs 0.35 μm type) is calculated for varying distance between them according to [Equation 2](#) with $d = 415$ nm (see [Table 5](#)). In [Figure 97 a](#)), the individual stray fields (black and blue curves) and their sum (red curves) are shown for two different spacings between them (magnetic moments pointing downwards with a value of 0.75 fAm^2 , see [Table 4](#)). Due to symmetry, the sum is always zero in the middle between the markers. However, the average magnitude strongly depends on their spacing, which is shown in [Figure 97 b](#)). For each distance D between the markers, the average field magnitude H_{av} in between is calculated according to:

$$H_{\text{av}}(D) = \frac{1}{D} \int_0^D dx |H(x) + H(D-x)| \quad \text{Equation 43}$$

The summation is carried out with the help of a MATLABTM program for the two stepsize values dx indicated in [Figure 97 b](#)). The respective results show the same dependence and only differ within the shaded area, which marks forbidden values with D smaller than the microsphere diameter. Thus, the stepsize is chosen small enough to guarantee numerical accuracy. H_{av} shows a minimum for $D = 0.47 \mu\text{m}$, which is also one of the two configurations displayed in [Figure 97 a](#)). In this case, a large proportion of the distance between the microspheres is affected by stray field compensation as there are three different points at which cancellation takes place. Increasing the separation from the minimum at $D = 0.47 \mu\text{m}$ results in larger average field magnitudes up to a maximum at $D = 1.20 \mu\text{m}$ as their mutual interference decreases and the sum approaches the form of two independent particles (see the other case displayed in [Figure 97 a](#)). From there on, H_{av} decreases again with increasing separation due to the growing proportion of almost unaffected space in between.

On the grounds of this model, sensor saturation should be expected at an average distance between the markers of $1.20 \mu\text{m}$, and the response should even decrease at higher loadings. Assuming a regular hexagonal arrangement of the labels on the sensor (see inset of [Figure 97 b](#)), a total number of three markers with radius r would be situated in a hexagonal unit cell with base length R , resulting in an absolute surface coverage A_{abs} of:

$$A_{\text{abs}} = \frac{2\pi}{\sqrt{3}} \left(\frac{r}{R} \right)^2$$

Equation 44

Taking the distance with maximum average field magnitude in the 1dim model as an approximation for the respective base length in the 2dim hexagonal arrangement, saturation should already be reached at a surface coverage of 7.7 % within this description ($r = 0.175 \mu\text{m}$ and $R = 1.20 \mu\text{m}$). Clearly, this is not the case even for markers specifically bound to DNA, for which saturation is reached around 40 % coverage (see Figure 96). This is a little less than half the maximum absolute coverage of about 91 % for closely packed spheres in an hexagonal configuration (i.e. $R = 2r$ in Equation 44). Furthermore, the implied decrease of the sensor signal for coverages higher than the saturation state is also not observed, the reason of which is probably found in the large size distribution of the real particles. Anyhow, it is clear that a description which only relies on the in-plane stray field magnitudes is not sufficient to explain the observed asymptotic growth function. Because the model does not take into account the reaction of the sensor to the induced stray fields, this may not be too surprising. Effectively, a meaningful description has to include micromagnetic modeling of the sensor, which has been presented in chapter 1 and 1.

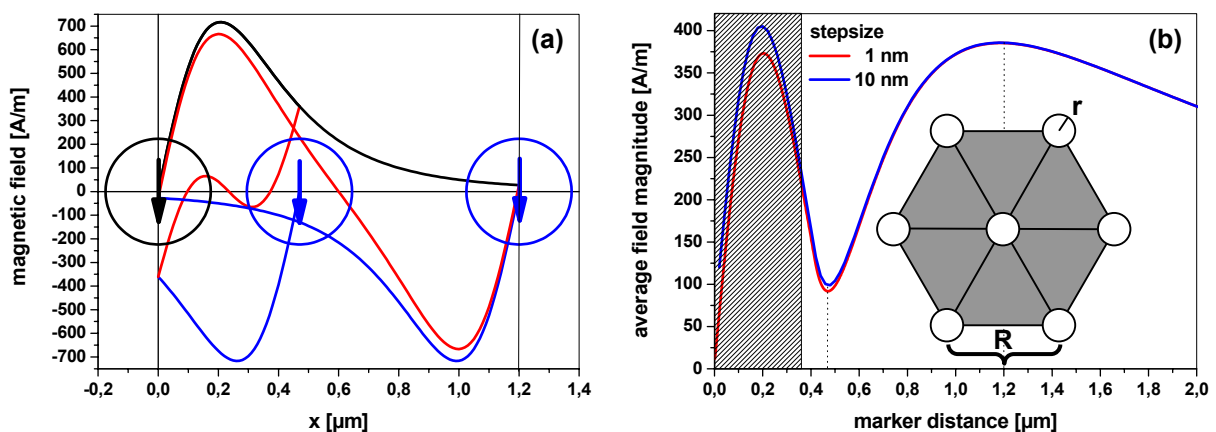


Figure 97: Effective in-plane stray field components in between two Bangs $0.35 \mu\text{m}$ markers
a) Absolute stray fields for a marker positioned at the origin (black curve) and another one further down the x-axis (two positions shown, blue curves). The markers' magnetizations and their positions (to scale) are also shown. The red curves indicate the sum of both stray fields in between the markers.

b) Integrated average stray field magnitude in between two markers as a function of spacing. The shaded area marks the minimum distance (markers are touching), and the inset visualizes the marker coverage at maximum stray field magnitude.

9. Summery and Outlook

In the future, easy-to-use portable lab-on-a-chip devices are expected to take over many of today's standard laboratory tasks in biomedicine and even open up completely new fields of application. For those systems, a molecular detection unit is required that is sensitive, versatile but easily automated and also integrable with standard CMOS technology. These requirements are hardly met by traditional molecular detection methods like fluorescence, but by combining magnetic labels with magnetoresistive sensing technology, it is possible to fulfill those conditions and even go beyond them. In this thesis, a possible approach towards that end is demonstrated, and the signals from various magnetic biosensor types are investigated in detail for the first time.

A summary of the necessary properties of magnetic labels for magnetoresistive biosensor applications is presented. Those requirements are mostly met by commercially available magnetic microspheres, which were initially introduced to separate desired molecules from an arbitrary bulk solution. Different types of microspheres are investigated concerning their molecular recognition to surface-immobilized labeled DNA, which leads to the conclusion that smaller particles are better suitable in this respect. Furthermore, the magnetic properties of different microsphere types are analyzed. Though smaller particles do produce less magnetic moments, their overall stray field efficiency is still comparable to larger markers as more labels fit onto a given sensor area. Here, we identify and evaluate the essential measurands and come to the conclusion that it is advantageous to use smaller markers due to their better binding capabilities at surfaces. Even though superparamagnetic microspheres are a good starting point, they do not yet represent the most ideal labels thinkable for magnetic biosensor applications. These could be ferromagnetic nanoparticles, the potentials of which are also discussed briefly.

Another crucial part of a successful magnetoresistive biosensor is its interface to the biological solutions. It has to guarantee reliable protection of the sensors at a minimum thickness for maximum sensitivity. At the same time, tight immobilization of large amounts of probe DNA strands has to be assured. In this work, we developed a novel SiO₂ / polymer bilayer with unrivaled thinness that gives consistent protection and proves to be superior to a plain glass surface in terms of probe DNA immobilization.

With regard to the actual magnetoresistive sensor, numerous designs based both on GMR and TMR are fabricated, characterized and tested with respect to their response to different types of magnetic labels. For the first time, the relevant signals are analyzed systematically under various conditions, and the results are strengthened qualitatively by micromagnetic simulations based on the oommf simulation code. Under suitable measurement conditions, both sensor types exhibit a response that depends linearly on the surface coverage of magnetic labels, which guarantees their usability as detectors of the abundance of label-bound analyte DNA in biosensor applications. For higher coverage levels, saturation of the sensor signals is observed and discussed within a stray field based model.

Furthermore, the two different sensor types are compared with respect to their sensitivity and applicability. As the possible measurement regime of the presented TMR sensor type is limited to reversible processes that prevent hysteretic behavior of the free magnetic layer, its actual sensitivity for the detection of magnetic labels is comparable to GMR type sensors. Since GMR type sensors are also more robust and easier to fabricate, they are chosen as the most prominent sensor type for the detection of relatively high concentrations of different DNA sequences, which

requires large-area sensors with sizes comparable to typical probe DNA spots. Contrary, due to their better scalability, TMR sensors are best employed for single molecule type experiments that require sensor areas in the range of the size of the employed magnetic labels.

In this work, we are also the first to present a comparative DNA detection analysis of our GMR type magnetic biosensor to a standard fluorescent detection method. In order to ensure maximum comparability, the procedures for both sensor types are carried out identically up to the addition of the relevant labels. As a result, both biosensor types are sensitive to the whole employed DNA concentration range (almost 3 orders of magnitude from 24 pM to 15 nM), with the signals limited by sensor saturation at the upper end and by sensitivity restrictions at the lower end. Still, the background signal for unspecific reference sequences is much smaller for the magnetic biosensor, resulting in a better sensitivity at low DNA concentrations. Thus, in addition to its intrinsic advantage of easy integration into portable devices and the compatibility with standard CMOS processing, magnetic biosensors can also compete with respect to biological sensitivity. Therefore, they are an ideal candidate for the detection units of future lab-on-a-chip devices.

Another advantage of magnetic biosensors is the possibility to manipulate molecules by applying forces onto their magnetic labels. These forces can be generated as magnetic gradient fields by on-chip current lines, which is especially important with respect to single molecule detection as transport by diffusion is no longer a practical option at those dilutions. By combining small TMR sensor elements in a dense MRAM-type arrangement with magnetic nanoparticles as labels and on-chip manipulation, a universal magnetic biochip could be realized that would be programmable to perform many different tasks. Currently, scientists from our research group are moving towards this vision.

Bibliography

Ref. 1: Ruderman, M.A., Kittel, C., 1954. Indirect Exchange Coupling of Nuclear Magnetic Moments by Conduction Electrons. *Physical Review Letters*, 96, 99-102

Ref. 2: Kasuya, T., 1956. A theory of metallic ferromagnetism and antiferromagnetism on zeners model. *Progress of Theoretical Physics*, 16, 45-57

Ref. 3: Yosida, K., 1957. Magnetic Properties of Cu-Mn Alloys. *Physical Review Letters*, 106, 893-898

Ref. 4: Grünberg, P., Schreiber, R., Pang, Y., Brodsky, M.B., Sowers, H., 1986. Layered magnetic structures: Evidence of antiferromagnetic coupling of Fe layers across Cr interlayers. *Physical Review Letters*, 57, 2442-2445

Ref. 5: Baibich, M.N., Broto, J.M., Fert, A., Van Dau, F.N., Petroff, F., Eitenne, P., Creuzet, G., Friedrich, A., Chazelas, J., 1988. Giant Magnetoresistance of (001)Fe/(001)Cr Magnetic Superlattices. *Physical Review Letters*, 61, 2472-2475

Ref. 6: Julliere, M., 1975. Tunneling between ferromagnetic films. *Physics Letters A*, 54 (3), 225-226

Ref. 7: Moodera, J.S., Kinder L.R., Wong T.M., Meservey, R., 1995. Large Magnetoresistance at Room Temperature in Ferromagnetic Thin Film Tunnel Junctions. *Physical Review Letters*, 74, 3273–3276

Ref. 8: Parkin, S.S.P., 1998. The magic of magnetic multilayers. *IBM Journal of Research and Development*, 42 (1), 3-6

Ref. 9: See for example the website of the Robert Bosch GmbH, www.bosch.de

Ref. 10: Prinz, G.A., 1999. Magnetoelectronics applications. *Journal of Magnetism and Magnetic Materials*, 200, 57-68

Ref. 11: Miller, M.M., Prinz, G.A., Lubitz, P., Hoines, L., Krebs, J.J., Cheng, S.F., Parsons, F.G., 1997. Novel absolute linear displacement sensor utilizing giant magnetoresistance elements. *Journal of Applied Physics*, 81 (8), 4284-4286

Ref. 12: Motorola Inc., press release, October 2003, www.motorola.com/mediacenter/news/detail/0,,3158_2591_23,00.html

Ref. 13: Black, Jr., W.C., Bodhisattva, D., 2000. Programmable logic using giant-magnetoresistance and spin-dependent tunneling devices (invited). *Journal of Applied Physics*, 87, 6674-6679

Ref. 14: Richter, R., Boeve, H., Bär, L., Bangert, J., Rupp, G., Reiss, G., Wecker, J., 2002. Field programmable spin-logic realized with tunnelling-magneto resistance devices. *Solid-State Electronics*, 46, 639-643

Ref. 15: Baselt, D.R., Lee, G.U., Natesan, M., Metzger, S.W., Sheehan, P.E., Colton, R.J., 1998. A biosensor based on magnetoresistive technology. *Biosensors & Bioelectronics*, 13, 731-739

Ref. 16: Edelstein, R.L., Tamanaha, C.R., Sheehan, P.E., Miller, M.M., Baselt, D.R., Whitman, L.J., Colton, R.J., 2000. The BARC biosensor applied to the detection of biological warfare agents. *Biosensors & Bioelectronics*, 14, 805-813

Ref. 17: Kricka, L.J., 2001. Microchips, microarrays, biochips and nanochips: personal laboratories for the 21st century. *Clinica Chimica Acta* 307, 219-223

- Ref. 18: Figeys, D., Pinto, D., 2000. Lab-on-a-chip: A revolution in biological and medical sciences. *Analytical Chemistry* 72 (9), 330A-335A**
- Ref. 19: Wang, J., 2000. From DNA biosensors to gene chips. *Nucleic Acid Research* 28 (16), 3011-3016**
- Ref. 20: Krishnan, M., Namasivayam, V., Lin, R., Pal, R., Burns, M.A., 2001. Microfabricated reaction and separation systems. *Current Opinion in Biotechnology*, 12, 92-98**
- Ref. 21: Thorsen, T., Maerkl, S.J., Quake, S.R., 2002. Microfluidic large-scale integration. *Science*, 298, 580-584**
- Ref. 22: Lagally, E.T., Simpson, P.C., Mathies, R.A., 2000. Monolithic integrated microfluidic DNA amplification and capillary electrophoresis analysis system. *Sensors and Actuators B*, 63, 138-146**
- Ref. 23: Anderson, R.C., Su, X., Bogdan, G.J., Fenton, J., 2000. A miniature integrated device for automated multistep genetic assays. *Nucleic Acids Research*, 28 (12), e60**
- Ref. 24: Gerion, D., Parak, W.J., Williams, S.C., Zanchet, D., Micheel, C.M., Alivisatos, A.P., 2002. Sorting fluorescent nanocrystals with DNA. *Journal of the American Chemical Society*, 124, 7070-7074**
- Ref. 25: Images taken from the homepage of Dr. Edward K. Wagner, <http://darwin.bio.uci.edu/~faculty/wagner/index.html>**
- Ref. 26: Agilent Technologies, www.agilent.com**
- Ref. 27: Affymetrix Inc., www.affymetrix.com**
- Ref. 28: Nanogen, Inc., www.nanogen.com**
- Ref. 29: Richter, A., Schwager, C., Hentze, S., Ansorge, W., Hentze, M. W. Muckenthaler, M., 2002. Comparison of fluorescent tag DNA labeling methods used for expression analysis by DNA microarrays. *Biotechniques*, 33, 620-630**
- Ref. 30: Alexa Fluor™ is a registered trademark of Molecular Probes Inc., www.probes.com**
- Ref. 31: CyDye™ fluorescent dyes are trademarks of Amersham Biosciences Corp., www.amershambiosciences.com**
- Ref. 32: Laser scanning confocal microscopy webpage, Olympus Corp., www.olympusconfocal.com/theory/fluorophoresintro.html**
- Ref. 33: Tyagi S, Kramer FR, 1996. Molecular beacons: Probes that fluoresce upon hybridization. *Nature Biotechnology*, 14, 303-308**
- Ref. 34: Stryer, L., 1978. Fluorescent energy transfer as a spectroscopic ruler. *Annual Review of Biochemistry*, 47, 819-846**
- Ref. 35: Steemers, F.J., Ferguson, J.A., Walt, D.R., 2000. Screening unlabeled DNA targets with randomly ordered fiber-optic gene arrays. *Nature Biotechnology*, 18, 91-94**
- Ref. 36: Efros, A.L., Rosen, M., 2000. The electronic structure of semiconductor nanocrystals. *Annual Review of Material Science*, 30, 475-521**
- Ref. 37: Moriarty, P., 2001. Nanostructured materials. *Reports on Progress in Physics*, 64, 297-381**

- Ref. 38: Parak, W.P., Gerion D., Pellegrino, T., Zanchet, D., Micheel, C., Williams, S.C., Boudreau, R., A Le Gros, M., Larabell, C.A., Alivisatos, A.P., 2003. Biological applications of colloidal nanocrystals. *Nanotechnology*, 14, R15-R27**
- Ref. 39: Hacia, J.G., 1999. Resequencing and mutational analysis using oligonucleotide microarrays. *Nature Genetics*, 21, Supplement 1, 42-47**
- Ref. 40: Lipshutz, R.J., Fodor, S.P.A., Gingeras, T.R., Lockhart, D.J., 1999. High density synthetic oligonucleotide arrays. *Nature Genetics*, 21, Supplement 1, 20-24**
- Ref. 41: Duggan, D.J., Bittner, M., Chen, Y., Meltzer, P., Trent, J.M., 1999. Expression profiling using cDNA microarrays. *Nature Genetics*, 21, Supplement 1, 10-14**
- Ref. 42: Ferguson, J.A., Boles, T.C., Adams, C.P., Walt, D.R., 1996. A fiber-optic DNA biosensor microarray for the analysis of gene expression. *Nature Biotechnology*, 14, 1681-1684**
- Ref. 43: Ferguson, J.A., Steemers, F.J., Walt, D.R., 2000. High-density fiber-optic DNA random microsphere array. *Analytical Chemistry* 72, 5618-5624**
- Ref. 44: Epstein, J.R., Walt, D.R., 2003. Fluorescence-based fibre optic arrays: a universal platform for sensing. *Chemical Society Reviews*, 32, 203-214**
- Ref. 45: Epstein, J.R., Lee, M., Walt, D.R., 2002. High-density fiber-optic genosensor microsphere array capable of zeptomole detection limits. *Analytical Chemistry* 74, 1836-1840**
- Ref. 46: Taton, T.A., Mucic, R.C., Mirkin, C.A., Letsinger, R.L., 2000. The DNA-mediated formation of supramolecular mono- and multilayered nanoparticle structures. *Journal of the American Chemical Society*, 122, 6305-6306**
- Ref. 47: Bao, P., Frutos, A.G., Greef, C., Lahiri, J., Muller, U., Peterson, T.C., Warden, L., Xie, X.Y., 2002. High-sensitivity detection of DNA hybridization on microarrays using resonance light scattering. *Analytical Chemistry*, 74, 1792-1797**
- Ref. 48: Kreibig, U., Vollmer, M., 1995. *Optical properties of metal clusters*. Springer Verlag, Berlin**
- Ref. 49: Reichert, J., Csaki, A., Kohler, J.M., Fritzsche, W., 2000. Chip-based optical detection of DNA hybridization by means of nanobead labeling. *Analytical Chemistry*, 72, 6025-6029**
- Ref. 50: Taton, T.A., Mirkin, C.A., Letsinger, R.L., 2000. Scanometric DNA array detection with nanoparticle probes. *Science*, 289, 1757-1760**
- Ref. 51: Fritzsche, W., Taton, T.A., 2003. Metal nanoparticles as labels for heterogeneous, chip-based DNA detection. *Nanotechnology*, 14, R63-R73**
- Ref. 52: Taton, T.A., Lu, G., Mirkin, C.A., 2001. Two-color labeling of oligonucleotide arrays via size-selective scattering of nanoparticle probes. *Journal of the American Chemical Society*, 123, 5164-5165**
- Ref. 53: He, L., Musick, M.D., Nicewarner, S.R., Salinas, F.G., Benkovic, S.J., Natan, M.J., Keating, C.D., 2000. Colloidal Au-enhanced surface plasmon resonance for ultrasensitive detection of DNA hybridization. *Journal of the American Chemical Society*, 122, 9071-9077**
- Ref. 54: Dequaire, M., Degrand, C., Limoges, B., 2000. An electrochemical metalloimmunoassay based on a colloidal gold label. *Analytical Chemistry*, 72, 5521-5528**
- Ref. 55: Nanosphere Inc., www.nanosphere-inc.com**

- Ref. 56: Invitrogen GmbH, www.invitrogen.com
- Ref. 57: Wang, J., Cai, X.H., Rivas, G., Shiraishi, H., 1996. Stripping potentiometric transduction of DNA hybridization processes. *Analytica Chimica Acta*, 326, 141-147
- Ref. 58: Ito, K., Hashimoto, K., Ishimori, Y., 1994. Novel DNA sensor for electrochemical gene detection. *Analytica Chimica Acta*, 286, 219
- Ref. 59: Millan, K.M., Saraullo, A., Mikkelsen, S.R., 1994. Voltametric DNA biosensor for cystic fibrosis based on a carbon paste electrode. *Analytica Chimica Acta*, 66, 2943-2948
- Ref. 60: Caruana, D.J., Heller, A., 1999. Enzyme-amplified amperometric detection of hybridization and of a single base pair mutation in an 18-Base oligonucleotide on a 7 μ m-diameter microelectrode. *Journal of the American Chemical Society*, 121, 769-774
- Ref. 61: Motorola Life Sciences, www.motorola.com/lifesciences
- Ref. 62: Umek, R.M., Lin, S.W., Vielmetter, J., Terbrueggen, R.H., Irvine, B., Yu, C.J., Kayyem, J.F., Yowanto, H., Blackburn, G.F., Farkas, D.H., Chen, Y.P., 2001. Electronic detection of nucleic acids - a versatile platform for molecular diagnostics. *Journal of Molecular Diagnostics*, 3, 74-84
- Ref. 63: Campas, M., Katakis, I., 2004. DNA biochip arraying, detection and amplification strategies. *Trends in Analytical Chemistry*, 23, 49-62
- Ref. 64: Wang, J., 1985. *Stripping analysis: principles, instrumentation and applications*. VCH Publishers, Deerfield Beach, Florida
- Ref. 65: Wang, J., Xu, D.K., Kawde, A.N., Polsky, R., 2001. Metal nanoparticle-based electrochemical stripping potentiometric detection of DNA hybridization. *Analytical Chemistry*, 73, 5576-5581
- Ref. 66: Alfonta, L., Katz, E., Willner, I., 2000. Sensing of acetylcholine by a tricomponent-enzyme layered electrode using faradaic impedance spectroscopy, cyclic voltammetry, and microgravimetric quartz crystal microbalance transduction methods. *Analytical Chemistry*, 72, 927-935
- Ref. 67: Patolsky, F., Lichtenstein, A., Willner, I., 2003. Highly sensitive amplified electronic detection of DNA by biocatalyzed precipitation of an insoluble product onto electrodes. *Chemistry – A European Journal*, 9, 1137-1145
- Ref. 68: Alberts, B., Bray, D., Lewis, J., Raff, M., Roberts, K., Watson, J.D., 1989. *Molecular biology of the cell*. Garland Publishing, Inc., New York & London
- Ref. 69: Salin, H., Vujasinovic, T., Mazurie, A., Maitrejean, S., Menini, C., Mallet, J., Dumas, S., 2002. A novel sensitive microarray approach for differential screening using probes labelled with two different radioelements. *Nucleic Acids Research*, 30, e17
- Ref. 70: Smith, D.W., *Molecular Biology Course BIMM 100, University of California at San Diego*, <http://www-biology.ucsd.edu/classes/bimm100.FA00/02.PhysMap1.html#B2>
- Ref. 71: Bernard, K., Auphan, N., Granjeaud, S., Victorero, G., Schmitt-Verhulst, A.M., Jordan, B.R., Nguyen, C., 1996. Multiplex messenger assay: Simultaneous, quantitative measurement of expression of many genes in the context of T cell activation. *Nucleic Acids Research*, 24, 1435-1442

- Ref. 72: Bertucci, F., Bernard, K., Loriol, B., Chang, Y.C., Granjeaud, S., Birnbaum, D., Nguyen, C., Peck, K., Jordan, B.R., 1999. Sensitivity issues in DNA array-based expression measurements and performance of nylon microarrays for small samples. *Human Molecular Genetics*, 8, 1715-1722**
- Ref. 73: Sauerbrey, G., 1959. Verwendung von Schwingquarzen zur Wägung dünner Schichten und zur Mikrowägung. *Zeitschrift für Physik*, 155, 206-222**
- Ref. 74: Janshoff, A., Dr., Galla, H.J., Steinem, C., 2000. Piezoelectric mass-sensing devices – an alternative to optical biosensors?. *Angewandte Chemie International Edition*, 39, 4004-4032**
- Ref. 75: Wang, J., Nielsen, P.E., Jiang, M., Cai, X.H., Fernandes, J.R., Grant, D.H., Ozsoz, M., Beglieter, A., Mowat, M., 1997. Mismatch sensitive hybridization detection by peptide nucleic acids immobilized on a quartz crystal microbalance. *Analytical Chemistry*, 69, 5200-5202**
- Ref. 76: Bardea, A., Dagan, A., Ben-Dov, I., Amit, B., Willner, I., 1998. Amplified microgravimetric quartz crystal-microbalance analyses of oligonucleotide complexes: a route to a Tay-Sachs biosensor device. *Chemical Communications*, 7, 839-840**
- Ref. 77: Tatsuma, T., Watanabe, Y., Oyama, N., Kitakizaki, K., Haba, M., 1999. Multichannel quartz crystal microbalance. *Analytical Chemistry*, 71, 3632-3636**
- Ref. 78: Katz, E., Willner, I., 2003. Probing biomolecular interactions at conductive and semiconductive surfaces by impedance spectroscopy: Routes to impedimetric immunosensors, DNA-Sensors, and enzyme biosensors. *Electroanalysis*, 15, 913-947**
- Ref. 79: Souteyrand, E., Cloarec, J.P., Martin, J.R., Wilson, C., Lawrence, I., Mikkelsen, S., Lawrence, M.F., 1997. Direct detection of the hybridization of synthetic homo-oligomer DNA sequences by field effect. *Journal of Physical Chemistry B*, 101, 2980-2885**
- Ref. 80: Berney, H., West, J., Haefele, E., Alderman, J., Lane, W., Collins, J.K., 2000. A DNA diagnostic biosensor: development, characterisation and performance. *Sensors and Actuators B*, 68, 100-108**
- Ref. 81: Dzyadevych, S.V., Soldatkin, A.P., Korpan, Y.I., Arkhypova, V.N., El'skaya, A.V., Chovelon, J.M., Martelet, C., Jaffrezic-Renault, N., 2003. Biosensors based on enzyme field-effect transistors for determination of some substrates and inhibitors. *Analytical and Bioanalytical Chemistry*, 377, 496-506**
- Ref. 82: Lippa, P.B., Sokoll, L.J., Chan, D.W., 2001. Immunosensors - principles and applications to clinical chemistry. *Clinica Chimica Acta*, 314, 1-26**
- Ref. 83: Fritz, J., Cooper, E.B., Gaudet, S., Sorger, P.K., Manalis, S.R., 2002. Electronic detection of DNA by its intrinsic molecular charge. *Proceedings of the National Academy of Sciences of the USA*, 99, 14142-14146**
- Ref. 84: Steiner, G., 2004. Surface plasmon resonance imaging. *Analytical and Bioanalytical Chemistry*, 379, 328-331**
- Ref. 85: Steiner, G., Sablinskas, V., Hubner, A., Kuhne, C., Salzer, R., 1999. Surface plasmon resonance imaging of microstructured monolayers. *Journal of Molecular Structure*, 509, 265-273**
- Ref. 86: Homola, J., 2003. Present and future of surface plasmon resonance biosensors. *Analytical and Bioanalytical Chemistry*, 377, 528-539**

Ref. 87: Bassil, N., Maillart, E., Canva, M., Levy, Y., Millot, M.C., Pissard, S., Narwa, W., Goossens, M., 2003. One hundred spots parallel monitoring of DNA interactions by SPR imaging of polymer-functionalized surfaces applied to the detection of cystic fibrosis mutations. *Sensors and Actuators B*, 94, 313-323

Ref. 88: IBIS Technologies BV, The Netherlands, www.ibis-spr.nl

Ref. 89: GWC Technologies Inc., USA, www.gwcinstruments.com

Ref. 90: Nelson, B.P., Grimsrud, T.E., Liles, M.R., Goodman, R.M., Corn, R.M., 2001. Surface plasmon resonance imaging measurements of DNA and RNA hybridization adsorption onto DNA microarrays. *Analytical Chemistry*, 73, 1-7

Ref. 91: He, L., Musick, M.D., Nicewarner, S.R., Salinas, F.G., Benkovic, S.J., Natan, M.J., Keating, C.D., 2000. Colloidal Au-enhanced surface plasmon resonance for ultrasensitive detection of DNA hybridization. *Journal of the American Chemical Society*, 122, 9071-9077

Ref. 92: Wang, J., Cai, X.H., Rivas, G., Shiraishi, H., Dontha, N., 1997. Nucleic-acid immobilization, recognition and detection at chronopotentiometric DNA chips. *Biosensors and Bioelectronics*, 12, 587-599

Ref. 93: Wang, J., Rivas, G., Fernandes, J.R., Paz, J.L.L., Jiang, M., Waymire, R., 1998. Indicator-free electrochemical DNA hybridization biosensor. *Analytica Acta Chimica*, 375, 197-203

Ref. 94: Wang, J., 1999. Towards genelectronics: Electrochemical biosensing of DNA hybridization. *Chemistry - A European Journal*, 5, 1681-1685

Ref. 95: Koehne, J., Chen, H., Li, J., Cassell, A.M., Ye, Q., Ng, H.T., Han, J., Meyyappan, M., 2003. Ultrasensitive label-free DNA analysis using an electronic chip based on carbon nanotube nanoelectrode arrays. *Nanotechnology*, 14, 1239-1245

Ref. 96: Dynal Biotech, www.dynal.no

Ref. 97: Larsson, K., Kriz, K., Kriz, D., 1999. Magnetic transducers in biosensors and bioassays. *Analisis*, 27, 617-621

Ref. 98: Kriz, C.B., Radevik, K., Kriz, D., 1996. Magnetic permeability measurements in bioanalysis and biosensors. *Analytical Chemistry*, 68, 1966-1970

Ref. 99: Matz, H., Drung, D., Hartwig, S., Gross, H., Kotitz, R., Muller, W., Vass, A., Weitschies, W., Trahms, L., 1998. A SQUID measurement system for immunoassays. *Applied Superconductivity*, 6, 577-583

Ref. 100: Chemla, Y.R., Crossman, H.L., Poon, Y., McDermott, R., Stevens, R., Alper, M.D., Clarke, J., 2000. Ultrasensitive magnetic biosensor for homogeneous immunoassay. *Proceedings of the National Academy of Sciences of the USA*, 97, 14268-14272

Ref. 101: Besse, P.A., Boero, G., Demierre, M., Pott, V., Popovic, R., 2002. Detection of a single magnetic microbead using a miniaturized silicon Hall sensor. *Applied Physics Letters*, 80, 4199-4201

Ref. 102: Ejsing, L., Hansen, M.F., Menon, A.K., Ferreira, H.A., Graham, D.L., Freitas, P.P., 2004. Planar Hall effect sensor for magnetic micro- and nanobead detection. *Applied Physics Letters*, 84, 4729-4731

Ref. 103: Mohri, K., Uchiyama, T., Panina, L.V., 1997. Recent advances of micro magnetic sensors and sensing application. *Sensors and Actuators A*, 59, 1-8

Ref. 104: Kurlyandskaya, G.V., Sanchez, M.L., Hernando, B., Prida, V.M., Gorria, P., Tejedor, M., 2003. Giant-magnetoimpedance-based sensitive element as a model for biosensors. *Applied Physics Letters*, 82, 3053-3055

Ref. 105: Bethke, C., Yakabchuk, H., Tarasenko, V., Hammer, H., Kisker, E., Koppers, E., Christoph, S., Zirwes, R., Muller, J., 2003. Detection of superparamagnetic markers with GMI-sensors. *Technisches Messen*, 70, 574-576

Ref. 106: Miller, M.M., Sheehan, P.E., Edelstein, R.L., Tamanaha, C.R., Zhong, L., Bounnak, S., Whitman, L.J., Colton, R.J., 2001. A DNA array sensor utilizing magnetic microbeads and magnetoresistive detection. *Journal of Magnetism and Magnetic Materials*, 225, 138-144

Ref. 107: Tamanaha, C.R., Whitman, L.J., 2004. Magnetic labeling and detection of biomolecules. *Encyclopedia of Materials: Science and Technology*, Elsevier, Amsterdam

Ref. 108: Rife, J.C., Miller, M.M., Sheehan, P.E., Tamanaha, C.R., Tondra, M., Whitman LJ, 2003. Design and performance of GMR sensors for the detection of magnetic microbeads in biosensors. *Sensors and Actuators A*, 107, 209-218

Ref. 109: Tondra, M., Porter, M., Lipert, R.J., 1999. Model for detection of immobilized superparamagnetic nanosphere assays labels using giant magnetoresistive sensors. *Journal of Vacuum Science and Technology A*, 18 (4), 1125-1129

Ref. 110: Graham, D.L., Ferreira, H., Bernardo, J., Freitas, P.P., Cabral, J.M.S., 2002. Single magnetic microsphere placement and detection on-chip using current line designs with integrated spin valve sensors: Biotechnological applications. *Journal of Applied Physics*, 91 (10), 7786-7788

Ref. 111: Lagae, L., Wirix-Speetjens, R., Das, J., Graham, D., Ferreira, H., Freitas, P.P.F., Borghs, G., De Boeck, J., 2002. On-chip manipulation and magnetization assessment of magnetic bead ensembles by integrated spin-valve sensors. *Journal of Applied Physics*, 91 (10), 7445-7447

Ref. 112: Ferreira, H.A., Graham, D.L., Freitas, P.P., Cabral, J.M.S., 2003. Biodetection using magnetically labeled biomolecules and arrays of spin valve sensors (invited). *Journal of Applied Physics*, 93, 7281-7286

Ref. 113: Graham, D.L., Ferreira, H.A., Freitas, P.P., Cabral, J.M.S., 2003. High sensitivity detection of molecular recognition using magnetically labelled biomolecules and magnetoresistive sensors. *Biosensors and Bioelectronics*, 18, 483-488

Ref. 114: Li, G.X., Joshi, V., White, R.L., Wang, S.X., Kemp, J.T., Webb, C., Davis, R.W., Sun, S.H., 2003. Detection of single micron-sized magnetic bead and magnetic nanoparticles using spin valve sensors for biological applications. *Journal of Applied Physics*, 93, 7557-7559

Ref. 115: Li, G.X., Wang, S.X., 2003. Analytical and micromagnetic modeling for detection of a single magnetic microbead or nanobead by spin valve sensors. *IEEE Transactions on Magnetics*, 39, 3313-3315

Ref. 116: Kim, H.J., Jang, S.H., Oh, K.H., Kim, T.S., Kim, K.Y., 2004. The fabrication of high sensitive spin-valve sensor for magnetic bead detection. *Physica Status Solidi A – Applied Research*, 201, 1961-1964

Ref. 117: Miller, M.M., Prinz, G.A., Cheng, S.F., Bounnak, S., 2002. Detection of a micron-sized magnetic sphere using a ring-shaped anisotropic magnetoresistance-based sensor: A model for a magnetoresistance-based biosensor. *Applied Physics Letters*, 81, 2211-2213

- Ref. 118: Brzeska, M., Panhorst, M., Kamp, P.B., Schotter, J., Reiss, G., Pühler, A., Becker, A., Brückl, H., 2004. Detection and manipulation of biomolecules by magnetic carriers. *Journal of Biotechnology*, 112, 25-33
- Ref. 119: Willner, I., Willner, B., 2001. Biomaterials integrated with electronic elements: en route to bioelectronics. *Trends in Biotechnology*, 19, 222-230
- Ref. 120: CrysTec GmbH, www.crystec.de
- Ref. 121: Leybold Vakuum GmbH, www.leyboldvac.de
- Ref. 122: Roth & Rau GmbH, RR 160 PQE oxygen plasm source, www.roth-rau.de
- Ref. 123: Thomas, A., 2003. Preparation and characterization of magnetic single and double barrier junctions. Doctoral's Thesis, University of Bielefeld, Department of Physics, Germany
- Ref. 124: Hüttinger Elektronik GmbH, PFG 300 RF generator, www.huettinger-elektronik.com
- Ref. 125: ALLRESIST GmbH, www.allresist.de
- Ref. 126: LEO series 1530 field emission electron microscope, www.leo-em.co.uk
- Ref. 127: Raith ELPHY Plus lithography system, www.raith.de
- Ref. 128: Heidelberg Instruments GmbH, DWL 66 direct write system, www.himt.de
- Ref. 129: Omnichrome Series 74 HeCd laser, www.mellesgriot.com
- Ref. 130: Thermo Electron Corp., www.thermo.com
- Ref. 131: Roth&Rau AG, UniLab system, www.roth-rau.de
- Ref. 132: Oxford Instruments, Link ISIS Series 300, www.oxford-instruments.com
- Ref. 133: Nanometrics Inc., Model 210 AFTMS, www.nanometrics.com
- Ref. 134: Veeco Instruments Inc., Model Nanoscope III, www.veeco.com
- Ref. 135: Olympus Corp., ultra sharp etched silicon probes, www.olympus.com
- Ref. 136: Justus, M., 2003. Magnetische Tunnelelemente mit Pulsplasma-oxidierten Barrieren und Elektroden aus Kobalt-Chrom Legierungen. Doctoral's Thesis, University of Bielefeld, Department of Physics, Germany
- Ref. 137: Keithley Instruments Inc., Model 2000 digital multimeter, www.keithley.com
- Ref. 138: Sypris Test & Measurement, Bell 6010 Hall Effect Gauss/Tesla meter, www.fwbell.com
- Ref. 139: Princeton Measurement Corporation, MicroMag Model 2900, www.princetonmeasurements.com
- Ref. 140: Personal discussions with P.B. Kamp, 2000-2003. Department of Biology, University of Bielefeld, Universitätsstraße 25, 33615 Bielefeld, Germany
- Ref. 141: Ali-Zade, R.A., 2004. Structure and magnetic properties of polymer microspheres filled with magnetite nanoparticles. *Inorganic Materials*, 40, 509-515

Ref. 142: O'Handley, R.C., 2000. Modern magnetic materials – principles and applications. John Wiley & Sons, Inc., New York

Ref. 143: Bozorth, R.M., 1978. Ferromagnetism. IEEE Press, The Institute of Electrical and Electronics Engineers, New York

Ref. 144: Jackson, J.D., 2001. Klassische Elektrodynamik. Walter de Gruyter GmbH & Co. KG, Berlin

Ref. 145: Spherotech Inc., www.spherotech.com

Ref. 146: Bangs Laboratories Inc., www.bangslabs.com

Ref. 147: Chemagen AG, www.chemagen.de

Ref. 148: Gmelin-Durrer, 1964. Metallurgie des Eisens. 4. Auflage, Band 1a, Verlag Chemie GmbH, Weinheim/Bergstr.

Ref. 149: National Institute of Standards and Technology, www.nist.gov

Ref. 150: Voet, D., Voet, J.G., 1994. Biochemie. VCH Verlagsgesellschaft mbH, Weinheim

Ref. 151: Protein Data Bank, www.rcsb.org/pdb

**Ref. 152: Images taken from Stefanie Freitag's web site:
www.faculty.washington.edu/stenkamp/stefanieweb/abstract.html**

Ref. 153: Le Trong, I., Freitag, S., Klumb, L.A., Chu, V., Stayton, P.S., Stenkamp, R.E., 2003. Structural studies of hydrogen bonds in the high-affinity streptavidin-biotin complex: mutations of amino acids interacting with the ureido oxygen of biotin. Acta Crystallographica Section D, 59, 1567-1573

Ref. 154: Weber, P.C., Ohlendorf, D.H., Wendoloski, J.J., Salamme, F.R., 1989. Structural origins of high-affinity biotin binding to streptavidin. Science, 243, 85-88

Ref. 155: Spherotech Inc., www.spherotech.com/tech.htm

Ref. 156: Cardarelli, F., 2000. Materials Handbook. Springer Verlag London

Ref. 157: Chemagen AG, www.chemagen.de/de_uk/uk/firstset_features.html

Ref. 158: Sun, S.H., Murray, C.B., 1999. Synthesis of monodisperse cobalt nanocrystals and their assembly into magnetic superlattices (invited). Journal of Applied Physics, 85, 4325-4330

Ref. 159: Puntès, V.F., Krishnan, K.M., Alivisatos, A.P., 2001. Colloidal nanocrystal shape and size control: The case of cobalt. Science, 291, 2115-2117

Ref. 160: Sun, S.H., Anders, S., Thomson, T., Baglin, J.E.E., Toney, M.F., Hamann, H.F., Murray, C.B., Terris, B.D., 2003. Controlled synthesis and assembly of FePt nanoparticles. Journal of Physical Chemistry B, 107, 5419-5425

Ref. 161: Dubois, E., Cabuil, V., Boue, F., Perzynski, R., 1999. Structural analogy between aqueous and oily magnetic fluids. Journal of Chemical Physics, 111, 7147-7160

Ref. 162: Berger, P., Adelman, N.B., Beckman, K.J., Campbell, D.J., Ellis, A.B., Lisensky, G.C., 1999. Preparation and properties of an aqueous ferrofluid. Journal of Chemical Education, 76, 943-948

- Ref. 163: Dresco, P.A., Zaitsev, V.S., Gambino, R.J., Chu, B., 1999. Preparation and properties of magnetite and polymer magnetite nanoparticles. *Langmuir*, 15, 1945-1951**
- Ref. 164: Santra, S., Tapeç, R., Theodoropoulou, N., Dobson, J., Hebard, A., Tan, W.H., 2001. Synthesis and characterization of silica-coated iron oxide nanoparticles in microemulsion: The effect of nonionic surfactants. *Langmuir*, 17, 2900-2906**
- Ref. 165: Zhao, X.J., Tapeç-Dytioco, R., Wang, K.M., Tan, W.H., 2003. Collection of trace amounts of DNA/mRNA molecules using genomagnetic nanocaptors. *Analytical Chemistry*, 75, 3476-3483**
- Ref. 166: Butler, R.F., Banerjee, S.K., 1975. Theoretical single-domain grain-size range in magnetite and titanomagnetite. *Journal of Geophysical Research*, 80, 4049-4058**
- Ref. 167: Onyiriuka, E.C., Kinney, L.D., Binkowski, N.J., 1997. Adhesion and delamination of tantalum and chromium films on glass. *Journal of Adhesion Science and Technology*, 11, 929-940**
- Ref. 168: Kuchling, H., 1995. *Taschenbuch der Physik*. Fachbuchverlag Leipzig GmbH**
- Ref. 169: Mathon, J., 1991. Exchange interactions and giant magnetoresistance in magnetic multilayers. *Contemporary Physics*, 32, 143-156**
- Ref. 170: Mott, N.F., 1964. Electrons in transition metals. *Advances in Physics*, 13, 325-420**
- Ref. 171: Parkin, S.S.P., More, N., Roche, K.P., 1990. Oscillations in exchange coupling and magnetoresistance in metallic superlattice structures: Co/Ru, Co/Cr, and Fe/Cr. *Physical Review Letters*, 64, 2304-2307**
- Ref. 172: Parkin, S.S.P., 1991. Systematic variation of the strength and oscillation period of indirect magnetic exchange coupling through the 3d, 4d, and 5d transition metals. *Physical Review Letters*, 67, 3598-3601**
- Ref. 173: Bloemen, P.J.H., Dejonge, W.J.M., Coehoorn, P., 1993. Interlayer coupling in Co/Os multilayers. *Journal of Magnetism and Magnetic Materials*, 121, 306-308**
- Ref. 174: Johnson, M.T., Coehoorn, R., de Vries, J.J., McGee, N.W.E., aan de Stegge, J., Bloemen, P.J.H., 1992. Orientational dependence of the oscillatory exchange interaction in Co/Cu/Co. *Physical Review Letters*, 69, 969-972**
- Ref. 175: Purcell, S.T., Folkerts, W., Johnson, M.T., McGee, N.W.E., Jager, K., aan de Stegge, J., Zeper, W.B., Hoving, W., 1991. Oscillations with a period of two monolayers in the antiferromagnetic exchange coupling in a (001) Fe/Cr/Fe sandwich structure. *Physical Review Letters*, 67, 903-906**
- Ref. 176: Stiles, M.D., 1993. Exchange coupling in magnetic heterostructures. *Physical Review B*, 48, 7238-7258**
- Ref. 177: Coehoorn, R., 1991. Period of oscillatory exchange interaction in Co/Cu and Fe/Cu multilayer systems. *Physical Review B*, 44, 9331-9337**
- Ref. 178: Levy, P.M., Ounadjela, K., Zhang, S., Wang, Y., Sommers C.B., Fert, A., 1990. Theory of magnetic superlattices: Interlayer exchange coupling and magnetoresistance of transition metal structures (invited). *Journal of Applied Physics*, 67, 5914-5919**

Ref. 179: Edwards, D.M., Mathon, J., Munitz, R.B., Phan, M.S., 1991. Oscillations in the exchange coupling of ferromagnetic layers separated by a nonmagnetic metallic layer. *Journal of Physics: Condensed Matter*, 3, 4941-4958

Ref. 180: Bruno, P., 1995. Theory of interlayer magnetic coupling. *Physical Review B*, 411-439

Ref. 181: Jones, B.A., 1998. Theory of exchange coupling in magnetic multilayers. *IBM Journal of Research and Development*, 42, 25-31

Ref. 182: Yafet, Y., 1987. Ruderman-Kittel-Kasuya-Yosida range function of a one-dimensional free electron gas. *Physical Review B*, 36, 3948-3949

Ref. 183: Anderson, P.W., 1961. Localized magnetic states in metals. *Physical Review Letters*, 124, 41-53

Ref. 184: Shi, Z.P., Levy, P.M., Fry, J.L., 1994. Interlayer magnetic coupling in metallic multilayer structures. *Physical Review B*, 49, 15159-15178

Ref. 185: Mathon, J., Villeret, M., Muniz, R.B., d'Albuquerque e Castro, J., Edwards, D.M., 1994. Quantum Well Theory of the Exchange Coupling in Co/Cu/Co(001). *Physical Review Letters*, 74, 3696-3699

Ref. 186: Grünberg, G., 1999. *Magnetische Schichtsysteme, Chapter B9: Zwischenschichtaustauschkopplung: Phänomenologische Beschreibung, Materialabhängigkeit. Sommerschule 1999 Forschungszentrum Jülich*

Ref. 187: Bürgler, D.E., 1999. *Magnetische Schichtsysteme, Chapter B10: Zwischenschichtaustauschkopplung: Abhängigkeit vom Schichtaufbau und der Qualität der Grenzflächen. Sommerschule 1999 Forschungszentrum Jülich*

Ref. 188: Edwards, D.M., Mathon, J., Munitz R.B., 1991. A resistor network theory of the giant magnetoresistance in magnetic superlattices. *IEEE Transactions on Magnetics*, 27, 3548-3552

Ref. 189: Mathon, J., 1988. Magnetism at transition metal surfaces. *Reports on Progress in Physics*, 51, 1-56

Ref. 190: Parkin, S.S.P., Bhadra, R., Roche, K.P., 1991. Oscillatory magnetic exchange coupling through thin copper layers. *Physical Review Letters*, 66, 2152-2155

Ref. 191: Parkin, S.S.P., Li, Z.G., Smith, D.J., 1991. Giant magnetoresistance in antiferromagnetic Co/Cu multilayers. *Applied Physics Letters*, 58, 2710-2712

Ref. 192: Parkin, S.S.P., 1994. Giant magnetoresistance and oscillatory interlayer coupling in polycrystalline transition metal multilayers. *Ultrathin Magnetic Structures II*, Springer Verlag Berlin, Heidelberg, New York

Ref. 193: Gurney, B.A., Speriosu V.S., Nozieres J.S., Lefakis H., Wilhoit D.R., Need O.U., 1993. Direct measurement of spin-dependent conduction electron mean free paths in ferromagnetic metals. *Physical Review Letters* 71, 4023-4026

Ref. 194: Gregg, J.F., Petej I., Jouguelet, E., Dennis, C., 2002. Spin electronics – a review. *Journal of Physics D: Applied Physics*, 35, R121-R155

Ref. 195: Tsymbal, E.Y., Pettifor, D.G., 2001. Perspectives of giant magnetoresistance. *Solid State Physics – Advances in Research and Applications*, 56, 113-237

Ref. 196: Camley, R.E., Barnas, J., 1989. Theory of giant magnetoresistance effects in magnetic layered structures with antiferromagnetic coupling. *Physical Review Letters*, 63, 664-667

- Ref. 197: Asano, Y., Oguri, A., Maekawa, S., 1993. Parallel and perpendicular transport in multilayered structures. *Physical Review B*, 48, 6192-6198**
- Ref. 198: Schep, K.M., Kelly, P.J., Bauer, G.E.W., 1998. Ballistic transport and electronic structure. *Physical Review B*, 57, 8907–8926**
- Ref. 199: Mathon, J., Umerski, A., Villeret, M., 1997. Oscillations with Co and Cu thickness of the current-perpendicular-to-plane giant magnetoresistance of a Co/Cu/Co(001) trilayer. *Physical Review B*, 55, 14378–14386**
- Ref. 200: Ashcroft, N.W., Mermin, N.D., 1976. *Solid State Physics*. Saunders College Publishing, Philadelphia, USA**
- Ref. 201: Landauer, R., 1988. Spatial variation of currents and fields due to localized scatterers in metallic conduction. *IBM Journal of Research and Development*, 32, 306**
- Ref. 202: Heitmann, S., 2000. Charakterisierung und Analyse von Cu/Py-Mehrlagenschichten mit variierenden Kupferschichtdicken. Diploma's Thesis, University of Bielefeld, Department of Physics, Germany**
- Ref. 203: Object Oriented MicroMagnetic Framework, <http://math.nist.gov/oommf>**
- Ref. 204: Gilbert, T.L., 1955. A Lagrangian formulation of the gyromagnetic equation of the magnetization field. *Physical Review Letters*, 100, 1243**
- Ref. 205: Sommerfeld, A., Bethe, H., 1933. *Handbuch der Physik*, vol. 24, part 2, page 333, Verlag Julius Springer, Berlin**
- Ref. 206: Tedrow, P.M., Meservey, R., 1971. Spin-dependent tunneling into ferromagnetic Nickel. *Physical Review Letters*, 26, 192-195**
- Ref. 207: Giaever, I., 1960. Energy gap in superconductors measured by electron tunneling. *Physical Review Letters*, 5, 147-148**
- Ref. 208: Tedrow, P.M., Meservey, R., 1973. Spin polarization of electrons tunneling from films of Fe, Co, Ni and Ga. *Physical Review B*, 7, 318-326**
- Ref. 209: LeClair, P., 2002. Fundamental aspects of spin polarized tunneling. PhD thesis, Technische Universiteit Eindhoven**
- Ref. 210: Papaconstantopoulos, D.A., 1986. *Handbook of the band structures of elemental solids*. Plenum, New York**
- Ref. 211: Stearns, B.A., 1977. Simple explanation of tunneling spin-polarization of Fe, Co, Ni and its alloys. *Journal of Magnetism and Magnetic Materials*, 5, 167-171**
- Ref. 212: Tsymbal, E.Y., Pettifor, D.G., 1997. Modeling of spin-polarized electron tunneling from 3d ferromagnets. *Journal of Physics – Condensed Matter*, 9, L411-L417**
- Ref. 213: Wolf, E.L., 1985. *Principles of electron tunneling spectroscopy*. Oxford University Press, London**
- Ref. 214: Simmons, J.G., 1963. Generalized formula for the electrical tunnel effect between similar electrodes separated by a thin insulating film. *Journal of Applied Physics*, 34, 1793-1803**
- Ref. 215: Stratton, R., 1962. Volt-current characteristics for tunneling through insulating films. *Journal of Physics and Chemistry of Solids*, 23, 1177-1190**

- Ref. 216: Brinkman, W.F., Dynes, R.C., Rowell, J.M., 1970. Tunneling conductance of asymmetrical barriers. *Journal of Applied Physics*, 41, 1915-1921**
- Ref. 217: Nolting, W., 1997. *Grundkurs Theoretische Physik 5 Quantenmechanik, Teil 2: Methoden und Anwendungen*. Friedrich Vieweg & Sohn Verlagsgesellschaft mbH, Braunschweig/Wiesbaden**
- Ref. 218: Bratkovski, A.M., 1997. Tunneling of electrons in conventional and half-metallic systems: towards very large magnetoresistance. *Physical Review B*, 56, 2344-2347**
- Ref. 219: Mathon, J., 1997. Tight-binding theory of tunneling giant magnetoresistance. *Physical Review B*, 56, 11801-11819**
- Ref. 220: Tsymbal, E.Y., Mryasov, O.N., LeClair, P.R., 2003. Spin-dependent tunneling in magnetic tunnel junctions. *Journal of Physics: Condensed Matter*, 15, R109-R142**
- Ref. 221: Moodera, J.S., Mathon, G., 1999. Spin polarized tunneling in ferromagnetic junctions. *Journal of Magnetism and Magnetic Materials*, 200, 248-273**
- Ref. 222: Slonczewski, J.C., 1989. Conductance and exchange coupling of two ferromagnets separated by a tunneling barrier. *Physical Review B*, 39, 6995-7002**
- Ref. 223: Meiklejohn, W.H., Bean, C.P., 1956. New magnetic anisotropy. *Physical Review* 102, 1413-1414**
- Ref. 224: Nogués, J., Schuller, I.K., 1999. Exchange bias. *Journal of Magnetism and Magnetic Materials*, 192, 203-232**
- Ref. 225: Beschoten, B., Tillmanns, A., Keller, J., Güntherodt, G., Nowak, U., Usadel, D., 2002. Domain state model for exchange bias: influence of structural defects on exchange bias in Co/CoO. *Advances in Solid State Physics*, 42, 419-431, Springer-Verlag Berlin**
- Ref. 226: Berkowitz, A.E., Takano, K., 1999. Exchange anisotropy – a review. *Journal of Magnetism and Magnetic Materials*, 200, 552-570**
- Ref. 227: Néel, N., 1962. On a new mode of coupling between the magnetizations of two thin ferromagnetic layers. *Comptes Rendus*, 255, 1676**
- Ref. 228: Zhang, J., White, R.M., 1996. Topological coupling in spin valve type multilayers. *IEEE Transactions on Magnetics*, 32, 4630-4635**
- Ref. 229: Kools, J.C.S., Kula, W., Mauri, D., Lin, T., 1999. Effect of finite magnetic film thickness on Néel coupling in spin valves. *Journal of Applied Physics*, 85, 4466-4468**
- Ref. 230: Tegen, S., Mönch, I., Schumann, J., Vinzelberg, H., Schneider, C.M., 2001. Effect of Néel coupling on magnetic tunnel junctions. *Journal of Applied Physics*, 89, 8169-8174**
- Ref. 231: Iwasaki, H., Saito, A.T., Tsutai, A., Sahashi, M., 1997. Excellent reliability of CoFe-IrMn spin valves. *IEEE Transactions on Magnetics*, 33, 2875-2877**
- Ref. 232: Fuke, H.N., Saito, K., Kamiguchi, Y., Iwasaki, H., Sahashi, M., 1997. Spin-valve giant magnetoresistive films with antiferromagnetic Ir-Mn layers. *Journal of Applied Physics*, 81, 4004-4006**
- Ref. 233: Anderson, G., Huai, Y., Miloslawski, L., 2000. CoFe/IrMn exchange biased top, bottom and dual spin valves. *Journal of Applied Physics*, 87, 6989-6991**

Ref. 234: Sauter, M., 2001. Skriptum zur Vorlesung "Technologie integrierter Schaltungen". Universität der Bundeswehr, München, <http://www.unibw-muenchen.de/ETTI/we2/sauter/homepage/TIS-1.pdf>

Ref. 235: Schmalhorst, J., 2001. Magnetische, thermische und dielektrische Stabilität von magnetischen Tunnelementen. Doctoral's Thesis, University of Bielefeld, Department of Physics, Germany

Ref. 236: Tsunoda, M., Nishikawa, K., Ogata, S., Takahashi, M., 2002. 60% magnetoresistance at room temperature in Co-Fe/Al-O/Co-Fe tunnel junctions oxidized with Kr-O₂ plasma. *Applied Physics Letters*, 80, 3135-3137

Ref. 237: Güntherodt, G., Rüdiger, U., 1999. Magnetische Schichtsysteme, Chapter A9: Magnetische Festkörper. Sommerschule 1999 Forschungszentrum Jülich

Ref. 238: Yagami, K., Tsunoda, M., Takahashi, M., 2001. Enhancement of exchange bias in Mn-Ir/Co-Fe based spin valves with an ultrathin Cu underlayer and in situ Mn-Ir surface modification. *Journal of Applied Physics*, 89, 6609-6611

Ref. 239: Stoner, E.C., Wohlfarth, E.P., 1948. A mechanism of magnetic hysteresis in heterogeneous alloys. *Philosophical Transactions of the Royal Society of London, Series A, Mathematical and Physical Sciences*, 240, 599-642

Ref. 240: Brückl, H., Brzeska, M., Brinkmann, D., Schotter, J., Reiss, G., Schepper, W., Kamp, P.B., Becker, A., 2004. Magnetoresistive Logic and Biochip. *Journal of Magnetism and Magnetic Materials* (in print)

Ref. 241: Kim, T., Park, S.J., Noh, J., Park, W., Song, I.H., Kim, Y.K., 2004. Current aspects and future perspectives of high-density MRAM. *Physica Status Solidi A - Applied Research*, 201, 1617-1620

Ref. 242: TeleChem International, Inc., SuperClean substrate, www.arrayit.com

Acknowledgements

First of all, I want to thank my supervisors Dr. Hubert Brückl and Prof. Günter Reiss from the Physics Department and their colleagues Dr. Anke Becker and Prof. Alfred Pühler in the Department of Genetics for bringing the magnetic biosensor project to life at the University of Bielefeld. Without their great efforts, financial support by the BMBF project “Magnetoresistive Biosensor” (grant number 13N7859) and later by the Sonderforschungsbereich 613 (“Physics of single molecule processes”) would not have been possible. In cooperation with their colleagues Dr. Andreas Hütten, Dr. Jan Schmalhorst and Dr. Willi Schepper, my supervisors were always open for discussions and, while allowing independent work at all times, provided qualified help whenever problems emerged on the path towards our common and well defined goal.

No less important was the productive and close cooperation with my colleague Dr. Paul-Bertram Kamp from the Department of Genetics. Without his expertise in all the practical matters of molecular biology and his fruitful input to the entire project, it would not have been possible to successfully realize the work described in this thesis.

As the group of people concerned with the biosensor project increased over time, I want to thank Michael Panhorst, Dirk Brinkmann and Monika Brzeska for their input and fruitful discussions. Concerning the analysis and interpretation of tunneling magnetoresistance, I would like to thank Dr. Jan Schmalhorst, Dr. Andy Thomas, Dr. Maik Justus and Dr. Karsten Rott for their expertise. The same is true concerning giant magnetoresistance for Dr. Andreas Hütten and Dr. Sonja Heitmann.

I also would like to thank Dr. Maik Justus, Dr. Andy Thomas and Dr. Karsten Rott for introducing me to the laboratory and helping me with all aspects like data acquisition and analysis, sputter-deposition or lithography. In particular, I want to thank Dr. Andy Thomas for realizing the image analysis software described in chapter 5.4.2 and Dr. Maik Justus and Andreas Stabaginski for programming the software that calculates the GMR and TMR ratios from the respective magnetization files of the oommf model system (see chapter 5.3 and 6.4). Furthermore, Dr. Maik Justus also provided decisive help in implementing the stray fields of magnetic markers into the oommf code, developed a program that automatically generates design files for spiral shaped sensor lines (see chapter 5.2) and realized the software for the Biot-Savart type field calculation of the Helmholtz coils.

Additionally, I would like to thank Jan Bornemeier for his help with wire-bonding, Dirk Meyners and Dirk Brinkmann for introducing me to the AFM, Inga Ennen and Daniela Sudfeld for carrying out AGM measurements and Dr. Andy Thomas and Marc Sacher for improving and upkeeping our main sputtering tool.

Furthermore, I want to thank Dr. Sonja Heitmann, Sven Kämmerer and Tobias Hempel for introducing me to the fabrication and analysis of giant magnetoresistance and improving and upkeeping the relevant machines and instruments.

I would also like to thank Dr. Ulf Kleineberg for allowing me to use the DekTak profilometer owned by the research group of Prof. Ulrich Heinzmann and for trying to remove resist remnants by their oxygen plasma machine.

Moreover, I want to show appreciation to the mechanical and the electronics workshop for their competent and mostly prompt implementation of my plans. In particular, I would like to thank J. Warmesbach for realizing the shielded differential amplifier setup described in chapter [2.8](#).

Additionally, I would like to thank Prof. Tomasz Stobiecki and Miroslaw Zoladz from the Department of Electrical Engineering at the University of Mining and Metallurgy in Krakow, Poland for their effort to directly image the magnetization reconfiguration induced by magnetic markers by Kerr microscopy.

Finally, I want to thank all my colleagues from the level D2 for the excellent helpfulness and great working atmosphere. I really enjoyed my time here.